

**Pore-scale Study of Flow and Transport in Energy Georeservoirs**

Ming Fan

Dissertation submitted to the faculty of the Virginia Polytechnic Institute and State  
University in partial fulfillment of the requirements for the degree of

Doctor of Philosophy  
In  
Mining Engineering

Cheng Chen, Chair  
Erik C. Westman  
Nino S. Ripepi  
Yanhui Han

June 19, 2019  
Blacksburg, Virginia

Keywords: fracture conductivity, proppant embedment and compaction, proppant  
mixture, single-/multiphase flow, fine particle migration

Copyright (2019)

## Pore-scale Study of Flow and Transport in Energy Georeservoirs

Ming Fan

### **ABSTRACT**

Optimizing proppant pack conductivity and proppant-transport and -deposition patterns in a hydraulic fracture is of critical importance to sustain effective and economical production of petroleum hydrocarbons. In this research, a numerical modeling approach, combining the discrete element method (DEM) with the lattice Boltzmann (LB) simulation, was developed to provide fundamental insights into the factors regulating the interactions between reservoir depletion, proppant-particle compaction and movement, single-/multiphase flows and non-Darcy flows in a hydraulic fracture, and fracture conductivity evolution from a partial-monolayer proppant concentration to a multilayer proppant concentration. The potential effects of mixed proppants of different sizes and types on the fracture conductivity were also investigated.

The simulation results demonstrate that a proppant pack with a smaller diameter coefficient of variation (COV), defined as the ratio of standard deviation of diameter to mean diameter, provides better support to the fracture; the relative permeability of oil was more sensitive to changes in geometry and stress; when effective stress increased continuously, oil relative permeability increased nonmonotonically; the combination of high diameter COV and high effective stress leads to a larger pressure drop and consequently a stronger non-Darcy flow effect. The study of proppant mixtures shows that mixing of similar proppant sizes (mesh-size-20/40) has less influence on the overall fracture conductivity than mixing a very fine mesh size (mesh-size-100); selection of proppant type is more important than proppant size selection when a proppant mixture is

used. Increasing larger-size proppant composition in the proppant mixture helps maintain fracture conductivity when the mixture contains lower-strength proppants. These findings have important implications to the optimization of proppant placement, completion design, and well production.

In the hydraulic-mechanical rock-proppant system, a fundamental understanding of multiphase flow in the formation rock is critical in achieving sustainable long-term productivity within a reservoir. Specifically, the interactions between the critical dimensionless numbers associated with multiphase flow, including contact angle, viscosity ratio, and capillary number ( $Ca$ ), were investigated using X-ray micro computed tomography (micro-CT) scanning and LB modeling. The primary novel finding of this study is that the viscosity ratio affects the rate of change of the relative permeability curves for both phases when the contact angle changes continuously. Simulation results also indicate that the change in non-wetting fluid relative permeability was larger when the flow direction was switched from vertical to horizontal, which indicated that there was stronger anisotropy in larger pore networks that were primarily occupied by the non-wetting fluid. This study advances the fundamental understanding of the multiphysics processes associated with multiphase flow in geologic materials and provides insight into upscaling methodologies that account for the influence of pore-scale processes in core- and larger-scale modeling frameworks.

During reservoir depletion processes, reservoir formation damage is an issue that will affect the reservoir productivity and various phases in fluid recovery. Invasion of formation fine particles into the proppant pack can affect the proppant pack permeability, leading to potential conductivity loss. The combined DEM-LB numerical framework was

used to evaluate the role of proppant particle size heterogeneity (variation in proppant particle diameter) and effective stress on the migration of detached fine particles in a proppant supported fracture. Simulation results demonstrate that a critical fine particle size exists: when a particle diameter is larger or smaller than this size, the deposition rate increases; the transport of smaller fines is dominated by Brownian motion, whereas the migration of larger fines is dominated by interception and gravitational settling; this study also indicates that proppant packs with a more heterogeneous particle-diameter distribution provide better fines control. The findings of this study shed lights on the relationship between changing pore geometries, fluid flow, and fine particle migration through a propped hydraulic fracture during the reservoir depletion process.

## Pore-scale Study of Flow and Transport in Energy Georeservoirs

Ming Fan

### **GENERAL AUDIENCE ABSTRACT**

Hydraulic fracturing stimulation design is required for unconventional hydrocarbon energy (e.g., shale oil and gas) extraction due to the low permeability and complex petrophysical properties of unconventional reservoirs. During hydrocarbon production, fractures close after pumping due to the reduced fluid pressure and increased effective stress in rock formations. In the oil and gas industry, proppant particles, which are granular materials, typically sand, treated sand, or man-made ceramic materials, are pumped along with fracturing fluids to prevent hydraulic fractures from closing during hydrocarbon extraction. In order to relate the geomechanical (effective stress), geometric (pore structure and connectivity), and transport (absolute permeability, relative permeability, and conductivity) properties of a proppant assembly sandwiched in a rock fracture, a geomechanics-fluid mechanics framework using both experiment and simulation methods, was developed to study the interaction and coupling between them. The outcome of this research will advance the fundamental understanding of the coupled, multiphysics processes with respect to hydraulic fracturing and benefit the optimization of proppant placement, completion design, and well production.

## DEDICATION

*To my lovely family members.*

*I love you all no matter what.*

## Acknowledgements

I would like to take this opportunity to express my sincere gratitude to my advisor, Dr. Cheng Chen for his advice and continuing support throughout the period of my Ph.D. study at Virginia Tech. I feel privileged to work in such an opportunistic and vibrant research group, which created a solid foundation for my professional growth. I would also like to give my special thanks to Dr. Yanhui Han for serving as my co-advisor and providing me guidance on finite element modeling and discrete element modeling, as well as training on Itasca software FLAC3D, PFC3D, and UDEC. Thanks are due to the members of my Ph.D. Advisory Committee, Dr. Erik Westman and Dr. Nino Ripepi, for their valuable time and efforts to review my dissertation.

Financial support to this study was provided by the Junior Faculty Award granted to Dr. Cheng Chen by Virginia Tech's Institute for Critical Technology and Applied Science. Special thanks are due to Dr. James McClure for his technical training on the multiphase flow studies, and Dr. Dustin Crandall and Miss Laura Dalton for their assistance in conducting laboratory multiphase flow experiments.

I appreciate the assistances from my fellow students, Xu Tang, Jing Zhang, Kaiwu Huang, Shushu Liu, Biao Li, Zihao Li, Yuntian Teng, Hongsheng Wang, Ruichang Guo, Fengshuang Du, Xinyu Tan, Yue Hu, Kaiyi Zhang.

Finally, I wish to thank my parents, Lianxiang Fu and Ziyu Fan, my brother Liang Fan, and my wife Ge Zhang for their love, encouragement, and supports as always.

# Table of Contents

Table of Contents .....	viii
List of Figures .....	xiii
List of Tables .....	xx
PREFACE.....	xxi
Chapter 1 – Introduction .....	1
1.1 Background.....	1
1.2 Research objectives and work scope.....	5
1.3 Organization of this dissertation .....	7
References.....	12
Chapter 2 - Interaction between Reservoir Depletion, Proppant Compaction, and Single- /Multiphase Flows in a Hydraulic Fracture .....	16
2.1. Introduction.....	17
2.2. Overview of Numerical Workflow .....	19
2.2.1 Basics of PFC3D.....	20
2.2.2 Discretization of 3D Proppant Pore Structure .....	21
2.2.3 Lattice Boltzmann Method for Single-Phase Flow Simulation .....	22
2.2.4 Lattice Boltzmann Method for Multiphase Flow Simulation .....	26
2.3. Proppant Compaction Studies.....	29
2.4. Results and Discussion .....	30



2.5. Conclusions and Implications .....	47
References.....	52
 Chapter 3 - Using an Experiment/Simulation-integrated Approach to Investigate Fracture-Conductivity Evolution and Non-Darcy Flow in a Proppant-supported Hydraulic Fracture .....	 58
3.1 Introduction.....	59
3.2 Overview of Technical Elements in Workflow .....	65
3.2.1 Optimal Partial-monolayer Proppant Concentration .....	65
3.2.2 Overview of the Experiment/Simulation-integrated Workflow and Compaction Studies.....	68
3.2.3 Embedment experiment and load–embedment correlation.....	72
3.2.4 Non-Darcy flow .....	74
3.2.5 Basics of PFC3D.....	77
3.2.6 Discretization of 3D proppant pore structure.....	78
3.2.7 Lattice Boltzmann method for single-phase flow simulation .....	78
3.3 Results and Discussion .....	82
3.4 Conclusions and Implications .....	99
References.....	104
 Chapter 4 - Investigating the Impact of Proppant Embedment and Compaction on Fracture Conductivity using a Continuum Mechanics, DEM, and LBM Coupled Approach.....	 112
4.1 Introduction.....	113

4.2 Numerical model description .....	114
4.2.1 Overview of numerical workflow .....	114
4.2.2 Coupling FLAC3D with PFC3D .....	115
4.2.3 Discretization of 3D Proppant Packs .....	116
4.2.4 Lattice Boltzmann Method for Single-Phase Flow Simulation .....	117
4.3 Proppant compression studies .....	118
4.4 Results and discussion .....	120
4.5 Conclusions and implications .....	128
References .....	129
Chapter 5 Combining Discrete Element Method with Lattice Boltzmann Modeling to Advance the Understanding of the Conductivity of Proppant Mixtures in a Propped Hydraulic Fracture .....	132
5.1 Introduction .....	133
5.2 Overview of Technical Elements in Workflow .....	137
5.2.1 DEM and PFC3D .....	137
5.2.2 Discretization of 3D proppant pore structure .....	139
5.2.3 Lattice Boltzmann method .....	139
5.2.4 Proppant embedment .....	142
5.3 Simulation Procedures .....	144
5.4 Simulation Results .....	147
5.4.1 Validation with embedment test .....	147
5.4.2 Effects of proppant concentration .....	149
5.4.3 Effects of loading stress .....	152

5.4.4 Effects of proppant size mixture .....	154
5.4.5 Effects of proppant type mixture .....	160
5.5 Conclusions and Discussions .....	165
References.....	168
Chapter 6 Comprehensive study of the interactions between the critical dimensionless numbers associated with multiphase flow in 3D porous media.....	174
6.1. Introduction.....	175
6.2. Methods.....	180
6.2.1 Core flooding experiments and X-ray micro-CT imaging.....	180
6.2.2. Lattice Boltzmann method for multiphase flow simulation .....	182
6.3. Important dimensionless numbers .....	186
6.4. Results and Discussion .....	189
6.4.1 Pore-scale contact angle measurement and SEM/EDX characterization .....	189
6.4.2 Comparison between CT-scanned and LB-simulated water/CO <sub>2</sub> distributions .....	192
6.4.3 Comprehensive sensitivity analyses for various combinations of dimensionless numbers.....	194
6.4.4 Effect of contact angle .....	198
6.4.5 Effect of viscosity ratio.....	199
6.4.6 Effect of Ca number.....	201
6.4.7 Effect of anisotropy and spatial heterogeneity.....	203
6.5. Conclusions.....	206
References.....	212

Chapter 7 Combining Discrete Element Method with Lattice Boltzmann Modeling to Advance the Understanding of the Slow Migration of Detached Fine Particles through a Proppant Supported Fracture .....	222
7.1 Introduction.....	223
7.2 Methods.....	226
7.2.1 Models for Particle Migration through Porous Media.....	226
7.3 Overview of Numerical Workflow .....	230
7.3.1 Basics of PFC3D.....	230
7.3.2 Discretization of 3D Proppant Pore Structure .....	231
7.3.3 Lattice Boltzmann Method for Single-Phase Flow Simulation .....	232
7.4 Pore Structure Generation.....	235
7.5 Results and Discussion .....	237
7.6 Conclusion .....	247
References.....	251
Chapter 8 Conclusions and future work.....	257
8.1 Conclusions.....	257
8.2 Future work.....	259
8.3 Contributions.....	261
Appendix Copyright releasing documents from publishers.....	263

## List of Figures

Figure 1.1. Flow chart for the relationship between chapters.....	12
Figure 2.1. a) D3Q19 lattice structure, and b) proppant particles and permeability tensor in the fracture . .....	25
Figure 2.2. a) DEM-simulated 16/30-mesh-size proppant assembly of 30 mm × 30 mm × 5 mm under effective stress of 10 psi, and b) corresponding LB-simulated pressure distribution within the pore space of the 2D cross section. ....	31
Figure 2.3. LB-simulated flow velocity magnitude distributions within the pore space of a proppant assembly under effective stress of a) 10 psi, and b) 2200 psi.....	32
Figure 2.4. Comparison between numerical results and laboratory measurements.....	32
Figure 2.5. X-ray CT images of proppant particle crushing and embedment in a hydraulic fracture of a shale rock under effective stresses of a) 0, and b) 3000 psi. ....	34
Figure 2.6. a) Compressed distance, b) porosity, and c) normalized permeability as functions of effective stress. ....	36
Figure 2.7. Normalized proppant pack permeabilities as functions of porosity. ....	37
Figure 2.8. Porosity and effective stress as functions of subdomain diameter. ....	38
Figure 2.9. a) Mean effective stress, b) mean porosity, and c) mean normalized permeability associated with corresponding standard deviations (dashed lines) as functions of subdomain diameter.....	40
Figure 2.10. Oil phase distributions in steady-state two phase flow observed for diameter COVs of a) 5%, and b) 19%, respectively.....	42

Figure 2.11. Relative permeability curves determined from pore-scale multiphase LB simulations for the geometries having a) 5% diameter COV; and b) 19% diameter COV. .... 44

Figure 2.12. Effective pore diameters for the geometries having a) 5% diameter COV; and b) 19% diameter COV..... 45

Figure 2.13. Pore size distribution determined from maximum inscribed spheres for the geometries having a) 5% diameter COV, and b) 19% diameter COV. .... 47

Figure 3.1. Mitigation of proppant embedment in a vertical fracture with increasing proppant concentration..... 68

Figure 3.2. A hybrid, experiment/simulation-integrated workflow for calculating proppant compaction, embedment, as well as the influence on fracture conductivity. .... 70

Figure 3.3. a) Proppant particles and permeability tensor in a fracture, and b) D3Q19 lattice structure..... 76

Figure 3.4. Correlation between  $d/D$  and  $L/D^2$  based on the laboratory penetrometer experiments. The tests were conducted on three samples from the same tight sandstone formation..... 83

Figure 3.5. 2D cross sections of PFC-generated proppant assemblies having a) full-monolayer structure, and b) partial-monolayer structure. The dimensions of the cross section are  $10\text{ mm} \times 10\text{ mm}$ . Proppant concentrations are  $0.22\text{ lb/ft}^2$  and  $0.10\text{ lb/ft}^2$ , respectively. .... 84

Figure 3.6. Development of a) fracture conductivity, b) permeability, and c) width as a function of proppant concentration. These curves were obtained from the hybrid,

experiment/simulation integrated workflow. Proppant particle size is homogeneous and equal to 0.63 mm. Effective compressive stress imposed on the proppant is 1,000 psi. ... 87

Figure 3.7. Comparison between the workflow-derived and laboratory-measured fracture conductivity versus proppant concentration curves..... 90

Figure 3.8. Role of proppant particle size and effective stress on the fracture conductivity versus proppant concentration curve.. ..... 92

Figure 3.9. Optimal partial-monolayer proppant concentration as a function of effective stress..... 93

Figure 3.10. LB-simulated pressure distributions within the pore space of proppant assemblies having a) 5% diameter COV, and b) 25% diameter COV..... 95

Figure 3.11. Normalized apparent permeability,  $k_{app}/D_e^2$ , as a function of the  $Re$  number under various diameter COVs and effective stresses..... 96

Figure 3.12. a) Non-Darcy effect coefficient, and b) dimensionless inertial resistance factor, as a function of effective stress..... 97

Figure 3.13. Relative non-Darcy effect coefficient,  $E$ , as a function of  $Re$  number under effective stress of a) 1,200 psi and b) 6,000 psi..... 99

Figure 4.1. Coupled FLAC3D/PFC3D model for simulating a fracture/proppant system with fracture closure stress being 68.9 Mpa (10,000 psi). (a) FLAC3D model simulating sandstone matrix, (b) PFC3D model simulating compressed proppant pack connected with sandstone matrix with 30/50-mesh-size, (c) FLAC3D model simulating shale matrix, (d) PFC3D model simulating compressed proppant pack connected with shale matrix with 30/50-mesh-size, (e) profile of the sandstone matrix bottom surface, (f) profile of the shale matrix bottom surface. .... 122

Figure 4.2. (a) Fracture width, (b) permeability, and (c) conductivity as functions of effective stress. The rock matrix are modeled with sandstone and shale material and proppant packs are modeled with 20/40 and 30/50 mesh sizes ..... 124

Figure 4.3 illustrates LB-simulated pressure distributions within the pore space of proppant assemblies having (a) 5% diameter COV, and (b) 20% diameter COV..... 125

Figure 4.4. Development of (a) fracture width, (b) normalized fracture permeability, and (c) normalized fracture conductivity as functions of effective stress for proppant packs with 5%, 12%, and 20% diameter COVs..... 126

Figure 5.1. An integrated simulation workflow for calculating proppant compaction, embedment, as well as the influence on fracture conductivity. .... 145

Figure 5.2. Correlation between  $d/D$  and  $L/D^2$  based on the laboratory penetrometer experiments; the tests were conducted on three samples from the same tight sandstone formation..... 147

Figure 5.3. Comparison between the simulation predicted and laboratory result at 1,000 psi closure pressure ..... 149

Figure 5.4. LB-simulated pressure distributions within the pore space of proppant assemblies with (a) mesh-size-20 particles; (b) mesh-size-40 particles; and (c) mesh-size-20/40 (mixing weight ratio 1:1) particles..... 150

Figure 5.5. Development of fracture conductivity as a function of proppant concentration under effective stress of 2,000 psi..... 152

Figure 5.6. Proppant packs were generated with proppant concentration of (a) 0.1 lb/ft<sup>2</sup>, (b) 0.3 lb/ft<sup>2</sup>, (c) 1 lb/ft<sup>2</sup>, and (d) 2 lb/ft<sup>2</sup>. The proppant packs were generated with mesh-size-20/40 (mass ratio 1:1)..... 153



Figure 5.7. Fracture conductivity as a function of proppant concentration for proppant packs with mesh size 20/40 (mass ratio 1:1) under various effective stresses ..... 154

Figure 5.8. Fracture conductivity as a function of proppant concentration for proppant mixtures with different mass ratios under effective stress of (a) 2,000 psi, (b) 4,000 psi, and (c) 6,000 psi..... 156

Figure 5.9. Probability density functions (PDFs) of overall pore velocity for proppant packs with proppant concentrations of 2 lb/ft<sup>2</sup> under effective stress of 6,000psi ..... 157

Figure 5.10. LB-simulated flow-velocity-magnitude distributions within the pore space of the proppant assemblies (a) mesh-size-20/40 particles; (b) mesh-size-20/100 particles (mixing mass ratio 1:1); the void space represents proppant particles ..... 159

Figure 5.11. Fracture conductivity as a function of proppant concentration for proppant packs with mesh-size-20/100 (mass ratio 1:1) and mesh-size-100 under various effective stresses. .... 160

Figure 5.12. LB-simulated flow-velocity-magnitude distributions within the pore space of the proppant assemblies under effective stress of 6,000 psi; the proppant packs were generated with mesh size ratios of (a) 5:5 (20:40) in the top panel and (b) 1:9 (20:40) in the bottom panel..... 161

Figure 5.13. Fracture conductivity as a function of proppant concentration for proppant packs following mesh-size-20/40 with different sand/ceramic mixing ratios (1:9 and 5:5) under effective stress (a) 2,000 psi, (b) 4,000 psi, and (c) 6,000 psi ..... 164

Figure 6.1. U.S. DOE-NETL micro-CT laboratory setup..... 181

Figure 6.2. Schematic plot of the spatial positions of the three computational domains. .... 191

Figure 6.3. Contact angle distribution at the pore scale measured directly from NETL’s 3D micro-CT image reconstructions.....	192
Figure 6.4. SEM/EDX characterization of sandstone surface rich in a) clay minerals, and b) quartz. ....	192
Figure 6.5. a) CT scanning image of two-fluid distribution in the sandstone at the pore scale, and b) corresponding LB-simulated two-fluid distribution at the pore scale. ....	194
Figure 6.6. Relative permeability vs. water saturation ( $S_w$ ) curves under two Ca numbers ( $Ca=1\times 10^{-4}$ and $Ca=1\times 10^{-3}$ ) and two viscosity ratios ( $M=0.25$ and $M=1$ ). ....	202
Figure 6.7. Relative permeability vs. wetting fluid saturation ( $S_w$ ) curves for fluid injection directions (a) from bottom to top in the z direction, (b) from top to bottom in the $-z$ direction, and (c) in the horizontal (x) direction.. ....	205
Figure 6.8. Relative permeability vs. wetting fluid saturation ( $S_w$ ) curves in the (a) top-section, and (b) bottom-section computational domains. ....	206
Figure 7.1. Proppant packs generated using PFC3D with diameter COV (a) 5% (b) 25% .....	236
Figure 7.2. LB-simulated pressure distributions within the pore space of proppant assemblies having a) 5% diameter COV, and b) 25% diameter COV.....	237
Figure 7.3. LB-simulated flow-velocity-magnitude distributions and associated velocity fields within the pore space of the proppant assembly under effective stress of (a) 1000 psi and (b) 6000 psi. ....	239
Figure 7.4. (a) Cumulative distribution function (CDF) and (b) probability density function (PDF) as a function of particle migration distance. ....	240

Figure 7.5. Deposition rate as a function of particle diameter under varying effective stresses. The proppant packs with diameter COV5% and COV25% are subjected to three effective stresses, namely a) 1000psi, (b) 3000 psi, (c) 6000 psi. .... 243

Figure 7.6. Probability density functions (PDFs) of overall Darcy velocity for (a) realization 1 and (b) realization 2 under different effective stresses and diameter COVs ..... 245

Figure 7.7. Probability density functions (PDFs) the transition time distributions for (a) realization 1 and (b) realization 2 under different effective stresses and diameter COVs ..... 247

## List of Tables

Table 3.1. Developments of fracture width, $h$ , porosity, $\phi$ , permeability, $k$ , and conductivity ( $k \cdot h$ ) with increasing proppant concentration..	66
Table 6.1 A literature review and relevant works on multiphase flow	188
Table 6.2. Twelve scenarios were considered in the two-phase LB flow simulations, based on comprehensive combinations between the three dimensionless numbers (M, Ca, and contact angle).	196
Table 6.3. Corey model parameters with $Ca=1 \times 10^{-4}$	197
Table 6.4. Corey model parameters with $Ca=1 \times 10^{-3}$	197
Table 7.1. Power law component $\alpha$ for two geometries	246

## PREFACE

This dissertation is submitted as a completion of the degree of Doctor of Philosophy at Virginia Polytechnic Institute and State University. This research described here was conducted by the author, Ming Fan, under the supervision of Dr. Cheng Chen in the Department of Mining & Minerals Engineering at Virginia Polytechnic Institute and State University.

This dissertation is established based on six manuscripts. Altogether, the dissertation includes, three peer-reviewed journal articles, one conference paper, and two journal articles to be submitted to journals for review.

Chapter 2 is published in the SPE journal, “Fan, M., McClure, J., Han, Y., Li, Z., and Chen, C. (2018). Interaction Between Proppant Compaction and Single-/Multiphase Flows in a Hydraulic Fracture”. In this chapter, the multiphase flow simulation work is conducted with the assistance of James McClure and Zhe Li. The rest of the work is conducted by Ming Fan under the guidance of other co-authors.

Chapter 3 is also published in the SPE journal, “Fan, M., J. E. McClure, Y. Han, N. Ripepi, E. Westman, M. Gu, and C. Chen (2019), Using an Experiment/Simulation-integrated Approach to Investigate Fracture Conductivity Evolution and Non-Darcy Flow in a Proppant-supported Hydraulic Fracture”. In this work, the nanoindentation tests were conducted by collaborators in Halliburton. The rest of the work is conducted by Ming Fan under the guidance of other co-authors.

Chapter 4 is published in the 2018 ARMA conference, “Fan, M., Y. Han, J. McClure, E. Westman, N. Ripepi, and C. Chen (2018), Investigating the Impact of Proppant

Embedment and Compaction on Fracture Conductivity using Continuum Mechanics, DEM, and LBM Coupling Approach, 52 US Rock Mechanics/Geomechanics Symposium (ARMA 2018), Seattle, WA, June 24-29". The whole work is conducted by Ming Fan under the guidance of other co-authors.

Chapter 5 will be submitted to a journal article for review. The whole work is conducted by Ming Fan under the guidance of other co-authors.

Chapter 6 is published in the journal of Fuel, "Fan, M., L. Dalton, J. McClure, N. Ripepi, E. Westman, D. Crandall, and C. Chen (2019), Comprehensive study of the interactions between the critical dimensionless numbers associated with multiphase flow in 3D porous media". The laboratory multiphase flow experiments were conducted by Dr. Dustin Crandall and Miss Laura Dalton. The Berea sandstone sample was scanned by Ming Fan with the scanning electron microscope (SEM). The simulation work is conducted by Ming Fan under the guidance of other co-authors.

Chapter 7 will be submitted to a journal article for review. The whole work is conducted by Ming Fan under the guidance of other co-authors.

The copyrights for releasing documents from publishers are listed in the appendix section.

# Chapter 1 – Introduction

## 1.1 Background

The demand for hydrocarbon resources has been increasing steadily, as a consequence of global economic growth. To meet the growing energy demand, unconventional hydrocarbon resource has attracted significant attention. However, unconventional hydrocarbon energy extraction from shale reservoirs is extremely challenging due to the low permeability and complex petrophysical properties of these rock formations. In general, permeability of shale reservoirs is typically at the levels of nanodarcy to microdarcy and porosity is often less than 10% (Chen et al. 2015). In order to achieve economical production rates from these tight shale oil/gas reservoirs, hydraulic fracturing is the most often used technology to enhance the production of petroleum hydrocarbons (Economides and Nolte, 2000; Gu and Mohanty, 2014; Chen et al., 2015; Ye et al., 2016). In a standard hydraulic fracturing operation, a massive quantity of fracturing fluids is injected, and then the fractures are generated and propagated perpendicular to the minimum principal stress so that hydrocarbons only have to travel a short distance from kerogen to larger fractures. During hydrocarbon production, the fluid pressure inside the well and fractures has to be reduced below the fluid pressure in the reservoir to allow the fluids to flow out from the reservoir to fractures and then the well. In this stage, pore pressure decreases, and thus the effective stress of the rock matrix increases. This mechanical loading process has the potential to close the induced hydraulic fractures. In the oil and gas industry, proppant particles, which are granular materials, typically sand, treated sand, or man-made ceramic materials, are pumped along with fracturing fluids to support the newly generated fractures during hydrocarbon production and to maintain

conductive channels during the reservoir depletion process (Liang et al., 2016). Reservoir rocks are elastoplastic materials with finite stiffness and limited strength. As reservoir pressure continues depleting, reservoir rocks transfer more loads to proppants; as a result, the elastic deformation and plastic damage of reservoir rocks in the regions contacting proppants increase and proppants penetrate into the rock formations, which causes reduction of the fracture conductivity. The compaction and particle rearrangement of the proppant pack will further reduce the fracture aperture. Therefore, a well understanding of proppant compaction and embedment, fracture closure, single-/multiphase flows, and non-Darcy flows in a hydraulic fracture filled with proppant particles is critical (Fan et al. 2018a, 2018b, 2019a).

In an induced hydraulic fracture, the permeability, porosity, pore size distribution, and other geometrical properties of the proppant pack regulate the flow and transport of water and hydrocarbons. During oil and gas production, pore pressure decreases, and thus the effective stress of the rock formation increases. Because of the increasing effective stress, proppant compaction, crushing, and embedment into rock formations occur, which result in fracture closure and conductivity reduction. During this mechanical loading process, there are complex coupling and interactions between effective stress increase, proppant particle compaction, and flow and transport properties (Terracina et al., 2010; Barree et al. 2003). This complicated, coupled process is not well-understood but extremely important, because it is directly relevant to the oil recovery factor. Advanced understanding of proppant-deposition and -transport patterns in a hydraulic fracture is critical for the performance of stimulated wells (Fan et al. 2018a, 2018b).

A well can be fractured multiple times during its production life. For each well fracturing process, different sizes and types of proppants can be used, and proppants of



different types and sizes are mixed together in some fracture zones. In addition, in hybrid completion designs, proppants of various sizes and types are often mixed together and incorporated into the pumping schedule. In order to achieve economical production rates from unconventional reservoir formations, sufficient conductivity in hydraulic fractures must be sustained (Zhang et al. 2017; Gu et al. 2017). The performance of proppant packs having mixed proppants of various mesh sizes and types are critical in maintaining fracture conductivity and economical production of hydrocarbons from the reservoir (Fan et al. 2018a). Generally, it is expected that a greater amount of large proppants will result in greater fracture conductivity, whereas small-size proppant particles are likely to downgrade the fracture conductivity (Schmidt et al. 2014; McDaniel and Willingham, 1978). In recent years, the 100-mesh-size proppants have been widely used in horizontal wells because they can easily be transported into deeper regions of the formation. However, it remains unclear as to how much the low-conductive proppant affects the fracture conductivity, i.e., the influence of mesh size and mass ratio of the low-conductive proppants on the fracture conductivity requires in-depth investigations.

In this hydraulic-mechanical rock-proppant system, a fundamental understanding of multiphase flow in the formation rock is critical in achieving sustainable, long-term productivity from a reservoir. Multiphase flow in three-dimensional porous media is affected by a substantial amount of geological and physical properties, among which relative permeability properties of fluids in the reservoir has received great interest. The relative permeability is not merely dependent on fluid saturation (Aggelopoulos and Tsakiroglou, 2008), but also a function of other geological and physical parameters such as stress condition, saturation history, viscosity ratio, capillary number ( $Ca$ ), and contact

angle (Avraam and Payatakes, 1999; Li et al. 2005; Lenormand et al. 1988). However, most of the pore-scale numerical simulation is conducted based on man-made or idealized porous media. Therefore, it is a crucial task to conduct direct, comprehensive analysis of multiphase flow in natural geological formations, which is commonly encountered in geological carbon sequestration and enhanced oil recovery (Fan et al. 2019b).

During the reservoir depletion process, reservoir formation damage is an issue that will affect the reservoir productivity and various phases of fluid recovery. When hydrocarbons are produced from the reservoir, fine particles produced within the reservoir formation can continuously invade into the proppant pack (Nguyen et al. 2007). A common assumption in the oil and gas industry is that, it is better for the fines released from a formation to transport through the proppant pack in a propped fracture (Nguyen et al. 2005). However, in an induced hydraulic fracture, because of the increasing effective stress, proppant compaction, crushing, and embedment into rock formations occur, which result in changes in the pore structure and connectivity. As a result, the fine particles may be trapped and retained in the proppant pack, resulting in permeability loss and the consequent production decline. Gravel pack completions were typically designed to minimize fines invasion into the proppant pack and to maximize fracture conductivity (Nguyen et al. 2005, 2008; Tiffin et al. 1998). Many studies demonstrate that a stable proppant pack and well-selected proppant sizes in a propped fracture is the key in preventing formation fine damage (Blauch et al. 1999; Zou et al. 2014). Therefore, understanding the role of proppant particle size and proppant pack pore structure changes on fine migration is paramount to minimize formation fine damage.

In the oil and gas industry, the computation of microscopic properties in an induced hydraulic fracture is critical, since the interactions between reservoir rock, pore space, and pore fluids at the microscopic scale govern the macroscopic reservoir properties. Pore scale modeling offers detailed descriptions of the permeability, porosity, pore-size distribution, and other geometric properties, which is critical in characterizing the petrophysical properties of the rock formation and is also directly relevant to the oil-recovery factor. Numerical investigations based on laboratory-scanned or computer-simulated microstructures provide significant insights into the coupled, multiphysics processes with respect to proppant compaction and embedment in a hydraulic fracture, and have the potential to contribute to the study of other geoenergy and geoenvironmental processes that involve single-/multiphase flows, non-Darcy flow, and fine particle migration within a fracture filled with granular materials and subject to closure pressures.

## **1.2 Research objectives and work scope**

The overarching goal of this study is to advance the understanding of proppant-transport and -deposition patterns in a hydraulic fracture and to identify features of proppant packing that will influence the hydraulic conductivity in a propped fracture. The DEM-LBM (e.g., PFC3D-lattice Boltzmann method) framework will first be developed. Through the developed framework, the influence of compressive stress and proppant-diameter heterogeneity on fracture conductivity, non-Darcy flow, and single-/multiphase flow will be studied. Next, the potential effects of mixed proppants having different sizes and types on the fracture conductivity and the relationship between changing pore

geometries, fluid flow, and fine migration through a propped hydraulic fracture during the reservoir depletion process will be explored. At the end, the effect of different combinations of Ca, contact angle, and viscosity ratio on the relative permeability curves of a rock-water-CO<sub>2</sub> system will be thoroughly studied. The objectives will be established and evaluated both experimentally and numerically in the following eight research tasks:

1. Develop the DEM-LBM framework to investigate the influence of proppant compaction, embedment, and diameter heterogeneity on fracture conductivity, non-Darcy flow, and single-/multiphase flows in a hydraulic fracture
2. Investigate porosity, permeability, fracture width development, and the relationship between porosity and permeability for proppant-packs having different diameter distributions during the reservoir depletion process
3. Conduct multiphase flow simulations and study the influence of reservoir depletion process on water and oil relative permeabilities
4. Investigate the role of proppant particle size, particle size heterogeneity, and effective stress on fracture conductivity evolution from a partial-monolayer concentration to a multilayer concentration
5. Combine DEM with LB modeling to discover the potential effects of mixed proppants of different sizes and types on the fracture conductivity
6. Combine micro-CT imaging with LB multiphase flow simulations to discover the effect of different combinations of Ca, contact angle, and viscosity ratio on the relative permeability curves in a rock-water-CO<sub>2</sub> system

7. Evaluate the role of fluid injection direction and micro-scale spatial heterogeneity of porous rock structure on the relative permeability curves
8. Combine DEM with LB modeling to discover the role of proppant particle size, particle size heterogeneity, and effective stress on the migration of fine particles in a proppant-supported fracture

These research tasks are interconnected. The entire research plan in this study can be grouped into four phases. The first phase of this study, including Tasks 1-4, is to develop the DEM-LB framework and to investigate the influence of proppant compaction, embedment, and diameter heterogeneity on fracture conductivity, non-Darcy flow, and single-/multiphase flows in a hydraulic fracture. The second phase of this study (Task 5) is to use the developed DEM-LB work to discover the potential effects of mixed proppants of different sizes and types on the fracture conductivity. The third phase of this study, including Tasks 6-7, is to combine micro-CT imaging with LB multiphase flow simulations to discover the effect of different combinations of Ca, contact angle, and viscosity ratio on the relative permeability curves of a rock-water-CO<sub>2</sub> system. The last phase of this study (Task 8) is to discover the role of proppant particle size, particle size heterogeneity, and effective stress on fine particle migration in petroleum reservoirs using the developed DEM-LB framework.

### **1.3 Organization of this dissertation**

The dissertation consists of eight chapters. Chapter 1 introduces the importance of this pore-scale study of flow and transport in energy georeservoirs, as well as the overall objectives and work scope (eight tasks will be addressed in the following six chapters).

In the second chapter, a geomechanics/fluid-mechanics coupled numerical workflow is introduced to study the interaction between proppant compaction and single-/multiphase flows, non-Darcy flows in a hydraulic fracture. Specifically, the Particle Flow Code (PFC) was used for DEM modeling to simulate effective-stress increase and proppant-particle movement and rearrangement under increasing mechanical loading caused by the reservoir depletion process. An in-house numerical code was developed to discretize the proppant pack, and then the pore structure is imported into the LB simulator as boundary conditions to simulate single-/multiphase flows in the compressed pore space to assess the influence of proppant compaction on the fracture permeability and relative permeability. Using the DEM/LB-integrated numerical workflow, one can relate the geomechanical (effective stress), geometric (pore structure and connectivity), and transport (absolute permeability, relative permeability, and conductivity) properties of a proppant assembly sandwiched in a rock fracture, and then study the interactions and coupling between them. This work also provides insight into the factors that regulate the complicated interactions between closure pressure, proppant pack geometry, multiphase flow, and non-Darcy flow.

In the third chapter, the interplay between fracture closure, proppant compaction, and proppant embedment into rock formations as well as the resulting optimal partial-monolayer proppant concentration in an induced hydraulic fracture is studied. A hybrid, experiment/simulation-integrated approach is used to study the interactions between the geomechanical, geometric, and transport properties of granular materials sandwiched in a rock fracture and subjected to compaction, aiming at advancing the understanding of fracture conductivity evolution from partial-monolayer proppant concentrations to

multilayer proppant concentrations. The findings of this study advance the fundamental understanding of the role of proppant embedment and compaction and will facilitate the development of optimization workflows that can be used to optimize proppant placement in hydraulic fractures and to maximize productivity.

In the fourth chapter, in order to account for the effect of rock formation stiffness on fracture conductivity, a continuum mechanics-DEM-LB coupling approach was developed to study the influence of effective stress, as well as proppant mesh-sizes and diameter distributions on the fracture conductivity. The continuum mechanics code, FLAC3D, was used to model rock formation deformation, the DEM code, PFC3D, was used to model proppant compaction and rearrangement, and FLAC3D-PFC3D coupling was used to determine extra fracture closure due to proppant embedment. The proppant pack was discretized and the pore structure was imported into the LB simulator to determine the permeability of the proppant pack. The effects of proppant mesh-sizes, proppant diameter distributions, rock formation properties, on the fracture conductivity were investigated. The coupled numerical workflow combining FLAC3D/PFC3D with LB simulator provides insights into the factors controlling the change of conductivity induced by proppant embedment and compaction, which has the potential to benefit the optimization processes for proppant placement, completion design, and well production.

In the fifth chapter, the proposed DEM-LB framework was used to investigate the potential effects of mixed proppants of different sizes and types on the fracture conductivity. DEM was used to capture the increase of effective stress and the resultant compaction, rearrangement, and embedment of proppants. The evolved pore structures of the compacted proppant pack was extracted from the DEM model and then imported into

the LB simulator as internal boundary conditions in pore-scale fluid flow simulations to measure the time-dependent permeability of the proppant pack inside the fracture. We first measured the conductivities and constructed conductivity curves for proppant packs with mesh size 20, 40, and 20/40 (mixing mass ratio 1:1) under varying proppant areal concentrations (proppant mass per unit area of fracture face). Simulations were then performed to measure the propped fracture conductivities of proppant packs with different mass mixing ratios, such as 1:9, 2:8, 3:7, 4:6, and 5:5, and different proppant mesh sizes, effective stresses, and proppant areal concentrations (ranging from partial monolayer to multilayer). The conductivities of mixtures of sands and ceramic proppants under different areal concentrations and effective stresses were also tested. Knowledge generated from this work has significant implications to the optimization of hydraulic fracturing and proppant placement designs.

In the sixth chapter, in order to understand multiphase flow phenomena in the formation rock, two-phase LB flow simulations were conducted directly based on the micro-CT scanned images. First, the range of contact angle was determined using micro-CT measurements at the pore scale. Second, the micro-CT scanned two-fluid distributions was compared with the LB-simulated water and CO<sub>2</sub> distribution. Third, the effect of different combinations of Ca, contact angle, and viscosity ratio on the relative permeability curves of the rock-brine-CO<sub>2</sub> system was thoroughly studied. This study also evaluated the role of micro-scale anisotropy and spatial heterogeneity on the relative permeability curves. Insights gained from this study will benefit the fundamental understanding of petrophysical properties associated with multiphase flow and relative permeability upscaling in natural geological formations.



In the seventh chapter, the discrete element method (DEM) is used to generate proppant packs and model the proppant pack compaction. The discretized pore structures from proppant packs can be used as interior boundary conditions for fluid flow simulations in the compressed pore space with the LB simulator. The LB method simulates the fluid flow at a pore scale, which is suitable to obtain pore scale flow characteristics of a proppant pack in this study. Here, the proposed DEM-LB framework was adopted to evaluate the role of proppant particle size heterogeneity (variation in proppant particle diameter) and effective stress on the migration of detached fine particles in a proppant supported fracture. The findings of this study shed lights on the relationship between changing pore geometries, fluid flow, and fines migration through a propped hydraulic fracture during the reservoir depletion process.

The main research findings from this study and future research needs are summarized in chapter 8. Chapters 2-7 discuss all technical issues that are interrelated to achieve the objectives of this study. Their relationships can be mapped as delineated in a flow chart in Figure 1.1.

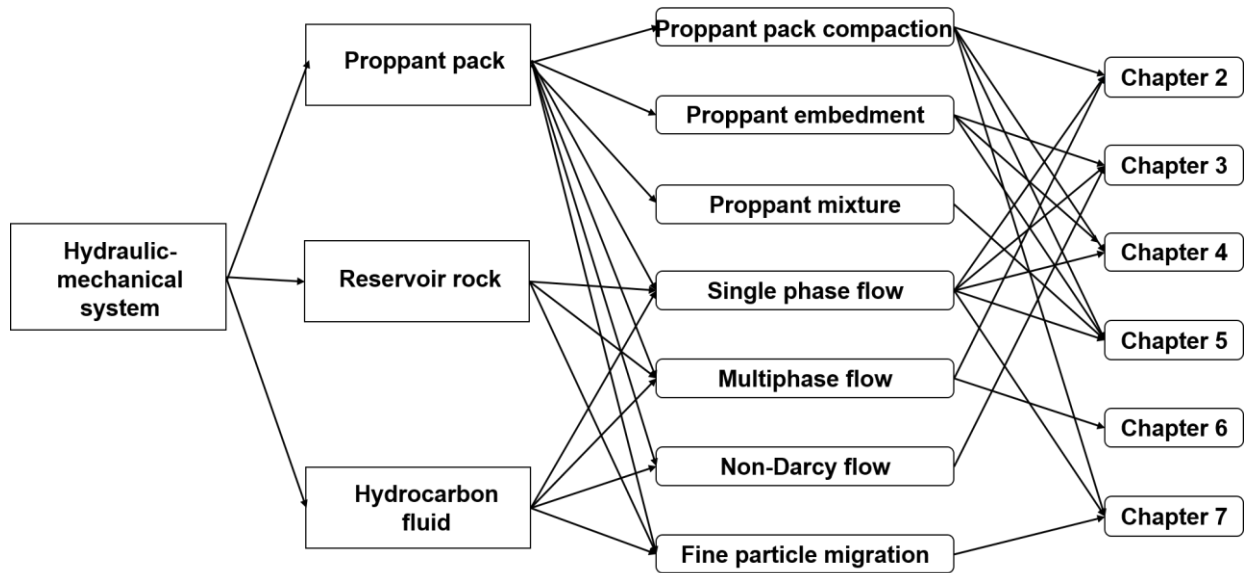


Figure 1.1. Flow chart for the relationship between chapters

## References

Aggelopoulos, C. A., & Tsakiroglou, C. D. (2008). The effect of micro-heterogeneity and capillary number on capillary pressure and relative permeability curves of soils. *Geoderma*, 148(1), 25-34.

Avraam, D. G., & Payatakes, A. C. (1999). Flow mechanisms, relative permeabilities, and coupling effects in steady-state two-phase flow through porous media. The case of strong wettability. *Industrial & engineering chemistry research*, 38(3), 778-786.

Barree, R. D., Cox, S. A., Barree, V. L. and Conway, M. W. (2003), Realistic Assessment of Proppant Pack Conductivity for Material Selection. Society of Petroleum Engineers. SPE-84306-MS, SPE Annual Technical Conference and Exhibition, 5-8 October, Denver, Colorado, doi:10.2118/84306-MS.

Blauch, M., Weaver, J., Parker, M., Todd, B., & Glover, M. (1999). New insights into proppant-pack damage due to infiltration of formation fines. In SPE Annual Technical Conference and Exhibition. Society of Petroleum Engineers.

Chen, C., Martysevich, V., O'Connell, P., Hu, D. and Matzar, L. (2015), Temporal Evolution of the Geometrical and Transport Properties of a Fracture/Proppant System under Increasing Effective Stress, SPE Journal, 20(3), 527-535, SPE-171572-PA. <http://dx.doi.org/10.2119/171572-PA>.

Economides M, Nolte K. (2000). Reservoir Stimulation. 3rd edition: John Wiley and Sons.

Fan, M., Han, Y., McClure, J., Westman, E., Ripepi, N., & Chen, C. (2018a). Investigating the Impact of Proppant Embedment and Compaction on Fracture Conductivity using a Continuum Mechanics, DEM, and LBM Coupled Approach. In 52nd US Rock Mechanics/Geomechanics Symposium. American Rock Mechanics Association.

Fan, M., McClure, J., Han, Y., Li, Z., & Chen, C. (2018b). Interaction between proppant compaction and single-/multiphase flows in a hydraulic fracture. SPE Journal, 23(04), 1-290.

Fan, M., J. E. McClure, Y. Han, N. Ripepi, E. Westman, M. Gu, and C. Chen (2019a), Using an Experiment/Simulation-integrated Approach to Investigate Fracture Conductivity Evolution and Non-Darcy Flow in a Proppant-supported Hydraulic Fracture, SPE Journal

Fan, M., L. Dalton, J. McClure, N. Ripepi, E. Westman, D. Crandall, and C. Chen (2019b), Comprehensive study of the interactions between the critical dimensionless numbers associated with multiphase flow in 3D porous media, Fuel, 252, 522-533.

Gu, M., & Mohanty, K. K. (2014). Effect of foam quality on effectiveness of hydraulic fracturing in shales. *International Journal of Rock Mechanics and Mining Sciences*, 70, 273-285.

Gu, M., Fan, M., & Chen, C. (2017). Proppant Optimization for Foam Fracturing in Shale and Tight Reservoirs. In *SPE Unconventional Resources Conference*. Society of Petroleum Engineers. Liang, F., Sayed, M., Al-Muntasheri, G. A., Chang, F. F., & Li,

L. (2016). A comprehensive review on proppant technologies. *Petroleum*, 2(1), 26-39

Li, H., Pan, C., & Miller, C. T. (2005). Pore-scale investigation of viscous coupling effects for two-phase flow in porous media. *Physical Review E*, 72(2), 026705.

Lenormand, R., Touboul, E., & Zarcone, C. (1988). Numerical models and experiments on immiscible displacements in porous media. *Journal of fluid mechanics*, 189, 165-187.

McDaniel, R. R., & Willingham, J. R. (1978). The effect of various proppants and proppant mixtures on fracture permeability. *SPE Annual Fall Technical Conference and Exhibition*. Society of Petroleum Engineers.

Nguyen, P. D., Weaver, J. D., Rickman, R. D., Dusterhoft, R. G., & Parker, M. A. (2007). Controlling formation fines at their sources to maintain well productivity. *SPE Production & Operations*, 22(02), 202-215.

Nguyen, P. D., Dusterhoft, R. G., & Clarkson, B. (2005). Control of formation fines to provide long-term conductivity in weak, unconsolidated reservoirs. *Offshore Technology Conference*.

Nguyen, P. D., Weaver, J. D., & Rickman, R. D. (2008). Prevention of geochemical scaling in hydraulically created fractures: laboratory and field studies. In SPE Eastern Regional/AAPG Eastern Section Joint Meeting. Society of Petroleum Engineers.

Schmidt, D., Rankin, P. E., Williams, B., Palisch, T., & Kullman, J. (2014). Performance of mixed proppant sizes. In SPE Hydraulic Fracturing Technology Conference. Society of Petroleum Engineers.

Tiffin, D. L., King, G. E., Larese, R. E., & Britt, L. K. (1998). New criteria for gravel and screen selection for sand control. In SPE Formation Damage Control Conference. Society of Petroleum Engineers.

Terracina, J. M., Turner, J. M., Collins, D. H. and Spillars, S. (2010). Proppant Selection and Its Effect on the Results of Fracturing Treatments Performed in Shale Formations. Society of Petroleum Engineers. doi:10.2118/135502-MS.

Zhi, Y., & Ahmad, G. (2016). Deformation properties of saw-cut fractures in Barnett, Mancos and Pierre shales. In 50th US Rock Mechanics/Geomechanics Symposium. American Rock Mechanics Association.

Zhang, F., Zhu, H., Zhou, H., Guo, J., & Huang, B. (2017). Discrete-element-method/computational-fluid-dynamics coupling simulation of proppant embedment and fracture conductivity after hydraulic fracturing. SPE Journal, 22(02), 632-644.

Zou, Y. S., Zhang, S. C., & Zhang, J. (2014). Experimental method to simulate coal fines migration and coal fines aggregation prevention in the hydraulic fracture. Transport in porous media, 101(1), 17-34.

## **Chapter 2 - Interaction between Reservoir Depletion, Proppant Compaction, and Single-/Multiphase Flows in a Hydraulic Fracture**

Ming Fan, and James McClure, Virginia Tech; Yanhui Han, Aramco Research Center – Houston; Zhe Li, Australia National University; Cheng Chen, Virginia Tech

### **Abstract**

Understanding of proppant transport and deposition patterns in a hydraulic fracture is vital for effective and economical production of petroleum hydrocarbons. In this research, a numerical modeling approach, combining discrete element method (DEM) with single-/multiphase lattice Boltzmann (LB) simulation, was adopted to advance the understanding of the interaction between reservoir depletion, proppant particle compaction, and single-/multiphase flows in a hydraulic fracture. DEM was used to simulate effective stress increase and the resultant proppant particle movement and rearrangement during the process of reservoir depletion due to hydrocarbon production. Simulated pore structure of the proppant pack was extracted and used as boundary conditions in the LB simulation to calculate the time-dependent permeability of the proppant pack. We first validated the DEM-LB numerical workflow, and the simulated proppant pack permeabilities as functions of effective stress were in good agreement with laboratory measurements. Furthermore, three proppant packs with the same average particle diameter but different diameter distributions were generated to study the role of proppant size heterogeneity (variation in particle diameter). Specifically, we used the coefficient of variation (COV) of diameter, defined as the ratio of standard deviation of diameter to mean diameter, to characterize the heterogeneity of particle size. We obtained

proppant pack porosity, permeability, and fracture width reduction (closure distance) as functions of effective stress. Under the same effective stress, a proppant pack with a higher diameter COV had lower porosity and permeability and larger fracture width reduction. This was because the high diameter COV gave rise to a wider diameter distribution of proppant particles; smaller particles were compressed into the pore space between larger particles with increasing stress, leading to larger closure distance and lower porosity and permeability. Using multiphase LB simulation, relative permeability curves were obtained, which are critical for larger-scale reservoir simulations under various effective stresses. The relative permeability of oil phase was more sensitive to changes in geometry and stress, compared to the wetting phase. This was due to the fact that the oil phase occupied larger pores; compaction of the proppant pack impacted the structure of the pores, since the pores were further from the grain contacts and thus more susceptible to collapse. It is also interesting to notice when effective stress increased continuously, oil relative permeability increased first and then decreased. This non-monotonic behavior was due to the non-monotonic development of pore structure and oil connectivity under increasing stress.

## **2.1. Introduction**

The demand for hydrocarbon resources has been increasing steadily as a consequence of global economic growth. In order to meet the growing energy demand, unconventional hydrocarbon energy (e.g., shale oil and gas) has attracted significant attention. However, hydrocarbon extraction from shale reservoirs is extremely challenging due to the low permeability and complex petrophysical properties of these formations. In general,

permeability of shale reservoirs typically ranges from nanodarcy to microdarcy and porosity is often less than 10% (Chen et al. 2015). Hydraulic fracturing is a widely used stimulation method for recovering hydrocarbons from unconventional reservoirs at an economically viable rate (Daneshy, 2009; Gaurav et al. 2012). Hydraulic fracturing aims to create low-resistance pathways (fractures) that are massive in number so that hydrocarbons only have to travel a short distance from kerogen to larger fractures (Chen et al. 2016). During hydrocarbon production, pore pressure decreases and thus the effective stress of the rock matrix increases. This mechanical loading process has the potential to close the induced hydraulic fractures. In the oil and gas industry, proppant particles, which are granular materials, typically sand, treated sand, or man-made ceramic materials, are pumped along with fracturing fluids in order to prevent hydraulic fractures from closing during reservoir depletion process and maintain conductive channels between the reservoir and wellbore. Therefore, the performance of proppant packs in the induced hydraulic fractures plays an important role on fracture conductivity and production rate.

In an induced hydraulic fracture, the permeability, porosity, pore size distribution, and other geometric properties of the proppant pack govern flow and transport of water and hydrocarbons. Because of increasing effective stress, proppant compaction, crushing, and embedment into rock formations occur, which result in fracture closure and conductivity reduction. During the mechanical loading process, there are complicated coupling and interactions between effective stress increase, proppant particle compaction, and flow and transport properties (Terracina et al. 2010; Barree et al. 2003; Zhang et al. 2017). This complicated, coupled process is not well-understood but extremely important because it



is directly relevant to the oil recovery factor. Advanced understanding of proppant transport and deposition patterns in a hydraulic fracture is vital for effective and economical production. Because it is difficult to study fracture conductivity and fracture/proppant interaction under in situ geological conditions, the numerical modeling method is often used as a powerful tool to describe and understand these multiphysics processes.

In this study, a geomechanics/fluid mechanics coupled numerical workflow is introduced to study the interaction and coupling between reservoir depletion, proppant compaction, and single-/multiphase fluid flows in a hydraulic fracture. The results of this research will identify and reveal various characteristics of proppant packing that may affect the hydraulic conductivity of proppant-supported fractures. The outcome of this research will benefit the fundamental understanding of the coupled, multiphysics processes with respect to hydraulic fracturing, and has the potential to contribute to the study of the other geoenery and geoenvironmental processes that involve single-/multiphase flows within a fracture filled with granular materials and subject to closure pressures. This research also provides an advantageous alternative to laboratory experiments.

## **2.2. Overview of Numerical Workflow**

In this study, the Particle Flow Code (PFC) was used for DEM modeling to simulate effective stress increase and proppant particle movement and rearrangement under increasing mechanical loading due to reservoir depletion. In proppant compaction simulation, the computational domain was cubic and the six boundaries were rigid walls.

The domain was then filled with proppant particles, which were generated randomly and followed known and well-controlled diameter distributions. Next, the top and bottom walls moved toward each other at a constant velocity, leading to proppant compaction and increasing effective stress between particles. In all simulations, the positions and geometric and mechanical properties of all individual particles were tracked. An in-house numerical code was developed to discretize the pore structure of the proppant pack and import it into the lattice Boltzmann (LB) model as boundary conditions to simulate single-/multiphase flows in the compressed pore space to assess the influence of proppant compaction on fracture permeability and relative permeability. Using the DEM-LB numerical workflow, one can relate the geomechanical (effective stress), geometric (pore structure and connectivity), and transport (absolute permeability, relative permeability, and conductivity) properties of a proppant assembly sandwiched in a rock fracture and then study the interactions and coupling between them.

### **2.2.1 Basics of PFC3D**

PFC3D is a three-dimensional (3D) discontinuum mechanics simulator (Itasca, 2008). It describes the movement and interaction of rigid, spherical particles using the DEM scheme, which was first introduced by Cundall (1971) for the analysis of rock mechanics problems and then applied to soils by Cundall and Strack (1979). In PFC3D, the spherical particles are generated independently and interact only at contacts or interfaces. The calculation cycle adopts a time-stepping algorithm, in which the position and velocity of each particle is determined by Newton's second law of motion, and the force-displacement relation is used to update the contact force at each contact. During

simulation, contacts can be created and separated simultaneously. However, Newton's second law of motion is not applied to boundary walls, since the motion of walls is specified by the user. The force-displacement relation is applied at each contact point, which is defined by a unit normal vector,  $n_i$ . When particles come into contact, the contact force is generated, which is determined by the relative displacement and specified stiffness between the two particles. The contact force can be decomposed into normal and shear components with respect to the contact plane, as illustrated in Equation 2.1. The normal contact force is computed by Equation 2.2. The magnitude of the shear contact force is initialized as zero and then incremented at each time step, as determined by Equation 2.3 (Itasca, 2008).

$$F_i = F_i^n + F_i^s \quad (2.1)$$

$$F_i^n = K^n U^n n_i \quad (2.2)$$

$$\Delta F_i^s = -k^s \Delta U_i^s \quad (2.3)$$

In these equations,  $F_i^n$  and  $F_i^s$  denote the normal and shear components of contact force;  $K^n$  is the normal stiffness at the contact, which relates total normal displacement to force;  $k^s$  is the shear stiffness, which relates incremental shear displacement to force;  $U^n$  is the contact displacement in the normal direction, and  $U_i^s$  is the shear component of the contact displacement.

### 2.2.2 Discretization of 3D Proppant Pore Structure

3D proppant pore structure from DEM simulation was discretized, extracted, and imported into the LB model as boundary conditions to simulate pore-scale, single-

/multiphase flows in the compressed pore space. Specifically, the 3D pore geometry was discretized using a 3D mesh grid having a resolution of 0.05 mm/pixel in the x-, y-, and z-directions. When the average proppant particle diameter is close to 1 mm, which is 20 times larger than the pixel size, the proppant pack geometry is well resolved with this resolution (Chen et al. 2009b).

### **2.2.3 Lattice Boltzmann Method for Single-Phase Flow Simulation**

The LB method is a numerical method for solving the Navier-Stokes equations and based on microscopic physical models and mesoscale kinetic equations (Chen and Doolen, 1998; Succi, 2001). In comparison with conventional fluid dynamic models, the LB method has many advantages. For example, it is explicit in evolution equation, simple to implement, natural to parallelize (Succi, 1991; Chen et al. 1992), and easy to incorporate new physics such as interactions at fluid-solid interface (Grunau et al. 1993; Han and Cundall, 2011, 2013).

The LB simulator used in this study has been validated by direct comparisons with analytical solutions and laboratory measurements (Chen et al. 2008, 2009a, 2013a). It was then optimized with high-performance graphics processing unit (GPU) parallel computing, which enhances the computational speed by a factor of 1,000 and led to an in-house LB code, GPU-enhanced lattice Boltzmann simulator (GELBS) (Chen et al. 2016). In this work, the D3Q19 lattice structure (19 velocity vectors in 3D space), presented in Figure 2.1a, was used because of its advantage in keeping a good balance between computational stability and efficiency (Chen et al. 2013b).

Particle distribution in the Bhatnagar-Gross-Krook (BGK)-based, single-relaxation-time LB equation is given by

$$f_i(\mathbf{x} + \mathbf{e}_i \Delta t, t + \Delta t) = f_i(\mathbf{x}, t) - \frac{f_i(\mathbf{x}, t) - f_i^{eq}(\rho, \mathbf{u})}{\tau}, \quad (i = 0, 1, 2 \dots 18) \quad (2.4)$$

where  $f_i(\mathbf{x}, t)$  is the particle-distribution function specifying the probability that fluid particles at lattice location  $\mathbf{x}$  and time  $t$  travel along the  $i^{\text{th}}$  direction;  $\mathbf{e}_i$  is the lattice velocity vector corresponding to direction  $i$ , defined as:

$$\begin{aligned} \mathbf{e}_0 &= (0, 0, 0), \quad \mathbf{e}_1 = (1, 0, 0)c, \quad \mathbf{e}_2 = (-1, 0, 0)c \\ \mathbf{e}_3 &= (0, 1, 0)c, \quad \mathbf{e}_4 = (0, -1, 0)c, \quad \mathbf{e}_5 = (0, 0, 1)c, \quad \mathbf{e}_6 = (0, 0, -1)c \\ \mathbf{e}_7 &= (1, 1, 0)c, \quad \mathbf{e}_8 = (-1, 1, 0)c, \quad \mathbf{e}_9 = (1, -1, 0)c, \quad \mathbf{e}_{10} = (-1, -1, 0)c \\ \mathbf{e}_{11} &= (0, 1, 1)c, \quad \mathbf{e}_{12} = (0, -1, 1)c, \quad \mathbf{e}_{13} = (0, 1, -1)c, \quad \mathbf{e}_{14} = (0, -1, -1)c \\ \mathbf{e}_{15} &= (1, 0, 1)c, \quad \mathbf{e}_{16} = (-1, 0, 1)c, \quad \mathbf{e}_{17} = (1, 0, -1)c, \quad \mathbf{e}_{18} = (-1, 0, -1)c \end{aligned}$$

where  $c = \Delta x / \Delta t$ , in which  $\Delta x$  is the lattice spacing and  $\Delta t$  is the time step;  $\tau$  is the dimensionless relaxation time related to kinematic viscosity by  $\nu = (2\tau - 1)\Delta x^2 / 6\Delta t$  ;

$f_i^{eq}(\rho, \mathbf{u})$  is the equilibrium distribution function selected to recover the macroscopic Navier-Stokes equations and given by

$$f_i^{eq}(\rho, \mathbf{u}) = \omega_i \rho \left[ 1 + \frac{3\mathbf{e}_i \cdot \mathbf{u}}{c^2} + \frac{9(\mathbf{e}_i \cdot \mathbf{u})^2}{2c^4} - \frac{3\mathbf{u}^2}{2c^2} \right] \quad (2.5)$$

where  $\omega_i$  is the weight coefficient calculated as:

$$\omega_i = \begin{cases} 1/3 & i = 0 \\ 1/18 & i = 1 \dots 6 \\ 1/36 & i = 7 \dots 18 \end{cases}$$

The macroscopic fluid density and velocity are calculated with the following two equations:

$$\rho = \sum_{i=0}^{18} f_i \quad (2.6)$$

and

$$\mathbf{u} = \frac{\sum_{i=0}^{18} f_i \mathbf{e}_i}{\rho} \quad (2.7)$$

Fluid pressure is calculated using  $p = c_s^2 \rho$ , where  $c_s$  is the speed of sound. In the LB D3Q19 model,  $c_s^2 = c^2/3$ .

In practice, two-relaxation-time and multi-relaxation-time LB schemes have been developed to mitigate numerical instability in simulating high-Reynolds-number flows and avoid nonlinear dependency of numerical error on fluid viscosity (Li and Huang, 2008; Ginzburg, 2008). In this study, we replaced the BGK-based collision operator with a two-relaxation-time collision operator and selected the optimal combination of the symmetric and asymmetric eigenfunctions (Ginzburg et al. 2010) in order to reduce numerical errors resulting from the bounce-back boundary condition.

For fluid flow simulation, we imposed a periodic boundary condition with a constant pressure difference,  $\Delta P$ , in the longitudinal direction and no-slip boundary conditions on the four lateral sides and interior solid surfaces (Inamuro et al. 1999; Chen et al. 2009a). The Reynolds number was always much smaller than one to ensure that the macroscopic flow was well within the Darcy regime. A small pressure difference,  $\Delta P$ , generated an adequately small Mach number and density variation, which are necessary for accurate simulation of incompressible flows using the LB method. More details about the LB simulator and associated GPU optimization can be found in our previous papers (Chen et al. 2009a; 2016).

At the continuum scale, the Darcy velocity,  $\mathbf{v}$ , is calculated by averaging the pore-scale flow velocity,  $\mathbf{u}$ , of each lattice node in the pore space throughout the entire computational domain. One can calculate the permeability tensor using the Darcy's law:

$$\mathbf{v} = -\frac{1}{\mu} \mathbf{k} \cdot \nabla p \quad (2.8)$$

where,  $\mathbf{v} = [v_x, v_y, v_z]^T$  is the Darcy velocity,  $\mathbf{k} = k_{ij} (i, j = x, y, z)$  is the permeability tensor, with  $i$  being the flow direction and  $j$  being the pressure gradient direction,  $\nabla p$  is the pressure gradient, and  $\mu$  is the dynamic viscosity of the fluid. The principal components of the permeability tensor are noted as  $k_{xx}$ ,  $k_{yy}$ , and  $k_{zz}$ , as presented in Figure 2.1b. Since the principal directions of the permeability tensor in this study are the same as the principal coordinate direction, the off-diagonal elements in the permeability tensor are zero, written as  $k_{ij} = 0 (i \neq j)$ .

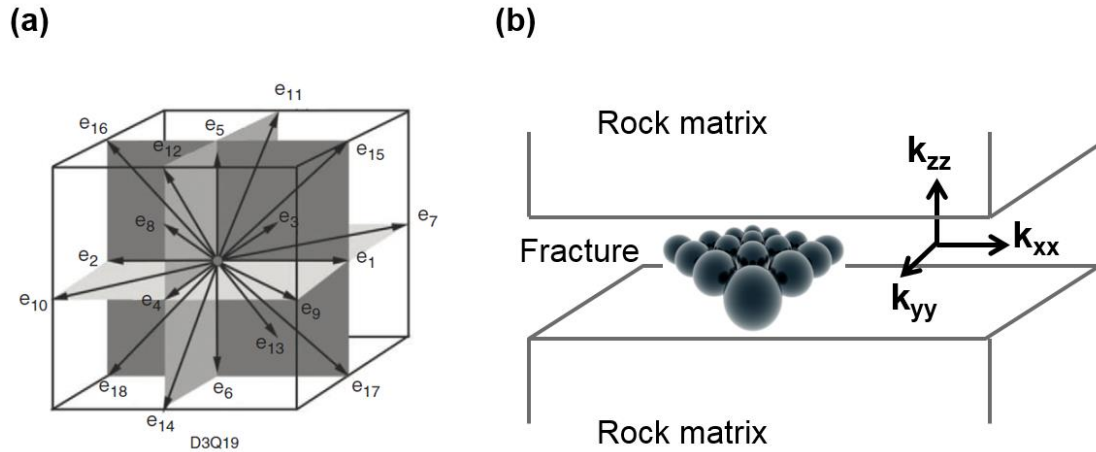


Figure 2.1. a) D3Q19 lattice structure, and b) proppant particles and permeability tensor in the fracture (figures modified from Chen et al., 2015).

#### 2.2.4 Lattice Boltzmann Method for Multiphase Flow Simulation

A multiphase extension of Darcy's law is typically used to describe two-fluid flow processes at the reservoir scale. The two-fluid system includes a wetting fluid ( $w$ ) as well as a non-wetting fluid ( $n$ ). The wetting fluid has a comparative affinity for the solid, and will tend to preferentially coat the rock surface as a result of the interfacial thermodynamics. As a consequence, the wetting and non-wetting fluid have a tendency to assume distinctly different configurations within the pore space, and the relative permeability is introduced to account for these configurational effects. The two-phase extension of Darcy's law is written as

$$v_i = (k_{ri} / \mu_i) \mathbf{k} \cdot (-\nabla p + \rho_i \mathbf{g}) \quad (2.9)$$

where  $\mu_i$ ,  $\rho_i$  and  $k_{ri}$  are respectively the dynamic viscosity, density, and relative permeability associated with fluid  $i=w, n$ . External body forces such as gravity are accounted for by the vector  $\mathbf{g}$ . Since  $k_{ri}$  is a relative quantity, it is dimensionless and usually attains a value between zero and one, although it is possible to measure relative permeability values greater than one in certain situations.

This work relies on a multi-relaxation time (MRT) LB scheme formulated for two-fluid flow according to the "color" model, originally proposed by Gustensen et al. (1991). In this work, the color model was implemented as described by McClure et al. (2014). Separate lattice Boltzmann equations (LBEs) were used to track mass transport for each fluid and the total momentum. The mass transport LBEs rely on a three-dimensional, seven discrete velocity (D3Q7) lattice structure, which requires only the first seven discrete velocity vectors in the D3Q19 lattice structure. The mass transport LBEs provide a solution for the densities of the two fluids,  $\rho_w$  and  $\rho_n$ , which in turn provide the



position of the two fluids and the location of the interface between them. The phase indicator field can consequently be computed from the fluid density as

$$\varphi = (\rho_n - \rho_w) / (\rho_n + \rho_w) \quad (2.10)$$

The value of the phase indicator field is constant within the pure phase regions occupied by each fluid, and varies between -1 and 1 in the interfacial region, which is diffuse. Based on this information, stresses that arise within the interfacial region (as a consequence of the interfacial tension) are incorporated into the momentum transport equation. The color gradient is defined as

$$\mathbf{C} = \nabla \varphi \quad (2.11)$$

In the LB formulation the color gradient is re-expressed in terms of its magnitude  $|C|$  and normal direction  $\mathbf{n} = \mathbf{C} / |C|$ . The D3Q7 mass transport distributions are initialized to match an equilibrium distribution where the flux of mass across the interface is minimized for each fluid:

$$g_{nq} = \omega_q \left[ \rho_n (1 + \mathbf{e}_q \cdot \mathbf{u}) + \beta (\mathbf{e}_q \cdot \mathbf{n}) \rho_w \rho_n / (\rho_w + \rho_n) \right] \quad (2.12)$$

$$g_{wq} = \omega_q \left[ \rho_w (1 + \mathbf{e}_q \cdot \mathbf{u}) - \beta (\mathbf{e}_q \cdot \mathbf{n}) \rho_w \rho_n / (\rho_w + \rho_n) \right] \quad (2.13)$$

where  $\beta$  is a parameter that controls the width of the interface and  $\mathbf{u}$  is the flow velocity (determined from the momentum transport LBE described below). The associated weights for the D3Q7 model are  $\omega_0 = 1/3$  and  $\omega_{1..6} = 1/9$ . The time evolution of fluid densities is then determined by applying a streaming step directly to the equilibrium distributions (with no relaxation process):

$$\rho_j(x, t + \Delta t) = \sum_q g_{jq}(x - \mathbf{e}_q \Delta t, t) \quad (j = w, n) \quad (2.14)$$

The mass transport LBEs exactly conserve the mass of each component.

The momentum transport is described by a D3Q19 MRT LBE,

$$f_q(x + \mathbf{e}_q \Delta t, t + \Delta t) - f_q(x, t) = M^*_{qi} \Lambda_i (m_i^{eq} - m_i) \quad (2.15)$$

where  $q, i = 0, 1, 2, \dots, 18$ . In the MRT formulation, a relaxation process is applied to a set of nineteen moments determined from the distributions, with the rate of the relaxation process determined by  $\Lambda_i$ . The relaxation rates are chosen to specify the fluid viscosity (Pan et al. 2006). The moments are obtained from a linear transformation,  $m_i = M_{iq} f_q$ .

The matrix  $M^*$  is the inverse of  $M$ . The equilibrium moments  $m_i^{eq}$  depend on the color gradient  $\mathbf{C}$  and the flow velocity  $\mathbf{u}$ . The non-zero equilibrium moments are

$$m_1^{eq} = (j_x j_x + j_y j_y + j_z j_z) + \alpha |\mathbf{C}| \quad (2.16)$$

$$m_9^{eq} = (2j_x j_x - j_y j_y - j_z j_z) + \alpha |\mathbf{C}| (2n_x n_x - n_y n_y - n_z n_z) / 2 \quad (2.17)$$

$$m_{11}^{eq} = (j_y j_y - j_z j_z) + \alpha |\mathbf{C}| (2n_y n_y - n_z n_z) / 2 \quad (2.18)$$

$$m_{13}^{eq} = j_x j_y + \alpha |\mathbf{C}| n_x n_y / 2 \quad (2.19)$$

$$m_{14}^{eq} = j_y j_z + \alpha |\mathbf{C}| n_y n_z / 2 \quad (2.20)$$

$$m_{15}^{eq} = j_x j_z + \alpha |\mathbf{C}| n_x n_z / 2 \quad (2.21)$$

where the parameter  $\alpha$  is linearly related to the interfacial tension and the fluid momentum is computed from the distributions

$$\mathbf{j} = \sum_q f_q \mathbf{e}_q \quad (2.22)$$

The specific forms for  $M$  and  $m_i^{eq}$  have been previously published in the literature, along with details on setting the relaxation rates,  $\Lambda_i$ , and boundary conditions for two-fluid flow in porous media (McClure et al. 2014). This formulation was used to measure

the relative permeability based on steady-state oil/water flows within a proppant assembly sandwiched in a rock fracture. An in-depth description of the approach used to estimate relative permeabilities from digital rock images using the color LBM is provided by Ramstad et al. (2012).

### **2.3. Proppant Compaction Studies**

To validate the numerical models, proppant pack permeability as a function of increased effective stress was simulated and then compared with laboratory data. In the laboratory, permeabilities were measured with proppant concentration of 2 lb/ft<sup>2</sup> between two Ohio sandstones (CARBOHSP, 2015). In DEM simulation, two proppant packs with 12/18 and 16/30 mesh sizes were generated at proppant concentration of 2 lb/ft<sup>2</sup>, leading to a fracture width of approximately 5 mm and multiple layers of proppant particles packed within the fracture space. The computational domain dimension in the x-y plane (the plane parallel to fracture face) was 30 mm × 30 mm. The fracture then closed in the z-direction (the direction normal to fracture face) at a constant velocity, which was adequately slow to avoid rapid surge of effective stress between proppant particles and allow fluid within the pore space to flow away in the lateral (x-y) direction, as illustrated in Figure 2.1b. In this way, the system is in the steady state, where the transient pore pressure change and resultant stress acting on the proppant particles are negligible. The four lateral walls were fixed because of the restriction from the surrounding particles outside the computational domain. The processes of proppant particle compaction, movement, and re-arrangement were simulated with the PFC code. Continuously increasing overall stress acting on the proppant pack, which resulted from continuous

fracture closure, was simulated. Corresponding pore structure of proppant pack was discretized at a resolution of 0.05 mm/pixel in all directions and then imported into the GELBS code as boundary conditions to simulate proppant pack permeability in the lateral (x-y) direction.

After validation of the numerical models, the second compaction study was conducted to investigate the influence of proppant particle size distribution. The initial dimension of the proppant pack was 20 mm × 20 mm × 20 mm with the resolution being 0.05 mm/pixel in all directions. Therefore, the pore structure of proppant pack was discretized into 400 × 400 × 400 lattice nodes. Three proppant packs with the same average particle diameter but different size distributions were generated. Specifically, the first proppant pack was generated following the 20/40 mesh size with an assumption of uniform distribution of particle diameter, leading to a mean diameter of 0.63 mm and standard deviation of 0.12 mm; the coefficient of variation (COV) of particle diameter, defined as the ratio of standard deviation of diameter to mean diameter, was therefore calculated as 19%. This proppant pack was referred to as the reference geometry. The other two proppant packs had the same mean particle diameter but different diameter COVs, with one being 5% and the other being 25%, which suggests that one was more homogeneous in proppant diameter and the other was more heterogeneous. Similar to the validation study, fracture closed in the z-direction and proppant pack permeabilities as functions of increased effective stresses were simulated with the numerical workflow.

#### **2.4. Results and Discussion**

Figure 2.2 illustrates the result of the validation study. Specifically, Figure 2.2a demonstrates the DEM-simulated 16/30-mesh-size proppant assembly under effective

stress of 10 psi. With such a low stress, proppant assembly compaction was not significant. A pressure gradient was imposed along the x-direction to drive single phase fluid flow through the pore space of the proppant assembly. Figures 2.2b illustrates LB-simulated pressure distribution within a 2D cross section cut along the x-y plane at the fracture center, with pressure presented in the LB unit.

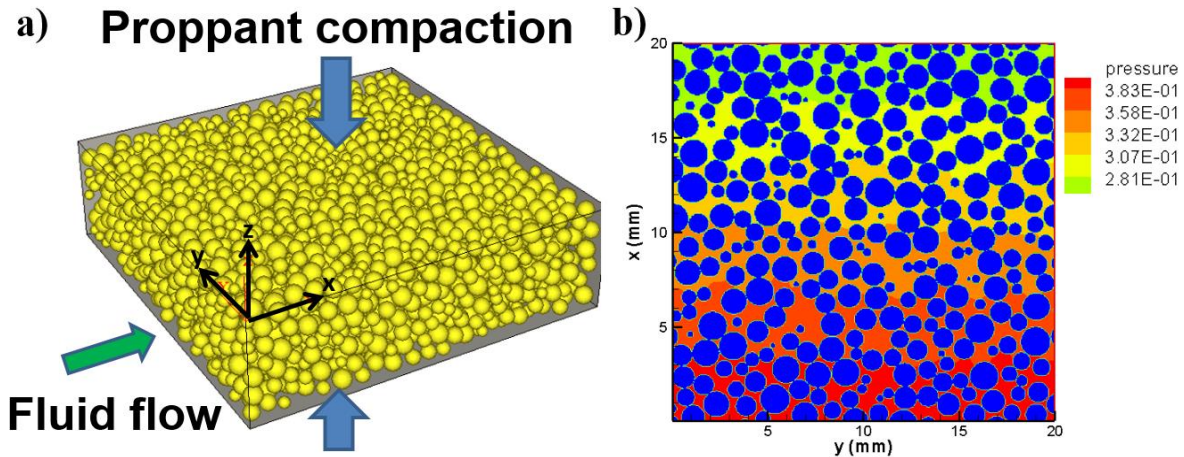


Figure 2.2. a) DEM-simulated 16/30-mesh-size proppant assembly of 30 mm  $\times$  30 mm  $\times$  5 mm under effective stress of 10 psi, and b) corresponding LB-simulated pressure distribution within the pore space of the 2D cross section.

Figure 2.3 illustrates LB-simulated flow velocity magnitude distributions within the 2D central cross section, when the effective stress was 10 psi and 2200 psi. Flow velocity magnitude was presented in the LB unit. Figure 2.3a illustrates that when the effective stress was 10 psi, pore size was relatively large and there existed multiple high-flow-velocity regions within the pore space, which suggested relatively good connectivity of the pore space. Conversely, under effective stress of 2200 psi, proppant assembly compaction was significant and pore size reduction was noticeable; pore space connectivity was consequently reduced, leading to local, preferential flow paths, as indicated by the black circle in Figure 2.3b, as well as increased heterogeneity in pore flow velocity.

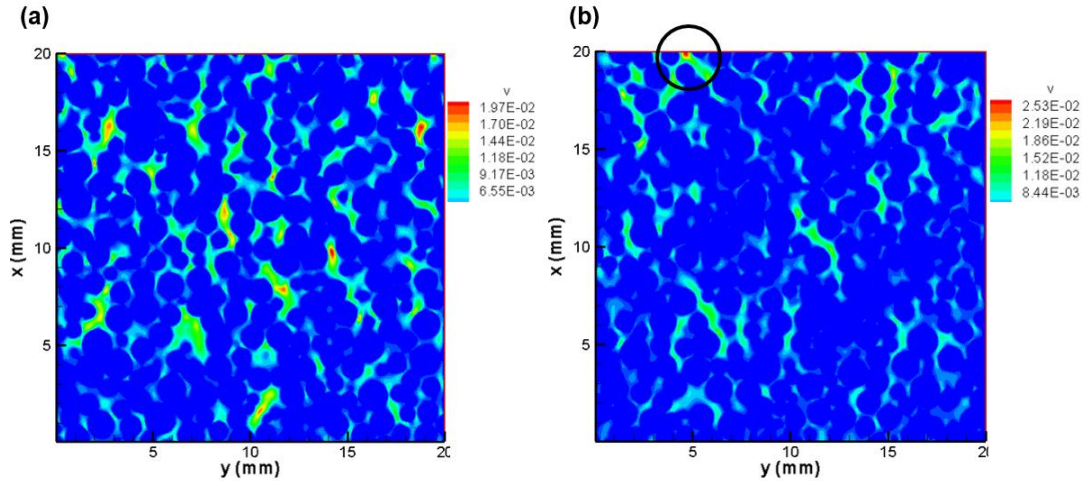


Figure 2.3. LB-simulated flow velocity magnitude distributions within the pore space of a proppant assembly under effective stress of a) 10 psi, and b) 2200 psi.

Figure 2.4 shows the comparison between LB-based numerical results and laboratory measurements. Numerical results were in good agreement with experimental data in the low-stress range, and permeability decreased as effective stress increased. However, when effective stress exceeded 4000 psi, laboratory-measured permeability declined rapidly to a level significantly lower than LB-simulated permeability.

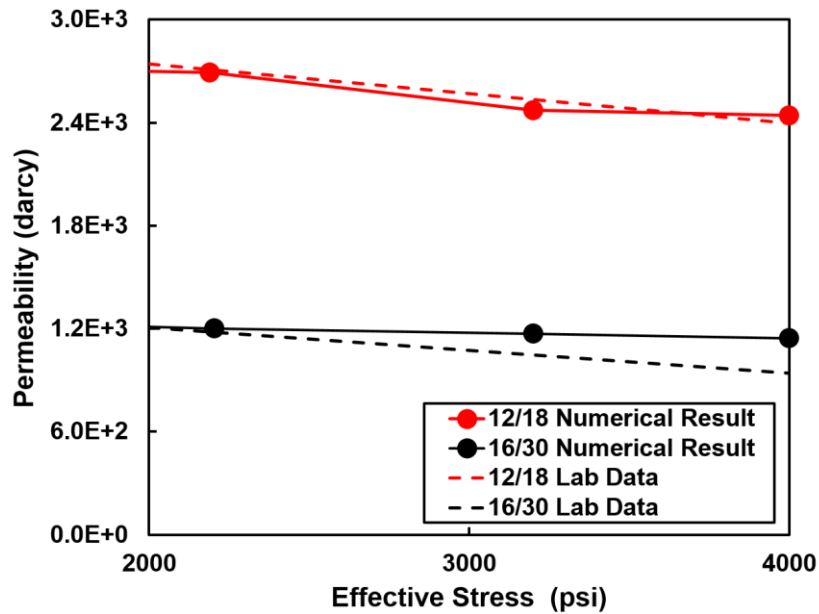


Figure 2.4. Comparison between numerical results and laboratory measurements

The discrepancy between numerical and laboratory results was due to proppant particle crushing and embedment under high mechanical stress. Figure 2.5 illustrates two CT images of proppant particles within a hydraulic fracture of a shale rock under effective stresses of 0 and 3000 psi (Chen et al. 2015). In this laboratory experiment, 20/40 mesh-size proppant particles were placed within the fracture to form a partial monolayer; the partial-monolayer proppant structure led to relatively high average stress imposed on each individual proppant particle, resulting in significant proppant crushing and embedment, as illustrated in the red circles. Proppant crushing and embedment within the high-stress range (greater than 4000 psi) resulted in rapid decline of proppant pack permeability.

Figure 2.6 presents the DEM/LB-simulated results for the three proppant packs used in the second compaction study. Specifically, Figure 2.6a presents the compressed distances (fracture width reductions) of the three proppant packs as functions of effective stress. Compressed distance increased with increasing effective stress. Under the same effective stress, the compressed distance for the proppant pack with 5% diameter COV was the smallest, whereas the compressed distance for the proppant pack with 25% diameter COV was the largest. This was because under the same effective stress, smaller particles within the proppant pack having a larger diameter COV moved relatively easier and were compressed into the pore space between bigger particles, leading to a larger fracture closure distance. This suggests that proppant packs with smaller diameter COVs, which are more homogeneous with respect to particle size distribution, provide better support to the fracture. Figure 2.6b presents the porosities of the proppant packs as functions of effective stress. It was observed that porosity decreased with the increase of

effective stress. Under the same effective stress, the proppant pack with 5% diameter COV showed the highest porosity and the proppant pack with 25% diameter COV showed the lowest porosity, which can be explained with the same mechanism described for Figure 2.6a.

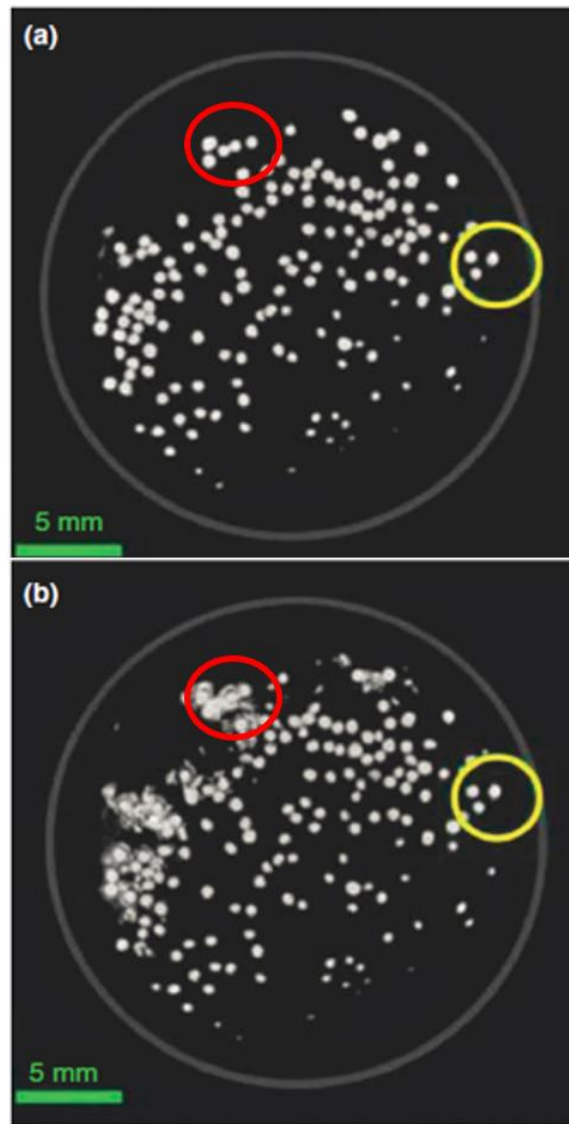


Figure 2.5. X-ray CT images of proppant particle crushing and embedment in a hydraulic fracture of a shale rock under effective stresses of a) 0, and b) 3000 psi. The red circle indicates proppant particle crushing after stress increase, whereas the yellow circle indicates unaffected particles (figures modified from Chen et al., 2015).



Because fluids were unable to penetrate rock surfaces (the top and bottom rock matrices were assumed non-permeable), they flowed along the x-y plane, as illustrated in Figure 2.1b. The principal components of the permeability tensor in the x- and y-directions were noted as  $k_{xx}$  and  $k_{yy}$ , respectively, which were referred to as lateral permeabilities and similar to each other because the proppant pack was isotropic in the x-y plane. In Dye's study (2013), they normalized the permeability by the square of the equivalent particle diameter, in order to minimize the effect of average diameter on the analysis of permeability. The equivalent particle diameter,  $D$ , is determined as:

$$D = 6 \times (1 - \phi) \times V / S \quad (2.23)$$

where  $\phi$  is the porosity,  $V$  is the volume of the entire computational domain, and  $S$  is the total surface area of proppant particles. In this study, we normalized the average lateral permeability (mean of  $k_{xx}$  and  $k_{yy}$ ) using  $D^2$  to obtain the dimensionless permeability. Figure 2.6c presents normalized permeabilities as functions of effective stress. As effective stress increased, normalized permeability decreased. Under the same effective stress, the proppant pack with 25% diameter COV had the lowest normalized permeability, whereas the proppant pack with 5% diameter COV had the highest normalized permeability. This was because a more homogenous particle diameter distribution led to higher porosity under the same effective stress, giving rise to higher proppant pack permeability.

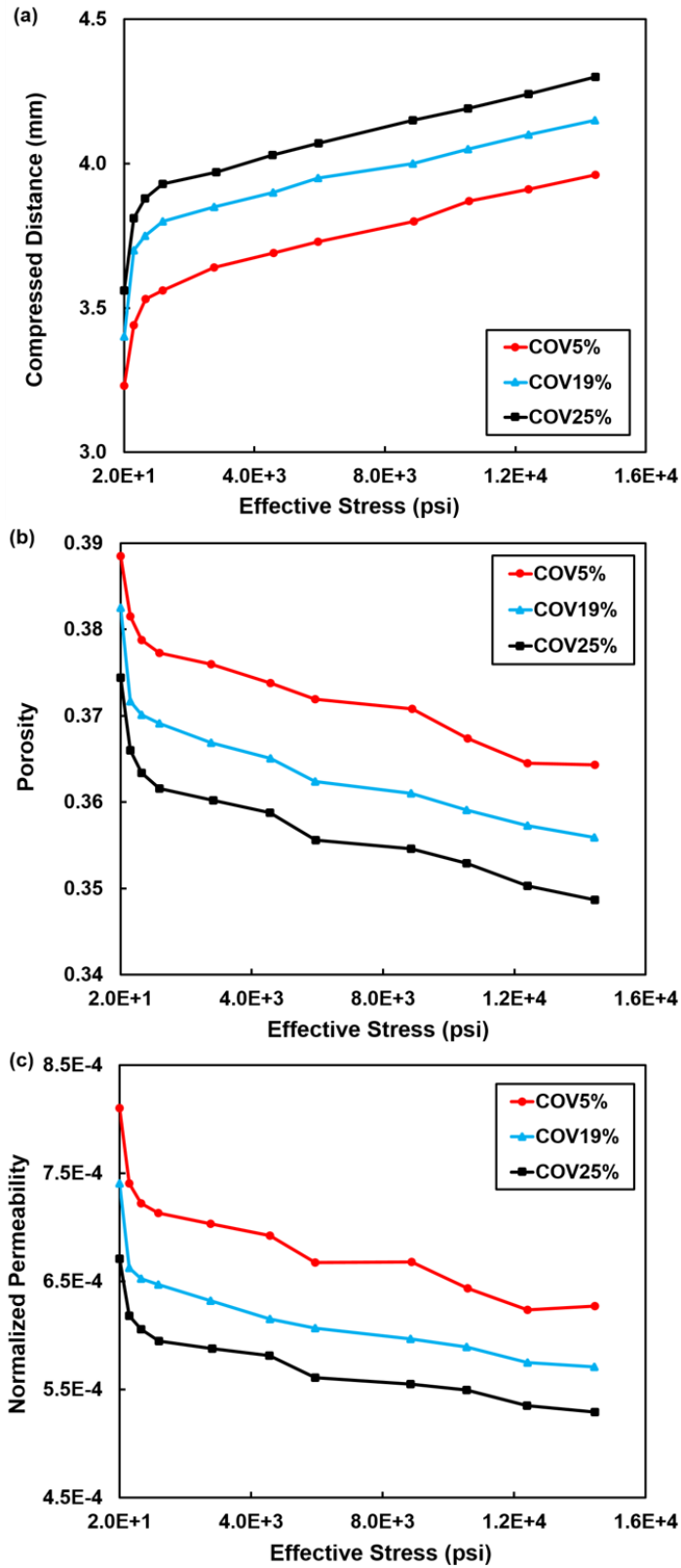


Figure 2.6. a) Compressed distance, b) porosity, and c) normalized permeability as functions of effective stress.

Figure 2.7 illustrates normalized permeabilities as functions of porosity. The relationship between porosity and normalized permeability demonstrated good consistency with the empirical Kozeny-Carmen equation which relates porosity to permeability; the power-law exponents were close to that found in our previous studies of permeability for spherical glass beads (Chen et al. 2008; 2009a). With the same porosity, a proppant pack with a lower diameter COV, which suggests a more homogeneous particle diameter distribution, had a higher permeability. This implies that a more homogeneous particle diameter distribution resulted in a more homogeneous pore size distribution, which was favorable for the enhancement of pore space connectivity and the overall permeability of the proppant pack.

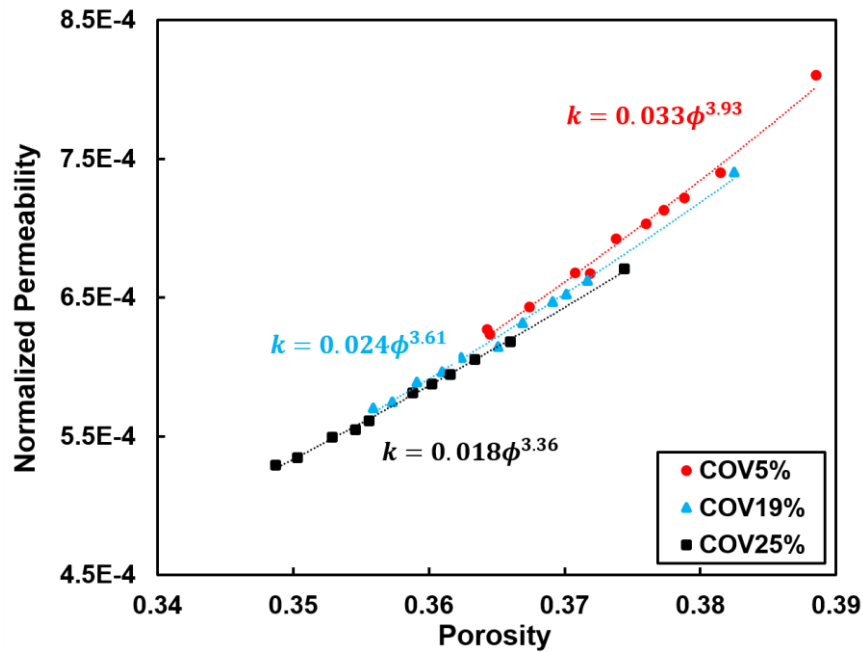


Figure 2.7. Normalized proppant pack permeabilities as functions of porosity.

Figure 2.8 presents porosity and effective stress as functions of subdomain diameter for the three proppant packs in order to evaluate the representative elementary volume (REV) size, which is the minimum subdomain size that demonstrates the macroscopic

properties. In this figure, the effective stress and porosity were calculated within a spherical subdomain with its center located at the center of the entire proppant pack. The subdomain diameter increased continuously and the corresponding porosity and effective stress were calculated. When subdomain diameter was small, significant oscillation in the values of porosity and effective stress was observed. As subdomain diameter increased and exceeded 8 mm, both porosity and effective stress stabilized for the three proppant packs. Therefore, 8 mm can be considered qualitatively as the REV size for all the three proppant packs, in terms of porosity and effective stress. Furthermore, all the three proppant packs demonstrated similar stable-state effective stresses (close to 3000 psi). In contrast, the stable-state porosity for a proppant pack with a higher diameter COV was lower. Specifically, stable-state porosities for COV5%, COV19%, and COV%25 were 0.367, 0.358, and 0.352, respectively. This was because a higher diameter COV resulted in a wider distribution of particle diameter, leading to a more heterogeneous proppant pack. Under increasing compressive stress, smaller proppant particles were compressed into the pore space between larger particles, giving rise to lower porosity.

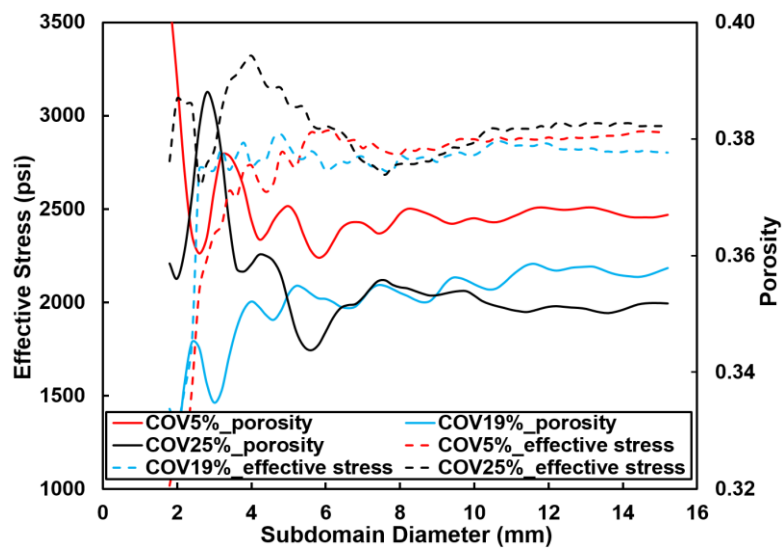


Figure 2.8. Porosity and effective stress as functions of subdomain diameter.

To account for spatial heterogeneity, we also conducted statistical representative elementary volume (sREV) analysis (Zhang et al. 2000; Chen et al. 2009a). Specifically, we fixed the subdomain diameter and moved it throughout the entire computational domain. At each subdomain location, we obtained the values of porosity, effective stress, and normalized permeability. Therefore, at the end of the iteration, we obtained a larger number of porosity, effective stress, and normalized permeability values, and were able to calculate the means and standard deviations. We then increased the subdomain diameter and repeated the process. Figure 2.9 illustrates mean effective stress, mean porosity, and mean normalized permeability associated with corresponding standard deviations (dashed lines), as functions of subdomain diameter. Specifically, the dashed lines indicate one standard deviation above and below the mean. As the diameter of the spherical subdomain increased, effective stress, porosity, and normalized permeability approached stable values and the standard deviations reduced; this suggests that the subdomain became more and more homogeneous with its size increasing. In this study, the size of sREV was defined as the subdomain diameter at which the ratio of standard deviation to mean was lower than 3%. For effective stress, sREV was found to be 7 mm, 9 mm, and 10 mm for COV5%, COV19%, and COV25%, respectively. For porosity, sREV was found as 3 mm, 3 mm, and 4 mm for COV5%, COV19%, and COV25%, respectively. For normalized permeability, sREV was found to be 11.6 mm, 11.2 mm, and 12.0 mm for COV5%, COV19%, and COV25%, respectively. Therefore, the entire proppant pack dimension (20 mm × 20 mm × 20 mm) was sufficiently large to demonstrate macroscopic values for all the three quantities (effective stress, porosity, and normalized permeability). Generally, the more heterogeneous the particle diameter distribution, the larger the sREV sizes.

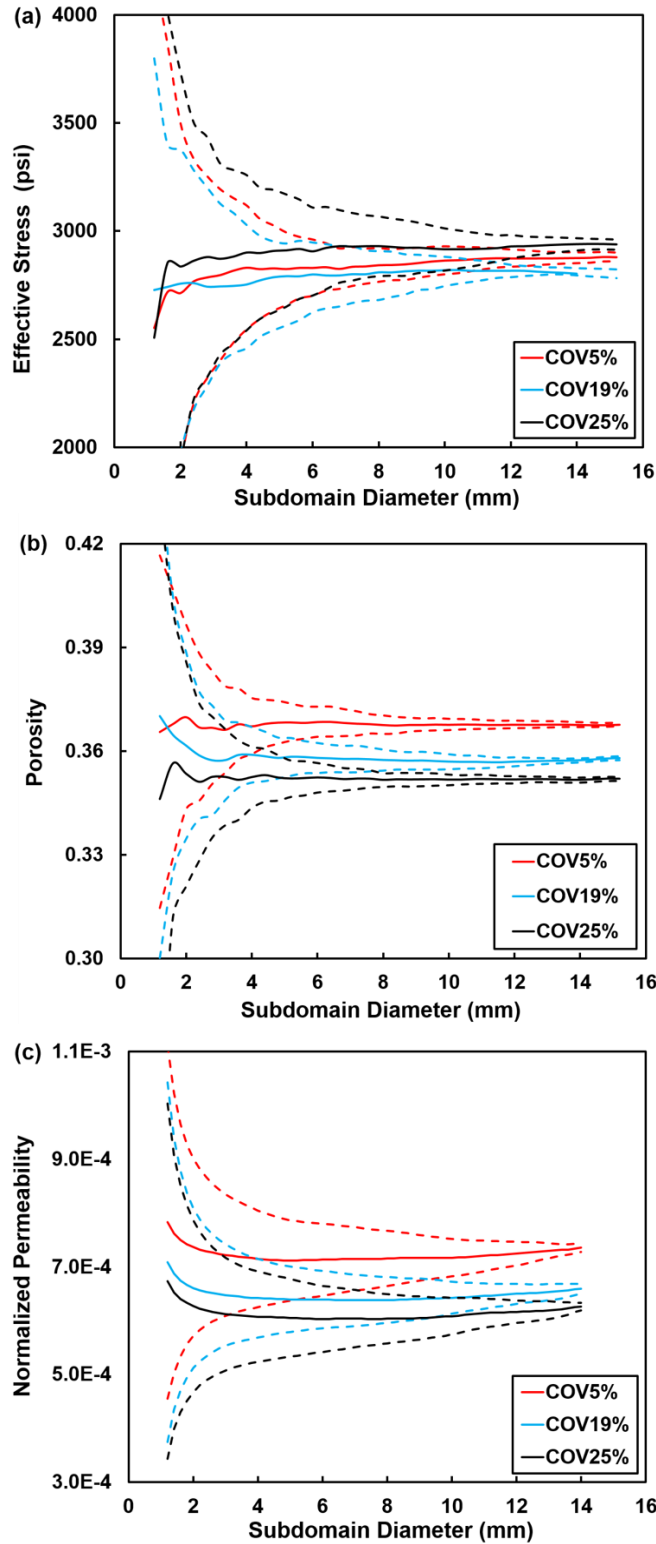


Figure 2.9. a) Mean effective stress, b) mean porosity, and c) mean normalized permeability associated with corresponding standard deviations (dashed lines) as functions of subdomain diameter.

Simulations of immiscible displacement of oil and water were performed on the basis of the 3D pore structure geometries generated by DEM compaction simulations. The pore geometry was extended in the main flow direction (x-direction) in a mirror-symmetry manner, in order to ensure a smooth transition between the inlet and outlet flows using a periodic boundary condition. In each geometry, fluid phases were initialized morphologically, based on an operation known as morphological opening (Yang et al., 2015), to achieve a range of fluid saturations. The oil was instantiated into the larger pores, consistent with water-wet porous media. For each configuration, simulations were performed to measure the relative permeability using the Titan supercomputer at Oak Ridge National Laboratory. Fluid flow was induced by applying a constant external body force with full periodic boundary conditions to mimic fractional flow experiments typically used to measure relative permeability in the laboratory (Ramstadt et al. 2012; Armstrong et al. 2016, 2017). Simulations were performed with a density and viscosity ratio each set to one. The contact angle was zero for all simulations. The capillary (Ca) number was within the range of  $2.95 \times 10^{-5} < Ca < 1.31 \times 10^{-4}$  for all simulations and computed based on the flow rate of the water phase, which varied as determined by the saturation. A total 100,000 time steps were sufficient to achieve stable values for the relative permeability. Figure 2.10 illustrates oil phase distributions in steady-state two-phase flow under effective stress of 670 psi observed for diameter COVs of 5% and 19%, respectively. The increased heterogeneity of the COV19% proppant geometry led to a more irregular pore structure and consequently more heterogeneous distribution of oil blobs. Furthermore, under low effective stress, irreducible water content was significantly

lower than residual oil content, because smooth proppant particle surface did not trap much water and the non-wetting oil blobs were trapped within big pores.

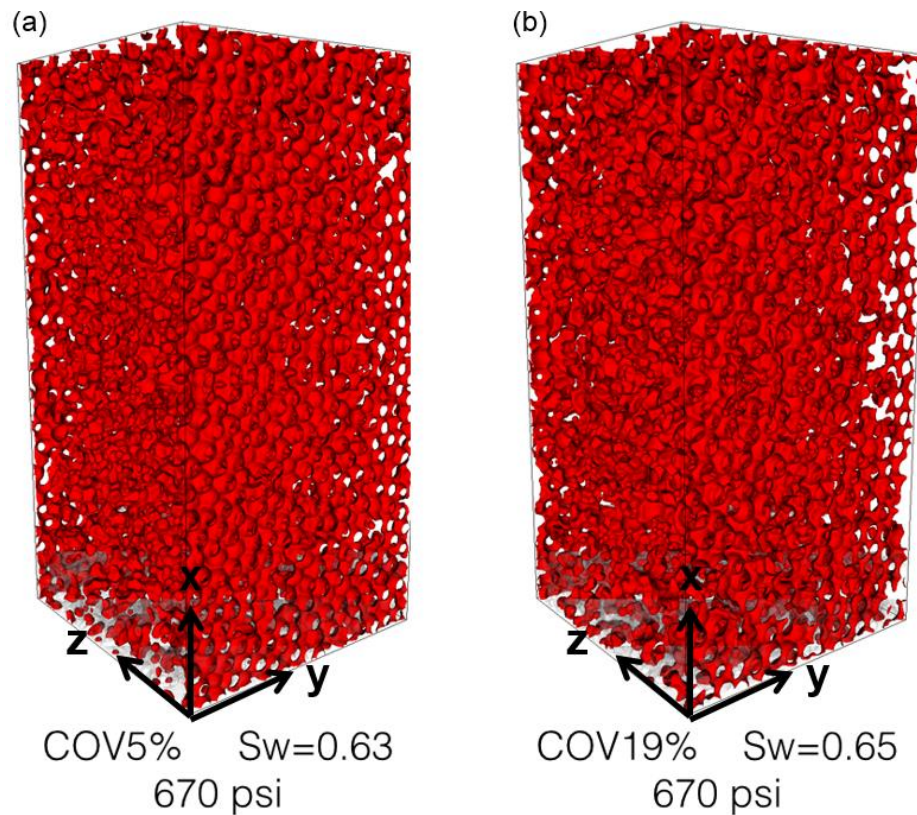


Figure 2.10. Oil phase distributions in steady-state two phase flow observed for diameter COVs of a) 5%, and b) 19%, respectively.

Figure 2.11 illustrates relative permeability curves determined from pore-scale DEM/LB simulation. Simulations were performed using the relatively homogeneous COV5% and more heterogeneous COV19% proppant geometries subjected to increasing effective stresses. As has been previously discussed, the leading-order effects on the flow due to proppant compaction result from the change in porosity. Compaction of the solid particles brings about a corresponding change in the permeability (i.e. Figure 2.7), an effect which is accounted for independently from the relative permeability based on the form of Equation 2.9. The implication is that any effects of proppant compaction on the



relative permeability are a consequence of other configurational effects, such as changes to the pore structure and connectivity. Specifically, Figure 2.11 shows that the relative permeability of the oil phase was more sensitive to changes in geometry and stress, as compared with the wetting phase. This was due to the fact that the oil phase occupied the larger pores; compaction of the proppant pack impacted the structures of the pores, since the pores were further from the grain contacts and thus more susceptible to collapse.

Figure 2.11 clearly illustrates that the variation of oil relative permeability in the COV19% geometry was significantly larger than that of the COV5% geometry. This was because smaller particles in the proppant assembly having a higher diameter COV migrated more easily within the pore space between larger particles. As a consequence, with identical stress increase, the proppant assembly having a higher diameter COV (i.e., a more heterogeneous particle diameter distribution) experienced more significant changes with respect to pore structure and connectivity, which directly led to larger variation of oil relative permeability.

It is also interesting to notice when effective stress increased continuously, oil relative permeability increased first and then decreased for the COV5% geometry at low and intermediate water saturations (35-60%), as presented in Figure 2.11a. This non-monotonic behavior was due to the non-monotonic development of oil connectivity under increasing stress. At low effective stress (670 psi), oil blobs were trapped within larger pores and relatively isolated from one another, leading to low oil connectivity and consequently low oil relative permeability. Under intermediate effective stress (2785 psi) and the same oil saturation, larger pores were squeezed and oil was forced to fill in smaller pores and pore throats, leading to more homogeneous oil distribution and

consequently improved oil connectivity, which gave rise to higher oil relative permeability. When effective stress increased to 4583 psi, a significant portion of pore throats were shut off, which negatively impacted oil connectivity and consequently reduced oil relative permeability. The non-monotonic dependence of oil relative permeability on effective stress confirmed that any effects of proppant compaction on the relative permeability are a consequence of other configurational effects, such as changes to the pore structure and connectivity.

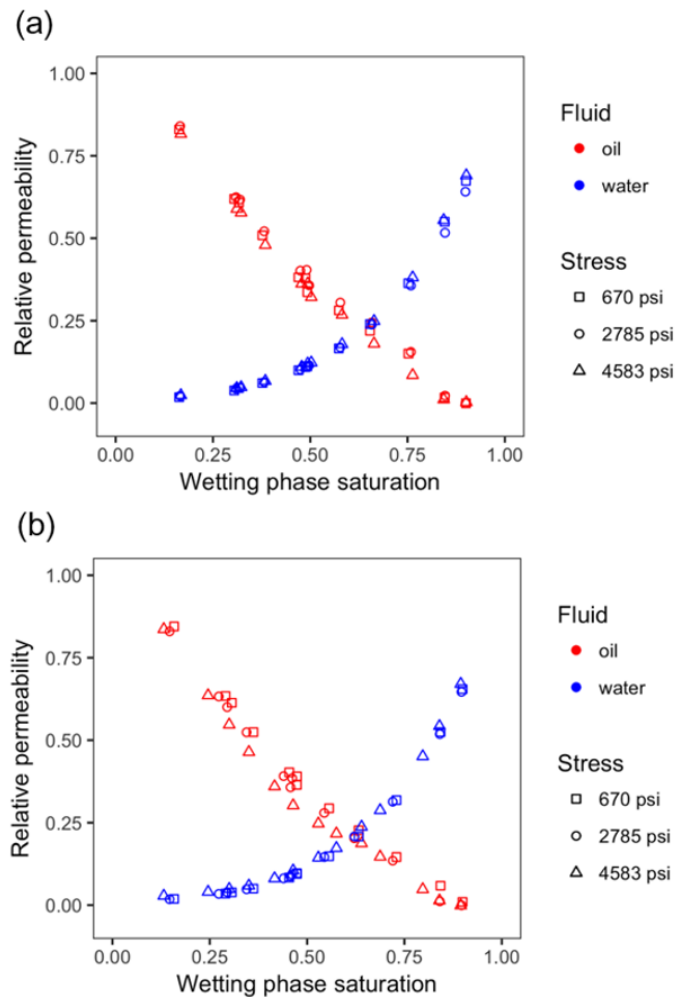


Figure 2.11. Relative permeability curves determined from pore-scale multiphase LB simulations for the geometries having a) 5% diameter COV; and b) 19% diameter COV.

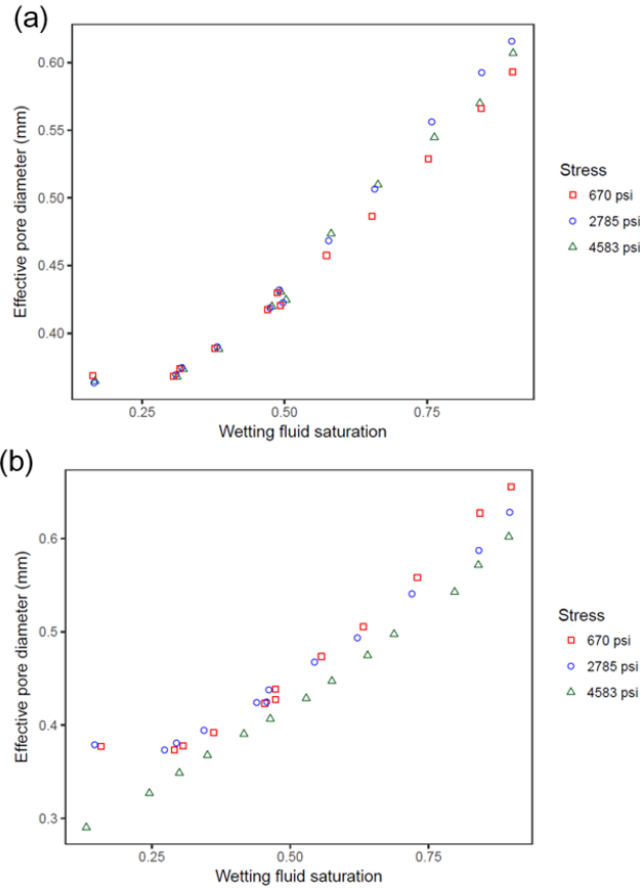


Figure 2.12. Effective pore diameters for the geometries having a) 5% diameter COV; and b) 19% diameter COV.

To confirm the hypothesis regarding the mechanism controlling the non-monotonic development of oil relative permeability, we calculated the average size of connected flow channels under increasing effective stress using the Laplace's law and LB-simulated capillary pressure curve. Specifically, in a 3D pore structure, the capillary pressure is related to the pore size on the basis of the Laplace's law:  $p_c = 2 \sigma \cos(\theta) / r$ , where  $p_c$  is capillary pressure,  $\sigma$  is interfacial tension coefficient,  $\theta$  is contact angle, and  $r$  is radius of the cylindrical flow channel. Based on the assumption of zero contact angle, the radius of the cylindrical flow channel is calculated as  $2\sigma/p_c$  and the effective pore diameter is thus  $4\sigma/p_c$ . Using this formula, we can show effective pore diameter as function of water

saturation on the basis of the LB-simulated capillary pressure curve, which plots  $p_c$  as function of water saturation. Results are presented in Figure 2.12. Figure 2.12a shows that the effective pore diameter in the COV5% geometry increased when effective stress increased to 2785 psi, and then decreased when the stress increased to 4583 psi. The non-monotonic development in the diameter of connected flow channel led to the non-monotonic development of oil relative permeability as illustrated in Figure 2.11a.

To further consider the impact of the proppant compaction on relative permeability, the pore structure for each geometry was quantified using the medial axis based method (Sheppard et al., 2005; Dong et al., 2009). More specifically, the pore space is first transformed into a medial axis, which is a 1D topological skeleton that runs along the middle of pore channels; the junctions in the skeleton then represent the basis for pore bodies, and the signed distance at each junction correspond to the radius of the maximum inscribed sphere, which represents the largest possible sphere that can fit within a particular region of the pore space without overlapping the solid or another sphere. Based on the medial axis approach, the relationship between the size distribution for the pore structure and the mechanical stress was determined as shown in Figure 2.13. It is noticeable that the COV5% geometry had narrower pore size distributions under all stresses with peak values higher than 0.2, whereas the COV19% geometry had wider pore size distributions under all stresses with peak values lower than 0.2. This was consistent with the fact the COV19% proppant assembly had a wider particle size distribution. While the overall structure of the pore space was similar for each material, certain regions of the pore space were more likely to collapse as a consequence of increasing stress. These changes to the pore structure were responsible for the changes to

the relative permeability as illustrated in Figure 2.11. As portions of the pore structure collapsed, fluid configurations must adjust accordingly. This altered the accessible flow pathways for each fluid.

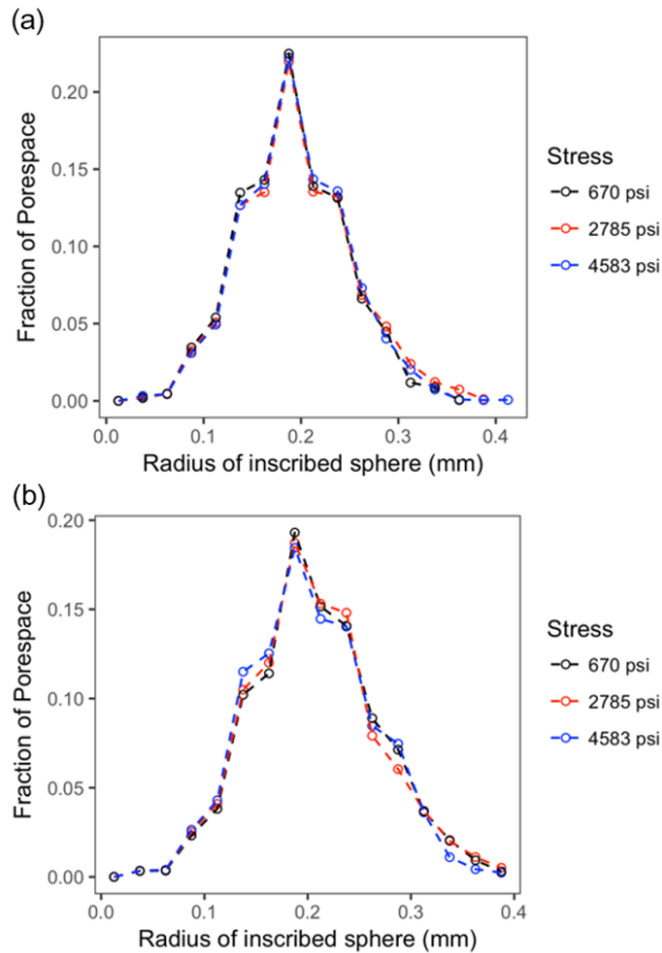


Figure 2.13. Pore size distribution determined from maximum inscribed spheres for the geometries having a) 5% diameter COV, and b) 19% diameter COV.

## 2.5. Conclusions and Implications

In this study, a geomechanics/fluid mechanics coupled numerical workflow was developed to study the interaction between proppant compaction and single-/multiphase flows in a hydraulic fracture. DEM was used to simulate the process of proppant particle compaction at different loading stresses. The pore structure geometries were then

extracted and imported into a LB model as boundary conditions for single-/multiphase flow simulations. Simulated proppant pack permeabilities were in good agreement with laboratory measurements within the low-stress range. Within the high-stress regime, laboratory-measured proppant pack permeabilities declined faster than those from numerical simulation, because of proppant embedment and crushing. This poses a pressing need for the numerical model to take into account the multiphysics processes in the high-stress regime. Under the same effective stress, a proppant pack with a smaller diameter COV, which implies a more homogeneous particle diameter distribution, had higher porosity and permeability and smaller fracture width reduction; these are all favorable for maintaining the fracture conductivity during the process of hydrocarbon extraction. Furthermore, the relationship between porosity and permeability can be fitted with the empirical Kozeny-Carman equation. The relative permeability of oil was more sensitive to changes in geometry and stress, compared to that of water. This was due to the fact that the oil phase occupied larger pores; compaction of the proppant pack impacted the structure of the pores, since the pores were further from the grain contacts and thus more susceptible to collapse. It is also interesting to notice when effective stress increased continuously, oil relative permeability in one proppant assembly increased first and then decreased. This non-monotonic behavior was due to the non-monotonic development of effective pore diameter under increasing stress.

After validation and calibration by comparisons with lab experimental data, the novel DEM/LB-integrated numerical workflow has the potential to advance fundamental knowledge and scientific understanding, because information on all individual voxels is known and can easily be tracked at the pore scale. Second, the system in modeling is

known and well controlled, which mitigates uncertainties often encountered in experimental setup and data acquisition. For instance, in this study we used computer modeling to generate proppant size distributions having different levels of heterogeneity by accurately controlling the size of all individual proppant particles. This is extremely challenging to accomplish in lab experiments. Third, comprehensive sensitivity analysis becomes possible in numerical modeling, especially with the help of high-performance parallel computing. For example, in this study the parallel two-phase LB code ran all scenarios concurrently on the Titan supercomputer. Relative permeabilities for all water saturations on the same curve were obtained simultaneously in less than two hours. To summarize, the numerical workflow combines DEM simulation with LB simulation and provides an insightful tool to study the complicated, multiphysics processes within a proppant/fracture system; it has the potential to become an advantageous alternative to conventional laboratory experiments.

The main contribution of this work is the development of a numerical tool for investigating the complicated interactions between the geomechanical, geometric, and transport properties of a proppant assembly sandwiched in a rock fracture. Specifically, the role of proppant size heterogeneity on the development of proppant pack porosity, permeability, scale dependency (REV analysis), relative permeability, and phase connectivity was studied and discussed when the effective stress increased continuously. With the help of high-performance parallel computing, this novel, DEM/LB-integrated approach is able to generate fracture-conductivity/proppant-concentration curves (Darin and Huitt, 1960; Brannon et al. 2004) under various closure pressures and proppant sizes within a short turnaround time, which can be directly used in larger-scale reservoir

simulations for comprehensive sensitivity analysis in order to optimize proppant placement in fractures (e.g., Gu et al. 2017). Furthermore, the developed numerical methods in this study have the potential to make broader impacts and contribute to the study of other geomechanical, geoenergy, and geoenvironmental processes that involve single-/multiphase flows within a fracture filled with granular materials and subject to closure pressure, such as rock mass instability, geologic carbon sequestration, and non-aqueous phase liquid transport.

### **Nomenclature**

$c_s$  = speed of sound in the LB model, m/s

$\mathbf{C}$  = color gradient vector,  $\text{m}^{-1}$

$D$  = diameter of proppant particle, m

$f_i$  = LB particle-distribution function

$f_i^{eq}$  = equilibrium LB particle-distribution function

$F_i$  = total contact force, N

$F_i^n$  = normal component of the contact force, N

$F_i^S$  = shear component of the contact force, N

$\mathbf{g}$  = gravitational acceleration vector,  $\text{m/s}^2$

$K^n$  = normal stiffness at the contact, N/m

$k^S$  = shear stiffness at the contact, N/m

$\mathbf{k}$  : permeability tensor,  $\text{m}^2$



$k_{ri}$  = relative permeability of fluid  $i$

$k_{xx}$  = principal component of permeability tensor in x-direction,  $m^2$

$k_{yy}$  = principal component of permeability tensor in y-direction,  $m^2$

$k_{zz}$  = principal component of permeability tensor in z-direction,  $m^2$

$P$  = fluid pressure, Pa

$S$  = total surface area of proppant particles,  $m^2$

$\mathbf{u}$  = pore-scale velocity vector, m/s

$U^n$  = normal component of contact displacement, m

$U^s$  = shear component of the contact displacement, m

$V$  = volume of computational domain,  $m^3$

$\mathbf{v}$  = Darcy flow velocity vector, m/s

$w$  = weight coefficient

$\phi$  = porosity

$\mu$  = dynamic viscosity, Pa s

$\rho$  = fluid density,  $kg/m^3$

$\varphi$  : Phase field indicator

### **Acknowledgements**

The authors acknowledge the support of a start-up package from Virginia Tech, the support of the Junior Faculty Award from Virginia Tech's Institute for Critical Technology and Applied Science, and the support of Aramco Services Company -

Houston. The parallel, multiphase LB flow simulation was supported by an award of computer time provided by the Department of Energy INCITE program. This research also used resources of the Oak Ridge Leadership Computing Facility, which is a DOE Office of Science User Facility supported under Contract DE-AC05-00OR22725.

## Reference

Armstrong, R.T., McClure, J.E., Berrill, M.A., Rucker, M., Schluter, S. and Berg S. (2016) Beyond Darcy's law: The Role of Phase Topology and Ganglion Dynamics for Two-fluid Flow. *Physical Review E*, 94(4): 043113.

Armstrong, R. T., McClure, J. E., Berill, M. A., Rucker, M., Schluter, S., & Berg, S. (2017) Flow Regimes During Immiscible Displacement. *Society of Petrophysicists and Well-Log Analysts*.58(01): 10-18.

Barree, R. D., Cox, S. A., Barree, V. L. and Conway, M. W. (2003), Realistic Assessment of Proppant Pack Conductivity for Material Selection. *Society of Petroleum Engineers*. SPE-84306-MS, SPE Annual Technical Conference and Exhibition, 5-8 October, Denver, Colorado, doi:10.2118/84306-MS.

Brannon, H. D., Malone, M. R., Rickards, A. R., Wood, W. D., Edgeman, J. R., & Bryant, J. L. (2004, January 1). Maximizing Fracture Conductivity with Proppant Partial Monolayers: Theoretical Curiosity or Highly Productive Reality? *Society of Petroleum Engineers*. doi:10.2118/90698-MS

Chen, C., Packman, A.I. and Gaillard, J.F. (2008), Pore-scale Analysis of Permeability Reduction Resulting from Colloid Deposition, *Geophysical Research Letters*, 35, L07404, doi:10.1029/2007GL033077.

Chen, C., Lau, B.L.T., Gaillard, J.F. and Packman, A.I. (2009a), Temporal Evolution of Pore Geometry, Fluid Flow, and Solute Transport Resulting from Colloid Deposition, *Water Resources Research*, 45, W06416, doi:10.1029/2008WR007252.

Chen, C., A. I. Packman, and J. F. Gaillard (2009b), Using X-ray micro-tomography and pore-scale modeling to quantify sediment mixing and fluid flow in a developing streambed, *Geophysical Research Letters*, 36, L08403, doi:10.1029/2009GL037157.

Chen, C., L. Zeng, and L. Shi (2013a), Continuum-scale convective mixing in geological CO<sub>2</sub> sequestration in anisotropic and heterogeneous saline aquifers, *Advances in Water Resources*, 53, 175-187.

Chen, C., Hu, D., Westacott, D. et al. (2013b), Nanometer-Scale Characterization of Microscopic Pores in Shale Kerogen by Image Analysis and Pore-Scale Modeling. *Geochemistry, Geophysics, Geosystems* 14 (10): 4066-4075. <http://dx.doi.org/10.1002/ggge.20254>.

Chen, C., Martysevich, V., O'Connell, P., Hu, D. and Matzar, L. (2015), Temporal Evolution of the Geometrical and Transport Properties of a Fracture/Proppant System under Increasing Effective Stress, *SPE Journal*, 20(3), 527-535, SPE-171572-PA. <http://dx.doi.org/10.2119/171572-PA>.

Chen, C., Wang, Z., Majeti, D., Vrvilo, N., Warburton, T., Sarkar, V. and Li, G. (2016), Optimization of Lattice Boltzmann Simulation with Graphics-Processing-Unit Parallel Computing and the Application in Reservoir Characterization, *SPE Journal*, SPE-179733-PA, <http://dx.doi.org/10.2118/179733-PA>.

Chen, H., Chen, S. and Matthaeus, W.H. (1992) Recovery of the Navier–Stokes equations using a Lattice-gas Boltzmann Method, *Phys. Rev. A* 45: 5339–5342.

Chen, S., and Doolen, G. D. (1998), Lattice Boltzmann Method for Fluid Flows, *Annu. Rev. Fluid Mech.*, 30, 329-364.

Cundall P.A. (1971), A Computer Model for Simulating Progressive Large Scale Movements in Blocky Rock Systems. In: proceedings of the third international rock mechanics symposium, 1: 2–8.

Cundall P.A., Strack ODL, (1979), A Discrete Numerical Model for Granular Assemblies. *Geotechnique*; 29:47-65.

CARBOHSP Technical Data Sheet, (2015), CARBO Ceramics Inc. <http://www.carboceramics.com/getattachment/c14298e6-f68a-4f27-821a-cab71f9fa061>.

Daneshy A. Factors Controlling the Vertical Growth of Hydraulic Fractures (2009), SPE 118789, proceedings of the SPE hydraulic fracturing technology conference, The Woodlands, TX. 19-22 January.

Darin, S.R. and J.L. Huitt, Effect of a Partial Monolayer of Propping Agent on Fracture Flow Capacity. *Transactions of the American Institute of Mining and Metallurgical Engineers*, 1960. 219(3): p. 31-37.

Dong, H., and Blunt, M.J., (2009), Pore-network Extraction from Micro-computerized-tomography Images, *Physical Review E*, 80(3): 036307.

Dye A.L., McClure J.E., Miller C.T. and Gray W.G. (2013), Description of Non-Darcy Flows in Porous Medium Systems. *Phys. Rev. E*, 87(3), 033012, doi:10.1103/PhysRevE.87.033012.

Gaurav A, Dao EK, Mohanty KK (2012), Evaluation of Ultralight-weight Proppants for Shale Fracturing. *J Petrol Sci Eng.*, 92: 82-8.

Ginzburg I. (2008), Consistent Lattice Boltzmann schemes for the Brinkman Model of Porous Flow and Infinite Chapman–Enskog Expansion. *Phys Rev E*, 77:066704.

Ginzburg I, d’Humières D, Kuzmin A. (2010), Optimal Stability of Advection-diffusion Lattice Boltzmann Models with Two Relaxation Times for Positive/negative Equilibrium. *J Stat Phys*, 139:1090-143.

Gu, M., M. Fan, and C. Chen (2017), Proppant Optimization for Foam Fracturing in Shale and Tight Reservoirs, SPE-185071-MS, SPE Canada Unconventional Resources Conference, Calgary, Alberta, Canada, February 15-16.

Gustensen, A.K., Rothman, D.H., Zaleski, S. and Zanetti, G. (1991), Lattice Boltzmann Model of Immiscible Fluids. *Physical Review A*, 43, 4320–4327.

Grunau, D., Chen, S. and Eggert, K. (1993), A Lattice Boltzmann Model for Multiphase Fluid Flows. *Phys. Fluids A* 5:2557-2562.

Han Y., and Cundall P.A. (2013) LBM-DEM Modeling of Fluid-solid Interaction in Porous Media, *Int. J. Numer. Anal. Meth. Geomech.* 37 (10): 1391-1407.

Han Y., P.A. and Cundall P.A. (2011) Lattice Boltzmann Modeling of Pore-scale Fluid Flow through Idealized Porous Media, *Int. J. Num. Meth. Fluids* 67 (11): 1720-1734.

Inamuro, T., Yoshino, M. and Ogino, F. (1999), Lattice Boltzmann Simulation of Flows in a Three-Dimensional Porous Structure. *Int. J. Numer. Methods Fluids* 29: 737-

748. [http://dx.doi.org/10.1002/\(SICI\)1097-0363\(19990415\)29:7<737::AID-FLD813>3.0.CO;2-H](http://dx.doi.org/10.1002/(SICI)1097-0363(19990415)29:7<737::AID-FLD813>3.0.CO;2-H).

Itasca Consulting Group, Inc. (2008), PFC3D – Particle Flow Code in 3 Dimensions, Version 4.0 User’s Manual. Minneapolis: Itasca.

Li Y, Huang P. (2008), A Coupled Lattice Boltzmann Model for Advection and Anisotropic Dispersion Problem in Shallow Water. *Adv Water Resour*, 31:1719-30.

McClure, J.E., Prins, J.F. and Miller, C.T. (2014) A Novel Heterogeneous Algorithm to Simulate Multiphase Flow in Porous Media on Multicore CPU-GPU Systems. *Computer Physics Communications*, 185(7):1865-1874.

Pan, C., Luo, L., Miller, C.T. (2006), An Evaluation of Lattice Boltzmann Schemes for Porous Medium Flow Simulation. *Computers and Fluids*, 35(8), 898–909.

Ramstad, T., Idowu, N., Nardi, C. and Øren, P-E. (2012) Relative Permeability Calculations from Two-phase Flow Simulations Directly on Digital Images of Porous Rocks. *Transport in Porous Media*.

Sheppard, A.P., Sok, R.M., and Averdunk, H., (2005), Improved Pore Network Extraction Methods, *International Symposium of the Society of Core Analysis*: 2125.

Succi, S., Benzi, R. and Higuera, F. (1991), The Lattice-Boltzmann Equation—a New Tool for Computational Fluid Dynamics. *Physica D* 47:219–30.

Succi, S. (2001), *The Lattice Boltzmann Equation for Fluid Dynamics and Beyond*, Oxford Univ. Press, New York.

Terracina, J. M., Turner, J. M., Collins, D. H. and Spillars, S. (2010, January 1). Proppant Selection and Its Effect on the Results of Fracturing Treatments Performed in Shale Formations. Society of Petroleum Engineers. doi:10.2118/135502-MS.

Yang F., Hingerl F., Xiao X., Liu Y., Wu Z., Benson S., and Toney M. (2015), Extraction of pore-morphology and capillary pressure curves of porous media from synchrotron-based tomography data. Sci. Rep. Vol. 5, 10635.

Zhang, D., Zhang R., Chen S., and Soll W. E. (2000), Pore Scale Study of Flow in Porous Media: Scale Dependency, REV, and Statistical REV, Geophys. Res. Lett., 27(8), 1195–1198, doi:10.1029/1999GL011101.

Zhang, F., Zhu, H., Zhou, H., Guo, J., & Huang, B. (2017). Discrete-Element-Method/Computational-Fluid-Dynamics Coupling Simulation of Proppant Embedment and Fracture Conductivity After Hydraulic Fracturing. Society of Petroleum Engineers. doi:10.2118/185172-PA

## **Chapter 3 - Using an Experiment/Simulation-integrated Approach to Investigate Fracture-Conductivity Evolution and Non-Darcy Flow in a Proppant-supported Hydraulic Fracture**

Ming Fan, James McClure, Virginia Tech; Yanhui Han, Aramco Research Center – Houston; Nino Ripepi, Erik Westman, Virginia Tech, Ming Gu, West Virginia University, Cheng Chen, Virginia Tech

### **Abstract**

Optimizing proppant-pack conductivity in a hydraulic fracture is of critical importance to sustaining effective and economical production of petroleum hydrocarbons. In this study, a hybrid, experiment/simulation-integrated workflow, which combines the discrete element method (DEM) and the lattice Boltzmann (LB) method with laboratory-measured load-embedment correlations, was developed to advance the understanding of fracture-conductivity evolution from partial-monolayer to multilayer concentrations. The influence of compressive stress and proppant-diameter heterogeneity on non-Darcy flow behaviors was also investigated. The DEM method was used to simulate effective-stress increase and the resultant proppant-particle compaction and rearrangement. Proppant-embedment distance was then determined using an empirical correlation obtained by fitting experimental data. The final pore structure of the proppant pack was imported into the LB simulator as interior boundary conditions of fluid-flow modeling in the calculation of time-dependent permeability of the proppant pack. To validate the integrated workflow, proppant-pack conductivity as a function of increasing proppant concentration was simulated and then compared with laboratory data. Good agreement was observed between the workflow-derived and



laboratory-measured fracture-conductivity vs. proppant-concentration curves. Furthermore, the role of proppant size, size heterogeneity, and closure pressure on the optimal partial-monolayer proppant concentration was investigated. The optimal partial-monolayer proppant concentration has important engineering implications, because one can achieve a considerable fracture conductivity using a partial-monolayer proppant structure, which has much lower material costs compared with the conventional multilayer proppant structures. To investigate the effect of non-Darcy flow on fracture conductivity, three proppant packs with the same average diameter but different diameter distributions were generated. Specifically, the coefficient of variation (COV) of diameter, defined as the ratio of standard deviation of diameter to mean diameter, was used to characterize the heterogeneity of particle size. The results of this research provide fundamental insights into the multiphysics processes regulating the conductivity evolution of a proppant-supported hydraulic fracture, as well as the role of compressive stress and proppant-size heterogeneity in non-Darcy flows.

**Keywords:** fracture conductivity, proppant, discrete element method, lattice Boltzmann, non-Darcy

### **3.1 Introduction**

Hydrocarbon extraction from unconventional reservoirs (e.g., shale oil and gas) is extremely challenging because of the low permeability and complex petrophysical properties of these rock formations. To achieve economical production rates from these tight shale oil/ gas reservoirs, the hydraulic-fracturing technique is widely used to enhance the production of petroleum hydrocarbons (Economides and Nolte 2000; Gu

and Mohanty 2014; Chen et al. 2015). The standard hydraulic-fracturing operation usually involves injecting a large quantity of fracturing fluids to create and propagate tensile fractures at a treatment pressure higher than the minimum principal stress (Ye and Ghassemi 2016). During hydrocarbon production, fractures close after pumping because of reduced fluid pressure and increased effective stress in the fractures (Fan et al. 2017a, 2018). To provide the long-term conductivity of the fracture, proppant slurries are pumped into the induced fracture to prevent hydraulic fractures from closing once the hydraulic-fracturing pressure is relieved (Liang et al. 2016). In well production, flow deviations from Darcy's law in the near-wellbore region and in propped hydraulic fractures are frequently observed (Newman and Yin 2013). This deviation is because of the non-Darcy flow effects inside the hydraulically fractured reservoir, which might lead to a significant pressure drop and reduction of fracture conductivity. Therefore, conductivity and non-Darcy-effect coefficient of a proppant-supported fracture are vital parameters in the design of hydraulic-fracturing stimulation.

Fracture conductivity measures the total flow rate through a unit length of a fracture and is calculated as the product of fracture permeability and fracture width. A sufficiently large fracture conductivity is critical for economically viable extraction of hydrocarbons from the reservoir. Fracture width and permeability depend closely on the amount of proppant placed in the fracture as well as the effective stress exerted on the proppant pack (Chen et al. 2015). The amount of proppant placed in a fracture is measured by proppant concentration, also known as proppant areal concentration, defined as the proppant mass per unit fracture-face area and usually in the unit of  $\text{lbm/ft}^2$  (Economides and Nolte 2000). To increase fracture conductivity, it is tempting to increase fracture width by

placing multiple layers of proppant particles in the fracture. By increasing the proppant concentration, the fracture width increases. However, the fracture width alone does not control the overall flow capacity of the fracture, because fracture conductivity (i.e., flow capacity of the fracture), by its definition, is determined by both the permeability of the proppant pack and the fracture width. Thus, increasing fracture permeability to obtain larger flow capacity is as important as increasing fracture width. In addition, because the price of manmade ceramic proppant is relatively high, ranging from USD 5/lbm to USD 10/lbm (Gu et al. 2015), it is of economic interest to use a lower proppant concentration.

Decreasing proppant concentration to form a partial-monolayer proppant pack has the potential to increase the overall fracture conductivity (Huitt and McGlothlin 1958; Darin and Huitt 1960), primarily because a partial-monolayer proppant structure has high porosity that leads to high fracture permeability. Several laboratory studies have shown that partial-monolayer proppant assemblies provide higher or equal fracture conductivity compared with conventional multilayer proppant assemblies (e.g., Brannon et al. 2004; Gaurav et al. 2010; Bestaoui-Spurr and Hudson 2017). In field testing, Parker et al. (2012) demonstrated that a lightweight, thermoplastic alloy (TPA) proppant can form a partial-monolayer structure and significantly enhance productivity. Specifically, in the Jonah Field, Wyoming, Parker et al. (2012) found that the 24-month cumulative gas production from the well using the TPA treatment was approximately 25% higher than that from the other three wells using the conventional multilayer proppant treatment, while the amount of TPA proppant was only 5% of the conventional proppant.

In an induced hydraulic fracture, the interplay between fracture closure, proppant compaction, and proppant embedment into the rock formation can lead to an optimal

partial-monolayer proppant concentration (Huitt and McGlothlin 1958; Darin and Huitt 1960), which will be discussed in detail later in this paper. In practice, many innovative fracturing products and design techniques have been developed to obtain relatively uniform partial-monolayer proppant coverage in a hydraulic fracture (e.g., Gu et al. 2015). The combination of slickwater pumping and ultralightweight proppant leads to uniform proppant distribution over the entire space of a vertical fracture, because the buoyancy of ultralightweight proppant in slickwater mitigates proppant settlement into the lower portion of the fracture (Bestaoui-Spurr and Hudson 2017).

Recently, several numerical modeling studies have been conducted to investigate the multiphysics processes associated with proppant compaction and embedment in a propped fracture. For example, Zhang et al. (2017) coupled the DEM with computational fluid dynamics to study the role of proppant embedment on fracture conductivity; this work involved direct simulations of millimeter-scale proppant particles in a multilayer proppant structure and bonded, micrometer-scale particles in the rock matrix. Bolintineanu et al. (2017) generated proppant-packed fractures using DEM simulations and then used finite-element flow simulations to measure fracture conductivity; this work numerically confirmed that in a partial-monolayer proppant structure, there is a dramatic increase in fracture conductivity because the decrease of proppant-volume fraction leads to open flow channels. However, the numerical model of Bolintineanu et al. (2017) did not account for proppant embedment on rock surfaces, which implies that the fracture width stays constant with partial-monolayer proppant concentrations.

Under increased effective stress, proppant compaction, rearrangement, and embedment can modify the proppant pore structure significantly within a hydraulic

fracture, which, associated with the relatively high pressure gradient near the wellbore, can result in detrimental non-Darcy flow effects. Many studies have shown that effective fracture conductivity and well productivity can experience a significant reduction because of the effects of non-Darcy flow (e.g., Zeng and Grigg 2006; Palisch et al. 2007; Macini et al. 2008). Therefore, fundamental studies of non-Darcy flow effects in a propped hydraulic fracture have the potential to achieve improved prediction of well performance and productivity decline. Fracture conductivity and non-Darcy-effect coefficient are typically measured according to the specific quality-control procedures outlined by the American Petroleum Institute (API) and the International Organization for Standardization (ISO) (Liang et al. 2016). In Schubarth and Milton-Taylor (2004), a series of crush tests were performed on several proppant types and sizes; the effect of median particle diameter on proppant-pack conductivity and the non-Darcy-effect coefficient was studied. Barree et al. (2003) outlined the influence of primary damage mechanisms and non-Darcy flow effect on final- fracture conductivity and proposed a method to optimize fracture stimulation design. Many laboratory measurements, correlations, and simulations were also performed to estimate the non-Darcy flow effect and its role on the relationship between flow rate and pressure drop in porous media (Milton-Taylor 1993; Miskimins et al. 2005; Palisch et al. 2007; Macini et al. 2008; Balhoff and Wheeler 2009; Newman and Yin 2013). Both experiments and simulations indicate that non-Darcy flow in fractures and reservoirs is a significant effect that limits the productivity of hydraulically fractured reservoirs.

This study used a hybrid, experiment/simulation-integrated approach to study the interactions between the geomechanical, geometric, and transport properties of granular

materials sandwiched in a rock fracture and subjected to compaction, aiming at advancing the understanding of fracture- conductivity evolution from partial-monolayer proppant concentrations to multilayer proppant concentrations. Specifically, the novelty and contribution of this study can be summarized as follows. First, a hybrid, experiment/simulation-integrated workflow was developed to study fracture-conductivity evolution under varying proppant areal concentrations. The experimental component in the workflow quantifies fracture-closure distance because of proppant embedment. This experiment/simulation- integrated approach achieves a balance between computational accuracy and efficiency. Second, the fracture-conductivity vs. proppant-concentration curves were measured over a wide range of proppant areal concentrations from less than 0.001 lbm/ft<sup>2</sup> to 5 lbm/ft<sup>2</sup>, which takes into account the transition from a partial-monolayer proppant structure to a multilayer proppant structure. The experiment/simulation-integrated workflow incorporates the important multiphysics processes over a wide range of proppant concentrations and, thus, is able to capture the nonmonotonic shape of the fracture-conductivity vs. proppant-concentration curve, which was shown in laboratory experiments (Brannon et al. 2004). Third, the role of proppant-particle size, particle-size heterogeneity (variation in proppant-particle diameter), and effective stress on the evolution of the fracture-conductivity vs. proppant-concentration curve was comprehensively studied and discussed. Fourth, comprehensive sensitivity analyses were conducted to investigate the influence of compressive stress and proppant-diameter heterogeneity on the non-Darcy flow effect. The findings of this study advance the fundamental understanding of the role of proppant embedment and compaction and will facilitate the development of optimization workflows that can be used to optimize

proppant placement in hydraulic fractures and to maximize productivity. This work also provides insight into the factors that regulate the complicated interactions between closure pressure, proppant-pack geometry, and non-Darcy flow.

## **3.2 Overview of Technical Elements in Workflow**

### **3.2.1 Optimal Partial-monolayer Proppant Concentration**

Figure 3.1 shows mitigation of proppant embedment in a vertical fracture when proppant concentration continuously increases. It is assumed that proppant crushing does not occur because high-strength ceramic proppant can withstand stress of higher than 10,000 psi (Liang et al., 2016). Development of fracture conductivity with increasing proppant concentration will go through four distinct stages, as outlined in Table 3.1.

**Stage 1:** Proppant concentration is low. Placing more proppant into the fracture will mitigate proppant embedment significantly, leading to fast-growing fracture width and permeability. On the other hand, placing more proppant into an empty fracture reduces fracture porosity, which has a negative effect on fracture permeability. Because permeability gain resulting from fracture-width increase surpasses permeability loss resulting from porosity reduction, the net effect is that fracture permeability increases, leading to increased fracture conductivity.

**Stage 2:** Permeability loss resulting from porosity reduction surpasses permeability gain resulting from fracture-width increase. Fracture permeability will decrease. However, when fracture permeability initially starts to drop, the rate of permeability reduction is lower than the rate of fracture-width increase; fracture conductivity is, thus, still increasing.

**Stage 3:** Fracture conductivity declines because the rate of permeability reduction surpasses the rate of fracture-width increase. The proppant concentration at the boundary between Stages 2 and 3, in which the fracture conductivity reaches the local maximum, is referred to as the “optimal partial-monolayer proppant concentration.” The corresponding local maximum on the conductivity curve is referred to as the “optimal partial-monolayer fracture conductivity.” The existence of the local maximum results from the competing relationship between fracture permeability and fracture width, because fracture conductivity is the product of fracture permeability and fracture width, and the evolution of fracture permeability is nonmonotonic as shown in Table 3.1. Stage 3 continues until the proppant assembly develops to a full monolayer.

**Stage 4:** Proppant develops to a multilayer assembly. Fracture porosity and permeability do not change significantly with increasing proppant concentration and fracture width, because the proppant pack is now a fully-packed porous medium and, its porosity and permeability are primarily controlled by the average grain and pore-throat sizes (Chen et al. 2008; 2009a).

**Table 3.1.** Developments of fracture width,  $h$ , porosity,  $\phi$ , permeability,  $k$ , and conductivity ( $k \cdot h$ ) with increasing proppant concentration. “↗”, “↘”, and “→” denote “increase”, “decrease”, and “stay constant”, respectively.

	$h$	$\phi$	$k$	Fracture conductivity ( $k \cdot h$ )	Geometry of proppant assembly
<b>Stage 1</b>	↗	↘	↗	↗	Partial monolayer
<b>Stage 2</b>	↗	↘	↘	↗	Partial monolayer
<b>Stage 3</b>	↗	↘	↘	↘	Partial monolayer to monolayer
<b>Stage 4</b>	↗	→	→	↗	Monolayer to multiplayer



The theory of optimal partial-monolayer proppant structure was developed decades ago (Huitt and McGlothlin, 1958; Darin and Huitt, 1960), but the field application had not been possible until the development of fracturing design using slickwater and ultra-lightweight proppant (Brannon et al. 2004). This paper shows that there are four distinct stages when the proppant packs develop from a partial-monolayer proppant structure to a multilayer proppant structure, as summarized in Table 3.1. The optimal partial-monolayer proppant concentration has important engineering implications and is economically tempting, because one can achieve considerable fracture conductivity using a partial-monolayer proppant structure, which has much lower material costs compared to the conventional multilayer proppant structures. Laboratory testing of fracture conductivity usually takes days to months (Weaver et al., 2009; Aven et al., 2013; Raysoni and Weaver, 2013). On the other hand, pure numerical modeling of proppant embedment and compaction in a propped hydraulic fracture can be computationally expensive when the particle number becomes large. In this study, a hybrid, experiment/simulation-integrated approach was developed to understand the role of proppant embedment and compaction by studying the complex interactions between the geomechanical, geometric, and transport properties within a fracture/proppant system. Specifically, proppant stress, deformation, and movement are simulated between two rigid walls. Effective stress on the particles in direct contact with fracture walls are extracted and then used to determine proppant embedment distance based on a laboratory-measured load-embedment correlation.

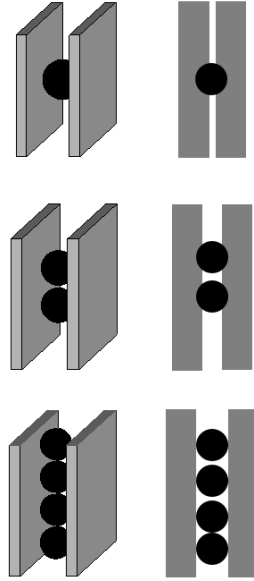


Figure 3.1. Mitigation of proppant embedment in a vertical fracture with increasing proppant concentration.

### 3.2.2 Overview of the Experiment/Simulation-integrated Workflow and Compaction Studies

This section aims to provide an overview of the experiment/simulation-integrated workflow as well as the compaction studies. Details of experimental setup and numerical methods will be given in later sections. In this work, a hybrid, experiment/simulation-integrated approach was developed to study proppant embedment and compaction in a hydraulic fracture, which is subjected to closure pressure and has a proppant concentration ranging from a partial-monolayer structure to a multilayer structure. First, a series of ballpoint penetrometer experiments were conducted on tight sandstone samples, which led to a semi-empirical correlation to relate mechanical loading exerted on a spherical particle to its embedment depth on rock surface (Huitt and McGlothlin, 1958; Darin and Huitt, 1960). Second, the DEM numerical simulation was carried out to find proppant stress, deformation, and rearrangement within a proppant assembly that was

sandwiched in two fracture walls and subjected to compressive stress (i.e., closure pressure). In a multilayer proppant assembly, compaction and rearrangement of proppant particles lead to reduction of the pore space between particles, which contributes to fracture width reduction (i.e., fracture closure). Third, effective stress on the particles in direct contact with the fracture walls was extracted. The stress information, combined with the laboratory-measured load-embedment correlation, was used to determine extra fracture closure distance resulting from proppant embedment. The final proppant pore structure in the steady state was imported into a lattice Boltzmann (LB) simulator (Chen et al. 2008, 2015) as interior boundary conditions of flow modeling to evaluate the role of proppant compaction and embedment on the changes of fracture permeability and conductivity. This hybrid, experiment/simulation-integrated approach has the advantage of identifying and quantifying fracture closure distances resulting from proppant compaction and embedment separately in a time-efficient manner. Figure 3.2 demonstrates a schematic workflow. This workflow was repeated on proppant assemblies having various proppant concentrations, leading to a fracture conductivity (md-ft) versus proppant concentration ( $\text{lb/ft}^2$ ) curve (abbreviated as “conductivity curve” hereafter).

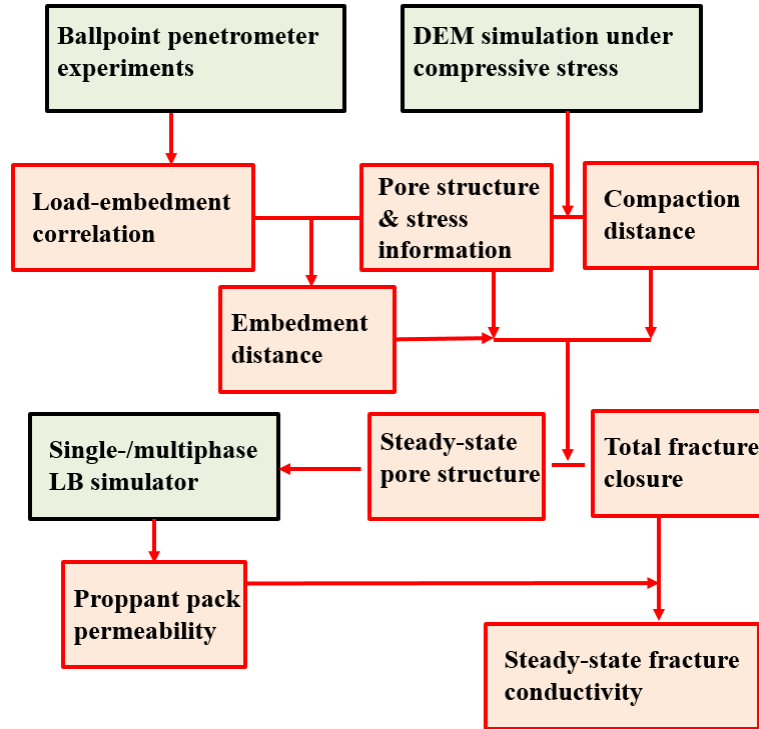


Figure 3.2. A hybrid, experiment/simulation-integrated workflow for calculating proppant compaction, embedment, as well as the influence on fracture conductivity.

In order to validate the experiment/simulation-integrated workflow, proppant pack conductivity as a function of increasing proppant concentration was simulated and then compared with laboratory data (Brannon et al. 2004). In the laboratory, the test was conducted on 20/40-mesh-size proppant particles to obtain the fracture conductivity under varying proppant concentrations, ranging from a partial-monolayer concentration of  $0.02 \text{ lb/ft}^2$  to a multilayer concentration of  $2 \text{ lb/ft}^2$ . In the DEM simulations, homogeneous proppant particles having diameter of  $0.63 \text{ mm}$ , the average of mesh-20 and mesh-40 sizes, were generated at various proppant concentrations and the proppant particles were packed within the fracture space uniformly. The computational domain dimensions in the x-y plane (the plane parallel to fracture face) were  $10 \text{ mm} \times 10 \text{ mm}$ . The fracture then closed in the z-direction (the direction normal to fracture face) at a

constant velocity, which was adequately slow to avoid rapid surge of effective stress between proppant particles and to allow fluid within the pore space to flow away in the lateral (x-y) directions. In this way, the system was in a steady state, where the transient pore pressure change and resultant stress acting on the proppant particles were negligible (Fan et al. 2018). The processes of proppant particle compaction, movement, and rearrangement were simulated using the DEM code. The embedment depth of proppant particles into the fracture walls were determined using the laboratory-measured load-embedment correlation (Darin and Huitt, 1960). Finally, steady-state pore structure of the proppant pack under a specific stress was discretized at a resolution of 0.01 mm per LB length unit in all directions and then imported into the LB simulator as interior boundary conditions of flow modeling to determine proppant pack permeability in the lateral (x-y) direction, as illustrated in Figure 3.3a.

After the comparison between the workflow-derived and laboratory-measured fracture conductivity versus proppant concentration curves, the first proppant compaction study was conducted to carry out comprehensive sensitivity analyses to unravel the role of proppant particle size and effective stress on the optimal partial-monolayer proppant concentration. Specifically, conductivity curves were obtained using the integrated workflow for three proppant sizes (0.63 mm, 0.45 mm, and 0.32 mm) under four effective stresses (1,000, 2,000, 4,000, and 6,000 psi). The three proppant assemblies had homogeneous sizes and the particle diameters were equal to the mean particle sizes of 20/40-mesh-size proppant, 30/50-mesh-size proppant, and 40/70-mesh-size proppant, respectively. Proppant concentration ranged from a partial-monolayer concentration of 0.004 lb/ft<sup>2</sup> to a multilayer concentration of 1 lb/ft<sup>2</sup>. The fracture conductivity versus

proppant concentration curves obtained from the hybrid, experiment/simulation-integrated workflow were plotted together to illustrate the influence of proppant particle size and effective stress on the optimal partial-monolayer proppant concentration.

The second proppant compaction study was conducted to investigate the role of proppant size heterogeneity (variation in particle diameter) and effective stress on non-Darcy flow. The initial dimensions of the proppant pack were 20 mm × 20 mm × 20mm. Three proppant packs having the same average particle diameter but different size distributions were generated. Specifically, the first proppant pack was generated following the 20/40 mesh size with an assumption of uniform distribution of particle diameter between mesh 20 and mesh 40. The coefficient of variation (COV) of particle diameter, defined as the ratio of standard deviation of particle diameter to mean particle diameter, was accordingly calculated as 19%. This proppant pack was referred to as the reference proppant assembly. The other two proppant packs had the same mean particle diameter (0.63 mm) but different diameter COVs, with one being 5% and the other being 25%, which suggests that one was more homogeneous whereas the other was more heterogeneous in terms of proppant size distribution. The proppant packs were compacted in the z direction under increasing closure pressures and non-Darcy flows were simulated using the LB simulator (Dye et al. 2013) at a spatial resolution of 0.0125 mm per LB length unit.

### **3.2.3 Embedment experiment and load–embedment correlation**

A series of ballpoint penetrometer experiments was conducted on tight sandstone samples, aiming to obtain the load-embedment correlation for estimating fracture closure

distance due to proppant embedment. The sandstone has a Brinell hardness number (BHN) of 35 kg/mm<sup>2</sup>. Specifically, the penetrometer experiments were conducted in the laboratory using a nanoindenter equipped with a tungsten carbide ball. Huitt and McGlothlin (1958) developed a semi-empirical correlation to relate mechanical loading exerted on a spherical particle to its embedment depth on rock surface. The model is based on the assumption that embedment depth is less than the particle radius (Lacy et al. 1998). This assumption was confirmed in our ballpoint penetrometer experiments, because of the high hardness of the tight sandstone resulting from vertical overburden compaction and intergranular cements. The correlation model is written as:

$$\frac{d}{D} = B^{1/2} \left( \frac{L}{D^2} \right)^{m/2} \quad (3.1)$$

where  $d$  is diameter of embedment impression on fracture wall (m),  $D$  is diameter of proppant particle (m),  $L$  is load on the proppant particle (N), and  $B$  and  $m$  are fitting coefficients, which are characteristics of the rock and obtained by fitting experimental data. Based on Equation 3.1 and geometry analysis, the fracture width that takes into account proppant embedment is calculated as (Huitt and McGlothlin, 1958; Darin and Huitt, 1960):

$$W_f = D \left[ 1 - B \left( \frac{P_e}{nD^2} \right)^m \right]^{1/2} \quad (3.2)$$

where  $W_f$  is the fracture width (m),  $P_e$  is load carried by the proppant particles per unit area (Pa), and  $n$  is the number of proppant particles per unit area (m<sup>-2</sup>). In this study, effective stress on the particles in direct contact with the fracture walls was determined using DEM simulation and then imported into Equation 3.2 to calculate the fracture

closure distance resulting from proppant embedment. It should be noted that although Huitt and McGlothlin's (1958) model is preferable in this study due to its simplicity and clear physical picture, multilayer-embedment correlations can also be used in the hybrid, experiment/simulation-integrated framework for weakly consolidated rocks where embedment depth is more than the particle radius, such as the ones developed by Guo et al. (2008) and Li et al. (2015).

### 3.2.4 Non-Darcy flow

Darcy's law, which dictates a linear correlation between Darcy flow velocity and pressure gradient, is widely used to describe fluid flow in porous media at low velocities (Reynolds [ $Re$ ] number  $<1$ ). However, deviations from the Darcy's law are frequently observed at high flow rates, especially in regions around the wellbore and in propped hydraulic fractures (Newman and Yin 2013). Considering the microscopic inertial effect, Forchheimer (1901) added a second-order velocity term to the Darcy's law to predict the pressure drop at higher velocities ( $Re > 1$ ).

$$-\nabla p = \frac{\mu v}{k} + \beta \rho v |v| \quad (3.3)$$

where  $p$  is pressure (Pa),  $\mu$  is dynamic viscosity (Pa s),  $k$  is permeability ( $m^2$ ),  $v$  is Darcy flow velocity (m/s),  $\beta$  is non-Darcy effect coefficient ( $m^{-1}$ ), i.e., the Beta factor, and  $\rho$  is fluid density ( $kg/m^3$ ). The second term of this equation represents the inertial force along with the viscous force in high  $Re$  number regions (Balhoff and Wheeler 2009). The Beta factor is an intrinsic property of the proppant pack which measures the tortuosity of the flow paths in the pore space; the more tortuous the flow paths, the higher magnitude of the Beta factor (Palisch et al. 2007). When the flow velocity is small, the quadratic term



(the second term on the right hand side of Equation 3.3) is negligible compared to the linear term; in this scenario the Forchheimer equation reduces to the Darcy's law.

In order to calculate the non-Darcy effect coefficient or Beta factor, Equation 3.3 is rearranged. The apparent permeability,  $k_{app}$ , is defined in Equation 3.4 (Balhoff and Wheeler 2009; Macini et al. 2008):

$$\frac{1}{k_{app}} = -\frac{\nabla p}{\mu v} = \frac{1}{k} + \beta \frac{\rho |v|}{\mu} \quad (3.4)$$

Unlike the absolute permeability, the apparent permeability is not an intrinsic property of the porous medium because it changes with flow velocity. As can be seen, the non-Darcy effect coefficient  $\beta$  can be obtained based on the linear correlation between  $\nabla p/\mu v$  and  $\rho|v|/\mu$ .

The non-Darcy flow simulation in this paper relied on a three-dimensional (3D), 19-velocity-vector (D3Q19), multiple-relaxation-time (MRT) lattice Boltzmann scheme. A D3Q19 lattice structure is presented in Figure 3.3b. In order to estimate the permeability under different velocities, the pressure gradient was increased, which led to increasing flow velocity. The LB scheme recovers the Navier-Stokes equations to the second-order accuracy and was validated within both the Darcy and non-Darcy regimes (McClure et al. 2014; Dye et al. 2013). The pore-scale velocity field was obtained by simulating a steady-state flow driven by an external force. In all simulations, a fully periodic boundary condition was used. In this study, we used Equation 3.4 to calculate the non-Darcy effect coefficient. Typically, the  $Re$  number is used to characterize the non-linear behavior. In this work, the  $Re$  number is defined as:

$$Re = \frac{\rho D_e |v|}{\mu} \quad (3.5)$$

where  $D_e$  is the equivalent particle diameter, a characteristic length of the proppant pack that takes into account the effect of proppant pack porosity and solid-void interfacial area (Fan et al., 2018):

$$D_e = 6 \times (1 - \phi) \times V / S \quad (3.6)$$

where  $\phi$  is the porosity,  $V$  is the volume of the entire computational domain, and  $S$  is the total surface area of proppant particles. In this research, the permeability is normalized by the square of the equivalent particle diameter,  $D_e^2$ , to obtain the dimensionless permeability (Dye et al., 2013; Fan et al., 2018).

The relative non-Darcy effect coefficient,  $E$ , is defined as the ratio of pressure gradient consumed in overcoming liquid-solid interactions to the total pressure gradient, as shown in Equation 3.7 (Zeng and Grigg, 2006). The higher the value of  $E$ , the stronger the non-Darcy flow effect.

$$E = \frac{\beta \rho v |v|}{-\nabla p} \quad (3.7)$$

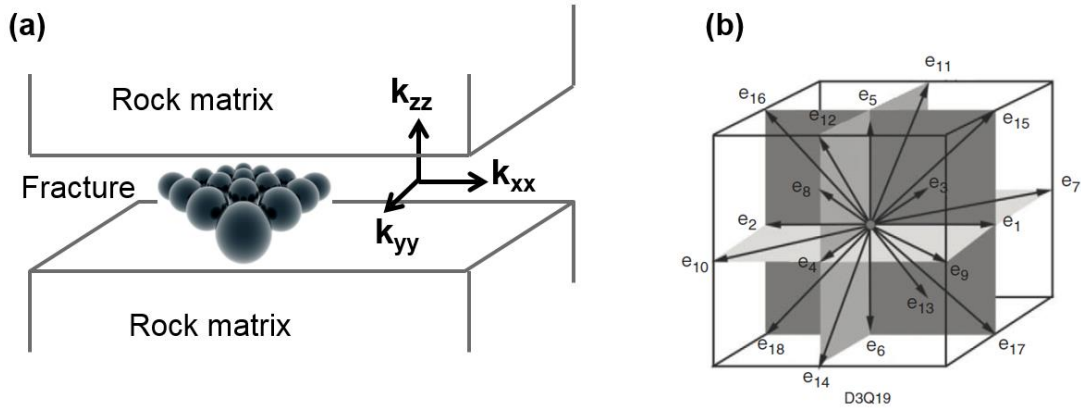


Figure 3.3. a) Proppant particles and permeability tensor in a fracture, and b) D3Q19 lattice structure. Figures were modified from Chen et al. (2015).

### 3.2.5 Basics of PFC3D

In this study, the Particle Flow Code (PFC) was used for DEM simulations. PFC3D is a 3D discontinuum mechanics simulator (Itasca 2008). It describes the movement and interaction of rigid, spherical particles using the DEM scheme, which was first introduced by Cundall (1971) for the analysis of rock mechanics problems and then applied to soils by Cundall and Strack (1979). In PFC3D, the spherical particles are generated independently and interact only at contacts or interfaces. The calculation cycle adopts a time-stepping algorithm, in which the position and velocity of each particle is determined by Newton's second law of motion, and the force-displacement relation is used to update the contact force at each contact. During the simulation, contacts can be created and separated. However, Newton's second law of motion is not applied to boundary walls, since the motion of walls is specified by the user. The force-displacement relation is applied at each contact point, which is defined by a unit normal vector,  $n_i$ . When particles come into contact, the contact force is generated, which is determined by the relative displacement and specified stiffness between the two particles. The contact force can be decomposed into normal and shear components with respect to the contact plane, as illustrated in Equation 3.8. The normal contact force is computed by Equation 3.9. The magnitude of the shear contact force is initialized as zero and then incremented at each time step, as determined by Equation 3.10 (Itasca, 2008).

$$F_i = F_i^n + F_i^s \quad (3.8)$$

$$F_i^n = K^n U^n n_i \quad (3.9)$$

$$\Delta F_i^s = -k^s \Delta U_i^s \quad (3.10)$$

In these equations,  $F_i^n$  and  $F_i^S$  denote the normal and shear components of the contact force, respectively;  $K^n$  is the normal stiffness at the contact, which relates the total normal displacement to the normal force;  $k^S$  is the shear stiffness, which relates the incremental shear displacement to the shear force;  $U^n$  is the contact displacement in the normal direction and  $U_i^S$  is the shear component of the contact displacement.

### **3.2.6 Discretization of 3D proppant pore structure**

The 3D proppant pore structure from the DEM simulation was discretized, extracted, and imported into the LB model as interior boundary conditions of fluid flow modeling to simulate pore-scale, single-phase Darcy and non-Darcy flows in the compressed pore space. Specifically, the 3D pore geometry was discretized with a 3D mesh grid having a resolution of 0.01 mm per LB length unit in the x, y, and z directions. When the single proppant particle diameter is close to 1 mm, which is 100 times larger than the LB length unit, the proppant pack geometry is well resolved (Chen et al. 2009b; Fan et al. 2018).

### **3.2.7 Lattice Boltzmann method for single-phase flow simulation**

The LB method is a numerical method for solving the Navier-Stokes equations and is based on microscopic physical models and mesoscale kinetic equations (Chen and Doolen 1998; Succi 2001). In comparison with conventional fluid dynamic models, the LB method has many advantages. For example, it is explicit in evolution equation, simple to implement, natural to parallelize (Succi 1991; Chen et al. 1992), and easy to incorporate new physics such as interactions at fluid-solid interface (Grunau et al. 1993; Han and Cundall 2011, 2013).

The LB simulator used in this study has been validated by direct comparisons with analytical solutions and laboratory measurements (Chen et al. 2008, 2009a, 2009b). It was then optimized with high-performance graphics processing unit (GPU) parallel computing, which enhanced the computational speed by a factor of 1,000 and led to an in-house LB code, GPU-enhanced lattice Boltzmann simulator (GELBS) (Chen et al. 2016). In this work, the D3Q19 lattice structure, as shown in Figure 3.3b, was used because of its advantage in achieving a good balance between computational stability and efficiency (Chen et al. 2013).

Particle distribution in the Bhatnagar-Gross-Krook (BGK)-based, single-relaxation-time LB equation is given by

$$f_i(\mathbf{x}+\mathbf{e}_i \Delta t, t+\Delta t) = f_i(\mathbf{x}, t) - \frac{f_i(\mathbf{x}, t) - f_i^{eq}(\rho, \mathbf{u})}{\tau}, \quad (i = 0, 1, 2 \dots 18) \quad (3.11)$$

where  $f_i(\mathbf{x}, t)$  is the particle-distribution function specifying the probability that fluid particles at lattice location  $\mathbf{x}$  and time  $t$  travel along the  $i^{th}$  direction;  $\mathbf{e}_i$  is the lattice velocity vector corresponding to direction  $i$ , defined as:

$$\begin{aligned} \mathbf{e}_0 &= (0, 0, 0), \mathbf{e}_1 = (1, 0, 0)c, \mathbf{e}_2 = (-1, 0, 0)c \\ \mathbf{e}_3 &= (0, 1, 0)c, \mathbf{e}_4 = (0, -1, 0)c, \mathbf{e}_5 = (0, 0, 1)c, \mathbf{e}_6 = (0, 0, -1)c \\ \mathbf{e}_7 &= (1, 1, 0)c, \mathbf{e}_8 = (-1, 1, 0)c, \mathbf{e}_9 = (1, -1, 0)c, \mathbf{e}_{10} = (-1, -1, 0)c \\ \mathbf{e}_{11} &= (0, 1, 1)c, \mathbf{e}_{12} = (0, -1, 1)c, \mathbf{e}_{13} = (0, 1, -1)c, \mathbf{e}_{14} = (0, -1, -1)c \\ \mathbf{e}_{15} &= (1, 0, 1)c, \mathbf{e}_{16} = (-1, 0, 1)c, \mathbf{e}_{17} = (1, 0, -1)c, \mathbf{e}_{18} = (-1, 0, -1)c \end{aligned}$$

where  $c = \Delta x / \Delta t$ , in which  $\Delta x$  is the lattice spacing and  $\Delta t$  is the time step;  $\tau$  is the dimensionless relaxation time related to kinematic viscosity by  $\nu = (2\tau - 1)\Delta x^2 / 6\Delta t$ ;  $f_i^{eq}(\rho, \mathbf{u})$  is the equilibrium distribution function selected to recover the macroscopic Navier-Stokes equations and given by

$$f_i^{eq}(\rho, \mathbf{u}) = \omega_i \rho \left[ 1 + \frac{3\mathbf{e}_i \cdot \mathbf{u}}{c^2} + \frac{9(\mathbf{e}_i \cdot \mathbf{u})^2}{2c^4} - \frac{3\mathbf{u}^2}{2c^2} \right] \quad (3.12)$$

where  $\omega_i$  is the weight coefficient calculated as:

$$\omega_i = \begin{cases} 1/3 & i = 0 \\ 1/18 & i = 1 \dots 6 \\ 1/36 & i = 7 \dots 18 \end{cases}$$

The macroscopic fluid density and velocity are calculated with the following two equations:

$$\rho = \sum_{i=0}^{18} f_i \quad (3.13)$$

and

$$\mathbf{u} = \frac{\sum_{i=0}^{18} f_i \mathbf{e}_i}{\rho} \quad (3.14)$$

Fluid pressure is calculated using  $p = c_s^2 \rho$ , where  $c_s$  is the speed of sound. In the LB D3Q19 model,  $c_s^2 = c^2/3$ .

In practice, two-relaxation-time and multi-relaxation-time LB schemes have been developed to mitigate numerical instability in simulating high-Re-number flows and avoid nonlinear dependency of numerical error on fluid viscosity (Li and Huang 2008; Ginzburg 2008). In this study, we replaced the BGK-based collision operator with a two-relaxation-time collision operator and then selected the optimal combination of the symmetric and asymmetric eigenfunctions (Ginzburg et al. 2010) in order to reduce numerical errors resulting from the bounce-back boundary condition.

For fluid flow simulation in the Darcy regime, we imposed a periodic boundary condition with a constant pressure difference,  $\Delta P$ , in the longitudinal direction and no-

slip boundary conditions on the four lateral sides and interior solid surfaces (Inamuro et al. 1999; Chen et al. 2009a). In Figure 3.3a, the main, longitudinal flow directions are the  $x$  and  $y$  directions. Because the particle packing is isotropic, permeabilities measured in these two directions should be the same. The  $Re$  number was always much smaller than one to ensure that the macroscopic flow was well within the Darcy regime. A small pressure difference,  $\Delta P$ , generated an adequately small Mach number and density variation, which are necessary for accurate simulation of incompressible flows using the LB method. More details about the LB simulator and associated GPU optimization can be found in our previous papers (Chen et al., 2009a, 2016).

At the continuum scale, the Darcy velocity,  $\mathbf{v}$ , is calculated by averaging the pore-scale flow velocity,  $\mathbf{u}$ , of each lattice node in the pore space throughout the entire computational domain. One can calculate the permeability tensor using the Darcy's law:

$$\mathbf{v} = -\frac{1}{\mu} \mathbf{k} \cdot \nabla p \quad (3.15)$$

where  $\mathbf{v} = [v_x, v_y, v_z]^T$  is the Darcy velocity,  $\mathbf{k} = k_{ij} (i, j = x, y, z)$  is the permeability tensor, with  $i$  being the flow direction and  $j$  being the pressure gradient direction,  $\nabla p$  is the pressure gradient, and  $\mu$  is the dynamic viscosity of the fluid. The principal components of the permeability tensor are noted as  $k_{xx}$ ,  $k_{yy}$ , and  $k_{zz}$ , as presented in Figure 3.3a. Since the principal directions of the permeability tensor in this study are the same as the principal coordinate directions, the off-diagonal elements in the permeability tensor are zero, written as  $k_{ij} = 0 (i \neq j)$ . More details about LB simulations of Darcy and non-Darcy flows in porous media can be found in our recent publications (Mcclure et al. 2014; Dye et al. 2013; Chen et al. 2009a; Fan et al. 2018).

### 3.3 Results and Discussion

The penetrometer experimental data from three nanoindentation tests were plotted in the form of  $d/D$  versus  $L/D^2$  for correlation analysis, as illustrated in Figure 3.4. The tests were conducted on three samples from the same tight sandstone formation. All the three tests demonstrated similar rock properties and showed strong power-law correlations between  $d/D$  and  $L/D^2$ . There were slight deviations between experimental data and model correlations in the low-stress range. This was because under low mechanical loading the tungsten carbide ball in the nanoindenter was not fully in contact with the rock surface because of rock surface roughness, leading to minor deviation in this stress range. However, the minor deviation had negligible influences because under this relatively low stress ( $\sim 150$  psi) the embedment depth was minimal. The values of  $m$  and  $B$  from Test 1 were determined as 0.555 and  $2.92 \times 10^{-5}$ , respectively. These values were used in Equation 3.2 to determine the embedment distance. It should be noted that the maximum mechanical loading in the penetrometer laboratory tests was around 1,200 psi. We assumed that the embedment depth is still less than the particle radius at higher stresses because of the high hardness of the rock, and the empirical load-embedment correlation is still valid at higher stresses. In practice, multilayer-embedment correlations can be used in the hybrid, experiment/simulation-integrated framework for weakly consolidated rocks where the embedment depth is more than the particle radius, such as the ones developed by Guo et al. (2008) and Li et al. (2015).



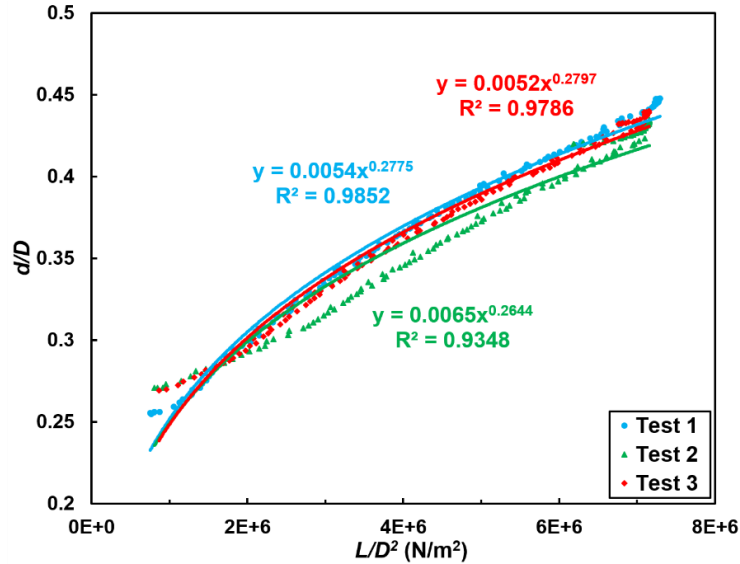


Figure 3.4. Correlation between  $d/D$  and  $L/D^2$  based on the laboratory penetrometer experiments. The tests were conducted on three samples from the same tight sandstone formation.

Figure 3.5 illustrates two-dimensional (2D) cross sections of PFC-generated proppant assemblies having a full monolayer structure and a partial-monolayer structure. The 2D cross sections were cut at the fracture center along the x-y plane as shown in Figure 3.3a. Proppant concentrations are  $0.22 \text{ lb/ft}^2$  and  $0.10 \text{ lb/ft}^2$  in Figures 3.5a and 3.5b, respectively. The proppant particles are homogeneous and the diameter is equal to  $0.63 \text{ mm}$ , the average of mesh-20 and mesh-40 sizes. By definition, a full-monolayer proppant pack is obtained when the fracture width is equal to one particle diameter and there is no void space in which additional proppant particles can be placed (Brannon et al. 2004). In the LB simulation of Darcy flow, a pressure gradient was imposed in the x and y directions to drive single phase fluid flow through the pore space of the proppant assembly.

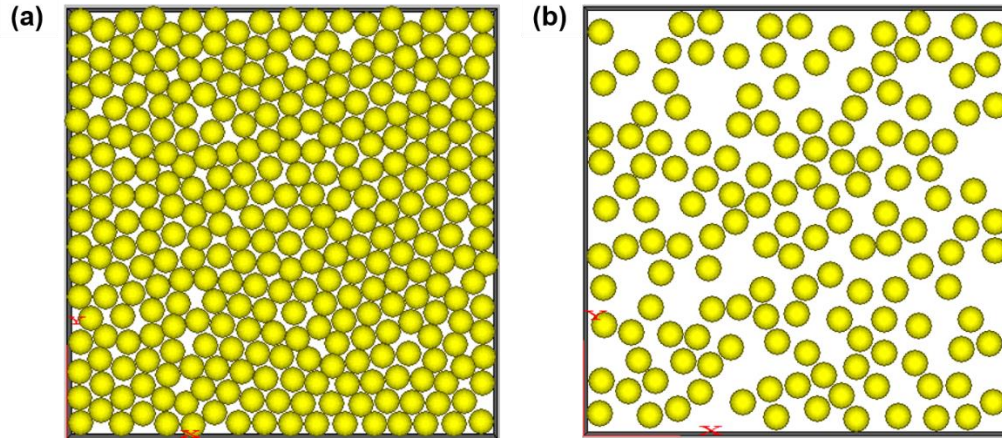


Figure 3.5. 2D cross sections of PFC-generated proppant assemblies having a) full-monolayer structure, and b) partial-monolayer structure. The dimensions of the cross section are 10 mm × 10 mm. Proppant concentrations are 0.22 lb/ft<sup>2</sup> and 0.10 lb/ft<sup>2</sup>, respectively.

The load-embedment correlation derived from the nanoindentation experiments was incorporated into the pore-scale DEM/LB-integrated numerical model, leading to the hybrid, experiment/simulation-integrated workflow that accounts for fracture conductivity reduction due to proppant embedment and compaction. Figure 3.6 illustrates that the hybrid, experiment/simulation-integrated approach is able to accurately capture the non-monotonic shape of the fracture conductivity versus proppant concentration curve. Proppant particles had a homogenous size of 0.63 mm. Effective stress was 1,000 psi. Zones 1, 2, and 3 represent the three phases in which fracture conductivity increases (Stages 1 & 2), decreases (Stage 3), and then increases again (Stage 4), as illustrated in Table 3.1. Fracture conductivity reached the local maximum (~10,000 md-ft) when proppant concentration was 0.03 lb/ft<sup>2</sup>, which is the optimal partial-monolayer proppant concentration, and reached the trough (~300 md-ft) at the full-monolayer concentration of 0.2 lb/ft<sup>2</sup>. Specifically, the optimal partial-monolayer proppant concentration (0.03 lb/ft<sup>2</sup>), obtained from this experiment/simulation-integrated framework, is close to those values

reported in the literature based on experimental methods, such as 0.07 lb/ft<sup>2</sup> (Gaurav et al., 2010), between 0.03 lb/ft<sup>2</sup> and 0.05 lb/ft<sup>2</sup> (Howard and Fast, 1970), 0.02 lb/ft<sup>2</sup> (Bestaoui-Spurr and Hudson, 2017), and less than 0.1 lb/ft<sup>2</sup> (Parker et al., 2012).

To the best of our knowledge, it is the first time that a fracture conductivity versus proppant concentration curve (Figures 3.6) is generated using a hybrid, experiment/simulation integrated approach. Specifically, the hybrid, experiment/simulation-integrated framework accounts for the important multiphysics processes over the full range of the conductivity curve from partial-monolayer proppant concentrations to multilayer proppant concentrations and thus is able to capture the local maximum of the conductivity curve (i.e., the optimal partial-monolayer fracture conductivity). The optimal partial-monolayer proppant concentration has practical engineering implications and is economically tempting, because one can achieve considerable fracture conductivity by designing a proppant pack at the optimal partial-monolayer proppant concentration, which has much lower material costs compared to the conventional multilayer proppant structures.

Any model that fails to account for proppant embedment and the resultant fracture width reduction will be unable to capture the non-monotonic shape of the conductivity curve as well as the local maximum of the curve. This is because the permeability of a porous medium is controlled by the characteristic lengths of the pore spaces (Chen et al. 2009a). In the partial-monolayer range (i.e., Zones 1 and 2 as shown in Figure 3.6), the fracture permeability,  $k$ , is controlled by both the fracture width,  $h$ , and fracture porosity,  $\phi$ . When the proppant areal concentration is very low, although continuously placing proppant particles into the partial-monolayer proppant structure reduces  $\phi$ , which has a

negative impact on  $k$ , the increased amount of proppant in the fracture space mitigates proppant embedment significantly and thus leads to fast-growing  $h$ , which has a positive impact on  $k$ . When the permeability gain resulting from the increase of  $h$  surpasses the permeability loss resulting from the reduction of  $\phi$ , the net effect is that the fracture permeability increases, which is exactly Stage 1 as illustrated in Table 3.1. If a model simply ignores the effect of proppant embedment on fracture width reduction, it is unable to account for the competing relationship between  $h$  and  $\phi$  and consequently will fail to accurately delineate the evolution of fracture conductivity in Stage 1. As a result, the model will demonstrate a faulty phenomenon in the range of ultralow proppant concentrations: the fracture conductivity monotonically increases and approaches the maximum possible value (i.e., the conductivity of an empty fracture) when the proppant concentration continuously decreases and approaches zero. This faulty simulation result within the partial-monolayer range is due to the "no-embedment" assumption, which assumes the fracture width stays constant (equal to proppant particle diameter) no matter how low the proppant concentration is.

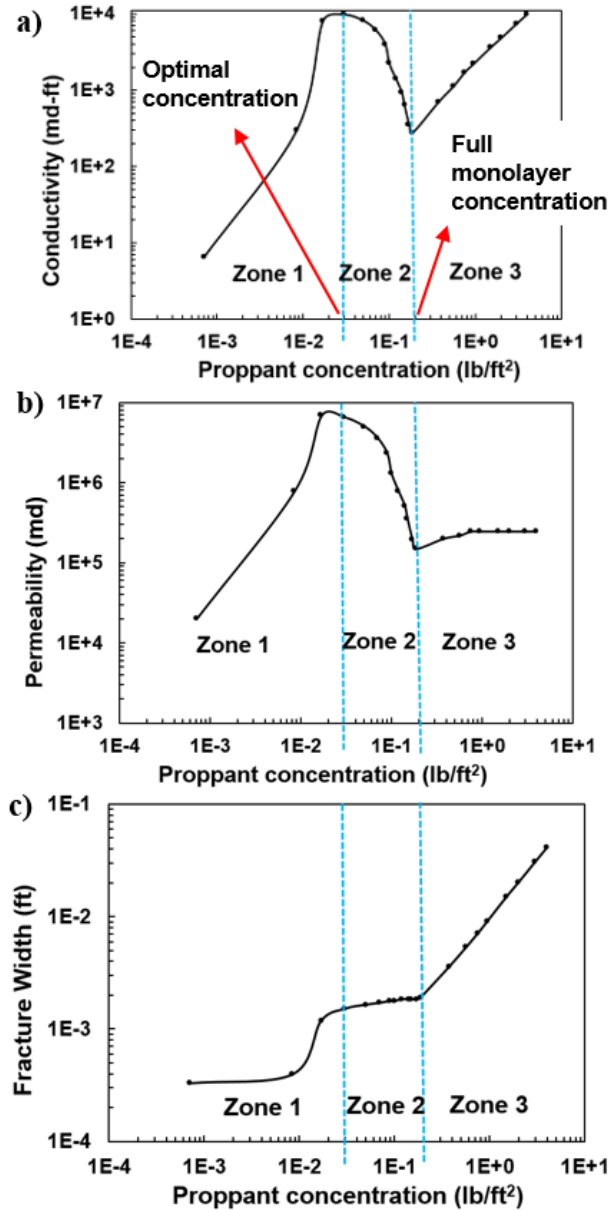


Figure 3.6. Development of a) fracture conductivity, b) permeability, and c) width as a function of proppant concentration. These curves were obtained from the hybrid, experiment/simulation integrated workflow. Proppant particle size is homogeneous and equal to 0.63 mm. Effective compressive stress imposed on the proppant is 1,000 psi.

Figure 3.7 compares the workflow-derived and laboratory-measured fracture conductivity versus proppant concentration curves. Both the workflow-derived and laboratory-measured curves were measured under effective stress of 1,000 psi. Specifically, “Lab data - heterogeneous” represents a conductivity curve measured in a laboratory

experiment (Brannon et al. 2004), where a 20/40-mesh-size heterogeneous proppant was used in a sandstone fracture, which suggests that the proppant size ranges from mesh 40 (0.42 mm) to mesh 20 (0.84 mm). “Integrated workflow - homogeneous” represents a conductivity curve derived from the hybrid, experiment/simulation-integrated workflow, where the proppant diameter was homogeneous and equal to 0.63 mm. “Integrated workflow - heterogeneous” represents a conductivity curve derived from the hybrid, experiment/simulation-integrated workflow, where the proppant diameter was heterogeneous and had a uniform distribution between mesh 40 (0.42 mm) and mesh 20 (0.84 mm), leading to a mean diameter of 0.63 mm. All the three curves illustrate the non-monotonic shape and the comparison shows an overall good agreement.

The heterogeneous-particle-size curves, from both the integrated workflow and laboratory experiment, show a higher optimal partial-monolayer proppant concentration compared to the homogeneous-particle-size curve obtained from the integrated workflow. This is because sandstone is sensitive to particle size heterogeneity, especially under low effective stress such as 1,000 psi used here. In the laboratory testing, under effective stress of 1,000 psi, the largest proppant particles were primarily responsible for supporting the fracture (Volk et al. 1981). Smaller particles were not fully used in supporting the fracture and thus more particles were required to obtain the optimal partial-monolayer fracture conductivity (i.e., the local maximum on the conductivity curve).

The optimal partial-monolayer fracture conductivity of the heterogeneous-particle-size curves, from both the integrated workflow and laboratory experiment, was slightly higher than that of the homogeneous-particle-size curve. This was because when

proppant concentration reaches the optimal partial-monolayer value, the fracture width is controlled by the largest particle sizes. For the homogeneous-particle-size curve, proppant particles had a homogeneous size of 0.63 mm. Conversely, for both the heterogeneous-particle-size curves, the largest particle size was 0.84 mm, leading to larger fracture width and consequently higher optimal partial-monolayer fracture conductivity.

In addition, when the proppant concentration was higher than 0.1 lb/ft<sup>2</sup>, the laboratory-measured heterogeneous-particle-size curve was slightly lower than the workflow-derived heterogeneous-particle-size curve. This was because in the integrated workflow the heterogeneous particle diameter strictly followed a uniform distribution from mesh 40 (0.42 mm) to mesh 20 (0.84 mm). However, in the laboratory experiment (Brannon et al. 2004) the heterogeneous particle diameter did not necessarily follow a uniform distribution; the only information provided is that a 20/40 proppant was used in the experiment, which means that the minimum proppant diameter was mesh 40 (0.42 mm) and the maximum proppant diameter was mesh 20 (0.84 mm). The uncertainty in the heterogeneous particle size distribution in the laboratory experiment was the primary source that caused the deviation between the workflow-derived and laboratory-measured conductivity curves. In fact, in practical engineering applications, it has been observed that a heterogeneous proppant sample generally has higher number fractions of smaller particles (Volk et al. 1981), i.e., the particle size distribution is heavily skewed toward the lower-end particle size. Therefore, based on this fact, it is reasonable to hypothesize that in Brannon's experiment (Brannon et al. 2004), the heterogeneous 20/40 proppant had higher number fractions of smaller particles, which caused the laboratory-measured

conductivity curve lower than that obtained from the integrated workflow where the heterogeneous proppant size followed a uniform distribution. In addition, the deviation of the heterogeneous proppant size followed a uniform distribution. In addition, the deviation of the laboratory heterogeneous proppant size distribution from a uniform distribution also affected its optimal partial-monolayer proppant concentration. Figure 3.7 illustrates that the optimal partial-monolayer proppant concentration of the laboratory-measured conductivity curve is higher than that of the workflow-derived conductivity curve. This is because the laboratory heterogeneous proppant had higher number fractions of smaller particles and thus more particles were required to obtain the local maximum on the conductivity curve.

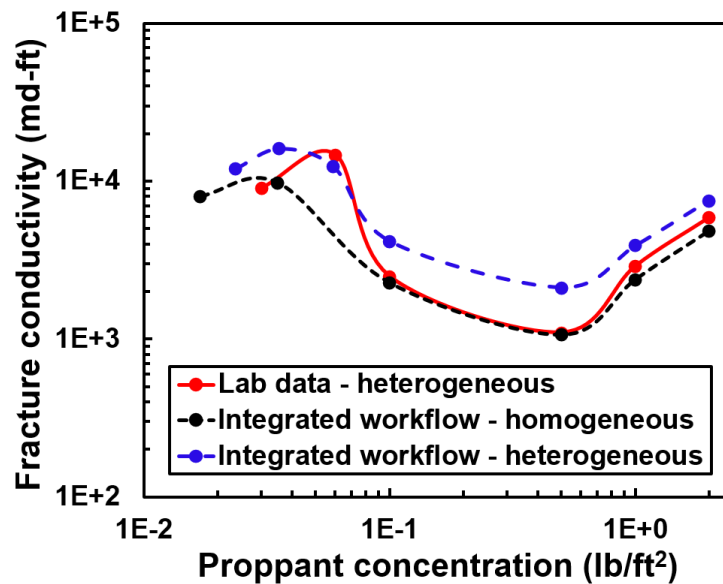


Figure 3.7. Comparison between the workflow-derived and laboratory-measured fracture conductivity versus proppant concentration curves. “Lab data - heterogeneous” represents a conductivity curve measured in a laboratory experiment (Brannon et al. 2004), where a 20/40-mesh-size heterogeneous proppant was used. “Integrated workflow - homogeneous” represents a conductivity curve derived from the hybrid, experiment/simulation-integrated workflow, where the proppant diameter was homogeneous and equal to 0.63 mm. “Integrated workflow - heterogeneous” represents a conductivity curve derived from the integrated workflow, where the proppant diameter was heterogeneous having a uniform distribution between mesh 40 (0.42 mm) and mesh 20 (0.84 mm).



Figures 3.6 and 3.7 demonstrate that the hybrid, experiment/simulation-integrated framework is able to account for the fundamental multiphysics processes that regulate the evolutions of fracture permeability and fracture width resulting from proppant embedment, rearrangement, and compaction. The comparison with the laboratory-measured curve shows an overall good agreement. The experiment/simulation-integrated approach achieves a balance between computational accuracy and efficiency and will facilitate comprehensive sensitivity analysis that aims to optimize proppant placement in hydraulic fractures. For example, one of our recent works (Gu et al. 2017) incorporated the experiment/simulation-integrated approach into a workflow for proppant pumping optimization. In this work, a large number of fracture conductivity versus proppant concentration curves were generated in a time-efficient manner using the integrated workflow and then imported into a reservoir simulator to determine the optimal curve that led to the highest return on fracturing investment (ROFI).

In order to study the role of proppant size and effective stress on fracture conductivity and the optimal partial-monolayer proppant concentration, the fracture conductivity versus proppant concentration curves were derived using the integrated workflow for three proppant sizes (0.63 mm, 0.45 mm, and 0.32 mm) under four effective stresses (1,000, 2,000, 4,000, and 6,000 psi), as demonstrated in Figure 3.8. The three proppant assemblies had homogeneous particle diameters of 0.63 mm, 0.45 mm, and 0.32 mm, respectively. For the same proppant particle size the optimal partial-monolayer fracture conductivity decreased with increasing effective stress, which was due to the decreased fracture permeability and width under higher stress. In the meanwhile, the optimal partial-monolayer proppant concentration increased with increasing effective stress,

because more proppant particles were required to keep the fracture open under higher stress. Therefore, it is expected that the optimal partial-monolayer proppant concentration will converge toward the full-monolayer proppant concentration when the effective stress is sufficiently high, because the embedment depth is close to the particle radius. In this scenario, the local maximum in the fracture conductivity versus proppant concentration curve will vanish and a multilayer proppant structure is desired over a partial-monolayer proppant structure. Under the same effective stress, the proppant pack having 0.63 mm particle diameter had the highest optimal partial-monolayer fracture conductivity whereas the proppant pack having 0.32 mm particle diameter had the lowest optimal partial-monolayer fracture conductivity. This resulted from the decreased fracture permeability and width in the proppant packs having smaller particle sizes.

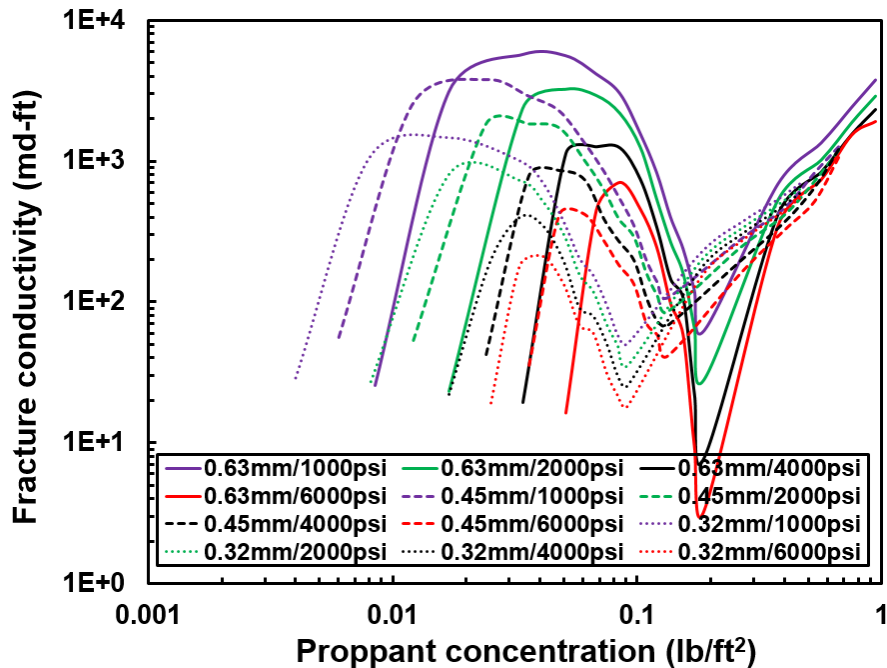


Figure 3.8. Role of proppant particle size and effective stress on the fracture conductivity versus proppant concentration curve. These curves were obtained from the hybrid, experiment/simulation integrated workflow. Three proppant sizes (0.63 mm, 0.45 mm, and 0.32 mm) and four effective stresses (1,000, 2,000, 4,000, and 6,000 psi) are considered, leading to twelve scenarios.

Figure 3.9 illustrates the optimal partial-monolayer proppant concentration as a function of effective stress for the three proppant assemblies having different particle diameters, based on the result from Figure 3.8. As discussed previously, higher effective stress led to a higher optimal partial-monolayer proppant concentration. Under the same effective stress, larger proppant had a higher optimal partial-monolayer proppant concentration because of its higher single-particle mass. The ratio of the optimal partial-monolayer proppant concentration to the full-monolayer proppant concentration (i.e., the ratio of proppant particle numbers between these two proppant concentrations) was calculated. It was interesting to find that the ratio was the same for all of the three proppant assemblies under the same effective stress. Specifically, the ratio was equal to 18%, 27%, 36%, and 45% under effective stresses of 1,000, 2,000, 4,000, and 6,000 psi, respectively. This, again, confirms that higher effective stress led to a higher optimal partial-monolayer proppant concentration because more particles were required to keep the fracture open.

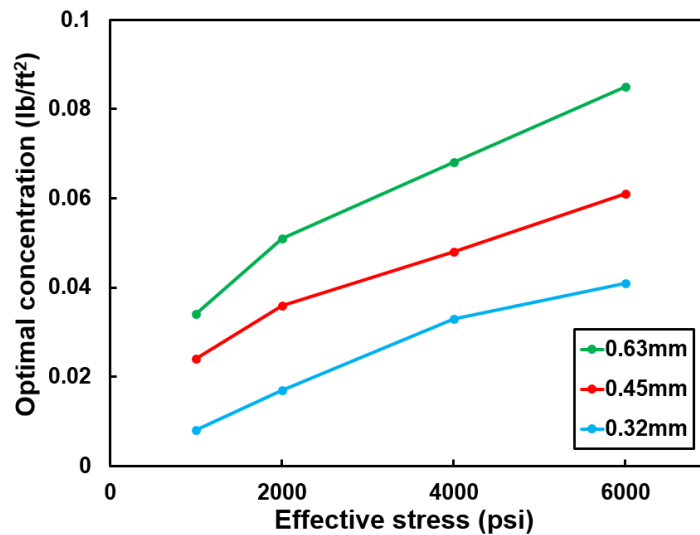


Figure 3.9. Optimal partial-monolayer proppant concentration as a function of effective stress.

It should be noted that the above discussed simulations of fracture conductivity (Figures 3.6-3.9) were conducted under  $Re$  numbers much lower than one. Therefore, the flow was in the Darcy regime and the fracture permeability used to calculate the fracture conductivity was the absolute permeability. As mentioned previously, the second proppant compaction study was conducted to investigate the role of proppant size heterogeneity (variation in particle diameter) and effective stress on non-Darcy flow and the resultant apparent permeability. During hydrocarbon production, hydrocarbon transport can be hindered by the loss of proppant pack conductivity resulting from non-Darcy flows, especially near the wellbore. Within a propped hydraulic fracture, non-Darcy flow effects have the potential to negatively influence productivity and stimulation effectiveness. It is thus important to understand the applicability of the Forchheimer's equation and to obtain accurate descriptions of flow and transport properties. Figure 3.10 illustrates LB-simulated pressure distributions within a 2D cross section cut along the x-y plane at the fracture center for proppant assemblies having diameter COVs of 5% and 25%. The pressure is presented in the LB unit. It can be seen that the proppant pack with diameter COV of 5% had a more homogeneous pore geometry whereas the proppant pack with diameter COV of 25% had a more heterogeneous pore geometry, because a higher diameter COV leads to a wider particle diameter distribution.

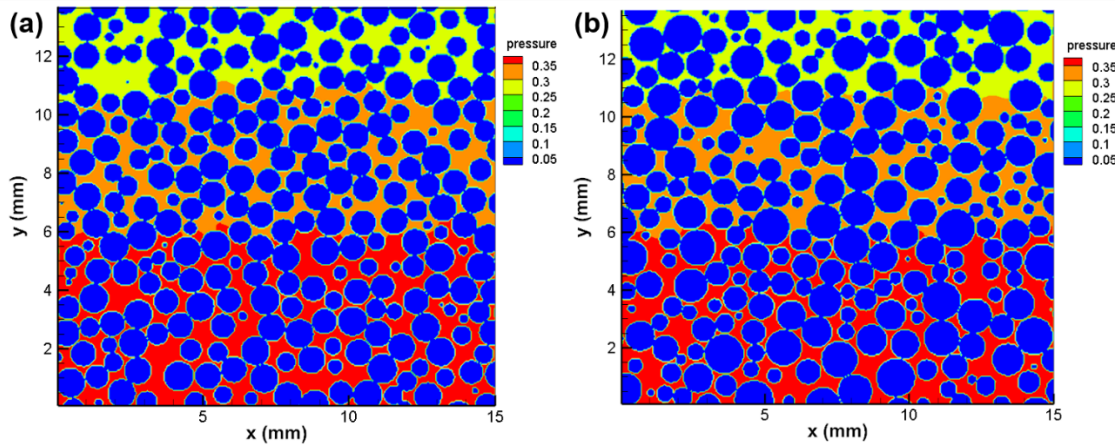


Figure 3.10. LB-simulated pressure distributions within the pore space of proppant assemblies having a) 5% diameter COV, and b) 25% diameter COV.

Figure 3.11 shows the normalized apparent permeability as a function of the  $Re$  number under varying effective stress in three proppant assemblies having diameter COVs of 5%, 19%, and 25%, separately. The normalized apparent permeability decreased with the increase of flow velocity (i.e., increasing  $Re$  number). At low  $Re$  numbers, the inertial force was small and the pressure force was primarily balanced by the viscous force. As the  $Re$  number increased, the inertial effect was no longer negligible and became more and more significant. Therefore, the variation of apparent permeability can be used to evaluate non-Darcy flow effects and the significance of inertial force. For the same proppant assembly, the normalized apparent permeability decreased with increasing effective stress, because the pore space was compressed to a higher extent under the higher effective stress. Under the same effective stress, the proppant pack having a larger diameter COV had a lower normalized apparent permeability. This was because under the same effective stress smaller particles within the proppant assembly having a larger diameter COV moved relatively easily and could be compressed into the

pore space between larger particles, leading to a smaller porosity and consequently a lower proppant pack permeability (Fan et al., 2017a, 2018).

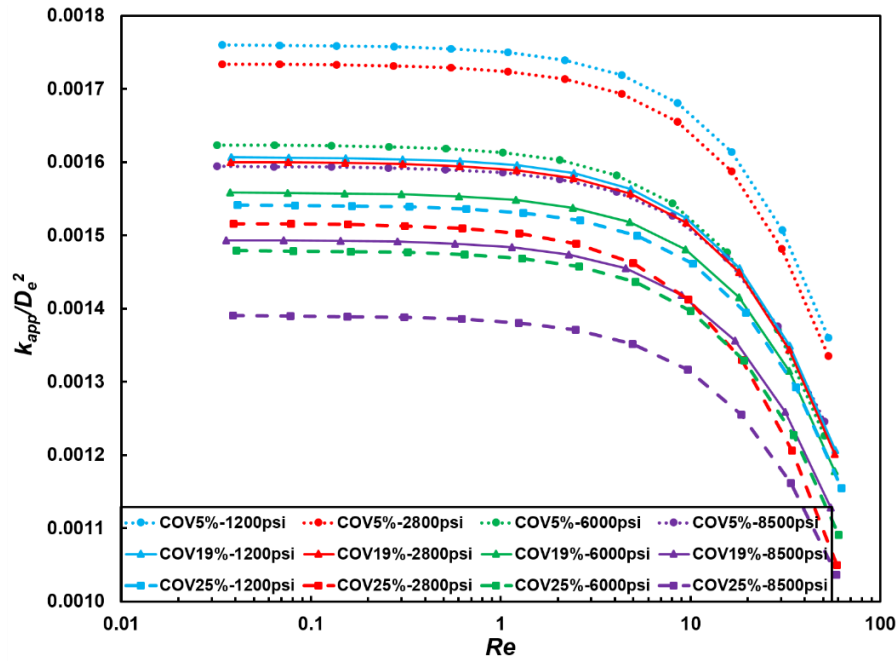


Figure 3.11. Normalized apparent permeability,  $k_{app}/D_e^2$ , as a function of the  $Re$  number under various diameter COVs and effective stresses.

For each proppant pack, 12 LB simulations were conducted at varying pressure gradients and the Darcy flow velocities were measured. Because the momentum boundary layer thickness decreased with increasing  $Re$  number in the LB simulation, a sufficiently high LB resolution, 0.0125 mm per LB length unit, was selected to resolve the momentum boundary layer. In this work, the non-Darcy effect coefficient,  $\beta$ , was calculated based on Equation 3.4. Figure 3.12a illustrates the calculated non-Darcy effect coefficient as a function of effective stress for the three proppant packs. Generally, the non-Darcy effect coefficient increased with increasing effective stress. This was because with the increase of effective stress, proppant particles were compacted and tortuosity of the pore space increased; more heterogeneous pore structures were formed, leading to more vortices and tortuous streamlines. Simulation results also showed that in general

under the same effective stress a proppant pack with a higher diameter COV had a higher non-Darcy effect coefficient due to the development of the more heterogeneous flow field and streamlines. The dimensionless inertial resistance factor, defined as  $\beta\sqrt{k}$ , was also calculated, as shown in Figure 3.12b. Both  $\beta$  and  $k$  are the intrinsic properties of the porous medium, which depend on the geometry of the pore space. Similarly, Figure 3.12b shows that the dimensionless inertial resistance factor increased with increasing effective stress and diameter COV.

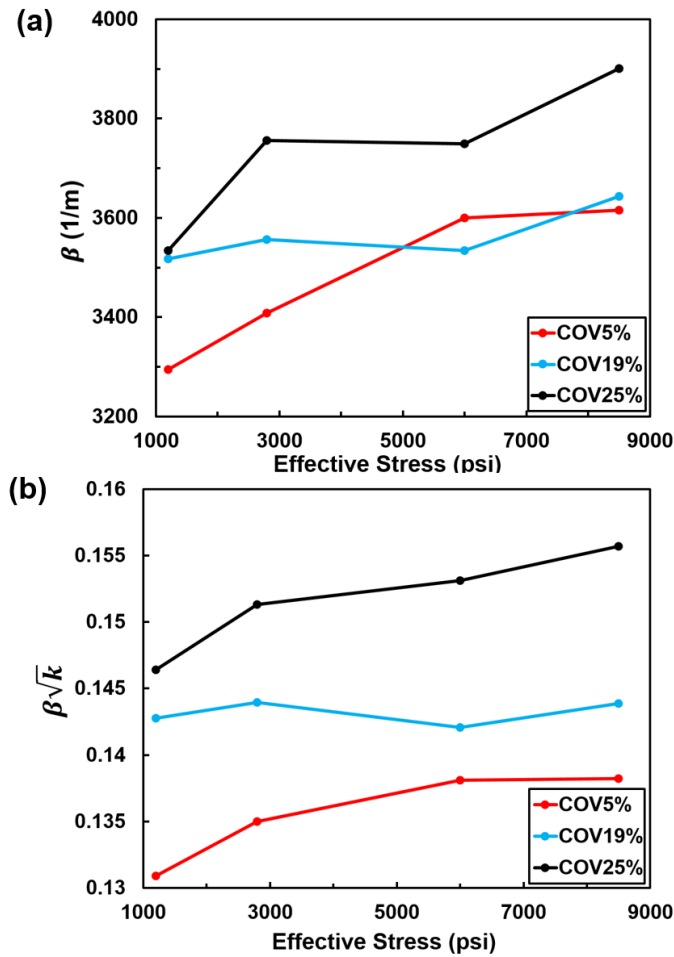


Figure 3.12. a) Non-Darcy effect coefficient, and b) dimensionless inertial resistance factor, as a function of effective stress.

With the increase of effective stress, the flow paths became more heterogeneous, leading to changes in flow directions. The cross sections of the flow paths increased and decreased alternately. Fluid particles accelerated through smaller pore throats and decelerated through larger pore volumes, leading to losses in both pressure and inertial energies. Figure 3.13 shows the relative non-Darcy effect coefficient,  $E$ , defined in Equation 3.7, as a function of the  $Re$  number for the three proppant packs at effective stresses of 1,200 psi and 6,000 psi. Simulation results showed that under a low effective stress the difference in non-Darcy effect was not noticeable between the relatively homogeneous (5% diameter COV) and heterogeneous (25% diameter COV) proppant packs. This implies that the coalescence between neighboring vortices in a proppant pack was relatively easier at lower effective stresses. When the proppant pack was subjected to a higher effective stress, the non-Darcy effect observed in the heterogeneous proppant pack was stronger than that in the homogeneous proppant pack. This again, indicates that the combination of high diameter COV and high effective stress leads to a larger pressure drop and stronger non-Darcy flow effect.



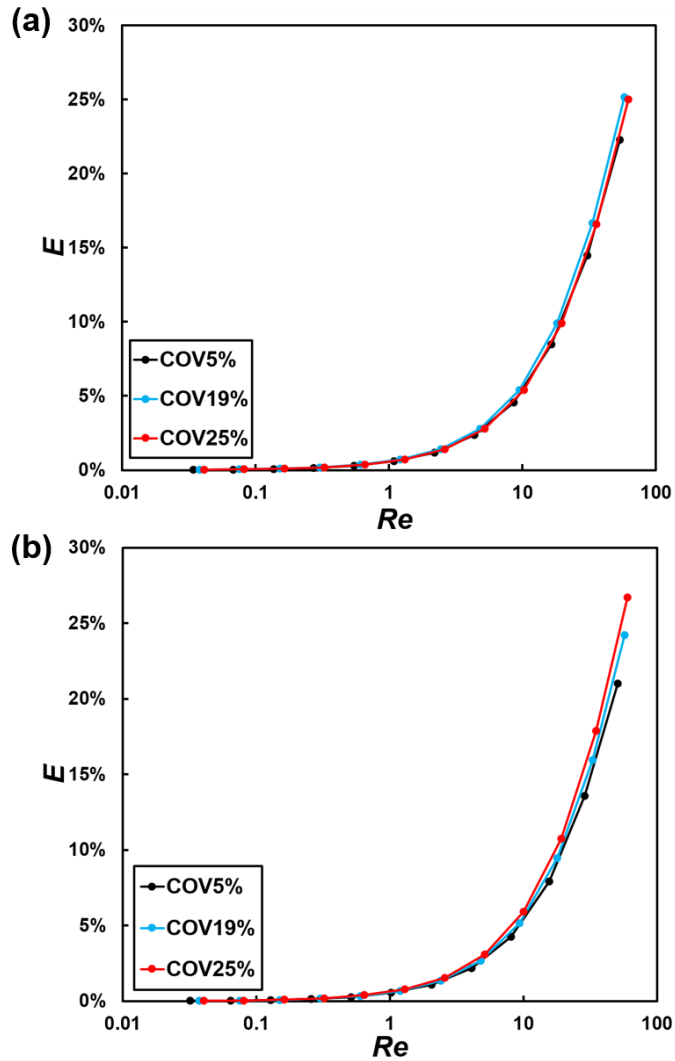


Figure 3.13. Relative non-Darcy effect coefficient,  $E$ , as a function of  $Re$  number under effective stress of a) 1,200 psi and b) 6,000 psi.

### 3.4 Conclusions and Implications

In this study, a hybrid, experiment/simulation-integrated framework was developed to study the evolution of hydraulic fracture conductivity under increasing proppant concentration, ranging from a partial-monolayer concentration to a multilayer concentration. This work has demonstrated that the development of fracture conductivity with increasing proppant concentration goes through four distinct stages as shown in

Table 3.1, which is one of the most important contributions of this study. In Stage 1, proppant concentration is very low. Placing more proppant into the fracture mitigates proppant embedment significantly, leading to fast-growing fracture width and permeability. On the other hand, placing more proppant into an empty fracture reduces fracture porosity. When permeability gain resulting from fracture width increase surpasses permeability loss resulting from porosity reduction, the net effect is that fracture permeability increases and leads to increased fracture conductivity. In Stage 2, permeability loss resulting from porosity reduction surpasses permeability gain resulting from fracture width increase. Fracture permeability will decrease. However, when fracture permeability initially starts to drop, the rate of permeability reduction is lower than the rate of fracture width increase; fracture conductivity is thus still increasing. In Stage 3, fracture conductivity declines because the rate of permeability reduction surpasses the rate of fracture width increase. The proppant concentration at the boundary between Stages 2 and 3, where the fracture conductivity reaches the local maximum, is referred to as the “optimal partial-monolayer proppant concentration”. Stage 3 continues until the proppant assembly develops to a full monolayer. In Stage 4, proppant develops to a multilayer assembly. Fracture porosity and permeability do not change significantly with increasing proppant concentration in this stage.

The influence of effective compressive stress and proppant diameter heterogeneity on non-Darcy flow was also investigated. The comparison between the workflow-derived and laboratory-measured fracture conductivity versus proppant concentration curves shows an overall good agreement. The role of proppant diameter, proppant diameter heterogeneity, and effective stress on the optimal partial-monolayer proppant

concentration was illustrated. The hybrid, experiment/simulation-integrated framework accounts for the fundamental multiphysics processes that regulate the evolutions of fracture permeability and fracture width resulting from proppant embedment, rearrangement, and compaction. To the best of our knowledge, it is the first time that a fracture conductivity versus proppant concentration curve is generated using a hybrid, experiment/simulation integrated approach. This approach achieves a balance between computational accuracy and efficiency and will facilitate comprehensive sensitivity analysis that aims to optimize proppant placement in hydraulic fractures in order to achieve the highest ROFI. Furthermore, the findings show that the combination of high diameter COV and high effective stress leads to a larger pressure drop and consequently stronger non-Darcy flow effect, because of the development of vortices and tortuous streamlines in the pore space.

The findings from this study advance the fundamental understanding of the role of proppant embedment and compaction on the evolution of the fracture conductivity versus proppant concentration curve. This work also provides insight into the factors that regulate the complicated interactions between closure pressure, proppant pack geometry, and non-Darcy flow. The outcome of this research will advance the fundamental understanding of the coupled, multiphysics processes with respect to hydraulic fracturing and will benefit the optimization processes for proppant placement, completion design, and well production.

## Acknowledgements

The authors acknowledge the support of the Junior Faculty Award from Virginia Tech's Institute for Critical Technology and Applied Science. The authors are also thankful to the support from Aramco Research Center – Houston and Virginia Tech's Advanced Research Computing Center.

## Nomenclature

$c_s$  = speed of sound in the LB model, m/s

$d$  = diameter of embedment impression on fracture wall, m

$D$  = diameter of proppant particle, m

$D_e$  = equivalent particle diameter, m

$f_i$  = LB particle-distribution function

$f_i^{eq}$  = equilibrium LB particle-distribution function

$F_i$  = total contact force, N

$F_i^n$  = normal component of the contact force, N

$F_i^S$  = shear component of the contact force, N

$K^n$  = normal stiffness at the contact, N/m

$k^S$  = shear stiffness at the contact, N/m

$\mathbf{k}$  : permeability tensor, m<sup>2</sup>

$k_{xx}$  = principal component of permeability tensor in x-direction, m<sup>2</sup>

$k_{yy}$  = principal component of permeability tensor in y-direction,  $m^2$

$k_{zz}$  = principal component of permeability tensor in z-direction,  $m^2$

$L$  = Load on the proppant particle, N

$n$  = number of proppant particles per unit area

$p$  = fluid pressure, Pa

$P_e$  = load carried by the proppant particles per unit area, Pa

$S$  = total surface area of proppant particles,  $m^2$

$\mathbf{u}$  = pore-scale velocity vector, m/s

$U^n$  = normal component of contact displacement, m

$U^s$  = shear component of the contact displacement, m

$V$  = volume of computational domain,  $m^3$

$\mathbf{v}$  = Darcy flow velocity vector, m/s

$w$  = weight coefficient

$W_f$  = fracture width, m

$\beta$  = non-Darcy effect coefficient ( $m^{-1}$ )

$\phi$  = porosity

$\mu$  = dynamic viscosity, Pa s

$\nu$  = kinematic viscosity,  $m^2/s$

$\rho$  = fluid density,  $kg/m^3$

## References

Aven, N.K., Weaver, J., Loghry, R., and Tang, T. 2013. Long-Term Dynamic Flow Testing of Proppants and Effect of Coatings. Society of Petroleum Engineers. doi:10.2118/165118-MS.

Balhoff, M. T. and Wheeler, M. F. 2009. A Predictive Pore-Scale Model for Non-Darcy Flow in Porous Media. Society of Petroleum Engineers. doi:10.2118/110838-PA.

Barree, R. D., Cox, S. A., Barree, V. L., and Conway, M. W. 2003. Realistic Assessment of Proppant Pack Conductivity for Material Selection. Society of Petroleum Engineers. doi:10.2118/84306-MS.

Bestaoui-Spurr, N. and Hudson, H. 2017. Ultra-Light Weight Proppant and Pumping Design Lead to Greater Conductive Fracture Area in Unconventional Reservoirs. Society of Petroleum Engineers. doi:10.2118/185435-MS.

Bolintineanu, D.S., Rao, R.R., Lechman, J.B., Romero, J.A., Jove-Colon, C.F., and Quintana, E.C., et al. 2017. Simulations of the effects of proppant placement on the conductivity and mechanical stability of hydraulic fractures. *Int J Rock Mech Min.*,100:188-98.

Brannon, H. D., Malone, M. R., Rickards, A. R., Wood, W. D., Edgeman, J. R., and Bryant, J. L. 2004. Maximizing Fracture Conductivity with Proppant Partial Monolayers: Theoretical Curiosity or Highly Productive Reality? Society of Petroleum Engineers. doi:10.2118/90698-MS.

Chen, C., Packman, A. I., and Gaillard, J. F. 2008. Pore-scale Analysis of Permeability Reduction Resulting from Colloid Deposition. *Geophysical Research Letters* 35: L07404. <https://doi.org/10.1029/2007GL033077>.

Chen, C., Lau, B. L. T., Gaillard, J. F. et al. 2009a. Temporal Evolution of Pore Geometry, Fluid Flow, and Solute Transport Resulting From Colloid Deposition. *Water Resources Research* 45: W06416. <https://doi.org/10.1029/2008WR007252>.

Chen, C., Packman, A. I., and Gaillard, J. F. 2009b. Using X-ray Micro-Tomography and Pore-Scale Modeling to Quantify Sediment Mixing and Fluid Flow in a Developing Streambed. *Geophysical Research Letters* 36: L08403 <https://doi.org/10.1029/2009GL037157>.

Chen, C., Hu, D., Westacott, D., and Loveless, D. 2013. Nanometer-Scale Characterization of Microscopic Pores in Shale Kerogen by Image Analysis and Pore-Scale Modeling. *Geochemistry, Geophysics, Geosystems* 14 (10): 4066-4075. <https://doi.org/10.1002/ggge.20254>.

Chen, C., Martysevich, V., O'Connell, P. et al. 2015. Temporal Evolution of the Geometrical and Transport Properties of a Fracture/Proppant System under Increasing Effective Stress. *SPE J.* 20 (3): 527–535. SPE-171572-PA. <https://doi.org/10.2118/171572-PA>.

Chen, C., Wang, Z., Majeti, D. et al. 2016. Optimization of Lattice Boltzmann Simulation with Graphics-Processing-Unit Parallel Computing and the Application in Reservoir Characterization. *SPE J.* 21 (4): 1425–1435. SPE-179733-PA. <https://doi.org/10.2118/179733-PA>.

Chen, H., Chen, S. and Matthaeus, W. H. 1992. Recovery of the Navier–Stokes Equations Using a Lattice-gas Boltzmann Method. *Phys. Rev. A* 45 (8):R5339–R5342. <https://doi.org/10.1103/PhysRevA.45.R5339>.

Chen, S. and Doolen, G. D. 1998. Lattice Boltzmann Method for Fluid Flows. *Annu. Rev. Fluid Mech.* 30: 329–364. <https://doi.org/10.1146/annurev.fluid.30.1.329>.

Cundall P.A. 1971. A Computer Model for Simulating Progressive Large-Scale Movements in Blocky Rock Systems. In *Proc. Int. Symp. Int. Rock Mech.* 2 (8).

Cundall P. A. and Strack, O. D. L. 1979. A Discrete Numerical Model for Granular Assemblies. *Geotechnique* 29 (1): 47–65. <https://doi.org/10.1680/geot.1979.29.1.47>.

Darin, S.R. and Huitt, J.L. 1960. Effect of a Partial Monolayer of Propping Agent on Fracture Flow Capacity, SPE 1291-G, Society of Petroleum Engineers.

Dye, A.L., McClure, J.E., Miller, C.T., and Gray, W.G. 2013. Description of Non-Darcy Flows in Porous Medium Systems. *Phys. Rev. E*, 87(3), 033012, [doi:10.1103/PhysRevE.87.033012](https://doi.org/10.1103/PhysRevE.87.033012).

Economides M, Nolte K. *Reservoir Stimulation*. 2000. 3rd edition: John Wiley and Sons.

Fan, M., McClure, J., Han, Y., Li, Z., and Chen, C. 2017a. Interaction between Proppant Packing, Reservoir Depletion, and Fluid Flow in Hydraulic Fractures. *Offshore Technology Conference*. [doi:10.4043/27907-MS](https://doi.org/10.4043/27907-MS).

Fan, M., Han, Y., McClure, J., and Chen, C. 2017b. Hydraulic Fracture Conductivity as a Function of Proppant Concentration under Various Effective Stresses: From Partial



Monolayer to Multilayer Proppants. Unconventional Resources Technology Conference. doi:10.15530/URTEC-2017-2693347.

Fan, M., McClure, J., Han, Y., Li, Z., and Chen, C. 2018. Interaction Between Proppant Compaction and Single-/Multiphase Flows in a Hydraulic Fracture. SPE-189985-PA. SPE J. doi:10.2118/189985-PA.

Forchheimer, P.: 1901. Wasserbewegung durch boden, Zeit. Ver. Deutsch. Ing. 45: 1781–1788.

Gaurav, A., Dao, E. K., and Mohanty, K. K. 2010. Ultra-Lightweight Proppants for Shale Gas Fracturing. Society of Petroleum Engineers. doi:10.2118/138319-MS.

Ginzburg, I. 2008. Consistent Lattice Boltzmann Schemes for the Brinkman Model of Porous Flow and Infinite Chapman–Enskog Expansion. Phys. Rev. E 77: 066704. <https://doi.org/10.1103/PhysRevE.77.066704>.

Ginzburg, I., d’Humières, D., and Kuzmin, A. 2010. Optimal Stability of Advection-diffusion Lattice Boltzmann Models with Two Relaxation Times for Positive/Negative Equilibrium. J. Stat. Phys. 139 (6): 1090–1143. <https://doi.org/10.1007/s10955-010-9969-9>.

Grunau, D., Chen, S., and Eggert, K. 1993. A Lattice Boltzmann Model for Multiphase Fluid Flows. Phys. Fluids A 5: 2557–2562. <https://doi.org/10.1063/1.858769>.

Gu M, Dao E, Mohanty KK. 2015. Investigation of ultra-light weight proppant application in shale fracturing. Fuel. 150:191-201.

Gu M, Mohanty KK. 2014. Effect of foam quality on effectiveness of hydraulic fracturing in shales. Int J Rock Mech Min. 70: 273-85.

Gu, M., Fan, M., and Chen, C. 2017. Proppant Optimization for Foam Fracturing in Shale and Tight Reservoirs. Society of Petroleum Engineers. doi:10.2118/185071-MS.

Guo, J.C, Lu, C., Zhao, J., and Wang, W. 2008. Experimental Research on Proppant Embedment. Journal of China Coal Society. 33(6):661-4.

Han Y. and Cundall P.A. 2013. LBM-DEM Modeling of Fluid-solid Interaction in Porous Media, Int. J. Numer. Anal. Meth. Geomech. 37 (10): 1391-1407.

Han Y., P.A., and Cundall P.A. 2011. Lattice Boltzmann Modeling of Pore-scale Fluid Flow through Idealized Porous Media, Int. J. Num. Meth. Fluids 67 (11): 1720-1734.

Howard, G.C. and Fast, C.R. 1970. Hydraulic Fracturing. Richardson, Texas: Society of Petroleum Engineers, Inc.

Huitt, J. L. and Mcglathlin, B. B. 1958. The Propping of Fractures in Formations Susceptible to Propping-sand Embedment. Drilling and Production Practice. American Petroleum Institute.

Inamuro, T., Yoshino, M. and Ogino, F. 1999. Lattice Boltzmann Simulation of Flows in a Three-Dimensional Porous Structure. Int. J. Numer. Methods Fluids 29: 737-748. [http://dx.doi.org/10.1002/\(SICI\)1097-0363\(19990415\)29:7<737::AID-FLD813>3.0.CO;2-H](http://dx.doi.org/10.1002/(SICI)1097-0363(19990415)29:7<737::AID-FLD813>3.0.CO;2-H).

Itasca Consulting Group, Inc. 2008. PFC3D – Particle Flow Code in 3 Dimensions, Version 4.0 User's Manual. Minneapolis: Itasca.

Lacy, L. L., Rickards, A. R., and Bilden, D. M. 1998. Fracture Width and Embedment Testing in Soft Reservoir Sandstone. Society of Petroleum Engineers. doi:10.2118/36421-PA.

Li Y, and Huang P. 2008. A Coupled Lattice Boltzmann Model for Advection and Anisotropic Dispersion Problem in Shallow Water. *Adv Water Resour*, 31:1719-1730.

Li, K.W., Gao, Y.P., Lyu, Y.C, and Wang, M. 2015. New Mathematical Models for Calculating Proppant Embedment and Fracture Conductivity. *SPE J.* 20(3):496-507.

Liang, F., Sayed, M., Al-Muntasheri, G. A., Chang F. F., and Li, L. 2016. A comprehensive review on proppant technologies, *Petroleum*, 2(1): 26–39.

Macini, P., Mesini, E. N., and Viola, R. 2008. *Non-Darcy Flow: Laboratory Measurements in Unconsolidated Porous Media.* Society of Petroleum Engineers. doi:10.2118/113772-MS.

McClure, J.E., Prins, J.F. and Miller, C.T. 2014. A Novel Heterogeneous Algorithm to Simulate Multiphase Flow in Porous Media on Multicore CPU-GPU systems. *Computer Physics Communications*, 185(7): 1865-1874.

Milton-Taylor, D. 1993. *Non-Darcy Gas Flow: From Laboratory Data to Field Prediction.* Society of Petroleum Engineers. doi:10.2118/26146-MS.

Miskimins, J. L., Lopez, H. D. J., and Barree, R. D. 2005. *Non-Darcy Flow in Hydraulic Fractures: Does It Really Matter?* Society of Petroleum Engineers. doi:10.2118/96389-MS.

Newman, M. S. and Yin, X. 2013. *Lattice Boltzmann Simulation of Non-Darcy Flow in Stochastically Generated 2D Porous Media Geometries.* Society of Petroleum Engineers. doi:10.2118/146689-PA.

Palisch, T. T., Duenckel, R. J., Bazan, L. W., Heidt, J. H., and Turk, G. A. 2007. *Determining Realistic Fracture Conductivity and Understanding its Impact on Well*

Performance - Theory and Field Examples. Society of Petroleum Engineers. doi:10.2118/106301-MS.

Parker, M. A., Ramurthy, K., and Sanchez, P. W. 2012. New Proppant for Hydraulic Fracturing Improves Well Performance and Decreases Environmental Impact of Hydraulic Fracturing Operations. Society of Petroleum Engineers. doi:10.2118/161344-MS.

Raysoni, N. and Weaver, J. 2013. Long-Term Hydrothermal Proppant Performance. Society of Petroleum Engineers. doi:10.2118/150669-PA.

Schubarth, S. and Milton-Taylor, D. 2004. Investigating How Proppant Packs Change Under Stress. Society of Petroleum Engineers. doi:10.2118/90562-MS.

Succi, S., Benzi, R., and Higuera, F. 1991. The Lattice-Boltzmann Equation—a New Tool for Computational Fluid Dynamics. *Physica D* 47:219–230. [https://doi.org/10.1016/0167-2789\(91\)90292-H](https://doi.org/10.1016/0167-2789(91)90292-H).

Succi, S. 2001. *The Lattice Boltzmann Equation for Fluid Dynamics and Beyond*. New York: Oxford University Press.

Volk, L. J., Raible, C. J., Carroll, H. B., and Spears, J. S. 1981. Embedment of High Strength Proppant into Low-Permeability Reservoir Rock. Society of Petroleum Engineers. doi:10.2118/9867-MS.

Weaver, J. D., Rickman, R. D., Luo, H., and Logrhy, R. 2009. A Study of Proppant Formation Reactions. Society of Petroleum Engineers. doi:10.2118/121465-MS.

Ye, Z. and Ghassemi, A. 2016. Deformation Properties of Saw-Cut Fractures in Barnett, Mancos and Pierre Shales. Proceeding: 50th US Rock Mechanics/Geomechanics Symposium, Houston, Texas.

Zeng, Z. and Grigg, R. 2006. A criterion for non-Darcy flow in porous media. *Transp. Porous Media.* 63(1): 57–69.

Zhang, F., Zhu, H., Zhou, H., Guo, J., and Huang, B. 2017. Discrete-Element Method/Computational-Fluid-Dynamics Coupling Simulation of Proppant Embedment and Fracture Conductivity after Hydraulic Fracturing. *SPE J.* doi:10.2118/185172-PA.

## **Chapter 4 - Investigating the Impact of Proppant Embedment and Compaction on Fracture Conductivity using a Continuum Mechanics, DEM, and LBM Coupled Approach**

Ming Fan, Virginia Tech; Yanhui Han, Aramco Research Center – Houston; James McClure, Erik Westman, Nino Ripepi, Cheng Chen, Virginia Tech

### **Abstract**

In this study, a numerical modeling approach was developed to advance the understanding of fracture conductivity at different effective stresses, proppant sizes and diameter distributions. The continuum mechanics code (e.g., FLAC3D) was employed to compute proppant embedment and DEM code (e.g., PFC3D) was used to calculate the proppant compaction and rearrangement. LBM simulation was performed on the evolved proppant pack to compute the time-dependent permeability of the proppant pack. Proppant packs with 20/40 and 30/50 mesh sizes were generated using the same average diameter but different diameter distributions. Specifically, we used the coefficient of variation (COV) of diameter (defined as the ratio of standard deviation of diameter to mean diameter) to characterize the heterogeneity of particle size. The influences of proppant sizes, distribution patterns and rock properties, on fracture conductivities were extensively studied. Simulations showed that, under the same effective stress, a proppant pack with a smaller diameter COV has higher fracture width, permeability and conductivity. Fracture conductivity increases with increasing proppant size but decreasing fracture closure stress. Proppant embedment increases with the decrease of rock formation's stiffness. The results of this research revealed various characteristics of

proppant packing that may affect the hydraulic conductivity of proppant-supported fractures.

#### **4.1 Introduction**

Hydraulic fracturing technique is widely used to enhance the production of unconventional hydrocarbon energy (e.g., shale oil and gas) from these tight shale oil/gas reservoirs. The standard hydraulic fracturing operations usually involves massive injections of fracturing fluids to create and propagate tensile fractures at a treatment pressure above the minimum principal stress (Ye and Ghassemi, 2016; Gu et al., 2017). However, during hydrocarbon production, pore pressure is reduced and effective stress of the rock matrix increases (Fan et al., 2017a). Proppants are widely used in hydraulic fracturing to prevent hydraulic fractures from closing during reservoir depletion thus maintain conductive channels between the reservoir and wellbore. The compressive stress acting on a fracture can cause proppant pack to compact and embed into fracture walls as well. Both compaction and embedment will lead to reduction in fracture aperture. Under increased effective stress, proppant compaction, rearrangement, and embedment can modify the proppant pore structure significantly within a hydraulic fracture. Optimizing proppant pack conductivity in a hydraulic fracture is of critical importance to sustain effective and economical production of petroleum hydrocarbons.

In order to achieve economical production rates from these tight formations, sufficient conductivity in hydraulic fractures should be sustained (Alramahi and Sundberg, 2012). In oil and gas industry, fracture conductivity is one of the most important factor to evaluate the effectiveness of hydraulic fracturing. Fracture conductivity measures the

total flow rate through a unit length of fracture and is determined as the product of fracture permeability and fracture width (Zhang et al., 2017). Fracture width and permeability depend closely on the strength of fracture rock formation as well as the interaction between proppant pack and rock formation (Chen et al., 2015). The proppant embedment is small in the rock formation with high stiffness, which in this case are helpful to maintain fracture aperture and conductivity. Therefore, proppant pack property as well as the strength of rock formation play an important role in maintaining fracture conductivity, which is critical for economically viable extraction of hydrocarbons from the reservoir.

In this study, a numerical modeling approach was developed to advance the understanding of fracture conductivity at different effective stresses, proppant sizes and diameter distributions. The outcome of this study provide insights into the factors controlling the change of conductivity induced by proppant embedment and compaction, which are helpful in optimizing proppant placement, completion design and well production.

## **4.2 Numerical model description**

### **4.2.1 Overview of numerical workflow**

In the presented numerical study, the rock matrix is modeled using elastic structural elements provided by FLAC3D and the proppant particles are modeled using PFC3D directly. The proppant embedment was calculated by FLAC3D and the proppant compaction and rearrangement under increasing mechanical loading was simulated using PFC3D. A constant velocity was applied to rock matrix to mimic the interaction between



rock matrix and proppants due to reservoir depletion. An in-house numerical code was developed to discretize the pore structure of the proppant pack and extract the geometric data for lattice Boltzmann (LB) measurement of proppant assembly's permeability. Using this numerical simulation, we are able to study factors controlling the change of conductivity induced by proppant embedment and compaction.

#### **4.2.2 Coupling FLAC3D with PFC3D**

FLAC3D (Fast Lagrangian Analysis of Continua) is a three-dimensional explicit finite-difference program for modeling three-dimensional mechanical behavior of rock and soil or other materials (Itasca, 2012). The shape of the object to be modeled can be fit by the user represented by elements within a three-dimensional grid. These elements behave according to defined stress-strain laws in response to applied initial and boundary conditions. On the other hand, PFC3D is a three-dimensional (3D) discontinuum mechanics simulator (Itasca, 2008), which describes the movement and interaction of rigid, spherical particles using the discrete/distinct element method (DEM). In PFC3D, the spherical particles are generated independently and interact only at contacts or interfaces. The calculation cycle adopts a time-stepping algorithm, in which the position and velocity of each particle is determined by Newton's second law of motion, and the force-displacement relation is used to update the contact force at each contact. During simulation, contacts can be created and separated simultaneously. The force-displacement relation is applied at each contact point. When particles come into contact, the contact force is generated, which is determined by the relative displacement and specified stiffness between the two particles.

In this coupled model, rock matrix is simulated with FLAC3D elastic constitutive model. Two rock types were studied: one with a relatively large Young's modulus being 19.3Gpa named sandstone in this paper, whereas the other with a smaller Young's modulus being 2.25GPa named weak shale. The proppant packs in contact with rock matrix were generated with PFC3D. A constant velocity was applied to rock matrix to compress the proppant pack. In order to couple the two codes, the base zones of FLAC3D model should correspond to the top faces of PFC3D model one by one. During the coupling, FLAC3D serves as the server and PFC3D acts as the client. FLAC3D cycles first and sends the base zone velocities to the top faces in PFC3D model. These velocities act as the loading on the proppant pack in PFC3D model and the calculated contact forces on its top faces are sent to the base zones in FLAC3D model. This back and forth sending and receiving velocities and contact forces continues until the equilibrium is reached.

#### **4.2.3 Discretization of 3D Proppant Packs**

3D proppant pore structure was discretized and extracted in order to obtain the transport properties using the LB simulation. Specifically, the 3D pore geometry was discretized using a 3D mesh grid having a resolution of 0.01 mm/pixel in the x-, y-, and z-directions. When the average proppant particle diameter is close to 1 mm, which is 100 times larger than the pixel size, the proppant pack geometry is well-resolved with this resolution (Chen et al., 2009b). In this manner, the proppant assembly from PFC3D simulation is converted to a discrete, 3D lattice structure, which will be used as interior and boundary conditions in the LB simulator for pore-scale, single-phase flow simulation.

#### 4.2.4 Lattice Boltzmann Method for Single-Phase Flow Simulation

The LB method is a numerical method for solving the Navier-Stokes equations and based on microscopic physical models and mesoscale kinetic equations (Chen and Doolen, 1998; Succi, 2001). The LB simulator used in this study has been validated by direct comparisons with analytical solutions and laboratory measurements (Chen et al., 2008, 2009a, 2009b). It was then optimized with high-performance graphics processing unit (GPU) parallel computing, which enhanced the computational speed by a factor of 1,000 and led to an in-house LB code, GPU-enhanced lattice Boltzmann simulator (GELBS) (Chen et al., 2016). In this work, the D3Q19 lattice structure was used because of its advantage in achieving a good balance between computational stability and efficiency (Chen et al., 2013).

Particle distribution in the Bhatnagar-Gross-Krook (BGK)-based, single-relaxation-time LB equation is given by

$$f_i(\mathbf{x} + \mathbf{e}_i \Delta t, t + \Delta t) = f_i(\mathbf{x}, t) - \frac{f_i(\mathbf{x}, t) - f_i^{eq}(\rho, \mathbf{u})}{\tau}, \quad (i = 0, 1, 2 \dots 18) \quad (4.1)$$

where  $f_i(\mathbf{x}, t)$  is the particle-distribution function specifying the probability that fluid particles at lattice location  $\mathbf{x}$  and time  $t$  travel along the  $i^{th}$  direction;  $\mathbf{e}_i$  is the lattice velocity vector corresponding to direction  $i$ ;  $\tau$  is the dimensionless relaxation time related to kinematic viscosity;  $f_i^{eq}(\rho, \mathbf{u})$  is the equilibrium distribution function selected to recover the macroscopic Navier-Stokes equations and given by

$$f_i^{eq}(\rho, \mathbf{u}) = \omega_i \rho \left[ 1 + \frac{3\mathbf{e}_i \cdot \mathbf{u}}{c^2} + \frac{9(\mathbf{e}_i \cdot \mathbf{u})^2}{2c^4} - \frac{3\mathbf{u}^2}{2c^2} \right] \quad (4.2)$$

where  $\omega_i$  is the weight coefficient calculated as:

$$\omega_i = \begin{cases} 1/3 & i = 0 \\ 1/18 & i = 1..6 \\ 1/36 & i = 7..18 \end{cases}$$

The macroscopic fluid density and velocity are calculated with the following two equations:

$$\rho = \sum_{i=0}^{18} f_i \quad (4.3)$$

and

$$\mathbf{u} = \frac{\sum_{i=0}^{18} f_i \mathbf{e}_i}{\rho} \quad (4.4)$$

Fluid pressure is calculated using  $p = c_s^2 \rho$ , where  $c_s$  is the speed of sound. In the LB D3Q19 model,  $c_s^2 = c^2/3$ . More details about LB simulations of Darcy flows in porous media can be found in our recent publications (Fan et al., 2018).

### 4.3 Proppant compression studies

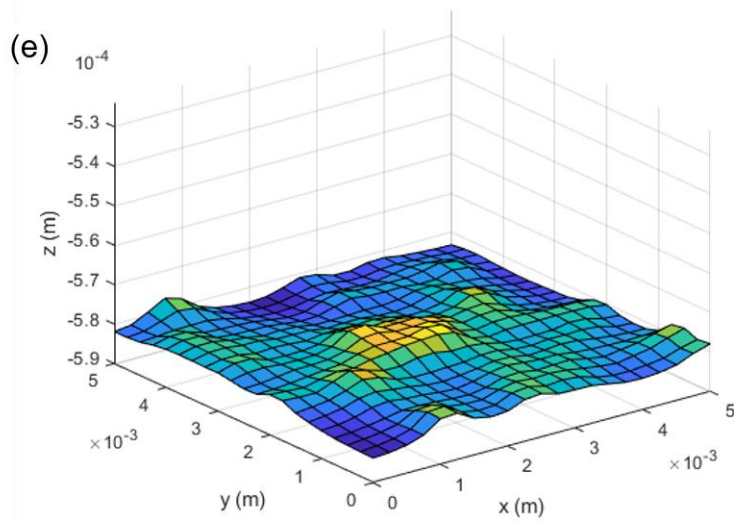
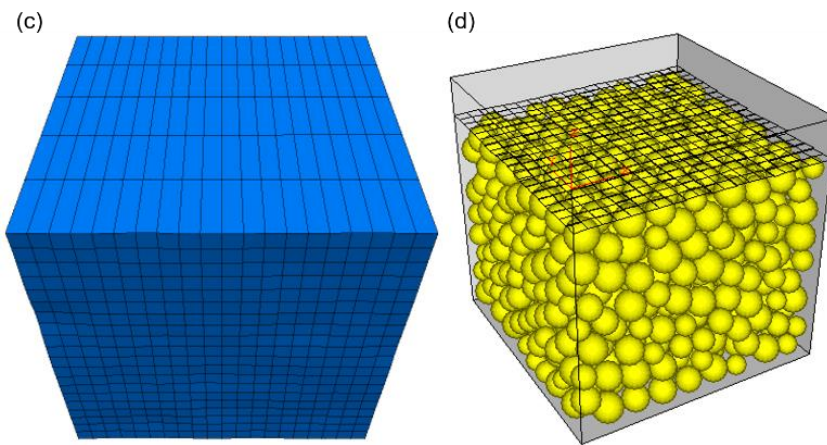
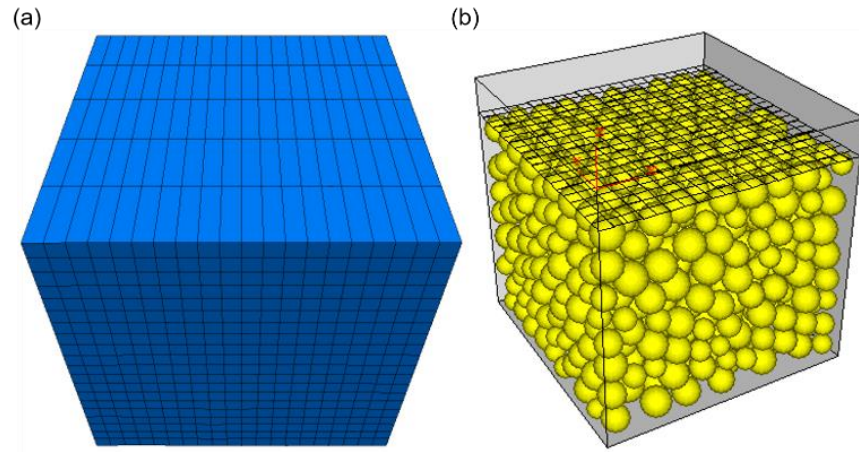
With the purpose of investigating the effect of rock matrix stiffness on proppant embedment and fracture conductivity, two proppant packs with mesh size 20/40 and 30/50 were generated at proppant concentration of 0.5 lb/ft<sup>2</sup> in PFC3D. In this study, a high strength ceramic proppant (CARBOHSP, 2015) properties (e.g., stiffness and density) were used in all the simulations with the purpose of avoiding proppant crushing under high effective stresses. The initial dimension for the two proppant packs was 5 mm × 5 mm × 5 mm. The effective stress on the proppant packs is slowly increased up to 68.9 Mpa (10,000 psi). The fracture then closed in the z-direction (the direction normal to

fracture face) at a constant velocity, which was adequately slow to avoid rapid surge of effective stress between proppant particles and allow fluid within the pore space to flow away in the lateral (x-y) directions. In this way, the system was in the steady state, where the transient pore-pressure changed and resultant stress acting on the proppant particles were negligible (Fan et al., 2018). The embedment of proppant particles into rock matrix as they are subjected to increasing loads was calculated using FLAC3D. Besides the embedment of proppants into the rock surface, the rock matrix deformation is neglected. The processes of proppant particle compression, movement, and re-arrangement were simulated with the PFC code. Corresponding pore structure of proppant pack was discretized at a resolution of 0.01 mm/pixel in all directions and then imported into the GELBS code as interior and boundary conditions to simulate proppant pack permeability in the lateral (x-y) direction.

The second compression study was conducted to investigate the role of proppant size heterogeneity (variation in particle diameter) and effective stress on fracture width, permeability, and conductivity. The initial dimension of the proppant pack was 5 mm × 5 mm × 5mm. Three proppant packs with the same average particle diameter but different size distributions were generated. Three proppant packs were generated following the 30/50 mesh size with diameter COVs being 5%, 12%, and 20%. The proppant packs were compressed in the z-direction and fracture conductivities as functions of increased effective stress were simulated.

#### 4.4 Results and discussion

Figure 4.1 illustrates the coupled FLAC3D and PFC3D model, which is used to mimic the fracture/proppant system with 68.9 Mpa (10,000 psi) fracture closure stress. FLAC3D is used to simulate rock matrix and PFC3D is used to model the proppant pack with 30/50-mesh-size particles. The base zones of FLAC3D model corresponds to the top faces of PFC3D model. For both two sets of simulations, the same proppant pack was used and subjected to same effective stresses. In the first set of simulation, the rock matrix is sandstone (Figure 4.1a) and the variation of heights on rock matrix bottom surface is 0.01 mm (Figure 4.1e). The embedment is small and only minor indentation on the surface of rock matrix was observed. In the second set of simulation, the rock matrix is shale (Figure 4.1c) and the variation of heights on rock matrix bottom surface is 0.06 mm (Figure 4.1f). Compared Figure 4.1a with Figure 4.1d, noticeable proppant embedment into the weak shale matrix was observed, which indicates that the proppant embedment increases with decreasing rock matrix stiffness. In these two sets of simulations, proppant packs are the same, therefore, the conductivity loss between these two systems is typically attributed to the reduction of fracture aperture due to proppant embedment. Fracture between rock matrices with higher stiffness is expected to maintain the fracture aperture and conductivity.



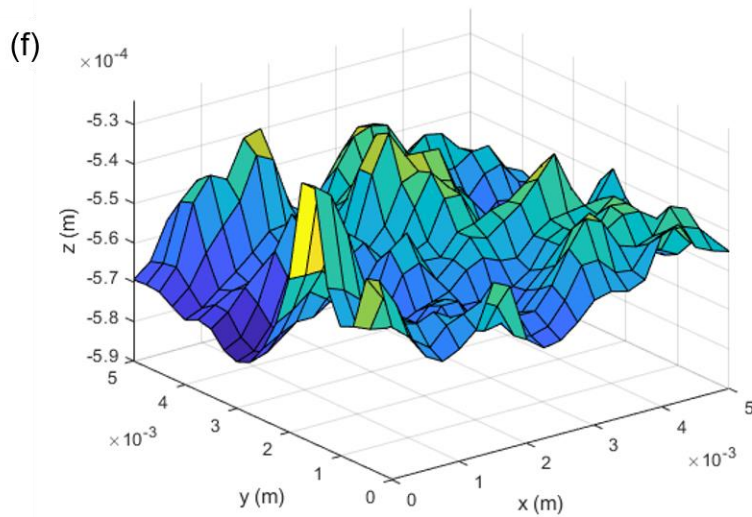


Figure 4.1. Coupled FLAC3D/PFC3D model for simulating a fracture/proppant system with fracture closure stress being 68.9 Mpa (10,000 psi). (a) FLAC3D model simulating sandstone matrix, (b) PFC3D model simulating compressed proppant pack connected with sandstone matrix with 30/50-mesh-size, (c) FLAC3D model simulating shale matrix, (d) PFC3D model simulating compressed proppant pack connected with shale matrix with 30/50-mesh-size, (e) profile of the sandstone matrix bottom surface, (f) profile of the shale matrix bottom surface.

Figure 4.2 presents the fracture width, permeability, and conductivity as functions of effective stress. As the effective stress increased, the fracture width became uneven due to the local indentation of rock matrix with proppant particles. The embedment of proppants was taken as average heights of the uneven rock matrix bottom surface and the fracture width was computed by subtracting the embedment from the height of proppant pack. The permeability of proppant pack was calculated by LB-simulator and fracture conductivity was determined by the product of aperture width and proppant pack permeability. The sandstone matrix/20-40-mesh-size proppant pack system had the highest fracture width, permeability and conductivity; whereas the shale matrix/30-50-mesh-size proppant pack system had the smallest fracture width, permeability, and conductivity. For the proppant packs with same mesh sizes, sandstone matrix system has



higher fracture aperture under the same effective stress, which mostly because the smaller proppant embedment into rock matrix (Figure 4.1a and 4.1d). This suggests that the rock matrix with higher stiffness provides better support to the fracture. For the same rock matrix, proppant packs with smaller proppant particles have smaller fracture width, permeability and conductivity. This was because under the same effective stress, particles in proppant packs with smaller proppant mesh sizes are smaller and can be compressed into the pore space between bigger particles, leading to a smaller fracture width; the pore space presented in the proppant pack are smaller, giving rise to a smaller fracture permeability and conductivity. This indicates that proppant packs with larger proppant particles provide a higher fracture conductivity under the same proppant concentration.

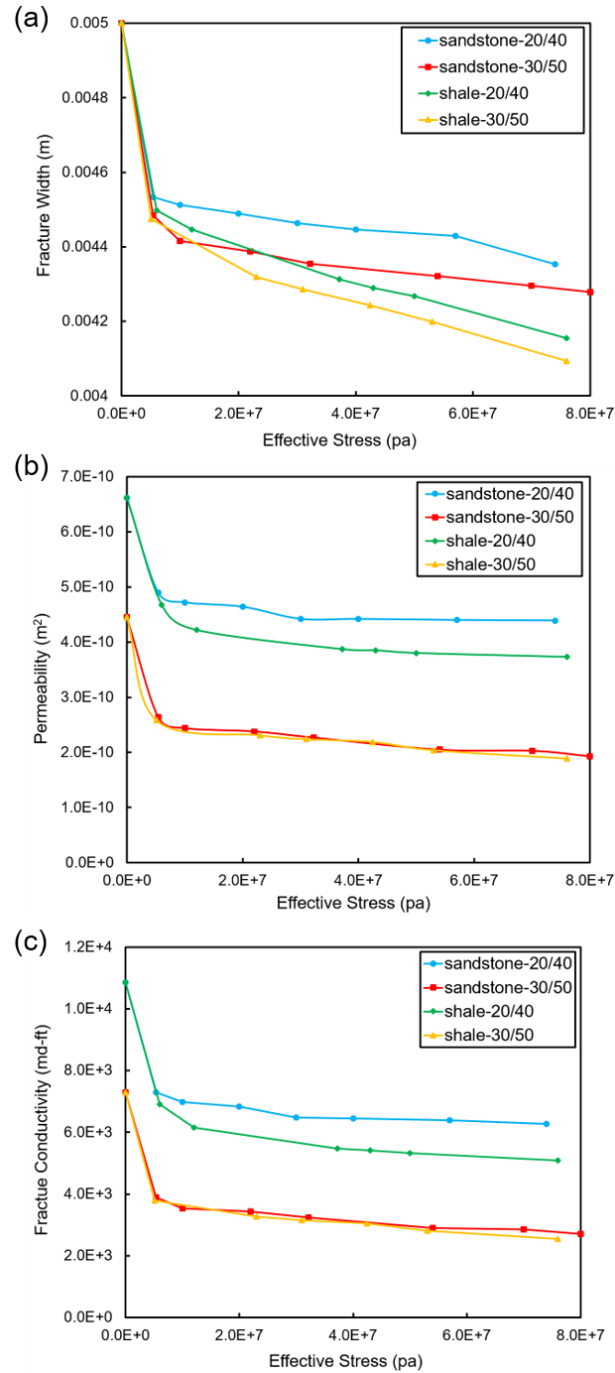


Figure 4.2. (a) Fracture width, (b) permeability, and (c) conductivity as functions of effective stress. The rock matrix are modeled with sandstone and shale material and proppant packs are modeled with 20/40 and 30/50 mesh sizes

As mentioned previously, the second proppant compaction study was conducted to investigate the role of proppant size heterogeneity (variation in particle diameter) and

effective stress on fracture width, permeability, and conductivity. Figure 4.3 illustrates LB-simulated pressure distributions within a 2D cross section cut along the x-y plane at the fracture center of proppant packs. The particles within the proppant assemblies were generated with 30/50 mesh size with diameter COVs of 5% and 20%. The pressure is presented in the LB unit. The proppant pack having diameter COV 5% had a more homogeneous particle diameter distribution, whereas the proppant pack having diameter COV 20% had a more heterogeneous particle diameter distribution.

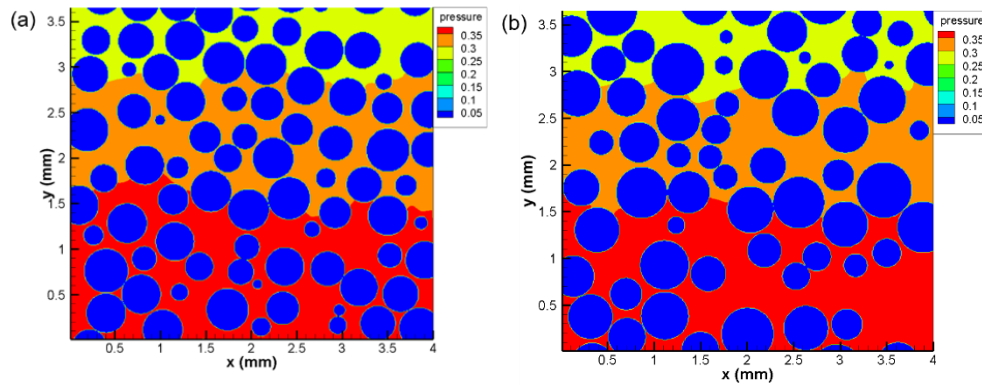


Figure 4.3 illustrates LB-simulated pressure distributions within the pore space of proppant assemblies having (a) 5% diameter COV, and (b) 20% diameter COV.

Figure 4.4 presents the simulation results for the three proppant packs in the second compression study with particle diameter COVs being 5%, 12%, and 20%, respectively. Figure 4.4a shows the fracture width as a function of the effective stress. Under the same effective stress, proppant pack with diameter COV5% had the highest fracture width whereas the proppant pack with diameter COV20% had the smallest fracture width. This was because proppant packs with larger diameter COVs had wider diameter distributions with more big particles and small particles. The smaller particles move more easily in the proppant assemblies with larger diameter COVs and can be pushed into the pore space between larger particles with increasing effective stress. This indicates that the proppant

pack with more homogeneous particle diameter distribution provides better support to the fracture (Fan et al., 2018).

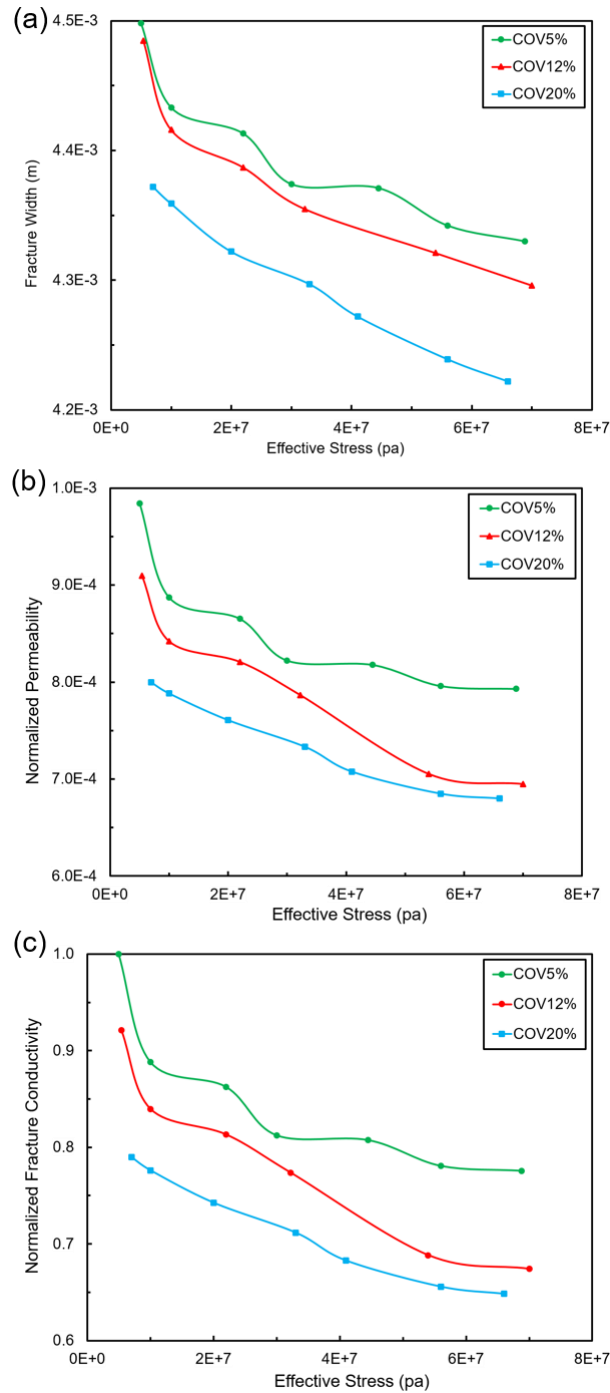


Figure 4.4. Development of (a) fracture width, (b) normalized fracture permeability, and (c) normalized fracture conductivity as functions of effective stress for proppant packs with 5%, 12%, and 20% diameter COVs

Figure 4.4b presents the normalized permeabilities as functions of effective stress. In this study, the permeabilities are normalized by the square of the equivalent particle diameter with the purpose of minimizing the effect of average diameter on the analysis of permeability (Dye et al, 2013; Fan et al, 2018). The equivalent particle diameter,  $D$ , is determined as:

$$D = 6 \times (1 - \phi) \times V / S \quad (4.5)$$

Where  $\phi$  is the porosity,  $V$  is the volume of the entire computational domain, and  $S$  is the total surface area of proppant particles. As effective stress increased, normalized permeability decreased. Under the same effective stress, the proppant pack with 20% diameter COV had the lowest normalized permeability, whereas the proppant pack with 5% diameter COV had the highest normalized permeability. This was because under the same effective stress, a more homogenous particle diameter distribution led to a higher porosity (smaller fracture width reduction), giving rise to higher proppant pack permeability. In order to illustrate fracture conductivity loss as effective stress increases, conductivities for three proppant packs at different effective stresses are normalized by conductivity of proppant pack with diameter COV5% at effective stress  $5 \times 10^6$  Pa, as shown in Figure 4.4c. It can be observed that proppant pack with diameter COV5% had the highest fracture conductivity, whereas the proppant pack with diameter COV20% had the lowest fracture conductivity. With identical stress increase, the proppant assembly having a more homogenous particle diameter distribution is helpful to maintain fracture conductivity for economic production rates (Fan et al., 2017b).

#### **4.5 Conclusions and implications**

In this study, a geomechanics-fluid mechanics coupled numerical workflow was developed to mimic the interaction between rock matrix and proppant as well as fluid flow in a hydraulic fracture during the process of the reservoir depletion. Effects of the rock stiffness, proppant sizes and diameter distributions, as well as effective stresses on fracture conductivity were investigated. Compared to weak shale, the proppant embedment into sandstone matrix is small, which indicates the rock matrix with higher stiffness is helpful to maintain fracture aperture and conductivity. Under the same effective stress, a proppant pack with a smaller diameter COV, which implies a more homogeneous particle diameter distribution, had higher fracture permeability and smaller fracture width reduction (i.e., compressed distance). With identical stress increase, the proppant pack with a more homogeneous particle diameter distribution experienced less dramatic changes with respect to pore structure and connectivity, which were favorable for maintaining the fracture conductivity and hydrocarbon transport during the process of hydrocarbon extraction.

This study indicates that a fracture/proppant system with stronger rock matrix and uniform proppant particle diameter distribution provides better support to the fracture, in terms of sustaining fracture conductivity during the process of reservoir depletion. The coupled numerical workflow combining FLAC3D/PFC3D with LB simulator provides insights into the factors controlling the change of conductivity induced by proppant embedment and compaction, which has the potential to benefit the optimization processes for proppant placement, completion design, and well production.

## **Acknowledgements**

The authors acknowledge the support of the Junior Faculty Award from Virginia Tech's Institute for Critical Technology and Applied Science. The authors are also thankful to the support from Aramco Services Company – Houston and Virginia Tech's Advanced Research Computing Center.

## **References**

Alramahi, B., and M. I. Sundberg. 2012. Proppant Embedment and Conductivity of Hydraulic Fractures In Shales. American Rock Mechanics Association.

Chen, C., A.I. Packman and J.F. Gaillard. 2008. Pore-scale Analysis of Permeability Reduction Resulting from Colloid Deposition, *Geophysical Research Letters*, 35, L07404, doi:10.1029/2007GL033077.

Chen, C., B.L.T. Lau, J.F. Gaillard and A.I. Packman. 2009a. Temporal Evolution of Pore Geometry, Fluid Flow, and Solute Transport Resulting from Colloid Deposition, *Water Resources Research*, 45, W06416, doi:10.1029/2008WR007252.

Chen, C., A. I. Packman, and J. F. Gaillard. 2009b. Using X-ray micro-tomography and pore-scale modeling to quantify sediment mixing and fluid flow in a developing streambed, *Geophysical Research Letters*, 36, L08403, doi:10.1029/2009GL037157.

Chen, C., D.D. Hu, D. Westacott and D. Loveless. 2013. Nanometer-Scale Characterization of Microscopic Pores in Shale Kerogen by Image Analysis and Pore-Scale Modeling. *Geochemistry, Geophysics, Geosystems* 14 (10): 4066-4075. <http://dx.doi.org/10.1002/ggge.20254>.

Chen, C., V. Martysevich, P. O'Connell, D. Hu and L. Matzar. 2015. Temporal Evolution of the Geometrical and Transport Properties of a Fracture/Proppant System under Increasing Effective Stress, SPE Journal, 20(3), 527-535, SPE-171572-PA. <http://dx.doi.org/10.2119/171572-PA>.

Chen, C., Z. Wang, D. Majeti, N. Vrvilo, T. Warburton, V. Sarkar and G. Li. 2016. Optimization of Lattice Boltzmann Simulation with Graphics-Processing-Unit Parallel Computing and the Application in Reservoir Characterization, SPE Journal, SPE-179733-PA, <http://dx.doi.org/10.2118/179733-PA>.

Chen, S., and G. D. Doolen. 1998. Lattice Boltzmann Method for Fluid Flows, Annu. Rev. Fluid Mech., 30, 329-364.

CARBOHSP Technical Data Sheet. 2015. Carbo Ceramics Inc. <http://www.carboceramics.com/getattachment/5a2b4ffd-0b0e-4ce9-9a4e-5da47ad97425/attachment>

Dye A.L., J.E. McClure, C.T. Miller and W.G. Gray. 2013. Description of Non-Darcy Flows in Porous Medium Systems. Phys. Rev. E, 87(3), 033012, doi:10.1103/PhysRevE.87.033012.

Fan, M., J. E. McClure, Y. Han, and C. Chen. 2017a. Interaction between Proppant Packing, Reservoir Depletion, and Fluid Flow in Hydraulic Fractures, OTC-27907-MS, Offshore Technology Conference (OTC) 2017, Houston, Texas, USA, May 1-4.

Fan, M., Y. Han, J. McClure, and C. Chen. 2017b. Hydraulic Fracture Conductivity as a Function of Proppant Concentration under Various Effective Stresses: From Partial Monolayer to Multilayer Proppants. Unconventional Resources Technology Conference (URTeC), Austin, Texas, July 24-26.



Fan, M., J. McClure, Y. Han, Z. Li, and C. Chen. 2018. Interaction Between Proppant Compaction and Single-/Multiphase Flows in a Hydraulic Fracture. Society of Petroleum Engineers. doi:10.2118/189985-PA

Gu, M., M. Fan, and C. Chen. 2017. Proppant Optimization for Foam Fracturing in Shale and Tight Reservoirs, in SPE Unconventional Resources Conference. Calgary, Alberta, Canada, 15-16 February.

Itasca Consulting Group, Inc. 2012. FLAC3D – Fast Lagrangian Analysis of Continua in 3 Dimensions, Version 5.0 User's Manual. Minneapolis: Itasca.

Itasca Consulting Group, Inc. 2008. PFC3D – Particle Flow Code in 3 Dimensions, Version 4.0 User's Manual. Minneapolis: Itasca.

Succi, S. 2001. The Lattice Boltzmann Equation for Fluid Dynamics and Beyond, Oxford Univ. Press, New York.

Ye, Z., A. Ghassemi, and S. Riley. 2016. "Fracture Properties Characterization of Shale Rocks." Proceeding: Unconventional Resources Technology Conference, San Antonio, Texas.

Zhang F.S., H.Y. Zhu, H.G. Zhou, J.C. Guo and B. Huang. 2017. Discrete-Element-Method/Computational-Fluid Dynamics Coupling Simulation of Proppant Embedment and Fracture Conductivity After Hydraulic Fracturing. Spe Journal. 22(2):632-44.

## **Chapter 5 Combining Discrete Element Method with Lattice Boltzmann Modeling to Advance the Understanding of the Conductivity of Proppant Mixtures in a Propped Hydraulic Fracture**

Ming Fan, Virginia Tech; Yanhui Han, Aramco Research Center – Houston; Ming Gu, West Virginia University; James McClure, Nino Ripepi, Erik Westman, Cheng Chen, Virginia Tech

### **Abstract**

Proppant selection in hydraulic fracturing operations is a critical economic and technical decision that will affect productivity and performance of the stimulated wells. In hybrid completion designs, proppants of various sizes and types are often mixed together and incorporated into the pumping schedule. Optimization of mixing proppants of various sizes and types has the potential to maximize proppant pack conductivity and, subsequently, the reservoir production performance. In this work, a numerical modeling approach, combining the Discrete Element Method (DEM) with lattice Boltzmann (LB) method, was adopted to investigate the potential effects of mixed proppants of different sizes and types on the fracture conductivity. DEM was used to capture the increase of effective stress and the resultant compaction, rearrangement, and embedment of proppants. The evolved pore structures of the compacted proppant pack was extracted from DEM model and then imported into the LB simulator as internal boundary conditions in pore-scale fluid flow simulation to measure the time-dependent permeability of the proppant pack inside the fracture. We first measured the conductivities and constructed conductivity curves for proppant packs with mesh size 20, 40, and 20/40 (mixing mass ratio 1:1) under varying proppant areal concentrations

(proppant mass per unit area of fracture face). The conductivity curve of the 20/40 mixture agrees well with laboratory data; it is also interesting to observe that it is lower than the curve derived based on the linear interpolation between those of uniform mesh size 20 and 40 curves. Simulations were also performed to measure the propped fracture conductivities of proppant packs with different mass mixing ratios, such as 1:9, 2:8, 3:7, 4:6, and 5:5, and different proppant mesh sizes, effective stresses, and proppant areal concentrations (ranging from partial monolayer to multilayer). The conductivities of mixtures of sands and ceramic proppants under different areal concentrations and effective stresses were also tested. Simulations indicated that larger-size ceramic proppants mixed with sands at lower concentrations could result in conductivity similar to that of proppant pack consisting of pure smaller-size ceramic proppants. Knowledge generated from this work has quite significant implications to the optimization of hydraulic fracturing and proppant placement designs.

### **Keywords**

Discrete Element Method; Lattice Boltzmann; Hydraulic Fracturing; Proppant Conductivity; Proppant Mixtures

### **5.1 Introduction**

During hydrocarbon production, pore pressure depletes and effective stress increases, which lead to the contraction of rock mass, reduction of fracture aperture, and compaction of proppant pack, and, subsequently, the reduction of reservoir formation's permeability, fracture conductivity, and hydrocarbon production [1, 2]. Proppants are placed in the hydraulically created fractures to prevent them from closing during reservoir depletion and, thus, the conductive channels between the reservoir and

wellbore can be maintained [3]. Therefore, correct selection and placement of proppants in the hydraulic fracturing operation is critical to the economic and technical success of well stimulation and production. In hybrid completion designs, proppants of various sizes and types are often mixed together and incorporated into the pumping schedule. Mixing proppants of various sizes and types has the potential to significantly affect the conductivity of proppant pack and production performance of reservoir.

Since the sieved sand was first introduced as proppants in hydraulic fracturing operations in 1947 [4], many different types of proppants have been developed. The most commonly used proppants are natural silica sands and manufactured ceramic proppants. Natural sands are more economical than ceramic proppants. In the application, natural sands need to be processed and graded with high-silica quartz. Due to their compressive strength limit, natural sands cannot be used when high closure pressure (e.g., >6,000 psi) is expected, instead ceramic proppants should be considered. Compared to natural sands, ceramic proppants are more uniform in size and shape with higher sphericity and roundness. Most ceramic proppants can withstand closure stress of 10,000 psi and even higher, while retaining high conductivity during hydrocarbon production. A drawback of the ceramic proppants is that, as an engineered product with a more complex manufacturing process, the cost of manufacturing ceramic proppants is several times more expensive than processing same amount of natural sands [5].

In order to achieve economical production rates from unconventional reservoir formations, sufficient conductivity in hydraulic fractures must be sustained [6, 7]. The performance of proppant packs with mixed proppants of various mesh sizes and types are critical in maintaining fracture conductivity and subsequently the economical production

of hydrocarbons from the reservoir [8]. Generally, it is expected that a greater amount of large proppants will result in greater fracture conductivity, so larger concentration of more conductive proppants tends to increase the fracture conductivity, while less conductive proppant pack is likely to downgrade the fracture conductivity [9, 10]. In recent years, the 100 mesh size proppants have been widely used in horizontal wells because they can more easily be transported into deep regions in the fractures. However, it remains unclear how much the low conductive proppant affects the fracture conductivity, i.e., the influence of mesh-size and mass ratio of the low conductive proppants on the fracture conductivity needs in-depth investigations.

Phatak et al. [11] presented a proppant selection study based on fracturing-to-production simulations. They found that larger proppants enhance the initial production rate because of the larger propped fracture width and permeability; smaller proppants offer less initial hydraulic conductivity but relatively higher average hydraulic conductivity over the life cycle, due to a larger propped length and effective stimulated reservoir volume (ESRV). Their studies indicated that the combination of proppants of different sizes optimizes production by maximizing initial production and slowing down the production decline. Kulkarni and Ochoa [12] developed a discrete approach by combining multi-particle finite element method (FEM) and ABAQUS and investigated the changes in proppant pack pore space as a function of pressure and proppant mixture composition. The results demonstrated that a higher percent of soft particles with softer rock formations provided the most stable pack condition, but resulted in deeper particle embedment and subsequent loss of permeability. Hu et al. [13] published a brief overview of using proppant of different types and percentages to determine the long-term

production and economical effectiveness of hydraulically fractured wells between 2011 and 2013. Based on the percentage and amount of each proppant types used in 72 wells in four different fields, they concluded that using high percentages and large amounts of ceramic proppants yielded higher production and estimated ultimate recovery (EUR); a large percentage of higher strength proppant can provide sufficient conductivity and crushing resistance to support long term production. Both simulations and field tests indicate that the assessment of the performance of mixing proppants of different types and sizes is critical to the hydraulic fracturing treatments for both oil and gas wells.

This study aims at advancing the understanding and optimizing the performance of mixing proppants of various types and sizes using a novel numerical method that integrates the DEM method with LB modeling. The discrete element method (DEM) [14] has proven to be very efficient in simulating the compaction of granular materials [2, 3, 8, 15, 16]. Particle Flow Code 3D (PFC3D) is used to generate proppant packs and model proppant pack compaction. The evolving discretized pore structures from proppant packs are used as interior boundary conditions in the lattice Boltzmann (LB) simulation of fluid flow through the compressed pore space. The simulation workflow was first verified by comparing numerical simulation results with laboratory data. Then, simulations were conducted to evaluate the potential effects on fracture conductivity under support of different proppant mixtures. The integrated approach provides an alternating or complementary tool, in addition to small-scale experiments, to assist proppant selection in hydraulic fracturing design. The outcome of this study provides insight into the role of sizes, types, mixing ratios and areal concentrations of proppants, and effective stresses on

the conductivity of a proppant-supported fracture and consequent productivity of the reservoir.

## **5.2 Overview of Technical Elements in Workflow**

In the presented numerical study, the proppant packs were modeled using particle assemblies in PFC3D [17]. The proppant embedment was estimated by a semi-empirical correlation, but the proppant compaction and rearrangement under increasing mechanical loading was directly determined by simulations. In the proppant compaction simulation, the computational domain was cubic and the six boundaries were rigid walls. The domain was then filled with proppant particles, which were generated following specified diameter distributions. Next, the top and bottom walls moved toward each other at a constant velocity, leading to proppant compaction and increasing effective stress between particles. In all simulations, the positions and geometric properties of all individual particles were tracked. An in-house numerical code was developed to discretize the pore structure of the proppant pack and extract the geometric data for lattice Boltzmann (LB) simulation to measure the permeability of proppant pack. Using this integrated simulation workflow, the influence of proppant mixtures on proppant pack's conductivity can be experimented.

### **5.2.1 DEM and PFC3D**

In this study, the PFC3D was used for DEM simulations. PFC3D is a 3D discontinuum mechanics simulator [17]. It describes the movement and interaction of rigid, spherical particles using the DEM scheme, which was first introduced by Cundall [18] for the

analysis of rock mechanics problems and then applied to soils by Cundall and Strack [14]. In PFC3D, the spherical particles are generated independently and interact only at contacts or interfaces. The calculation cycle adopts a time-stepping algorithm, in which the position and velocity of each particle is determined by Newton's second law of motion, and the force-displacement relation is used to update the contact force at each contact. During the simulation, contacts can be created and separated. However, Newton's second law of motion is not applied to boundary walls, since the motion of walls is specified by the user. The force-displacement relation is applied at each contact point, which is defined by a unit normal vector,  $n_i$ . When particles come into contact, the contact force is generated, which is determined by the relative displacement and specified stiffness between the two particles. The contact force can be decomposed into normal and shear components with respect to the contact plane, as illustrated in Equation 5.1. The normal contact force is computed by Equation 5.2. The magnitude of the shear contact force is initialized as zero and then incremented at each time step, as determined by Equation 5.3 [17].

$$F_i = F_i^n + F_i^s \quad (5.1)$$

$$F_i^n = K^n U^n n_i \quad (5.2)$$

$$\Delta F_i^s = -k^s \Delta U_i^s \quad (5.3)$$

In these equations,  $F_i^n$  and  $F_i^s$  denote the normal and shear components of the contact force, respectively;  $K^n$  is the normal stiffness at the contact, which relates the total normal displacement to the normal force;  $k^s$  is the shear stiffness, which relates the



incremental shear displacement to the shear force;  $U^n$  is the contact displacement in the normal direction and  $U_i^S$  is the shear component of the contact displacement.

### **5.2.2 Discretization of 3D proppant pore structure**

The evolving 3D proppant pore structures from the DEM simulation were discretized, extracted and imported into the LB models as the interior boundaries in the simulation of single-phase Darcy flow through the compressed porous proppant pack. Specifically, the 3D pore geometry was discretized with a 3D mesh grid having a resolution of 0.02 mm per LB length unit in the x, y, and z directions.

### **5.2.3 Lattice Boltzmann method**

The LB method is a mesoscopic physics based numerical method for recovering the Navier-Stokes equations through solving a set of kinetic equations at mesoscale [19, 20]. In comparison with conventional fluid dynamic models, the LB method has many advantages. For example, it is explicit in evolution equation, simple to implement, natural to parallelize [21, 22], and easy to incorporate new physics such as interactions at fluid-solid interface [23-25].

The LB simulator used in this study has been validated by direct comparisons with analytical solutions and laboratory measurements [26-28]. It was then optimized with high-performance graphics processing unit (GPU) through parallel computing, which enhanced the computational speed by a factor of 1,000 and led to an in-house LB code, GPU-enhanced lattice Boltzmann simulator (GELBS) [29]. In this work, the D3Q19

lattice structure was used because of its advantage in achieving a good balance between computational stability and efficiency [30].

Particle distribution in the Bhatnagar-Gross-Krook (BGK)-based, single-relaxation-time LB equation is given by

$$f_i(\mathbf{x}+\mathbf{e}_i \Delta t, t+\Delta t) = f_i(\mathbf{x}, t) - \frac{f_i(\mathbf{x}, t) - f_i^{eq}(\rho, \mathbf{u})}{\tau}, \quad (i = 0, 1, 2 \dots 18) \quad (5.4)$$

where  $f_i(\mathbf{x}, t)$  is the particle-distribution function specifying the probability that fluid particles at lattice location  $\mathbf{x}$  and time  $t$  travel along the  $i^{th}$  direction;  $\mathbf{e}_i$  is the lattice velocity vector corresponding to direction  $i$ , defined as:

$$\begin{aligned} \mathbf{e}_0 &= (0, 0, 0), \mathbf{e}_1 = (1, 0, 0)c, \mathbf{e}_2 = (-1, 0, 0)c \\ \mathbf{e}_3 &= (0, 1, 0)c, \mathbf{e}_4 = (0, -1, 0)c, \mathbf{e}_5 = (0, 0, 1)c, \mathbf{e}_6 = (0, 0, -1)c \\ \mathbf{e}_7 &= (1, 1, 0)c, \mathbf{e}_8 = (-1, 1, 0)c, \mathbf{e}_9 = (1, -1, 0)c, \mathbf{e}_{10} = (-1, -1, 0)c \\ \mathbf{e}_{11} &= (0, 1, 1)c, \mathbf{e}_{12} = (0, -1, 1)c, \mathbf{e}_{13} = (0, 1, -1)c, \mathbf{e}_{14} = (0, -1, -1)c \\ \mathbf{e}_{15} &= (1, 0, 1)c, \mathbf{e}_{16} = (-1, 0, 1)c, \mathbf{e}_{17} = (1, 0, -1)c, \mathbf{e}_{18} = (-1, 0, -1)c \end{aligned}$$

where  $c = \Delta x / \Delta t$ , in which  $\Delta x$  is the lattice spacing and  $\Delta t$  is the time step;  $\tau$  is the dimensionless relaxation time related to kinematic viscosity by  $\nu = (2\tau - 1)\Delta x^2 / 6\Delta t$ ;  $f_i^{eq}(\rho, \mathbf{u})$  is the equilibrium distribution function selected to recover the macroscopic Navier-Stokes equations and given by

$$f_i^{eq}(\rho, \mathbf{u}) = \omega_i \rho \left[ 1 + \frac{3\mathbf{e}_i \cdot \mathbf{u}}{c^2} + \frac{9(\mathbf{e}_i \cdot \mathbf{u})^2}{2c^4} - \frac{3\mathbf{u}^2}{2c^2} \right] \quad (5.5)$$

where  $\omega_i$  is the weight coefficient calculated as:

$$\omega_i = \begin{cases} 1/3 & i = 0 \\ 1/18 & i = 1 \dots 6 \\ 1/36 & i = 7 \dots 18 \end{cases}$$

The macroscopic fluid density and velocity are calculated with the following two equations:

$$\rho = \sum_{i=0}^{18} f_i \quad (5.6)$$

and

$$\mathbf{u} = \frac{\sum_{i=0}^{18} f_i \mathbf{e}_i}{\rho} \quad (5.7)$$

Fluid pressure is calculated using  $p = c_s^2 \rho$ , where  $c_s$  is the speed of sound. In the LB D3Q19 model,  $c_s^2 = c^2/3$ .

In practice, two-relaxation-time and multi-relaxation-time LB schemes have been developed to mitigate numerical instability in simulating high-Re-number flows and avoid nonlinear dependency of numerical error on fluid viscosity [31, 32]. In this study, we replaced the BGK-based collision operator with a two-relaxation-time collision operator and then selected the optimal combination of the symmetric and asymmetric eigenfunctions [33] in order to reduce numerical errors resulting from the bounce-back boundary condition.

For fluid flow simulation in the Darcy regime, we imposed a periodic boundary condition with a constant pressure difference,  $\Delta P$ , in the longitudinal direction and no-slip boundary conditions on the four lateral sides and interior solid surfaces [27, 34]. In this study, the main, longitudinal flow directions are the x and y directions (note, in two separate 1D flow models). Because the particle packing is isotropic, permeabilities measured in these two directions should be the same or very close. The  $Re$  number was always much smaller than one to ensure that the macroscopic flow was well within the

Darcy regime. A small pressure difference,  $\Delta P$ , generated an adequately small Mach number and density variation, which are necessary for accurate simulation of incompressible flows using the LB method. More details about the LB simulator and associated GPU optimization can be found in our previous papers [27, 29].

At the continuum medium scale, the Darcy velocity,  $\mathbf{v}$ , is calculated by averaging the pore-scale flow velocity,  $\mathbf{u}$ , of each lattice node in the pore space throughout the entire computational domain, at steady-state flow. One can calculate the permeability tensor using the Darcy's law:

$$\mathbf{v} = -\frac{1}{\mu} \mathbf{k} \cdot \nabla p \quad (5.8)$$

where  $\mathbf{v} = [v_x, v_y, v_z]^T$  is the Darcy velocity,  $\mathbf{k} = k_{ij} (i, j = x, y, z)$  is the permeability tensor, with  $i$  being the flow direction and  $j$  being the pressure gradient direction,  $\nabla p$  is the pressure gradient, and  $\mu$  is the dynamic viscosity of the fluid. The principal components of the permeability tensor are noted as  $k_{xx}$ ,  $k_{yy}$ , and  $k_{zz}$ . Since the principal directions of the permeability tensor in this study are the same as the principal coordinate directions, the off-diagonal elements in the permeability tensor are zero, written as  $k_{ij} = 0 (i \neq j)$ . More details about LB simulations of Darcy flows in porous media can be found in our recent publications [3, 27].

#### 5.2.4 Proppant embedment

A series of ballpoint penetrometer experiments was conducted on tight sandstone samples, aiming to obtain the load-embedment correlation for estimating fracture closure distance due to proppant embedment. The sandstone has a Brinell hardness number

(BHN) of 35 kg/mm<sup>2</sup>. Specifically, the penetrometer experiments were conducted in the laboratory using a nanoindenter equipped with a tungsten carbide ball. Huitt and McGlothlin [35] developed a semi-empirical correlation to relate mechanical loading exerted on a spherical particle to its embedment depth on rock surface. The model is based on the assumption that embedment depth is less than the particle radius [36]. This assumption was confirmed in our ballpoint penetrometer experiments, because of the high hardness of the tight sandstone resulting from vertical overburden compaction and intergranular cements. Laboratory data indicated that the load and embedment can be correlated as:

$$\frac{d}{D} = B^{1/2} \left( \frac{L}{D^2} \right)^{m/2} \quad (5.9)$$

where  $d$  is diameter of embedment impression on fracture wall (m),  $D$  is diameter of proppant particle (m),  $L$  is load on the proppant particle (N), and  $B$  and  $m$  are fitting coefficients, which are characteristics of the rock and obtained by fitting experimental data. Based on Eq. (1) and geometry analysis, the fracture width that takes into account proppant embedment is calculated as [35, 37]:

$$W_f = D \left[ 1 - B \left( \frac{P_e}{nD^2} \right)^m \right]^{1/2} \quad (5.10)$$

where  $W_f$  is the fracture width (m),  $P_e$  is load carried by the proppant particles per unit area (Pa), and  $n$  is the number of proppant particles per unit area (m<sup>-2</sup>). In this study, effective stress on the particles in direct contact with the fracture walls was determined using DEM simulation and then imported into Eq. (10) to calculate the fracture closure distance resulting from proppant embedment.

### 5.3 Simulation Procedures

In this work, an integrated simulation approach was developed to understand the performance of mixing proppants of various sizes, types, and mass ratios in a proppant pack, which is subjected to increasing effective stresses and has a proppant concentration ranging from a partial-monolayer structure to a multilayer structure. First, the proppant load-embedment relationship was constructed based on a semi-empirical correlation, which related mechanical loading exerted on a spherical particle to its embedment depth on rock surface [35, 37]. Second, the DEM numerical simulation was carried out to determine proppant stress, deformation, and rearrangement within a proppant assembly that was sandwiched by two fracture walls and subjected to compressive stress (i.e., closure pressure). In a multilayer proppant assembly, compaction and rearrangement of proppant particles lead to reduction of the pore space between particles, which contributes to fracture width reduction (i.e., fracture closure). Third, effective stress on the particles in direct contact with the fracture walls was extracted. The stress information, combined with the load-embedment correlation, was used to determine extra fracture closure distance resulting from proppant embedment. The updated proppant pore structure in the steady state was imported into a LB simulator [26, 29] as interior boundary conditions to determine fracture permeability and conductivity. In this study, fines migration and potential influence on proppant pack permeability is neglected during fluid flow through proppant packs. Figure 5.1 demonstrates a schematic workflow. This workflow was repeated on proppant assemblies having various proppant concentrations, leading to a fracture conductivity (md-ft) versus proppant concentration (lb/ft<sup>2</sup>) curve.

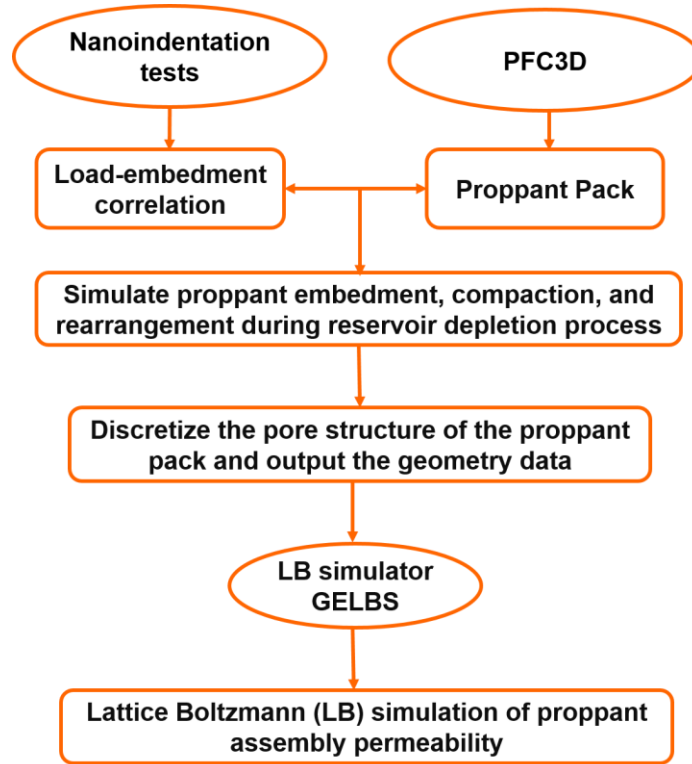


Figure 5.1. An integrated simulation workflow for calculating proppant compaction, embedment, as well as the influence on fracture conductivity.

In order to validate the integrated simulation workflow, proppant pack conductivity as a function of increasing proppant concentration was simulated and then compared with laboratory data [38]. In the laboratory, the test was conducted on 20/40-mesh-size proppant particles to obtain the fracture conductivity under varying proppant concentrations, ranging from a partial-monolayer concentration of  $0.02 \text{ lb/ft}^2$  to a multilayer concentration of  $2 \text{ lb/ft}^2$ . In the DEM simulations, heterogeneous proppant particles having a uniform distribution between mesh 40 (0.42 mm) and mesh 20 (0.84 mm), were generated at various proppant concentrations. The computational domain dimensions in the x-y plane (the plane parallel to fracture face) were  $10 \text{ mm} \times 10 \text{ mm}$ . The fracture was then closed in the z-direction (the direction normal to fracture face) at a constant velocity, which was adequately slow to avoid rapid surge of effective stress

between proppant particles and to allow fluid within the pore space to flow away in the lateral (x-y) directions. In this way, the system was in a pseudo-steady state, where the transient pore pressure changed but the effects of transient stress variation on the proppant particles were negligible [3]. The processes of proppant particle compression, movement, and re-arrangement were simulated with the PFC code. The embedment depth of proppant particles into the fracture walls were determined using the load-embedment correlation [37]. In this study, ceramic proppants with strong mechanical properties (e.g., stiffness and density) [39], mixed sands which have a relative low stiffness, were mixed to study the impact of mixed proppants of different sizes and types on the resulted fracture conductivity. Corresponding pore structure of the proppant pack was discretized at a resolution of 0.02 mm/pixel in all directions and then imported into the GELBS code as interior and boundary conditions to simulate proppant pack permeability in the lateral (x-y) directions.

With the target of investigating the effect of proppant mixtures on the evolution of proppant pack conductivities, proppant packs with proppant mesh-size 20, mesh-size 40, mesh-size 20/40 (mass ratio 5:5) were first generated with varying proppant concentrations, ranging from a partial-monolayer concentration of 0.02 lb/ft<sup>2</sup> to a multilayer concentration of 2 lb/ft<sup>2</sup>. The computational domain has extensions of 10 mm × 10 mm in the x-y plane (the plane parallel to fracture face). The effective stress was 2,000 psi. Then the validated model was applied to investigate the propped fracture conductivity for different mass mixing ratios, such as 1:9, 2:8, 3:7, 4:6, and 5:5, with different proppant mesh sizes, effective stresses, and proppant areal concentrations (ranging from partial monolayer to multilayer). In the end, the mixtures of sand and



ceramic proppants with different mesh-size ratios under different proppant concentrations and effective stresses were tested. In this study, proppants of different sizes and types generated by PFC3D were mixed uniformly by weight throughout the proppant pack.

## 5.4 Simulation Results

### 5.4.1 Validation with embedment test

The penetrometer experimental data from three nanoindentation tests were plotted in the form of  $d/D$  versus  $L/D^2$  for correlation analysis, as illustrated in Figure 5.2. The tests were conducted on three samples from the same tight sandstone formation. All three tests demonstrated similar rock properties and showed strong power-law correlations between  $d/D$  and  $L/D^2$ . The values of  $m$  and  $B$  from Test 1 were determined as 0.555 and  $2.92 \times 10^{-5}$ , respectively. These values were used in Eq. (10) to determine the embedment depth. Note, here we assumed that the embedment depth is less than the particle radius.

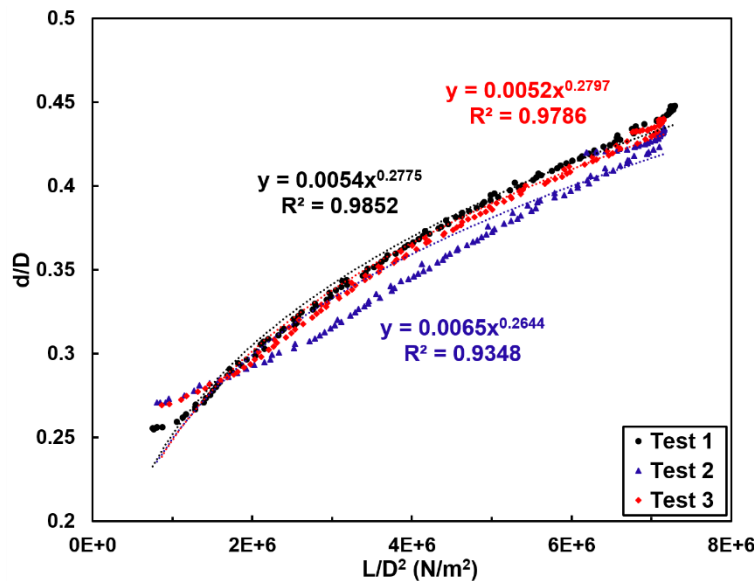


Figure 5.2. Correlation between  $d/D$  and  $L/D^2$  based on the laboratory penetrometer experiments; the tests were conducted on three samples from the same tight sandstone formation.

Figure 5.3 illustrates the comparison between the simulation-predicted and laboratory-measured fracture conductivity versus proppant concentration curves. In the laboratory test, 20/40-mesh-size heterogeneous proppant particles, ranging from a maximum multilayer concentration 2 lb/ft<sup>2</sup> down to a partial monolayer concentration 0.02 lb/ft<sup>2</sup>, were placed between sandstone samples [38]. In the numerical simulation, the proppant diameter was heterogeneous with a uniform distribution between mesh 40 (0.42 mm) and mesh 20 (0.84 mm), leading to a mean diameter of 0.63 mm. Both the simulation-predicted and laboratory-measured conductivity curves were measured under effective stress of 1,000 psi. The conductivity curves predicted by numerical models were in good agreement with experimental data. The data showed the lower concentrations of partial monolayer proppant packs provided higher fracture conductivities than those of multilayer proppant packs. In the numerical simulation, the particle diameter strictly followed a uniform distribution from mesh 20 to mesh 40. However, the proppant particles used in the experiment did not necessarily follow the uniform distribution. This uncertainty in the heterogeneous particle size distribution may be responsible for the observed difference between the laboratory measured and simulation predicted conductivity curves.

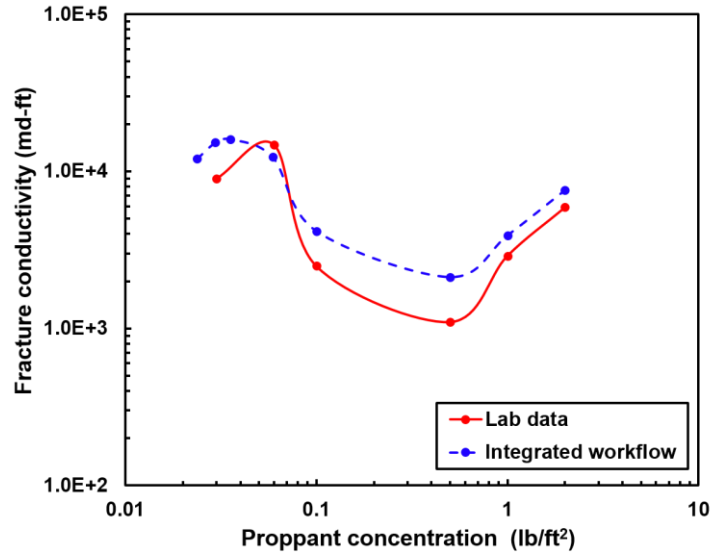


Figure 5.3. Comparison between the simulation predicted and laboratory result at 1,000 psi closure pressure; the laboratory experimental data are taken from Brannon et al. [38]

#### 5.4.2 Effects of proppant concentration

Figure 5.4 illustrates LB-simulated pressure distributions within a 2D cross section cut along the x-y plane at the fracture center for three proppant packs with the proppant concentration of 2 lb/ft<sup>2</sup>. The pressure is presented in the LB unit. In Figure 5.4a, the proppant pack was generated with mesh-size-20 (0.84mm) particles; in Figure 5.4b, the proppant pack was generated with mesh-size-40 (0.42mm) particles; and in Figure 5.4c, the proppant pack was generated with mesh-size-20/40 particles. It can be seen that the two mesh-size proppant particles in Figure 5.4c were generated uniformly in the proppant pack with mixing mass ratio of 1:1.

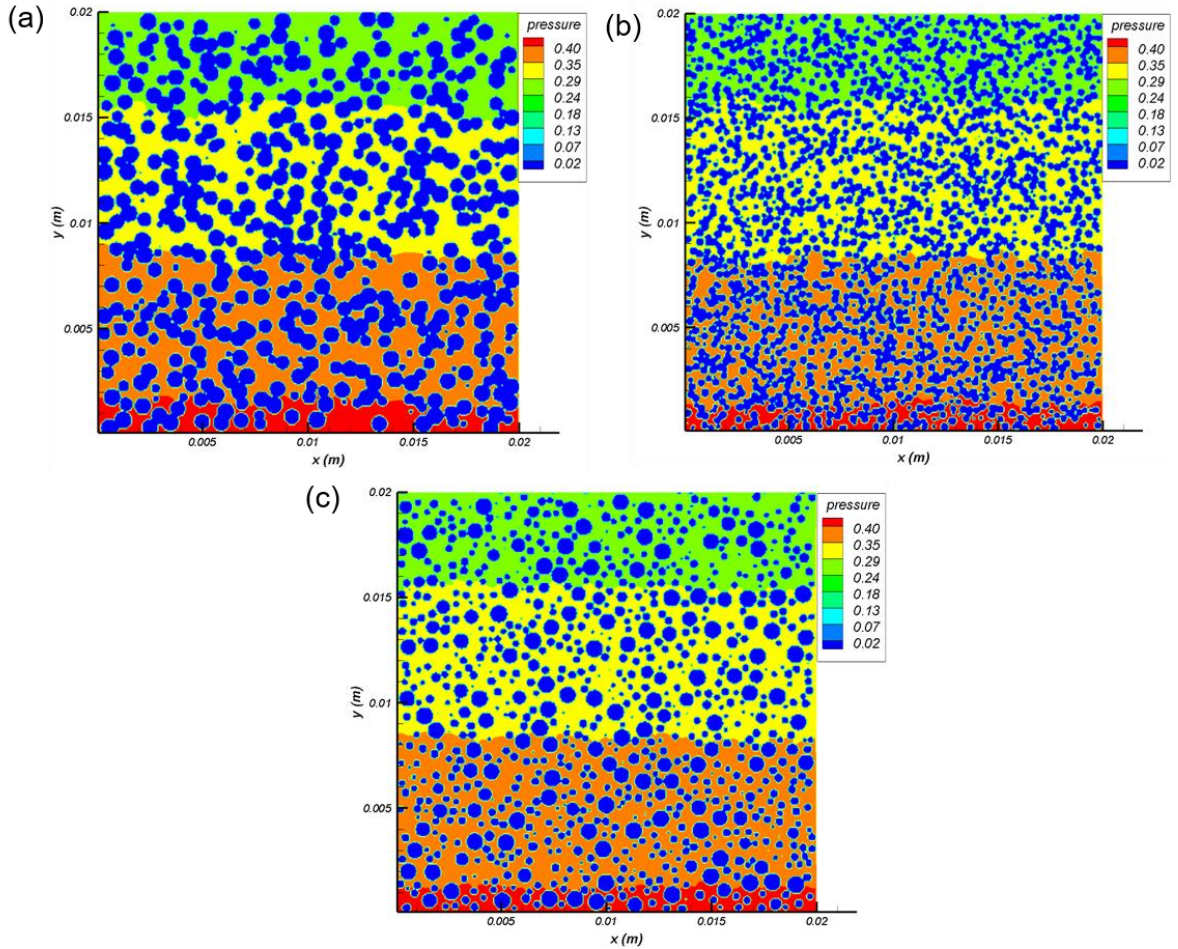


Figure 5.4. LB-simulated pressure distributions within the pore space of proppant assemblies with (a) mesh-size-20 particles; (b) mesh-size-40 particles; and (c) mesh-size-20/40 (mixing weight ratio 1:1) particles.

Figure 5.5 presents the development of fracture conductivity as a function of proppant concentration under effective stress of 2,000 psi. The fracture conductivity versus proppant concentration curves were predicted with numerical simulation following three proppant sizes (mesh-size-20, mesh-size-40, mesh-size-20/40 (mass ratio 1:1)) under various proppant concentrations ranging from 0.02 lb/ft<sup>2</sup> to 2 lb/ft<sup>2</sup>, as demonstrated in Figure 5.5. The green dotted curve was linearly interpolated from mesh-20 and mesh-40 curves. For all curves, it can be seen that the fracture conductivity first increased, then

decreased, and then increased again. Fracture conductivity reached the local maximum when proppant concentration was 0.05 lb/ft<sup>2</sup>, which is the optimal partial-monolayer proppant concentration, and reached the trough at the full monolayer concentration of 0.2 lb/ft<sup>2</sup>. Then the fracture conductivity increased again with increasing proppant concentrations when the proppant pack developed to multilayers. This is because, in the partial-monolayer range, the fracture permeability is controlled by both the fracture width and fracture porosity. The competition between these two factors leads to a non-monotonic shape of fracture conductivity curve. Under the same proppant pack concentration, the proppant pack with mesh-size-40 has lowest fracture conductivity, while the proppant pack with mesh-size-20 has highest fracture conductivity. In the oil industry, it is widely accepted to use linear interpolation to find the 20/40-mixture conductivity curve based on the conductivity curves of uniform mesh-20 and mesh-40 particle sizes. Our simulations showed that, the mixing mesh-size-20/40 fracture conductivities were lower than the linear interpolation conductivities from mesh-size-20 and mesh-size-40 curves. In other words, the permeability of a mixture comprised of 50% (by weight) of mesh-size-20 and 50% of the mesh-size-40 is not in the halfway between the permeabilities of the single components. This indicates that the conductivity of mixed proppant pack is not simply the mathematic average of conductivities of two proppant packs with uniform proppant sizes.

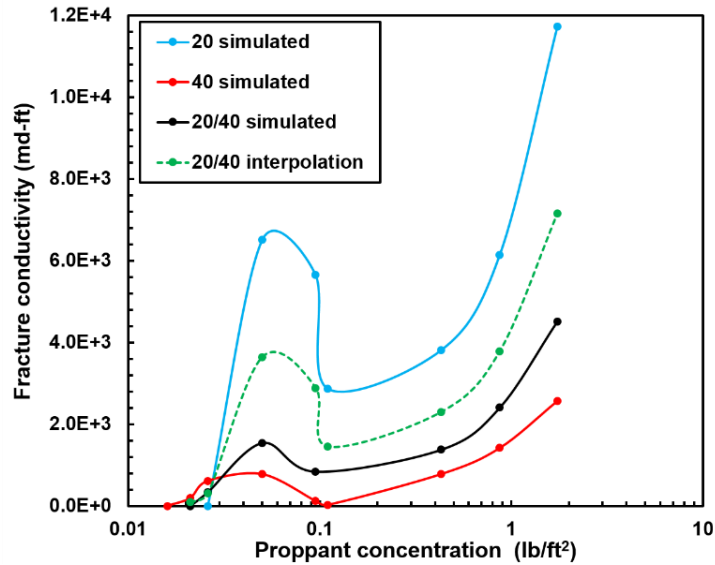


Figure 5.5. Development of fracture conductivity as a function of proppant concentration under effective stress of 2,000 psi; the blue curve was from proppant packs with mesh size 20; the red curve was from proppant packs with mesh size 40; the black curve was from proppant packs with mesh size 20/40 (mass ratio 1:1); the green curve was from the linear interpolation of blue curve and red curve.

### 5.4.3 Effects of loading stress

Figure 5.6 illustrates four proppant packs with the proppant concentration of 0.1 lb/ft<sup>2</sup>, 0.3 lb/ft<sup>2</sup>, 1 lb/ft<sup>2</sup>, and 2 lb/ft<sup>2</sup>, respectively. The proppant particles in each proppant pack were generated with mesh-size-20/40 (mass ratio 1:1). The applied stress on the four proppant packs was slowly increased up to 6,000 psi at a constant loading velocity, mimicking the laboratory test in which the fluid within the pore space is allowed to flow away in the lateral direction, and rapid surge of effective stress between proppant particles can be avoided [3].

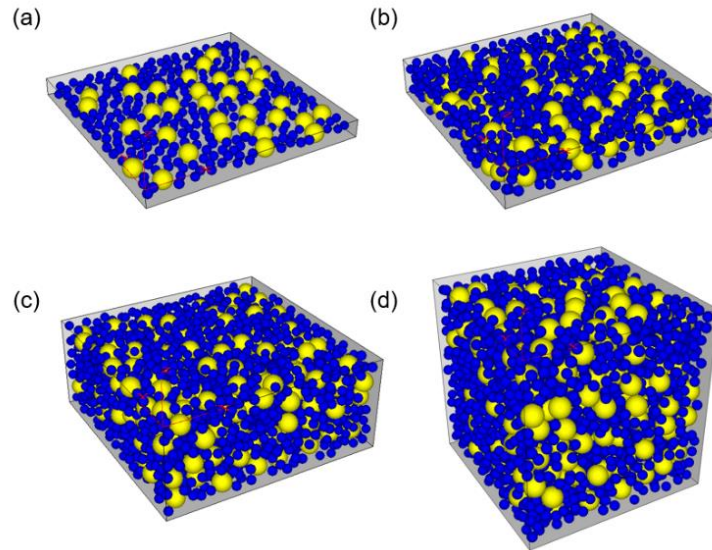


Figure 5.6. Proppant packs were generated with proppant concentration of (a) 0.1 lb/ft<sup>2</sup>, (b) 0.3 lb/ft<sup>2</sup>, (c) 1 lb/ft<sup>2</sup>, and (d) 2 lb/ft<sup>2</sup>. The proppant packs were generated with mesh-size-20/40 (mass ratio 1:1).

Figure 5.7 illustrates fracture conductivity as a function of proppant concentration for proppant packs with mesh size 20/40 (mass ratio 1:1) under three effective stresses (2,000, 4,000, and 6,000 psi). With proppant concentration increasing, the fracture conductivity increased, decreased, and then increased again when proppant packs developed from partial monolayers to multilayers. The local maximum (when proppant concentration is lower than 0.1 lb/ft<sup>2</sup>) on the conductivity curve is referred to as the “optimal partial-monolayer fracture conductivity” (OPMFC). It can be seen that the OPMFC decreased with increasing effective stress, because the permeability and width of fracture decreased under higher loading stress. In the meanwhile, the partial-monolayer proppant concentration at OPMFC increased with increasing loading stress, because more proppant particles were required to keep the fracture open under higher effective stress. Therefore, it is expected that the OPMFC will converge toward the full-monolayer proppant concentration when the loading stress is sufficiently high, because the

embedment depth is close to the particle radius. In this scenario, the local maximum in the fracture conductivity versus proppant concentration curve will vanish and a multilayer proppant pack is desired over a partial-monolayer proppant pack.

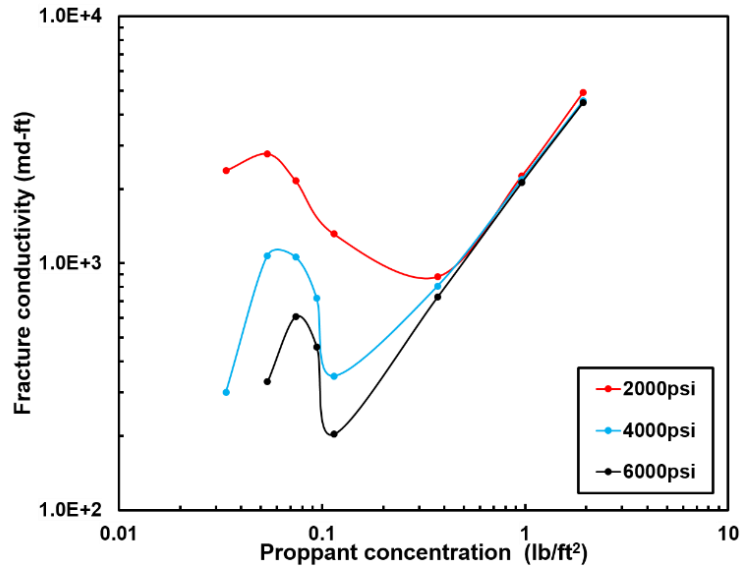


Figure 5.7. Fracture conductivity as a function of proppant concentration for proppant packs with mesh size 20/40 (mass ratio 1:1) under various effective stresses

#### 5.4.4 Effects of proppant size mixture

Figure 5.8 illustrates fracture conductivity as a function of proppant concentration under three effective stresses. The proppant packs were generated with 20/40-mesh-size and different mass mixing ratios, such as 1:9, 2:8, 3:7, 4:6, and 5:5. It can be seen that, the fracture conductivity decreased with increasing effective stress due to the reduced fracture width and permeability. The proppant packs with mass ratio 5:5 had highest fracture conductivity for all three effective stresses. Before proppant packs developed to a full monolayer, large size proppant concentration had a larger influence on the fracture conductivity. However, when the proppant packs developed to multilayers, the differences in fracture conductivities between different proppant mixtures became



smaller. When proppant packs develop to multilayers, the proppant pack is now a fully-packed porous medium, its porosity and permeability are primarily controlled by the average grain and pore throat size. As the mixed proppants in the proppant pack are close in mesh-size, the changes in permeability and fracture width among different mixing ratios are similar, resulting in smaller differences in proppant pack conductivities. The performance of the mixture of mesh-20 and mesh-40 proppants indicates that the choice between mesh-size-20/40 different mass ratios appears not to be a significant factor in hydraulic fracturing design.

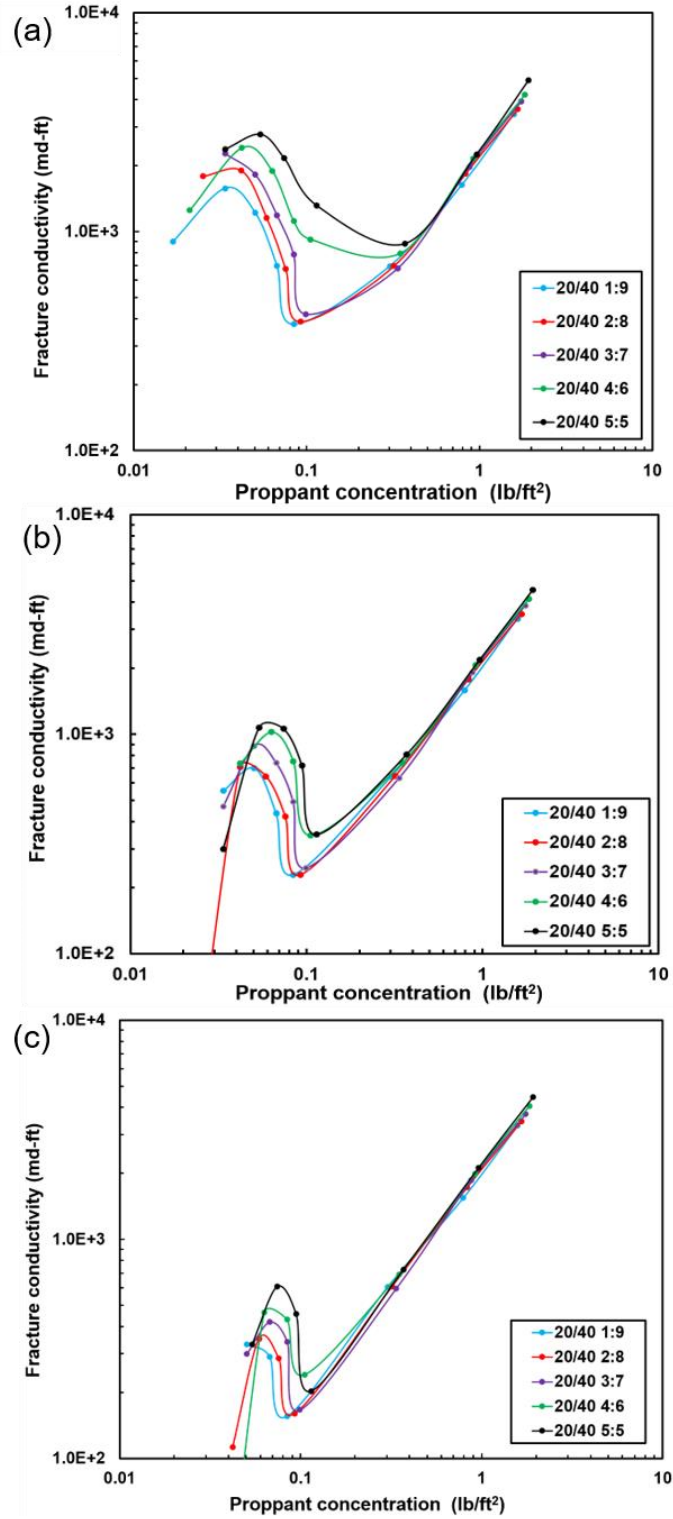


Figure 5.8. Fracture conductivity as a function of proppant concentration for proppant mixtures with different mass ratios under effective stress of (a) 2,000 psi, (b) 4,000 psi, and (c) 6,000 psi

In order to quantify the difference of the flow velocity magnitudes among proppant packs with different mixing ratios, the pore scale velocities on a voxel-by-voxel basis, i.e., at every node in the LB simulation, were examined and, then the flow velocity distribution probability density functions (PDFs) were constructed. The PDFs of pore velocity distributions for proppant packs with proppant concentrations of 2 lb/ft<sup>2</sup> under effective stress of 6,000psi were plotted in Figure 5.9. The proppant pack with mesh size 20/40 mixing ratio 1:9 had highest PDF of low-range velocities and smallest PDF of high-range velocities. However, the velocity variances between different mixing ratios became less significant in high-velocity regions. With the same pressure gradient, the similar velocities led to similar permeabilities for proppant packs with different mixing ratios, as confirmed by smaller differences in proppant pack conductivities when proppant develops to a multilayer assembly.

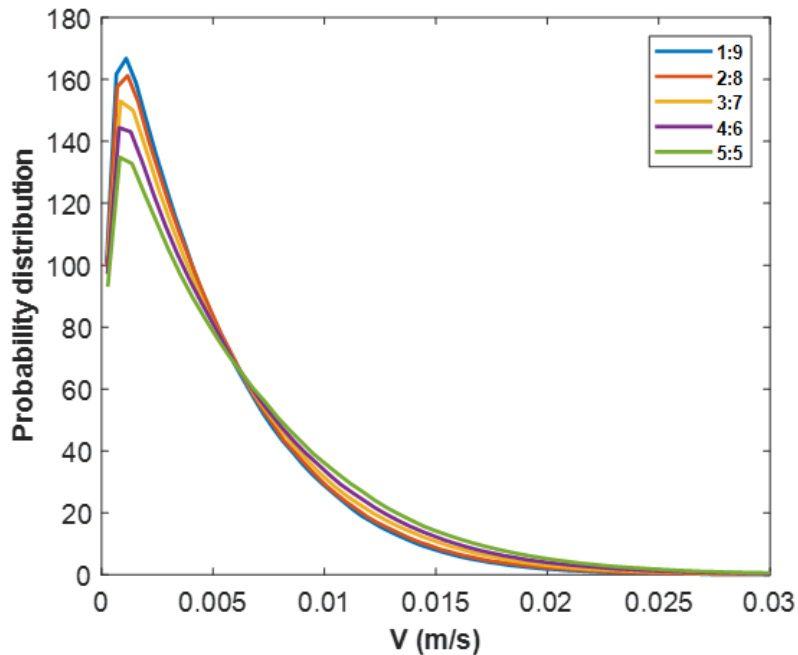


Figure 5.9. Probability density functions (PDFs) of overall pore velocity for proppant packs with proppant concentrations of 2 lb/ft<sup>2</sup> under effective stress of 6,000psi

Figure 5.10 illustrates LB-simulated flow-velocity-magnitude distributions within 2D cross-sections cut along the x-y plane at the fracture center for two proppant packs with the proppant concentration of 2 lb/ft<sup>2</sup>. The flow-velocity-magnitude is presented in the LB unit. The proppant particles in proppant packs were generated following mesh-size-20/40 and -20/100 (mass ratio 5:5), respectively. The effective stress on the proppant pack was slowly increased up to 6,000 psi at a constant mechanical loading velocity. It can be seen that the mesh-size-100 (0.149mm) is very small compared to the mesh-size-20 (0.84mm), which leads to large porosity and permeability reduction when proppant packs are fully packed. In Figure 5.10a, there existed multiple high-flow-velocity regions within the pore space, which suggested relatively good connectivity of the pore space. Conversely, in Figure 5.10b, the pore space connectivity was significantly reduced, which suggested that the very fine mesh-size proppants could block the flow channels, and consequently reduce the proppant pack permeability. Furthermore, under the same effective stress, the smaller particles moved relatively more easily and can be pushed into pore space between larger particles, giving rise to smaller porosity and permeability.

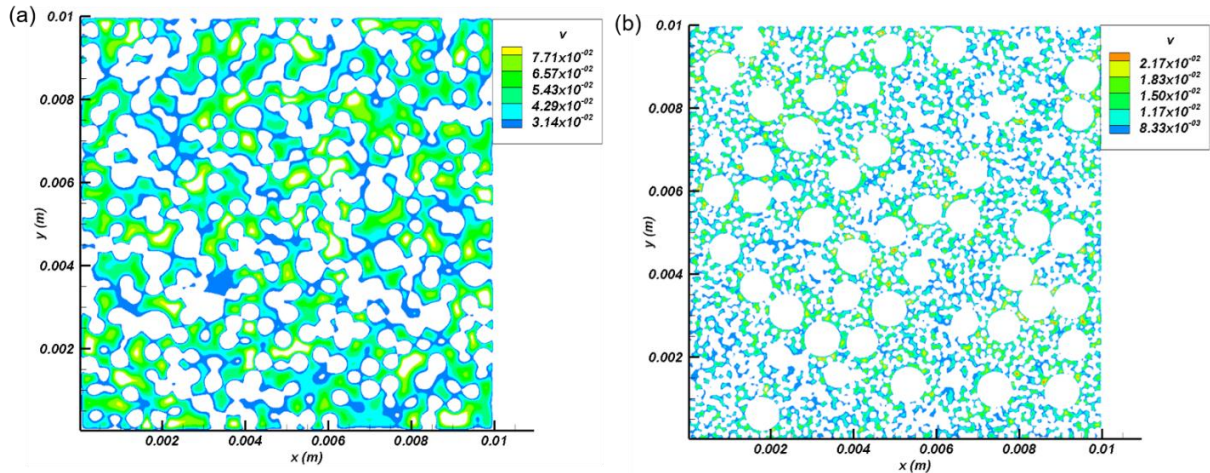


Figure 5.10. LB-simulated flow-velocity-magnitude distributions within the pore space of the proppant assemblies (a) mesh-size-20/40 particles; (b) mesh-size-20/100 particles (mixing mass ratio 1:1); the void space represents proppant particles

In order to investigate how the proppant packs perform when mixed with a much finer proppant mesh size, a mixture of mesh-size-20 and -100 under different proppant concentrations and effective stresses were tested. Figure 5.11 illustrates fracture conductivity as a function of proppant concentration for proppant packs with mesh size 20/100 (mass ratio 1:1) and mesh-size-100 under three effective stresses (2,000, 4,000, and 6,000 psi). As mentioned above, for the mesh-size-20/100 proppant packs subjected to the same effective stress loading, the smaller mesh-size-100 proppant pack resulted in larger compression distance and permeability reduction, which gave rise to smaller fracture conductivity (in comparison with proppant packs with mesh-size-20/40). When proppant packs developed to multilayers, the conductivities for uniform mesh-size-100 and mesh-size-20/100 proppant mixture were very close. The very fine mesh size has the greatest influence on fracture conductivity. This indicates that the fine mesh size dominates the fracture conductivity, because fine size particles invade and occupy pore

space more easily. However, when proppant pack structure is a monolayer, the larger mesh-size-20 plays a big role in local optimal fracture conductivity evolution.

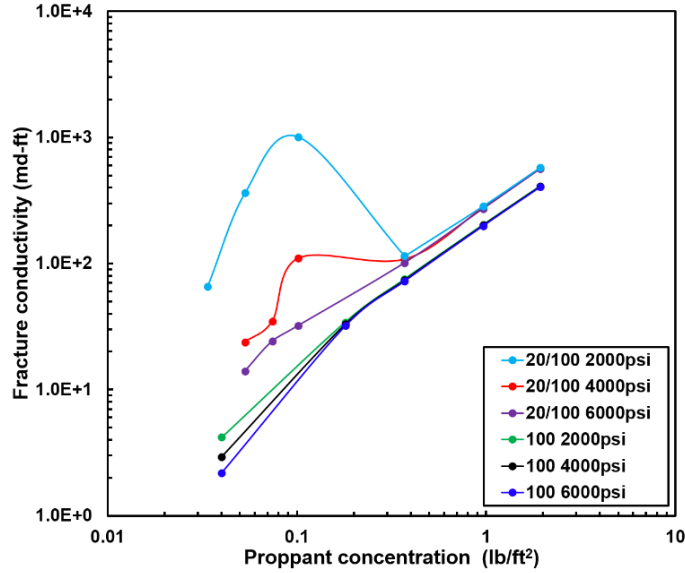


Figure 5.11. Fracture conductivity as a function of proppant concentration for proppant packs with mesh-size-20/100 (mass ratio 1:1) and mesh-size-100 under various effective stresses.

#### 5.4.5 Effects of proppant type mixture

Figure 5.12 illustrates LB-simulated flow-velocity-magnitude distributions within the 2D central cross sections of proppant packs under effective stress of 6,000 psi. Flow-velocity magnitude was presented in the LB unit. The proppant packs were generated with mesh-size-20/40 sand and ceramic mixtures and with a proppant concentration of 2 lb/ft<sup>2</sup>. In the top panel, each proppant pack was generated following mesh size 20/40 with mass ratio 5:5; in the bottom panel, each proppant pack was generated following mesh size 20/40 with mass ratio 1:9. For each panel, the proppant packs were generated with sand and ceramic mixture ratios of 25%:75%, 50%:50%, and 75%:25%, respectively. With the increasing concentration of sand, the high-flow-velocity regions within the pore space

reduced, which indicated that the proppant assembly compaction was nontrivial and pore-space connectivity was consequently reduced. It can also be seen that, the proppant packs generated with more large particles had more preferential flow paths, which indicated that the proppant packs mixed with more large particles provided better support to open the fracture.

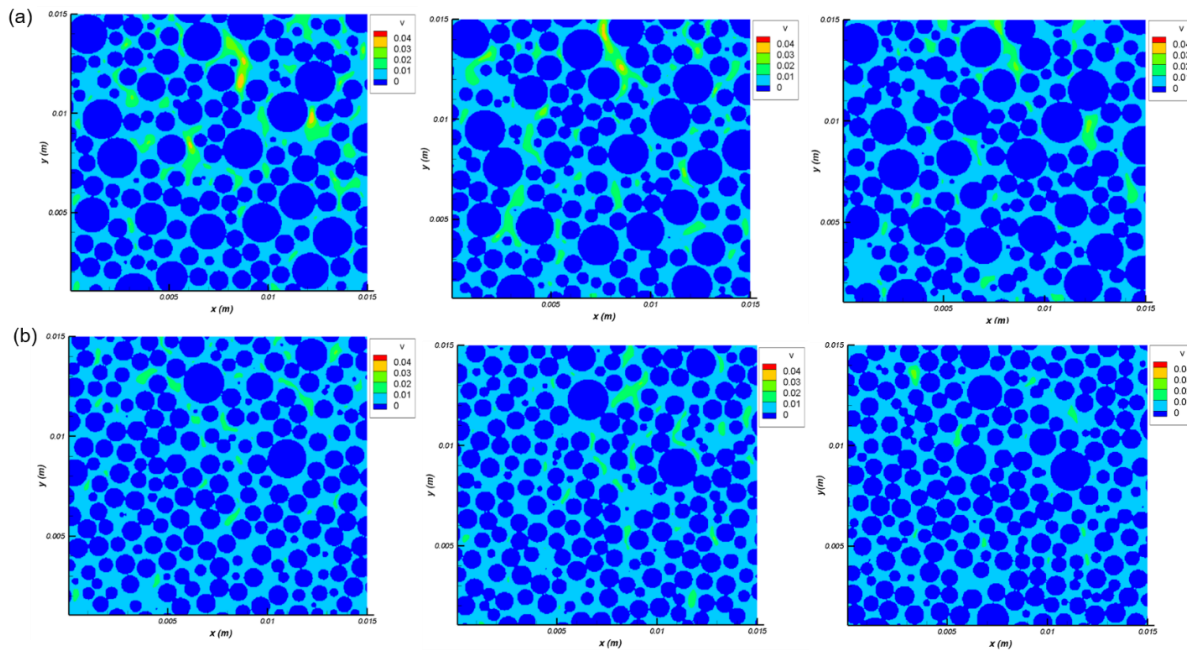


Figure 5.12. LB-simulated flow-velocity-magnitude distributions within the pore space of the proppant assemblies under effective stress of 6,000 psi; proppant packs were generated following mesh-size-20/40 ceramic proppants and sand mixtures with a proppant concentration of 2 lb/ft<sup>2</sup>; the proppant packs were generated with mesh size ratios of (a) 5:5 (20:40) in the top panel and (b) 1:9 (20:40) in the bottom panel; from left to right, the sand and ceramic mixing ratios are 25%:75%, 50%:50%, and 75%:25%, respectively; the green color regions indicate high-flow-velocity regions.

With the target of investigating the proppant pack performance at various sand and ceramic proppant combinations, the blends of sand and ceramic proppants under different proppant concentrations and effective stresses were tested. Figure 5.13 shows fracture conductivity as a function of proppant concentration under various effective stresses and sand/ceramic mixing ratios. As expected, the proppant pack conductivity decreased with

increasing effective stress for three sand/ceramic proppant mixtures. Under the same effective stress, blends of 25% sand with 75% ceramic proppants provided higher conductivities relative to 75% sand mixed with 25% ceramic proppants. When proppant packs were subjected to 2,000 psi effective stress, the proppant pack conductivity differences between three sand/ceramic proppant mass ratios were relatively small. However, with the increase of effective stress, the increasing composition of sand proppants highlights the difference in proppant pack conductivity. The proppant pack conductivity for sand/ceramic mixing ratio 75%:25% had a more significant drop than the proppant pack with sand/ceramic mixing ratio 25%:75%. This indicates that proppant packs mixed with larger amount of sand cannot maintain sufficient fracture conductivity when subjected to higher effective stresses.

Figure 5.13 also illustrates proppant pack performance between uniform ceramic proppant and sand/ceramic proppant blends. As expected, the proppant pack with uniform ceramic proppants has highest proppant pack conductivity under three effective stresses. With the increase of effective stress, fracture conductivity difference became more pronounced with increasing sand/ceramic mixing ratios. This is because, when lower strength proppants were subjected to higher effective stress, they failed to provide enough support to the fracture, leading to a larger fracture closure and subsequent fracture conductivity reduction. Under the same effective stress, the conductivity difference for proppant size mixtures (with same ceramic/sand mixing ratio) was less pronounced compared to proppant type mixtures (with same 20/40-mesh size mixing ratio), which may suggest that proppant size combination is less pronounced than proppant type combination. The proppant pack with uniform ceramic proppants



following 20/40-mesh size ratio 1:9 has the proppant pack conductivity close to the proppant pack with sand/ceramic mass ratio 25%:75% following 20/40-mesh size ratio 5:5. This indicates that using larger size proppants helps maintain the proppant pack conductivity when mixed with lower strength proppants. This study also shows that higher concentrations of more conductive proppant (ceramic proppant) can help maintain fracture conductivity even under higher effective stress. It should be noted that, in this study, proppant crushing is not considered. High-strength ceramic proppant can withstand stress of higher than 10,000 psi [5], while sand can be crushed at around 6,000 psi effective stress [40]. Under higher effective stress, the lower strength proppants will dominate the fracture conductivity if their mixing ratio is high.

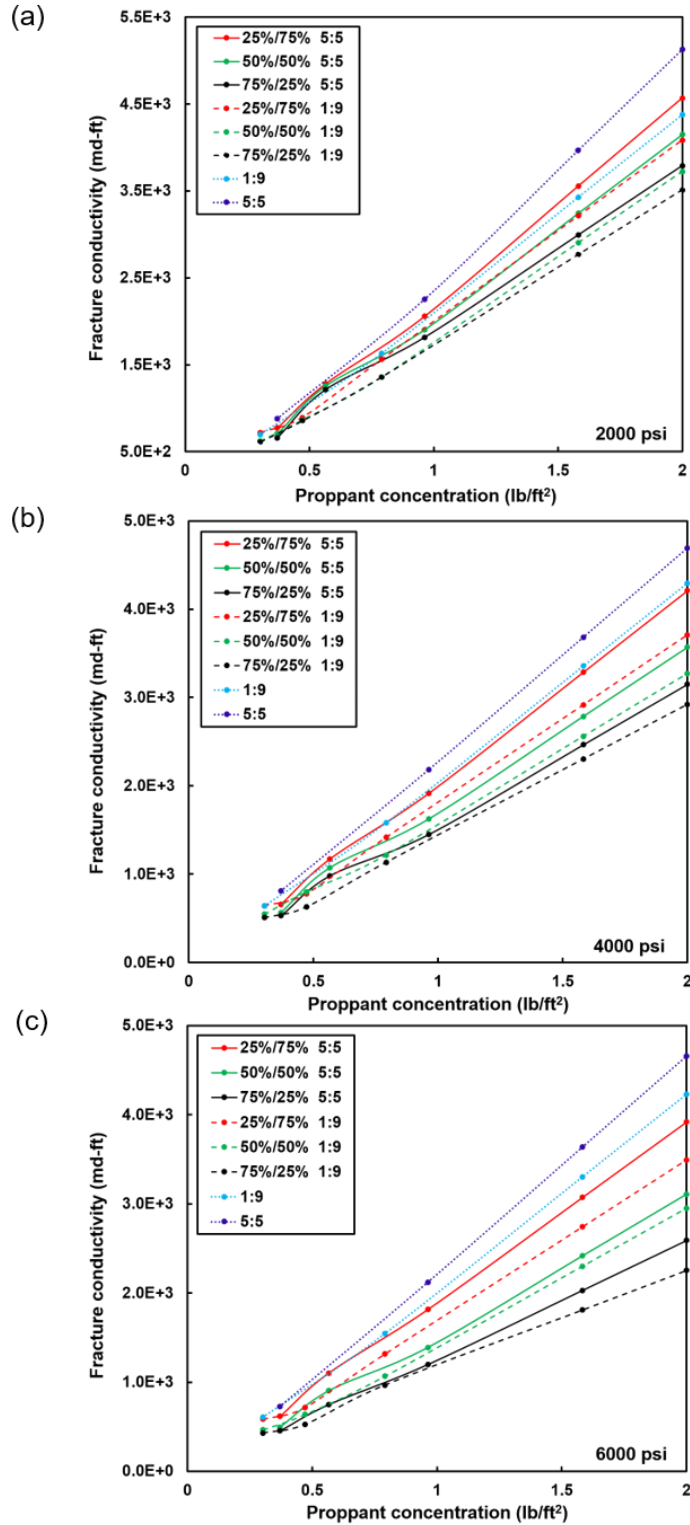


Figure 5.13. Fracture conductivity as a function of proppant concentration for proppant packs following mesh-size-20/40 with different sand/ceramic mixing ratios (1:9 and 5:5) under effective stress (a) 2,000 psi, (b) 4,000 psi, and (c) 6,000 psi; the dark and light

blue dot lines represent ceramic proppant packs generated following 20/40-mesh size ratio 5:5 and 1:9, respectively; the solid lines represent proppant packs generated following 20/40-mesh size ratio 5:5 with three sand/ceramic mixtures; the dashed lines represent proppant packs generated following 20/40-mesh size ratio 1:9 with three sand/ceramic mixtures.

## **5.5 Conclusions and Discussions**

In this study, an integrated numerical simulation workflow was developed to investigate the potential effect of proppant mixture on fracture conductivity. The integrated simulation workflow was first verified by comparing numerical simulation results with laboratory data. The comparison between the simulation-predicted and laboratory-measured fracture conductivity versus proppant concentration curves shows an overall good agreement. Then simulations were designed to investigate how the proppant pack perform when mixing particles with different size and type ratios. The choice between mesh-size-20/40 different mass ratios does not appear to be a significant factor in affecting fracture conductivity. This suggests that mixing of similar proppant sizes has little influence on fracture conductivity. However, proppant packs with mesh-size-20 and -100 proppant mixtures showed much lower fracture conductivities than those with mesh-size-20 and -40 proppant mixtures. This indicates that the fine mesh size proppants dominate the overall fracture conductivity. In addition, the study also indicates that the mixture conductivity cannot be obtained through arithmetically averaging the conductivities from proppant packs with two uniform proppant sizes, and the mixture conductivity is lower than the linearly interpolated conductivity. In the end, fracture conductivity simulations relative to different proppant mesh size and type combinations under various effective stresses and proppant concentrations were measured. Increasing sand concentration decreased the proppant pack conductivity, which may indicate that

selection of proppant type is more important than proppant size when mixing proppants. Increasing larger size proppant composition relative to smaller size proppant helps to maintain fracture conductivity when mixed with lower strength proppants.

It is common that proppants of different sizes and types are often mixed together and incorporated into the pumping schedule in the completion and stimulation designs. The fracture conductivity versus proppant concentration curves reveal the proppant mixture performance under various effective stresses. Mixing proppants with various sizes and types has the potential to influence proppant pack conductivity and reservoir production. Compared to selecting proppant types in the mixture, the choice of proppant mesh size mass ratios has less effect on the overall fracture conductivity. Mixing with mesh-size-100 proppants can reduce fracture conductivity significantly. In the high stress regime, the sand proppants experience substantial crushing, which has not been well studied and requires extensive laboratory experiments and numerical modeling efforts.

## **Nomenclature**

$c$ : Lattice speed

$c_s$ : Speed of sound

$d$ : Diameter of embedment impression on fracture wall

$D$ : Diameter of proppant particle

$e_i$ : Lattice velocity vector

$f_i$ : Particle-distribution function

$F_i^n$  :Normal components of the contact force

$F_i^S$  :Shear components of the contact force

$K^n$  :Normal stiffness at the contact;

$k^S$  :Shear stiffness at the contact

$k$  :Permeability tensor

$L$  :Load on the proppant particle

$n$  :Number of proppant particles per unit area

$P$  : Fluid pressure

$\nabla p$  :Pressure gradient

$\rho$  :Density

$P_e$  :Load carried by the proppant particles per unit area

$\tau$  :Dimensionless relaxation time

$t$  :Time

$\Delta t$  :Time step

$u$  :Flow velocity

$v$  :Darcy velocity

$U^n$  :Contact displacement in the normal direction

$U_i^S$  :Shear component of the contact displacement

$\mu$  :Dynamic viscosity

$\nu$ : Kinematic viscosity

$\omega_i$ : Weights for D3Q19 model

$W_f$ : Fracture width

$\Delta x$ : Lattice spacing

$x$ : Location

## References

1. Sun, Z., H. Tang, D.N. Espinoza, M.T. Balhoff, and J.E. Killough, Discrete element modeling of grain crushing and implications on reservoir compaction. *Journal of Petroleum Science Engineering*, 2018. 171: p. 431-439.
2. Fan, M., J. McClure, Y. Han, Z. Li, and C. Chen. Interaction between Proppant Packing, Reservoir Depletion, and Fluid Flow in Hydraulic Fractures. in *Offshore Technology Conference*. 2017. Offshore Technology Conference.
3. Fan, M., J. McClure, Y. Han, Z. Li, and C. Chen, Interaction between proppant compaction and single-/multiphase flows in a hydraulic fracture. *SPE Journal*, 2018. 23(04): p. 1,290-1,303.
4. Montgomery, C.T. and M.B. Smith, Hydraulic fracturing: history of an enduring technology. *Journal of Petroleum Technology*, 2010. 62(12): p. 26-40.
5. Liang, F., M. Sayed, G.A. Al-Muntasheri, F.F. Chang, and L. Li, A comprehensive review on proppant technologies. *Petroleum*, 2016. 2(1): p. 26-39.
6. Zhang, F., H. Zhu, H. Zhou, J. Guo, and B. Huang, Discrete-element-method/computational-fluid-dynamics coupling simulation of proppant embedment and fracture conductivity after hydraulic fracturing. *Spe Journal*, 2017. 22(02): p. 632-644.

7. Gu, M., M. Fan, and C. Chen. Proppant Optimization for Foam Fracturing in Shale and Tight Reservoirs. in SPE Unconventional Resources Conference. 2017. Society of Petroleum Engineers.
8. Fan, M., Y. Han, J. McClure, E. Westman, N. Ripepi, and C. Chen. Investigating the Impact of Proppant Embedment and Compaction on Fracture Conductivity using a Continuum Mechanics, DEM, and LBM Coupled Approach. in 52nd US Rock Mechanics/Geomechanics Symposium. 2018. American Rock Mechanics Association.
9. Schmidt, D., P. Rankin, B. Williams, T. Palisch, and J. Kullman. Performance of mixed proppant sizes. in SPE Hydraulic Fracturing Technology Conference. 2014. Society of Petroleum Engineers.
10. McDaniel, R.R. and J.R. Willingham. The effect of various proppants and proppant mixtures on fracture permeability. in SPE Annual Fall Technical Conference and Exhibition. 1978. Society of Petroleum Engineers.
11. Phatak, A., O. Kresse, O.V. Neuvonen, C. Abad, C.-e. Cohen, V. Lafitte, P. Abivin, X. Weng, and K.W. England. Optimum Fluid and Proppant Selection for Hydraulic Fracturing in Shale Gas Reservoirs: a Parametric Study Based on Fracturing-to-Production Simulations. in SPE Hydraulic Fracturing Technology Conference. 2013. Society of Petroleum Engineers.
12. Kulkarni, M.C. and O. Ochoa, Mechanics of light weight proppants: A discrete approach. *Composites Science Technology*, 2012. 72(8): p. 879-885.
13. Hu, K., J. Sun, J. Wong, and B.E. Hall. Proppants selection based on field case studies of well production performance in the Bakken shale play. in SPE Western North American and Rocky Mountain Joint Meeting. 2014. Society of Petroleum Engineers.

14. Cundall, P.A. and O.D. Strack, A discrete numerical model for granular assemblies. *geotechnique*, 1979. 29(1): p. 47-65.
15. Zhu, H., J. Shen, and F. Zhang, A fracture conductivity model for channel fracturing and its implementation with Discrete Element Method. *Journal of Petroleum Science Engineering*, 2019. 172: p. 149-161.
16. Fan, M., Y. Han, and C. Chen. Hydraulic fracture conductivity as a function of proppant concentration under various effective stresses: from partial monolayer to multilayer proppants. in *Unconventional Resources Technology Conference*, Austin, Texas, 24-26 July 2017. 2017. American Association of Petroleum.
17. Itasca Consulting Group, I., PFC3D – Particle Flow Code in 3 Dimensions, Version 4.0 User’s Manual. Minneapolis: Itasca. 2008.
18. Cundall, P.A., A Computer Model for Simulating Progressive Large-Scale Movements in Blocky Rock Systems. *Proc. Int. Symp. Int. RockMech*, 1971. 2 (8).
19. Chen, S. and G.D. Doolen, Lattice Boltzmann method for fluid flows. *Annual review of fluid mechanics*, 1998. 30(1): p. 329-364.
20. Succi, S., *The lattice Boltzmann equation: for fluid dynamics and beyond*. 2001: Oxford university press.
21. Succi, S., R. Benzi, and F. Higuera, The lattice Boltzmann equation: a new tool for computational fluid-dynamics. *Physica D: Nonlinear Phenomena*, 1991. 47(1-2): p. 219-230.
22. Chen, H., S. Chen, and W.H. Matthaeus, Recovery of the Navier-Stokes equations using a lattice-gas Boltzmann method. *Physical Review A*, 1992. 45(8): p. R5339.



23. Grunau, D., S. Chen, and K. Eggert, A lattice Boltzmann model for multiphase fluid flows. *Physics of Fluids A: Fluid Dynamics*, 1993. 5(10): p. 2557-2562.
24. Han, Y. and P.A. Cundall, Lattice Boltzmann modeling of pore - scale fluid flow through idealized porous media. *International Journal for Numerical Methods in Fluids*, 2011. 67(11): p. 1720-1734.
25. Han, Y. and P.A. Cundall, LBM–DEM modeling of fluid–solid interaction in porous media. *International Journal for Numerical Analytical Methods in Geomechanics*, 2013. 37(10): p. 1391-1407.
26. Chen, C., A.I. Packman, and J.F. Gaillard, Pore - scale analysis of permeability reduction resulting from colloid deposition. *Geophysical Research Letters*, 2008. 35(7).
27. Chen, C., B.L. Lau, J.F. Gaillard, and A.I. Packman, Temporal evolution of pore geometry, fluid flow, and solute transport resulting from colloid deposition. *Water resources research*, 2009. 45(6).
28. Chen, C., A.I. Packman, and J.F. Gaillard, Using X - ray micro - tomography and pore - scale modeling to quantify sediment mixing and fluid flow in a developing streambed. *Geophysical Research Letters*, 2009. 36(8).
29. Chen, C., Z. Wang, D. Majeti, N. Vrvilo, T. Warburton, V. Sarkar, and G. Li, Optimization of lattice Boltzmann simulation with graphics-processing-unit parallel computing and the application in reservoir characterization. *SPE Journal*, 2016. 21(04): p. 1,425-1,435.
30. Chen, C., D. Hu, D. Westacott, and D. Loveless, Nanometer - scale characterization of microscopic pores in shale kerogen by image analysis and pore - scale modeling. *Geochemistry, Geophysics, Geosystems*, 2013. 14(10): p. 4066-4075.

31. Li, Y. and P. Huang, A coupled lattice Boltzmann model for advection and anisotropic dispersion problem in shallow water. *Advances in Water Resources*, 2008. 31(12): p. 1719-1730.
32. Ginzburg, I., Consistent lattice Boltzmann schemes for the Brinkman model of porous flow and infinite Chapman-Enskog expansion. *Physical Review E*, 2008. 77(6): p. 066704.
33. Ginzburg, I., D. d'Humières, and A. Kuzmin, Optimal stability of advection-diffusion lattice Boltzmann models with two relaxation times for positive/negative equilibrium. *Journal of Statistical Physics*, 2010. 139(6): p. 1090-1143.
34. Inamuro, T., M. Yoshino, and F. Ogino, Lattice Boltzmann simulation of flows in a three - dimensional porous structure. *International journal for numerical methods in fluids*, 1999. 29(7): p. 737-748.
35. Huitt, J. and B. McGlothlin Jr. The propping of fractures in formations susceptible to propping-sand embedment. in *Drilling and Production Practice*. 1958. American Petroleum Institute.
36. Lacy, L., A. Rickards, and D. Bilden, Fracture width and embedment testing in soft reservoir sandstone. *SPE drilling completion*, 1998. 13(01): p. 25-29.
37. Darin, S. and J. Huitt, Effect of a partial monolayer of propping agent on fracture flow capacity. *Petroleum transactions, AIME*, 1960.
38. Brannon, H.D., M.R. Malone, A.R. Rickards, W.D. Wood, J.R. Edgeman, and J.L. Bryant. Maximizing fracture conductivity with proppant partial monolayers: theoretical curiosity or highly productive reality? in *SPE Annual Technical Conference and Exhibition*. 2004. Society of Petroleum Engineers.

39. Ceramics Inc, C. CARBOHSP Technical Data Sheet.

[http://www.carboceramics.com/getattachment/5a2b4ffd-0b0e-4ce9-9a4e-](http://www.carboceramics.com/getattachment/5a2b4ffd-0b0e-4ce9-9a4e-5da47ad97425/attachment)

[5da47ad97425/attachment](http://www.carboceramics.com/getattachment/5a2b4ffd-0b0e-4ce9-9a4e-5da47ad97425/attachment) 2015.

40. Kurz, B.A., D.D. Schmidt, and P.E. Cortese. Investigation of improved conductivity and proppant applications in the Bakken formation. in SPE Hydraulic Fracturing Technology Conference. 2013. Society of Petroleum Engineers.

## **Chapter 6 Comprehensive study of the interactions between the critical dimensionless numbers associated with multiphase flow in 3D porous media**

Ming Fan, Virginia Tech; Laura E. Dalton, National Energy Technology Laboratory; James McClure, Nino Ripepi, Erik Westman, Virginia Tech; Dustin Crandall, National Energy Technology Laboratory; and Cheng Chen, Virginia Tech

### **Abstract**

Multiphase flow in porous media is of great interest in many engineering applications, such as geologic carbon sequestration, enhanced oil recovery, and groundwater contamination and remediation. In order to advance the fundamental understanding of multiphase flow in complex three-dimensional (3D) porous media, the interactions between the critical dimensionless numbers, including the contact angle, viscosity ratio, and capillary (Ca) number, were investigated using X-ray micro-computed tomography (micro-CT) scanning and lattice Boltzmann (LB) modeling. In this study, the 3D pore structure information was extracted from micro-CT images and then used as interior boundary conditions of flow modeling in a pore-scale LB simulator to simulate multiphase flow within the pore space. A Berea sandstone sample was scanned and then two-phase flow LB simulations were performed based on the micro-CT images. The LB-simulated water/CO<sub>2</sub> distributions agreed well with the micro-CT scanned images. Simulation results showed that a decreasing contact angle causes a decrease in wetting-fluid relative permeability and an increase in non-wetting fluid relative permeability. A rising Ca number increases both wetting and non-wetting fluid relative permeabilities. An increasing viscosity ratio (the ratio of non-wetting fluid viscosity to wetting fluid

viscosity) facilitates the increase of non-wetting fluid relative permeability and mitigates the reduction of wetting fluid relative permeability, when the contact angle decreases continuously. The primary novel finding of this study is that the viscosity ratio affects the rate of change of the relative permeability curves for both phases when the contact angle changes continuously. To the best of our knowledge, it is the first time that comprehensive interactions between these dimensionless numbers are demonstrated in a sandstone sample based on real 3D structures. We also investigated the role of the changes of flow direction and sample location on relative permeability curves. Simulation results showed that the change in non-wetting fluid relative permeability was larger when the flow direction was switched from vertical to horizontal, which indicated that there was stronger anisotropy in larger pore networks that were primarily occupied by the non-wetting fluid.

**Keywords:** lattice Boltzmann, multiphase flow, capillary number, viscosity ratio, contact angle

## 6.1. Introduction

Understanding multiphase flow in three-dimensional (3D) porous media is of significant interest in many engineering applications, such as geologic carbon sequestration (e.g., [1-4]) enhanced oil recovery [5], and groundwater contamination and remediation [6]. Multiphase flow in geologic formations is a complex process influenced by a large number of physical and geologic properties, among which relative permeability is one of the most important and thus has attracted the most attention. It has long been recognized that relative permeability is not only a function of fluid saturation [7, 8], but also depends

strongly on several other physical parameters such as contact angle, viscosity ratio, capillary (Ca) number, saturation history, and stress condition [9-11]. Therefore, advanced understanding of these physical parameters at the pore scale, as well as the complicated interactions between them, has important implications for accurate prediction of larger-scale multiphase transport processes, such as the migration and trapping of injected CO<sub>2</sub> in geologic reservoirs [12].

Based on U.S. Department of Energy (DOE)'s methodology [13], CO<sub>2</sub> storage resource estimate for saline formations is related to the microscopic displacement efficiency,  $E_d$ , which ranges from 0.35 to 0.76 in clastic formations over the 10% to 90% probability range. However, recent core analysis [12] at the DOE's National Energy Technology Laboratory (NETL) showed that some sandstones can have  $E_d$  significantly lower than 0.35 due to strong heterogeneity. The uncertainties associated with microscopic and macroscopic estimations of carbon storage imply that advanced studies of multiphase flow in geologic formations is critical to address the fundamental questions that remain unanswered. For example, what is the interaction between contact angle, Ca number, and CO<sub>2</sub>/water viscosity ratio, as well as its role on larger-scale relative permeability curves in natural 3D geologic formations? This work aims to combine laboratory experiments with numerical modeling to address this fundamental question associated with multiphase flow during geologic carbon sequestration.

Relative permeability can be measured in the laboratory using core flooding experiments, including the steady-state and unsteady-state methods. In the steady-state method, two immiscible fluids are injected simultaneously at constant flow rates, and relative permeability is measured directly based on its definition after the pressure drop

and flow rate stabilize [14]. However, the steady-state method is time-consuming because it can take up to several hours or even several days to reach the desired equilibrium conditions [15]. On the other hand, the unsteady-state method, which is a displacement process, is relatively fast and can mimic the real flooding process in underground reservoirs. However, it is an indirect method and relative permeability is calculated rather than being measured directly, which can be greatly affected by measurement errors and uncertainties resulting from the varying capillary pressure gradient and saturation gradient [11, 15]. Because of these practical challenges in laboratory experiments, direct pore-scale numerical modeling of multiphase flow based on digital rock images has become a powerful alternative approach to derive the relative permeability and to help interpret experimental measurements.

The numerical approaches to determine transport properties in the pore space can be divided into two primary categories, the network modelling and direct modeling methods [16]. In the pore network modeling method, a topologically representative network is first extracted from micro-CT images and then used for the computations of the governing transport equations [17, 18]. The advantages of this method are faster computational speeds and infinite resolutions compared to the direct modeling method. However, it is challenging to generate geometrically equivalent pore networks and to discretize the pore space into simple geometrical objects such as nodes and bonds [19, 20]. Compared to the network modeling method, the direct modeling method solves the flow and transport governing equations directly using micro-CT images (or other digital images of the pore geometry, such as scanning electron microscopy) as the boundary conditions of flow modeling. One of the most widely used and successful direct modeling methods is the

lattice Boltzmann (LB) method, which accommodates highly complex pore geometries and is straightforward to implement [21]. With improvements in computer power and developments of new computational platforms, such as graphical processing unit (GPU) enhanced parallel computations [22], large-scale, high-resolution numerical simulations based on the LB method have been possible to simulate multiphase flow in complex, 3D porous media [23-27].

Two-phase flow properties in porous media have been extensively studied using the LB method due to its capability in coping with irregular flow paths and modeling the behaviors of fluid-solid and fluid-fluid interactions. Li et al. [11] investigated the effects of Ca number, wettability, and viscosity ratio on the relative permeability through a sphere-packed porous medium based on the LB method. They found an increasing contact angle increased wetting fluid relative permeability while decreasing non-wetting fluid relative permeability; a larger viscosity ratio or Ca number increases the relative permeability of the non-wetting fluid, whereas it has a relatively lesser influence on that of the wetting fluid. A similar study [28] reported the same effect of increasing Ca numbers and viscosity ratios on the variation of relative permeability in a two-dimensional (2D) porous structure. In Ghassemi and Pak's work [29], the LB method was used to analyze the relationships between relative permeability and wetting fluid saturation in a 2D porous medium; they showed that the viscosity ratio had a much more remarkable effect on the relative permeability of the non-wetting fluid than the wetting fluid. Furthermore, studies on the effect of contact angle on relative permeability using the LB method [30, 31] showed that wettability has a larger influence on the relative permeability of the non-wetting fluid. Although these previous pore-scale investigations



of relative permeability based on the LB method have generated remarkable results, most of the pore structures are on the basis of man-made or idealized porous media, such as glass bead and polyethylene bead packs [32], computer-generated 3D sphere-packed porous media [11, 30], and computer-generated 2D pore structures with solid and void blocks [28, 29, 31, 33]. Moreover, most of the previous simulation works did not have direct comparisons with laboratory experiments, especially if the 2D or 3D pore geometries were generated by computer modeling. Direct, comprehensive analysis of multiphase flow properties in the complex 3D pore space of natural geologic formations, which is commonly encountered in geologic carbon storage processes, has become a crucial task. However, to the best of our knowledge, there have been no pore-scale numerical simulations reported in the literature to study the complicated interactions between contact angle, viscosity ratio, and Ca number associated with the multiphase flow within a pore geometry directly based on microstructural images of 3D natural rocks.

In this work, two-phase LB flow simulations were conducted directly based on the 3D pore structural information of a Berea sandstone sample, which was acquired by micro-CT scanning at DOE's NETL [12, 34-36]. First, a two-phase core flooding experiment was conducted on the Berea sandstone at DOE's NETL. Second, the distribution of contact angles was measured at the pore scale using micro-CT scanning. Third, LB two-phase flow modeling was conducted using the CT images of the sandstone as internal boundaries of flow modeling, and the initial condition of the LB modeling matched the imbibition process in the X-ray CT scanning stage. The LB-simulated two-fluid distribution was then compared with the micro-CT scanned two-fluid distribution at the

pore scale. Fourth, the influence of various combinations of contact angle, viscosity ratio, and Ca number on the relative permeability curves of the CO<sub>2</sub>-water-rock system was comprehensively investigated. This study also evaluated the role of fluid injection direction (horizontal vs. vertical, and upward vs. downward) and micro-scale heterogeneity (different locations of the computational domain center) on the relative permeability curves. The combination of micro-CT imaging and LB multiphase flow simulation based on real, 3D rock structures has the potential to advance fundamental understanding of the multiphysics processes associated with multiphase flow in geologic materials, which provides insights into upscaling methodologies to account for the influence of pore-scale processes in core- and larger-scale modeling frameworks.

## **6.2. Methods**

### **6.2.1 Core flooding experiments and X-ray micro-CT imaging**

The core flooding experiments and X-ray micro-CT scanning were conducted at DOE's NETL (Figure 6.1). The Berea sandstone core sample was 1.6 inches in length and 0.25 inch in diameter, with a porosity of 24.2%. The relatively small sample diameter (0.25 inch) was because that the high CT scanning resolution (2.36  $\mu\text{m}/\text{pixel}$ ) limited the total sample size in order to achieve an optimal X-ray transmission ratio. The core flooding setup was connected to a pressure vessel containing the core sample and mounted on the sample stage in the micro-CT scanner. The core flooding experiment involved CO<sub>2</sub>-saturated brine injection (Step 1), followed by a CO<sub>2</sub> injection (Step 2), and lastly a final brine injection (Step 3). This process was implemented to mimic the imbibition process that was accounted for in the initial condition of the LB model, which will be discussed

later. The brine used in this experiment was a Potassium Iodide (KI) brine solution with a 5 wt% concentration, which increased the density of the wetting fluid and thus increased the micro-CT contrast between brine and scCO<sub>2</sub> sufficiently [37]. The flowrate was 0.05 ml/min, and 10 pore volumes (3.1 ml) of each fluid in each step were injected through the sample. The flow rate led to Ca number of  $6.6 \times 10^{-8}$ , which was in the range (between  $3 \times 10^{-9}$  and  $3 \times 10^{-5}$ ) of the Ca numbers encountered in CO<sub>2</sub> aquifer storage projects [20]. During the core flooding experiment, the pore pressure was 1,800 psi and the confining pressure was 2,100 psi. The flow-through temperature was 24°C for all injections. After Step 3, the sample was set to shut-in conditions, pore pressure was fixed at 1,800 psi, temperature was increased to the supercritical condition (48°C), and the sample sat for 24 hours before micro-CT scanning allowing CO<sub>2</sub> to transition from the liquid state and fluid distribution to settle in the steady state. For simplicity, hereafter we refer to the wetting fluid as water in the following sections of this paper, although it should be noted that the wetting fluid used in the laboratory experiment was CO<sub>2</sub> saturated 5 wt% KI brine.

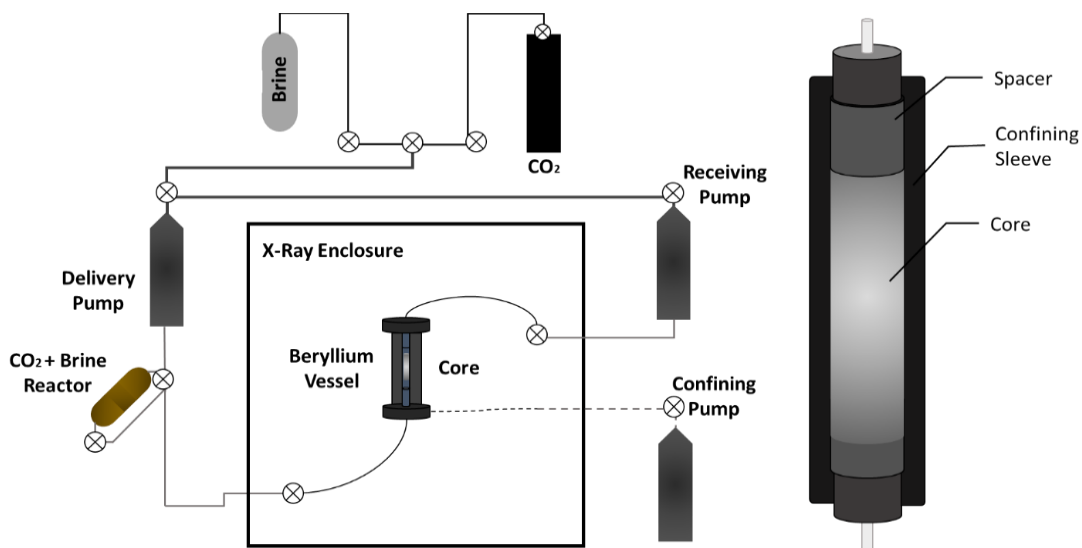


Figure 6.1. U.S. DOE-NETL micro-CT laboratory setup.

### 6.2.2. Lattice Boltzmann method for multiphase flow simulation

The LB method is a numerical method for solving the Navier-Stokes equations and based on microscopic physical models and mesoscale kinetic equations [38-43]. In comparison with conventional fluid dynamic models, the LB method has many advantages. For example, it is explicit in the evolution equation, simple to implement, natural to parallelize [22, 44-46], and easy to incorporate new physics such as interactions at fluid-solid interfaces [47-49].

A multiphase extension of Darcy's law is most typically used to describe two-fluid flow processes at the reservoir scale. The two-fluid system includes a wetting fluid ( $w$ ) and a non-wetting fluid ( $n$ ). The wetting fluid has a relatively higher affinity for the solid, and will tend to preferentially coat the rock surface as a result of the interfacial thermodynamics. As a consequence, the wetting and non-wetting fluid have a tendency to assume distinctly different configurations within the pore space. The relative permeability,  $k_{ri}$ , is introduced to account for these configurational effects, and the two-phase extension of Darcy's law is frequently written as

$$v_i = (k_{ri} / \mu_i) \mathbf{k} \cdot (-\nabla p + \rho_i \mathbf{g}) \quad (6.1)$$

where  $v_i$ ,  $\mu_i$ ,  $\rho_i$  and  $k_{ri}$  are respectively the Darcy velocity, dynamic viscosity, density, and relative permeability associated with fluid  $i=w, n$ .  $\mathbf{k}$  and  $\nabla p$  are the permeability tensor and pressure gradient. External body forces such as gravity are accounted for by the vector  $\mathbf{g}$ . Since  $k_{ri}$  is a relative quantity, it is dimensionless and usually attains a value between zero and one, although it is possible to measure relative permeability values greater than one in certain situations.

This work relies on a multi-relaxation time (MRT) LB scheme formulated for two-fluid flow according to the “color” model, originally proposed by Gustensen et al.[50]. In this work, the color model was implemented as described by McClure et al.[24]. Separate LB equations (LBEs) were used to track mass transport for each fluid and the total momentum. Two discrete velocity sets for two phase flows are considered, in which momentum transport LBEs rely on a 3D, 19 discrete velocity (D3Q19) lattice structure and the mass transport LBEs rely on a 3D, seven discrete velocity (D3Q7) lattice structure. In the D3Q19 lattice structure, the lattice velocity vectors corresponding to direction  $q$ , where  $q=0,1,2,\dots,18$ , is defined as:

$$\begin{aligned}
\mathbf{e}_0 &=(0,0,0), \mathbf{e}_1=(1,0,0)c, \mathbf{e}_2=(-1,0,0)c \\
\mathbf{e}_3 &=(0,1,0)c, \mathbf{e}_4=(0,-1,0)c, \mathbf{e}_5=(0,0,1)c, \mathbf{e}_6=(0,0,-1)c \\
\mathbf{e}_7 &=(1,1,0)c, \mathbf{e}_8=(-1,1,0)c, \mathbf{e}_9=(1,-1,0)c, \mathbf{e}_{10}=(-1,-1,0)c \\
\mathbf{e}_{11} &=(0,1,1)c, \mathbf{e}_{12}=(0,-1,1)c, \mathbf{e}_{13}=(0,1,-1)c, \mathbf{e}_{14}=(0,-1,-1)c \\
\mathbf{e}_{15} &=(1,0,1)c, \mathbf{e}_{16}=(-1,0,1)c, \mathbf{e}_{17}=(1,0,-1)c, \mathbf{e}_{18}=(-1,0,-1)c
\end{aligned}$$

where  $c = \Delta x / \Delta t$ , in which  $\Delta x$  is the lattice spacing and  $\Delta t$  is the time step. In the D3Q7 lattice structure, the velocity vectors match the first seven discrete velocities in the D3Q19 lattice structure.

The mass transport LBEs provide a solution for the densities of the two fluids,  $\rho_w$  and  $\rho_n$ , which provide the position of the two fluids and the location of the interface between them. The phase indicator field can consequently be computed from the fluid densities as

$$\varphi = (\rho_n - \rho_w) / (\rho_n + \rho_w) \tag{6.2}$$

The value of the phase indicator field is constant within the pure phase regions occupied by each fluid, and varies between -1 and 1 in the interfacial region, which is diffuse. Based on this information, stresses that arise within the interfacial region (as a

consequence of the interfacial tension) are incorporated into the momentum transport equation. The color gradient is defined as:

$$\mathbf{C} = \nabla \phi \quad (6.3)$$

In the LB formulation the color gradient is re-expressed in terms of its magnitude  $|\mathbf{C}|$  and normal direction  $\mathbf{n} = \mathbf{C}/|\mathbf{C}|$ . The D3Q7 mass transport distributions are initialized for each of the two components based on the associated densities and the fluid velocity to match an equilibrium distribution where the flux of mass across the interface is minimized for each fluid:

$$g_{nq} = \omega_q \left[ \rho_n (1 + \mathbf{e}_q \cdot \mathbf{u}) + \beta (\mathbf{e}_q \cdot \mathbf{n}) \rho_w \rho_n / (\rho_w + \rho_n) \right] \quad (6.4)$$

$$g_{wq} = \omega_q \left[ \rho_w (1 + \mathbf{e}_q \cdot \mathbf{u}) - \beta (\mathbf{e}_q \cdot \mathbf{n}) \rho_w \rho_n / (\rho_w + \rho_n) \right] \quad (6.5)$$

where  $\beta$  is a parameter that controls the width of the interface and  $\mathbf{u}$  is the flow velocity (determined from the momentum transport LBE described below). The associated weights for the D3Q7 model are  $\omega_0 = 1/3$  and  $\omega_{1\dots6} = 1/9$ . The time evolution of fluid densities is then determined by applying a streaming step directly to the equilibrium distributions (with no relaxation process):

$$\rho_i(\mathbf{x}, t + \Delta t) = \sum_q g_{iq}(\mathbf{x} - \mathbf{e}_q \Delta t, t) \quad (i=w,n) \quad (6.6)$$

The mass transport LBEs exactly conserve the mass of each component.

The momentum transport is described by a D3Q19 MRT LBE:

$$f_q(\mathbf{x} + \mathbf{e}_q \Delta t, t + \Delta t) - f_q(\mathbf{x}, t) = M_{qi}^* \Lambda_i (m_i^{eq} - m_i) \quad (6.7)$$

where  $q=0,1,2,\dots,18$ ,  $i=0,1,2,\dots,18$ ;  $f_q(\mathbf{x},t)$  is the particle-distribution function specifying the probability that fluid particles at lattice location  $\mathbf{x}$  and time  $t$  travel along the  $q^{th}$

direction, known as collision step;  $f_q(\mathbf{x} + \mathbf{e}_q \Delta t, t + \Delta t)$  is streaming step moves distributions between adjacent lattice sites. In the MRT formulation, a relaxation process is applied to a set of nineteen moments determined from the distributions, with the rate of the relaxation process determined by  $\Lambda_i$ . The relaxation rates are chosen to specify the fluid viscosity [51]. The moments are obtained from a linear transformation,  $m_i = M_{iq} f_q$ . The matrix  $M_{qi}^*$  is the inverse of  $M_{iq}$ . The equilibrium moments  $m_i^{eq}$  depend on the color gradient  $\mathbf{C}$  and the flow velocity  $\mathbf{u}$ . The macroscopic fluid density and velocity are calculated with the following two equations:

$$\rho = \sum_{q=0}^{18} f_q \quad (6.8)$$

and

$$\mathbf{u} = \frac{\sum_{q=0}^{18} f_q \mathbf{e}_q}{\rho} \quad (6.9)$$

Fluid pressure is calculated using  $p = c_s^2 \rho$ , where  $c_s$  is the speed of sound. In the LB D3Q19 model,  $c_s^2 = c^2/3$ .

The non-zero equilibrium moments are

$$m_1^{eq} = (j_x j_x + j_y j_y + j_z j_z) + \alpha |\mathbf{C}| \quad (6.10)$$

$$m_9^{eq} = (2j_x j_x - j_y j_y - j_z j_z) + \alpha |\mathbf{C}| (2n_x n_x - n_y n_y - n_z n_z) / 2 \quad (6.11)$$

$$m_{11}^{eq} = (j_y j_y - j_z j_z) + \alpha |\mathbf{C}| (2n_y n_y - n_z n_z) / 2 \quad (6.12)$$

$$m_{13}^{eq} = j_x j_y + \alpha |\mathbf{C}| n_x n_y / 2 \quad (6.13)$$

$$m_{14}^{eq} = j_y j_z + \alpha |\mathbf{C}| n_y n_z / 2 \quad (6.14)$$

$$m_{15}^{eq} = j_x j_z + \alpha |\mathbf{C}| n_x n_z / 2 \quad (6.15)$$

where the parameter  $\alpha$  is linearly related to the interfacial tension and the fluid momentum is computed from the distributions

$$\mathbf{j} = \sum_q f_q \mathbf{e}_q \quad (6.16)$$

The specific forms for  $\mathbf{M}$  and  $m_i^{eq}$  have been previously published in the literature, along with details on setting the relaxation rates,  $\Lambda_i$ , and boundary conditions for two-flow in porous media (see [24]). This formulation was used to measure the relative permeability based on steady-state two-fluid flow within 3D images of a digital rock geometry. An in-depth description of the approach used to estimate relative permeability from digital rock images using the color LB method is provided by Ramstad et al. [15]. More details about the LB multiphase flow simulator used in this study can be found in our recent publications [24, 52, 53].

### 6.3. Important dimensionless numbers

In this study, the role of the critical dimensionless numbers on multiphase flows in 3D, complex porous media was investigated. These dimensionless numbers included the contact angle, Ca number, and viscosity ratio.

Wettability plays a significant role in determining multiphase fluid flow and distribution in porous media. It is defined as “the tendency of one fluid to spread on or adhere to a solid surface in the presence of other immiscible fluids” [54]. Wettability can be expressed in a more convenient and precise manner by measuring the angle of contact



at the liquid-solid surface. According to Iglauer et al. [55], a CO<sub>2</sub>-brine-rock system is considered completely water-wet for a contact angle of 0°, strongly water-wet for 0°-50°, weakly water-wet for 50°-70°, intermediate wet for 70°-110°, weakly CO<sub>2</sub>-wet for 110°-130°, strongly CO<sub>2</sub>-wet for 130°-180°, and completely CO<sub>2</sub>-wet for a contact angle of 180°. Existing studies showed, with the decrease of the relative adhesion of the wetting fluid to the solid surface at a given wetting fluid saturation, the non-wetting fluid's relative permeability decreases whereas the wetting fluid's relative permeability increases [14, 56, 57].

In natural geologic reservoir rocks, the wetting fluid preferentially coats the majority of the rock surfaces and tends to be held in the smaller pores. On the other hand, the non-wetting fluid tends to be repelled from the rock surfaces, occupy the center of large pores, and flow in the center of channels. At high Ca numbers, the viscous force dominates the flow and thus the mobility of both fluids increases. Conversely, as the Ca number decreases, two-phase flow might be blocked in some places due to the capillary resistance [58], leading to decreased mobility of both fluids. The Ca number, defined in Equation 6.17 [15], measures the ratio of the viscous force to the capillary force:

$$Ca = \frac{\mu_{nw} u_t}{\sigma} \quad (6.17)$$

where  $\mu_{nw}$  is the non-wetting fluid dynamic viscosity,  $u_t$  is the total average Darcy flow velocity, and  $\sigma$  is the interfacial tension between wetting and non-wetting fluids.

The viscosity ratio also has a critical effect on the relative permeability characteristics of a reservoir rock, which is defined as the ratio of the non-wetting fluid viscosity to the wetting fluid viscosity:

$$M = \mu_{nw} / \mu_w \quad (6.18)$$

where  $\mu_w$  is the dynamic viscosity of the wetting fluid. When the Ca number is small, the fluid viscosity ratio has little effects on the relative permeability because most of the fluid interfaces are immobilized in narrow throats [58]. Conversely, when the Ca number increases, the relative importance of the viscous force and capillary force changes. In this study, in order to study the dynamic effects of Ca number and viscous ratio on relative permeability curves, two Ca numbers ( $Ca = 1 \times 10^{-4}$  and  $Ca = 1 \times 10^{-3}$ ) and two viscosity ratios ( $M=0.25$  and  $M=1$ ) were investigated. For each combination of Ca and M, three contact angles were used in the LB two-phase flow simulation.

A literature review of relevant studies on LB simulations of multiphase flow in porous media was summarized in Table 6.1. In the table, the computational domain size is measured using the lattice length unit (lu) in LB modeling. Based on the review, this paper is the first pore-scale LB multiphase flow modeling work that studies the comprehensive interactions between all the three dimensionless numbers (contact angle, Ca, and M) in the 3D pore spaces of a real reservoir rock, as well as their role on the larger-scale relative permeability curves in the rock.

**Table 6.1** A literature review and relevant works on multiphase flow

Reference	Material	Dimension	Domain size (lu)	Resolution ( $\mu\text{m}/\text{lu}$ )	Dimensionless numbers	Relative Permeability Curves
This work	Berea Sandstone	3D	$800 \times 800 \times 600$	2.36	Ca, M, contact angle	Yes
Zhao et al. 2017 [59]	Sandstone	2D	$3600 \times 1920$	N/A <sup>1</sup>	Ca, M, contact angle	Yes
Gu et al. 2018 [60]	Berea Sandstone	2D	$2644 \times 2117$	0.67	M, contact angle	Yes
Ramstad et al. 2010 [19]	Bentheimer Sandstone	3D	$256 \times 256 \times 256$	6.67	Ca	Yes

Ramstad et al. 2012 [15]	Bentheimer and Berea sandstone	3D	$256 \times 256 \times 256$	6.67	M	Yes
Boek & Venturoli 2010 [61]	Bentheimer and Berea sandstone	3D	$128 \times 128 \times 128$	4.9	N/A	Yes
Li et al. 2014 [62]	Sandstone	3D	$200 \times 200 \times 50$	3.7	N/A	No
Alpak et al. 2018 [63]	Gildehauser sandstone	3D	$512 \times 512 \times 512$	4	N/A	Yes
Landry et al. 2014 [32]	glass bead and polyethylene bead packs	3D	$200 \times 200 \times 200$	26	contact angle	Yes
Li et al. 2005 [11]	computer-generated sphere-packed porous media	3D	$96 \times 96 \times 96$	N/A	Ca, M, contact angle	Yes
Liu et al. 2013 [64]	computer-generated pore structures with solid and void blocks	2D	$1728 \times 1200$	N/A	Ca, M	No
Liu et al. 2014 [65]	computer-generated pore structures with solid and void circles	2D	$2816 \times 2689$	1.5	Ca	No
Ghassemi and Pak, 2011[29]	computer-generated pore structures with solid and void blocks	2D	$261 \times 261$	$2 \times 10^4$	Ca, M, contact angle	Yes

1. “N/A” denotes “not available”.

## 6.4. Results and Discussion

### 6.4.1 Pore-scale contact angle measurement and SEM/EDX characterization

In the LB simulations, the discrete, digitalized rock microstructure was obtained directly from DOE-NETL’s 3D micro-CT scanned images of the Berea sandstone sample. The sandstone was scanned in top, middle, and bottom sections separately in order to obtain a larger field of view that can account for spatial heterogeneity. In each section, a computational domain of  $800 \times 800 \times 600$  pixels in the x, y, and z directions was

reconstructed based on the CT images, where  $z$  is the vertical direction. Note that  $800 \times 800$  pixels (in the  $x$ - $y$  plane) is the maximum possible dimensions that can be achieved after removing the outer air areas. The lattice spacing is equal to the CT image pixel size, thus the LB model had a resolution of  $2.36 \mu\text{m}/\text{lu}$ , the same as the CT image resolution. The distance from the bottom face of the top computational domain to the top face of the middle computational domain was  $0.354 \text{ mm}$ , and the distance from the bottom face of the middle computational domain to the top face of the bottom computational domain was  $1.345 \text{ mm}$ , as illustrated in Figure 6.2. Pore-scale contact angles were measured on micro-CT images of the  $\text{scCO}_2$ -brine-sandstone systems throughout all the three computational domains based on NETL's 3D micro-CT reconstructions, and the distribution curve is illustrated in Figure 6.3. Specifically, we used three plane views and the ImageJ Angle tool to process images in 3D space and then manually measure the contact angles [37]. The frequency of each contact angle was counted and then normalized by the total number of measured contact angles. Pore-scale contact angle measurements showed that the contact angles had a minimum value of  $8.6^\circ$ , a maximum value of  $104.3^\circ$ , a mean value of  $46.2^\circ$ , and a median value of  $45.4^\circ$ . The mean and median contact angles fell in the range of  $0^\circ$ - $50^\circ$ , which is strongly water-wet based on the definition of Iglauer et al. [55]. The relatively wide range between the minimum and maximum contact angles suggests heterogeneous rock surface wettability. The variation in rock surface wettability results from heterogeneous surface mineralogy and roughness. In order to confirm this hypothesis, we used the facilities of scanning electron microscope/energy-dispersive X-ray spectroscopy (SEM/EDX) housed in Virginia Tech's Nanoscale Characterization and Fabrication Laboratory to characterize the Berea

sandstone's surface roughness and mineralogy. Figure 6.4 demonstrates the results of the SEM/EDX characterization. Specifically, Figures 6.4a and 6.4b illustrate rock surfaces rich in clay and quartz minerals, respectively, and both of them demonstrate high surface roughness. The areas marked by yellow rectangles were analyzed using EDX, and it was confirmed that sample surface in Figure 6.4a was rich in clay whereas the sample surface in Figure 6.4b was rich in quartz. In fact, a significant portion of rock surfaces rich in various clay minerals were observed in this particular sandstone sample. These observations explain the relatively wide range of contact angle distribution as illustrated in Figure 6.3.

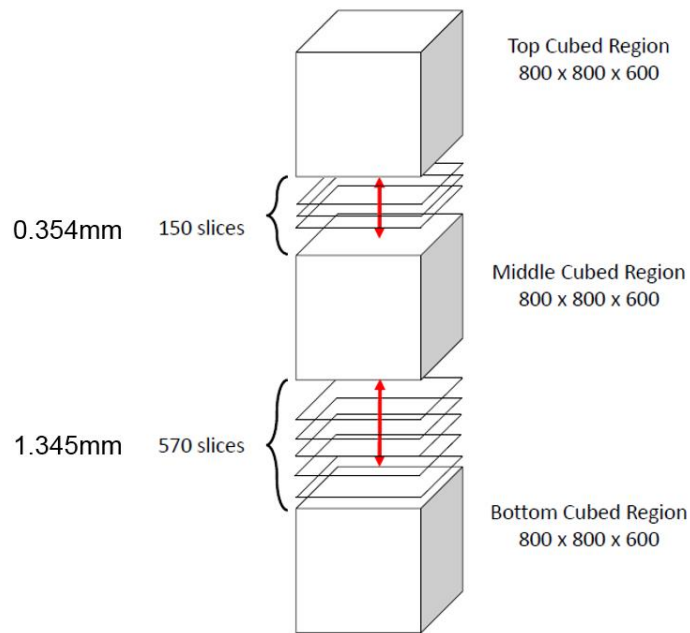


Figure 6.2. Schematic plot of the spatial positions of the three computational domains.

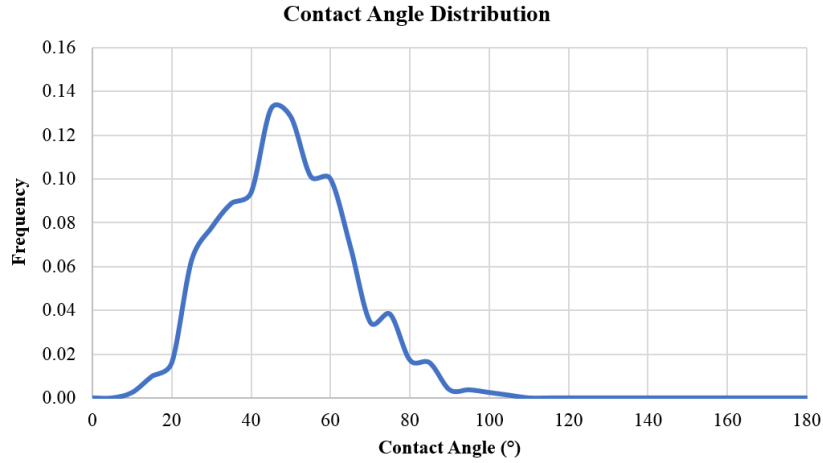


Figure 6.3. Contact angle distribution at the pore scale measured directly from NETL’s 3D micro-CT image reconstructions.

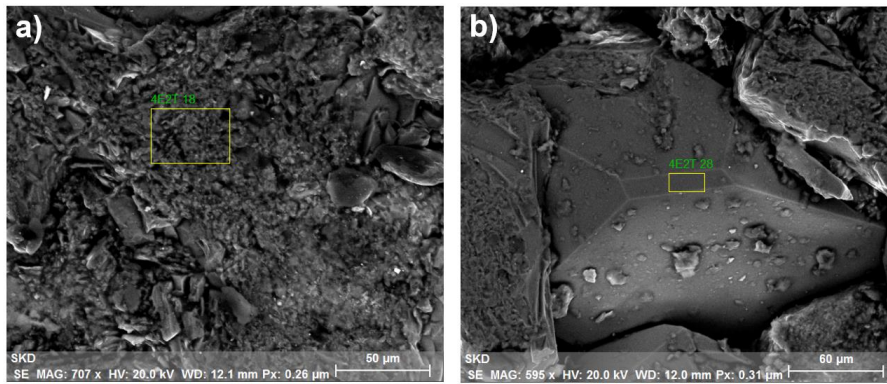


Figure 6.4. SEM/EDX characterization of sandstone surface rich in a) clay minerals, and b) quartz.

#### 6.4.2 Comparison between CT-scanned and LB-simulated water/CO<sub>2</sub> distributions

Figure 6.5 illustrates the comparison between micro-CT-scanned and LB-simulated images of CO<sub>2</sub> and water distributions in the pore space of the Berea sandstone. The sandstone pore structure was from the middle-section computational domain. Viscosity ratio was 1:4, Ca number was  $1 \times 10^{-4}$ , and the contact angle was equal to 45°. Figure 6.5a is the X-ray CT scanned two-fluid distribution in the sandstone whereas Figure 6.5b is

the corresponding LB-simulated two-fluid distribution. The picture is a 2D cross section perpendicular to the main-flow ( $z$ ) direction and has dimensions of  $1.89 \text{ mm} \times 1.89 \text{ mm}$  ( $800 \text{ lu} \times 800 \text{ lu}$ ). The water is blue,  $\text{CO}_2$  is pink, and sandstone is white. In this study, we refer to water and  $\text{CO}_2$  as the wetting and non-wetting fluids, respectively. In the LB multiphase flow simulations, fluid phases were initialized morphologically, based on an operation known as morphological opening [33, 53], in order to achieve a range of fluid saturations. The  $\text{CO}_2$  was instantiated into the larger pores, consistent with water-wet porous media. Multiphase fluid flow was induced by applying a constant external body force with full periodic boundary conditions to mimic fractional flow experiments typically used to measure relative permeability in the laboratory [15, 66, 67]. In this way, we managed to simulate steady-state two-phase flows through the rock sample in the imbibition process [53], which was consistent with the fluid distribution in the CT scanning stage. Comparison between micro-CT-scanned and LB-simulated two-fluid distributions showed an overall good agreement that  $\text{CO}_2$  was trapped in the center of larger pores, primarily due to the imbibition process associated with relatively low Ca numbers in the laboratory experiment and LB multiphase flow simulation.

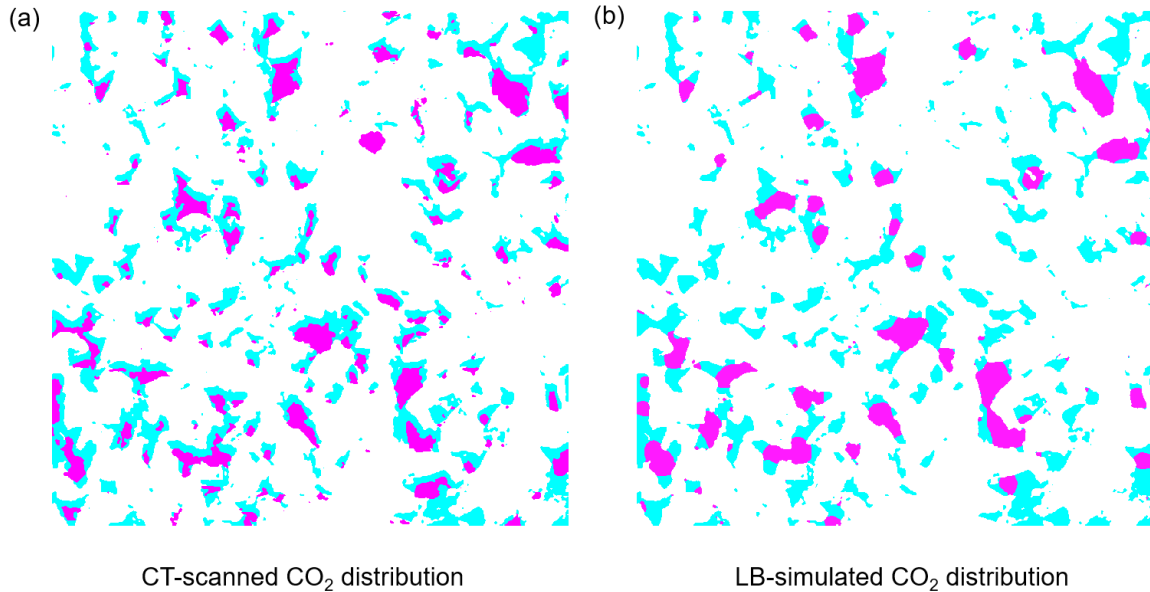


Figure 6.5. a) CT scanning image of two-fluid distribution in the sandstone at the pore scale, and b) corresponding LB-simulated two-fluid distribution at the pore scale. The water is blue, CO<sub>2</sub> is pink, and sandstone is white. The pore geometry was a 2D horizontal cross section cut from the 3D X-ray CT image reconstruction of the middle-section computational domain. This cross section is perpendicular to the main-flow ( $z$ ) direction and has dimensions of 1.89 mm  $\times$  1.89 mm (800 lu  $\times$  800 lu). The distance from the 2D cross section to the bottom of the computational domain is 0.8 mm.

### 6.4.3 Comprehensive sensitivity analyses for various combinations of dimensionless numbers

With the range of contact angles determined at the pore scale based on micro-CT scanning and the LB multiphase flow model calibrated by comparing CT-scanned and LB-simulated two-fluid distributions, we conducted comprehensive sensitivity analyses for various combinations of the dimensionless numbers. The simulation information is summarized in Table 6.2. In this study, two viscosity ratios (1:4 and 1:1) and two Ca numbers ( $10^{-3}$  and  $10^{-4}$ ), associated with three contact angles (0, 45, and 90 degrees), were investigated in the middle section sample. The three selected contact angles covered the majority of the contact angle range demonstrated in Figure 6.3. Comprehensive



combinations between these dimensionless numbers led to twelve scenarios in the LB multiphase flow simulations conducted on the middle-section computational domain, as illustrated in Table 6.2. It should be noted that the lowest Ca number used in this comprehensive numerical sensitivity study is  $10^{-4}$ , which is higher than the Ca number in the core flooding experiments ( $6.6 \times 10^{-8}$ ). Before the comprehensive sensitivity analyses, we calculated relative permeability curves for Ca numbers of  $10^{-3}$ ,  $10^{-4}$ , and  $10^{-5}$ . The difference in relative permeability curves between Ca numbers of  $10^{-4}$  and  $10^{-5}$  is much smaller than the difference between Ca numbers of  $10^{-4}$  and  $10^{-3}$ . This suggests, when the Ca number decreases to  $10^{-4}$  or a lower level, the capillary force dominates over the inertial force. Therefore, the two-fluid transport mechanisms under Ca numbers of  $6.6 \times 10^{-8}$  and  $10^{-4}$  are both dominated by the capillary force, which leads to similar properties of two-fluid transport and distribution in the pore space. From the perspective of LB modeling, we chose  $10^{-4}$  as the lower bound of the Ca number because its relatively higher flow velocity, compared to that in the case of  $Ca = 6.6 \times 10^{-8}$ , can significantly reduce the computational time needed to reach the equilibrium state in the LB two-phase flow simulations and reduce the spurious velocity currents that start to interfere when the Ca number is lower than  $10^{-4}$ .

**Table 6.2.** Twelve scenarios were considered in the two-phase LB flow simulations, based on comprehensive combinations between the three dimensionless numbers (M, Ca, and contact angle).

Viscosity ratio between CO <sub>2</sub> and water (M)	Ca = 1×10 <sup>-3</sup>		Ca = 1×10 <sup>-4</sup>	
	0°	Contact angle	0°	Contact angle
1:4 (0.25)	0°		0°	
	45°	Contact angle	45°	Contact angle
	90°		90°	
1:1 (1)	0°		0°	
	45°	Contact angle	45°	Contact angle
	90°		90°	

Figure 6.6 demonstrates the role of different combinations of Ca number, viscosity ratio, and contact angle on the relative permeability curves, based on the LB multiphase flow simulations conducted on the middle section of the Berea sandstone sample. Specifically, Figures 6.6a and 6.6b have viscosity ratios of 1:1 and 1:4, respectively, with the Ca number fixed at 1×10<sup>-4</sup>; Figures 6.6c and 6.6d have viscosity ratios of 1:1 and 1:4, respectively, with the Ca number fixed at 1×10<sup>-3</sup>. For each combination of the Ca number and viscosity ratio, contact angles of 0°, 45°, and 90° were simulated, leading to twelve scenarios as demonstrated in Table 6.2. Based on simulated data, Corey model was used to fit the simulated relative permeability curves. Corey model is an often used approximation of relative permeability, which is a power law based on the normalized water saturation. If  $S_{wir}$  is the irreducible saturation of water,  $S_{orw}$  is the residual saturation of CO<sub>2</sub> after water flooding, the normalized water saturation is defined in Equation 6.19:

$$S_w^* = \frac{S_w - S_{wir}}{1 - S_{wir} - S_{orw}} \quad (6.19)$$

The Corey models for fitting the relative permeability curves of water and CO<sub>2</sub> are then illustrated in Equations 6.20 and 6.21:

$$k_{rw} = k_{rw}^o S_w^{*N_w} \quad (6.20)$$

$$k_{ro} = k_{ro}^o (1 - S_w^*)^{N_o} \quad (6.21)$$

where  $k_{rw}$  is the relative permeability of water;  $k_{ro}$  is the relative permeability of CO<sub>2</sub>;  $k_{rw}^o$  is the maximum relative permeability for water when  $S_w^*=1$ ;  $k_{ro}^o$  is the maximum relative permeability for CO<sub>2</sub> when  $S_w^*=0$ ;  $N_w$  is the power-law exponent for the water curve; and  $N_o$  is the power-law exponent for the CO<sub>2</sub> curve. The fitted Corey model parameters are listed in Tables 6.3 and 6.4.

**Table 6.3.** Corey model parameters with  $Ca=1 \times 10^{-4}$

Ca $1 \times 10^{-4}$	Contact angle	$S_{wir}$	$S_{orw}$	$N_w$	$N_o$	$k_{rw}^o$	$k_{ro}^o$
Viscosity ratio 1:1	0°	0.2	0.05	3.035	2.919	0.97	0.85
	45°	0.15	0.07	3.414	2.782	0.98	0.9
	90°	0.1	0.08	3.455	3.091	0.99	0.85
Viscosity ratio 1:4	0°	0.25	0.07	3.201	4.879	0.81	0.49
	45°	0.2	0.08	3.177	3.803	0.8	0.606
	90°	0.15	0.09	2.552	4.199	0.79	0.61

**Table 6.4.** Corey model parameters with  $Ca=1 \times 10^{-3}$

Ca $1 \times 10^{-3}$	Contact angle	$S_{wir}$	$S_{orw}$	$N_w$	$N_o$	$k_{rw}^o$	$k_{ro}^o$
Viscosity ratio 1:1	0°	0.2	0.04	2.513	1.047	0.99	0.876
	45°	0.15	0.06	2.45	0.987	0.91	0.89
	90°	0.1	0.07	2.172	1.159	0.93	0.893
Viscosity ratio 1:4	0°	0.23	0.05	2.508	1.641	0.8	0.58
	45°	0.19	0.07	2.362	1.583	0.75	0.66
	90°	0.14	0.08	1.878	1.694	0.81	0.75

#### 6.4.4 Effect of contact angle

The contact angle is one of the most important dimensionless numbers in two-phase displacement through a porous media, and its effect was studied at  $0^\circ$ ,  $45^\circ$ , and  $90^\circ$ . From Figure 6.6, it is observed that when the contact angle decreased both the wetting (water) and non-wetting ( $\text{CO}_2$ ) fluid relative permeability curves moved to the right, which implies that the wetting fluid relative permeability decreased whereas the non-wetting fluid relative permeability increased. In addition, Corey model fitting showed that  $S_{wir}$  increased whereas  $S_{orw}$  decreased when contact angle decreased continuously, as illustrated in Tables 6.3 and 6.4. In this water-wet sandstone, the wetting fluid tends to coat the rock surfaces to form a thin water film and occupies most of the small pores. A decreasing contact angle led to an increasing affinity between water and the solid surfaces which pushed water toward the rock surfaces and thus led to higher resistance and lower relative permeability for water. Furthermore, because the capillary pressure increased with the decreasing contact angle, it took more energy for the wetting fluid to move and it might be trapped in small pores, which reduced the overall connectivity and consequently the relative permeability of the wetting fluid. On the other hand, because the non-wetting fluid occupies larger pores and flows in the center of flow channels, a decreasing contact angle will push the wetting fluid toward the solid surfaces and thus reduce its competition with the non-wetting fluid flow; this process is favorable to the overall flow rate of the non-wetting fluid, leading to the increase of non-wetting fluid relative permeability. Similar results have been observed through experiments conducted by Donaldson and Thomas [57] and reported by Li et al. [11] and Ghassemi and Pak [29] through numerical simulations. It is also interesting to notice that at the contact angle of

90°, both wetting and non-wetting fluid relative permeability curves are far away from the other curves (i.e., the 0° and 45° curves). This geometric effect can be attributed to special fluid configurations at this angle, with which both fluids have less affinity to the rock surfaces.

#### **6.4.5 Effect of viscosity ratio**

To investigate the effect of viscosity ratio on relative permeability curves, two viscosity ratios ( $M=1:1$  and  $M=1:4$ ) were considered in the LB multiphase flow simulations. Specifically, a viscosity ratio of 1:4 between CO<sub>2</sub> and water is typical of scCO<sub>2</sub> injection in deep saline aquifers [1, 68]. As discussed previously, when the Ca number is fixed, a decreasing contact angle (i.e., increasing affinity between water and rock surfaces) caused both water and CO<sub>2</sub> relative permeability curves to move to the right, implying that the water relative permeability decreases whereas the CO<sub>2</sub> relative permeability increases under the impact of the decreasing contact angle. In the case of  $Ca = 10^{-4}$  and with a continuously decreasing contact angle, increasing the viscosity ratio from 1:4 (see Figure 6.6b) to 1:1 (see Figure 6.6a) facilitates the increase of CO<sub>2</sub> relative permeability (i.e., the distance between the three CO<sub>2</sub> relative permeability curves becomes larger) while mitigating the reduction of water relative permeability (i.e., the distance between the three water relative permeability curves becomes smaller). This is because the wetting fluid tends to coat the solid surfaces as a thin film whereas the non-wetting fluid tends to occupy larger pores and thus experiences a hydraulic slip at the two-phase interface, which is well known as the lubrication effect [11, 28, 29, 31, 59, 69, 70]. Increasing the viscosity ratio has the potential to enhance the lubrication effect [11, 31],

because the thin wetting fluid layer, which is located between the non-wetting fluid and rock surfaces, becomes less viscous relative to the non-wetting fluid and thus enables the non-wetting fluid to flow more easily. In the meanwhile, when the viscosity ratio increases the wetting fluid becomes less viscous relative to the non-wetting fluid, which is also favorable for the mobility of the wetting fluid and thus mitigates the reduction of the wetting fluid relative permeability under the impact of a decreasing contact angle. Similar phenomena can be observed in the case of  $Ca = 10^{-3}$  (see Figures 6.6c and 6.6d). Based on these observations, it is clear that the viscosity ratio affects the rate of change of the relative permeability curves for both wetting and non-wetting fluids, when the contact angle varies continuously.

In the literature, most works studied the role of viscosity ratio when the contact angle was fixed. Several groups reported that a larger viscosity ratio enhances the non-wetting fluid relative permeability whereas the wetting fluid relative permeability is relatively insensitive to the change of viscosity ratio at a fixed contact angle [11, 28, 29, 31, 71, 72]. In contrast, the primary novel finding in this paper is that the viscosity ratio affects the rate of change of the relative permeability for both phases when the contact angle changes continuously. This new finding is critical and has important implications to geologic CO<sub>2</sub> storage, because natural reservoir rocks have heterogeneous contact angles at the pore scale. As a consequence, the dependence of relative permeability curves on the viscosity ratio will be complicated due to the heterogeneous contact angles.

#### 6.4.6 Effect of Ca number

In the LB simulations, the Ca number was adjusted by changing the external body force with all the other parameters fixed. In Figure 6.6, it is observed, at a fixed wetting fluid saturation and under the same viscosity ratio, both wetting and non-wetting fluid relative permeabilities increased with the increasing Ca number (e.g., comparing Figures 6.6a with 6c, or comparing Figures 6.6b with 6.6d). In addition, Figure 6.6 illustrates that the curvature of the relative permeability curves under  $Ca=10^{-3}$  was lower than that under  $Ca=10^{-4}$ , which suggests that the relative permeability curves under  $Ca=10^{-3}$  were straighter. This is consistent with the finding that the values of  $N_o$  and  $N_w$  under  $Ca=10^{-3}$  are significantly lower than those under  $Ca=10^{-4}$ , as shown in Tables 6.3 and 6.4. This is because an increasing Ca number enhances the inertial force relative to the capillary force, which helps both wetting and non-wetting fluids to overcome the capillary resistance and to form more well-connected flow pathways, leading to increased mobility and relative permeability for both fluids.

To summarize, in this study it is the first time that LB multiphase flow simulation is used to demonstrate the comprehensive interactions between contact angle, viscosity ratio, and Ca number, as well as their role on the relative permeability curves within a complex, 3D sandstone sample, of which the pore structural information is directly obtained by non-invasive X-ray micro-CT imaging. Our comprehensive sensitivity analyses illustrated that the impact of the changing contact angle on relative permeability curves depends primarily on both the viscosity ratio and Ca number. In the literature, most works studied the role of viscosity ratio when the contact angle was fixed. Conversely, this study shows that the viscosity ratio affects the rate of change of the

relative permeability for both fluids when the contact angle changes continuously. Simulation results are consistent with fundamental multiphase flow physics and imply that these critical dimensionless numbers, which are associated with water/CO<sub>2</sub> multiphase flows with respect to geologic carbon storage, are interconnected and must be studied in a holistic manner.

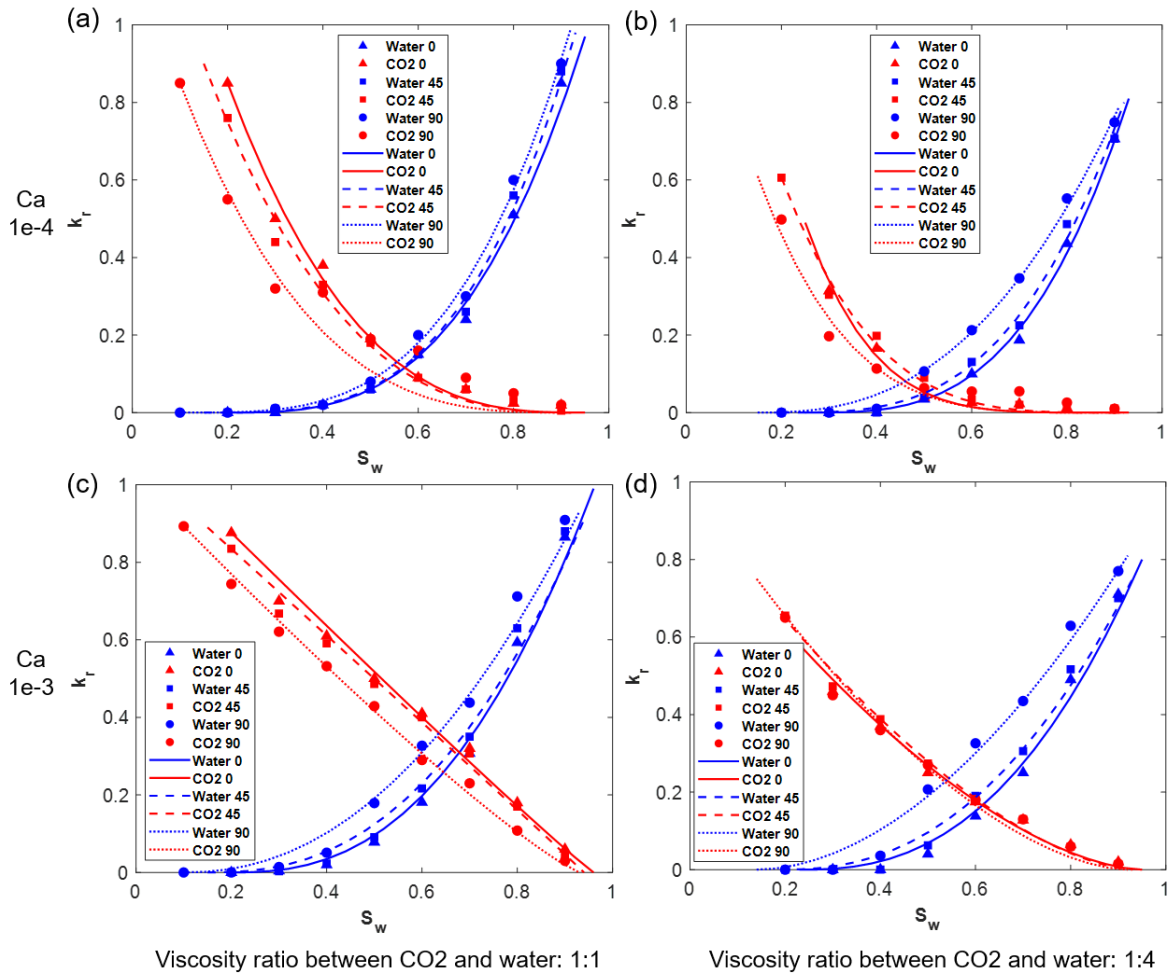


Figure 6.6. Relative permeability vs. water saturation ( $S_w$ ) curves under two Ca numbers ( $Ca=1\times 10^{-4}$  and  $Ca=1\times 10^{-3}$ ) and two viscosity ratios ( $M=0.25$  and  $M=1$ ). The data points are LB-simulated relative permeabilities and the curves are from Corey model fitting. Contact angles of  $0^\circ$ ,  $45^\circ$ , and  $90^\circ$  were simulated for each combination of Ca number and viscosity ratio. The computational domain was the middle section of the Berea sandstone sample.



#### 6.4.7 Effect of anisotropy and spatial heterogeneity

In previous numerical simulations, fluid flow was in the  $z$  direction (upward). In order to study the effect of flow direction anisotropy, we ran a LB simulation with flow in the  $-z$  direction (downward). Both LB simulations (upward and downward flow directions) were conducted on the middle-section Berea sandstone with  $Ca=1\times 10^{-4}$ ,  $M=0.25$ , and contact angle  $\theta = 0^\circ, 45^\circ, \text{ and } 90^\circ$ . From Figure 6.7a and 6.7b, it is observed that the relative permeability curves are slightly different between the two flow directions. Because the flow paths are heterogeneous, flipping the flow direction changes the final non-wetting fluid configuration in the 3D pore space even when all the other flow conditions are the same. This affects both the wetting and non-wetting fluid relative permeabilities measured in the final, steady state. The implication from this simulation is that multiphase fluid configurations assume different geometries in the 3D pore space depending on the flow direction.

On the same middle-section Berea sandstone sample and with the same  $Ca$  number and viscosity ratio, we simulated the multiphase flow scenario with flow in the  $x$  (horizontal) direction, as shown in Figure 6.7c. By comparing Figure 6.7a and Figure 6.7c, it can be found that the relative permeability curves for both fluids changed and the change in the non-wetting fluid relative permeability curves was larger after the flow direction was switched to the  $x$  direction. As discussed previously, the non-wetting fluid tends to occupy larger pore networks and to flow in the middle of channels, whereas the wetting fluid tends to occupy smaller pore networks and to flow near rock surfaces. The fact that the non-wetting fluid relative permeability experienced a more significant change after flow direction switch implies that the larger pore networks demonstrate stronger anisotropy (difference of flow path connectivity between the  $x$  and  $z$  directions) compared to the smaller pore networks. This is reasonable because the number of larger

pores is much less than that of smaller pores in sedimentary rocks [38, 73], leading to stronger anisotropic effects in the larger pore networks in terms of pore throat size and pore space connectivity, which consequently affects the relative permeability of the non-wetting fluid to a more noticeable extent.

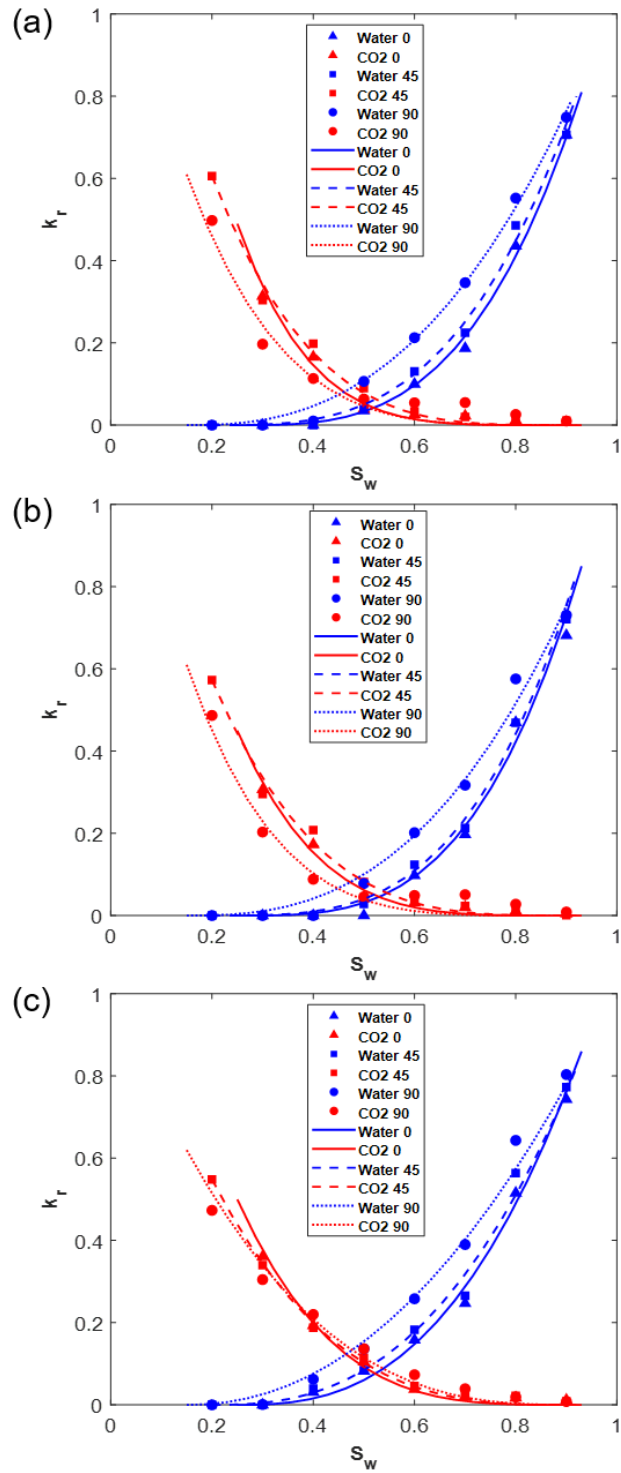


Figure 6.7. Relative permeability vs. wetting fluid saturation ( $S_w$ ) curves for fluid injection directions (a) from bottom to top in the  $z$  direction, (b) from top to bottom in the  $-z$  direction, and (c) in the horizontal ( $x$ ) direction. The simulations were conducted on the middle-section computational domain with  $Ca=1 \times 10^{-4}$  and  $M=0.25$ . The data points are LB-simulated relative permeabilities and the curves are from Corey model fitting.

We also conducted LB multiphase flow simulations in the top- and bottom-section computational domains, with  $Ca=1\times 10^{-4}$  and  $M=1$ . The flow direction was upward in the  $z$  (vertical) direction in both computational domains. The distance between top section center and bottom section center is 4.53 mm. Figure 6.8 illustrates that there were noticeable changes in both the wetting and non-wetting fluid relative permeability curves, which implies that pore geometry heterogeneity can be observed even over such a small distance. Therefore, special attention should be paid to these micro-scale heterogeneities for relative permeability analysis. Moreover, insight gained from the studies of small-scale heterogeneity will benefit the understanding of relative permeability upscaling in geologic formations.

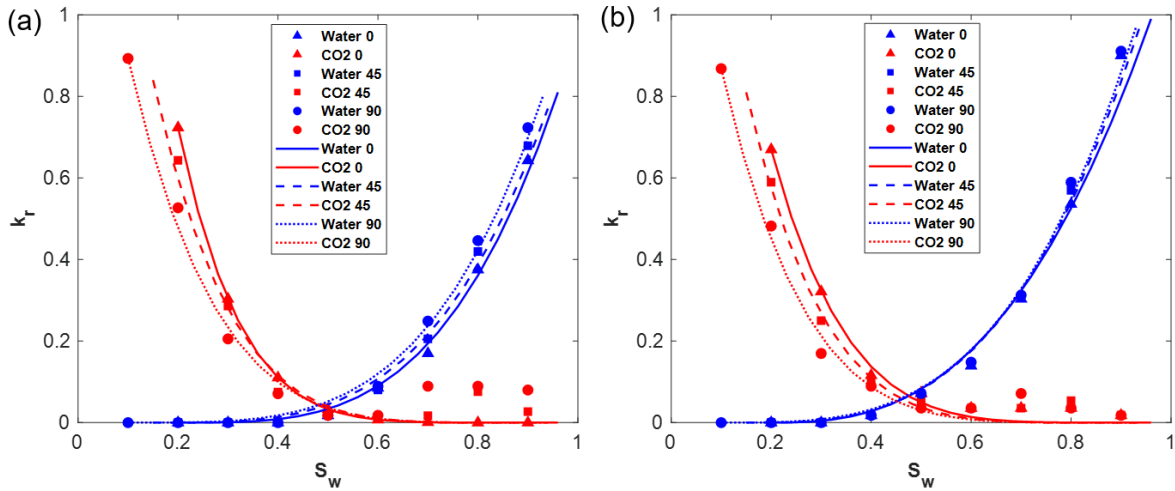


Figure 6.8. Relative permeability vs. wetting fluid saturation ( $S_w$ ) curves in the (a) top-section, and (b) bottom-section computational domains. In the simulations,  $Ca=1\times 10^{-4}$  and  $M=1$ . The data points are LB-simulated relative permeabilities and the curves are from Corey model fitting.

## 6.5. Conclusions

The main focus of this research is on the dependence of relative permeability curves on the contact angle,  $Ca$  number, viscosity ratio, as well as the various combinations

between them. The influence of anisotropy and micro-scale spatial heterogeneity of the rock sample on the relative permeability curves was also studied. The LB-simulated water/CO<sub>2</sub> distribution agreed well with the micro-CT-scanned water/CO<sub>2</sub> distribution, which validated the capability of the LB method in simulating multiphase flow in complex, 3D porous media. Simulation results showed that a decreasing contact angle causes a decrease in wetting fluid relative permeability and an increase in non-wetting fluid relative permeability. A rising Ca number increases both wetting and non-wetting fluid relative permeabilities, because the higher inertial force favors the mobility of both fluids. An increasing viscosity ratio facilitates the increase of non-wetting fluid relative permeability and mitigates the reduction of wetting fluid relative permeability, when the contact angle decreases continuously. This is because the lubrication effect is stronger when the wetting fluid viscosity is reduced, leading to enhanced non-wetting fluid relative permeability. The reduced wetting phase viscosity is also favorable for the mobility of the wetting fluid, which mitigates the decrease of the wetting fluid relative permeability when the contact angle decreases continuously. These phenomena demonstrated that the role of the changing contact angle on relative permeability curves depends primarily on both the viscosity ratio and Ca number.

In the literature, most works studied the role of viscosity ratio when the contact angle was fixed. Several groups reported that a larger viscosity ratio enhances the non-wetting fluid relative permeability whereas the wetting fluid relative permeability is relatively insensitive to the change of viscosity ratio at a fixed contact angle. In contrast, the primary novel finding of this study is that the viscosity ratio affects the rate of change of the relative permeability for both phases when the contact angle changes continuously.

This new finding is critical and has significant implications to geologic CO<sub>2</sub> storage because natural reservoir rocks have heterogeneous contact angles at the pore scale. To the best of our knowledge, it is the first time that comprehensive interactions between these dimensionless numbers are demonstrated in a real 3D sandstone sample using LB multiphase flow simulations. The simulation results are consistent with fundamental multiphase flow physics and imply that these critical dimensionless numbers, which are associated with water/CO<sub>2</sub> multiphase flows with respect to geologic carbon storage, are interconnected and must be studied in a holistic manner. We also investigated the role of the changes of fluid injection direction and sample location on relative permeability curves. Simulation results showed that the change in non-wetting fluid relative permeability was larger when the flow direction was switched from vertical to horizontal, which indicated that there was stronger anisotropy in larger pore networks that tended to be occupied by the non-wetting fluid.

The well-controlled core flooding and X-ray micro-CT experiments provided accurate pore structural information and pore-scale contact angle measurements as inputs for the LB multiphase flow model. Our future work will aim to study the role of sub-pore-scale heterogeneity of surface wettability on larger-scale relative permeability curves. In this paper, the combination of micro-CT imaging and LB multiphase flow simulation is a promising tool for advancing fundamental understanding of the interactions between the critical dimensionless numbers that regulate multiphase flow in complicated 3D pore space. Moreover, this study has the potential to advance fundamental understanding of the multiphysics processes associated with multiphase flow in geologic materials, which provides insight into upscaling methodologies that aim

to account for the influence of pore-scale processes in core- and larger-scale modeling frameworks.

### **Acknowledgements**

The authors acknowledge the support of the Junior Faculty Award from Virginia Tech's Institute for Critical Technology and Applied Science and the computational resources from Virginia Tech's Advanced Research Computing Center. The authors are also thankful to the support from the National Energy Technology Laboratory Research Participation Program, sponsored by the U.S. Department of Energy and administered by the Oak Ridge Institute for Science and Education.

### **Nomenclature**

$c$  : Lattice speed

$c_s$  : Speed of sound

$C$  : Color gradient

$Ca$  : Capillary number

$e_q$  : Lattice velocity vector

$f_q$  : Particle-distribution function

$\mathbf{g}$  : Gravity vector

$g_{iq}$  : Mass transport distribution

$\mathbf{j}$  : Fluid momentum

$\mathbf{k}$  : Permeability tensor

$k_{ri}$  : Relative permeability

$k_{rw}$  : Wetting phase relative permeability

$k_{ro}$  : Non-wetting phase relative permeability

$k_{rw}^o$  : End point of wetting phase saturation

$k_{ro}^o$  : End point of non-wetting phase saturation

$M_{iq}$  : Transformation matrix

$M_{qi}^*$  : Inverse of  $M_{iq}$

$m_i^{eq}$  : Equilibrium moments

$M$  : Viscosity ratio

$\mathbf{n}$  : Unit normal vector of the color gradient

$N_w$  : Corey wetting phase exponent

$N_o$  : Corey non-wetting phase exponent

$P$  : Fluid pressure

$\nabla p$  : Pressure gradient



$\rho_i$  : Density

$S_{wir}$  : Irreducible saturation of wetting phase

$S_{orw}$  : Residual saturation of non-wetting phase after wetting phase flooding

$S_w$  : Wetting phase saturation

$S_w^*$  : Normalized wetting phase saturation

$t$  : Time

$\Delta t$  : Time step

$\mathbf{u}$  : Flow velocity

$v_i$  : Darcy velocity

$u_t$  : Total average Darcy flow velocity

$\mu_{nw}$  : Dynamic viscosity of the non-wetting fluid

$\mu_w$  : Dynamic viscosity of the wetting fluid

$\mu_i$  : Dynamic viscosity

$\omega_q$  : Weights for D3Q7 model

$\Delta x$  : Lattice spacing

$\mathbf{x}$  : Location

$\varphi$  : Phase field indicator

$\Lambda_i$  : Rate of the relaxation process

$\alpha$  : A parameter that linearly related to the interfacial tension

$\beta$  : A parameter that controls the width of the interface

$\sigma$  : Interfacial tension between wetting and non-wetting fluids

## References

1. Chen, C. and D. Zhang, Pore-scale simulation of density-driven convection in fractured porous media during geological CO<sub>2</sub> sequestration. *Water Resources Research*, 2010. **46**(11).
2. Chen, C., L. Zeng, and L. Shi, Continuum-scale convective mixing in geological CO<sub>2</sub> sequestration in anisotropic and heterogeneous saline aquifers. *Advances in water resources*, 2013. **53**: p. 175-187.
3. Szulczewski, M.L., et al., Lifetime of carbon capture and storage as a climate-change mitigation technology. *Proceedings of the National Academy of Sciences*, 2012. **109**(14): p. 5185-5189.
4. Middleton, R.S., et al., The cross-scale science of CO<sub>2</sub> capture and storage: from pore scale to regional scale. *Energy Environmental Science*, 2012. **5**(6): p. 7328-7345.
5. Orr, j.F. and J. Taber, Use of carbon dioxide in enhanced oil recovery. *Science*, 1984. **224**(4649): p. 563-569.

6. Keller, A.A., M.J. Blunt, and P.V. Roberts, Behavior of nonaqueous phase liquids in fractured porous media under two-phase flow conditions. *Transport in Porous Media*, 2000. **38**(1-2): p. 189-203.
7. Aggelopoulos, C. and C. Tsakiroglou, The effect of micro-heterogeneity and capillary number on capillary pressure and relative permeability curves of soils. *Geoderma*, 2008. **148**(1): p. 25-34.
8. Tsakiroglou, C., D. Avraam, and A. Payatakes, Transient and steady-state relative permeabilities from two-phase flow experiments in planar pore networks. *Advances in water resources*, 2007. **30**(9): p. 1981-1992.
9. Avraam, D. and A. Payatakes, Flow mechanisms, relative permeabilities, and coupling effects in steady-state two-phase flow through porous media. The case of strong wettability. *Industrial engineering chemistry research*, 1999. **38**(3): p. 778-786.
10. Lenormand, R., E. Touboul, and C. Zarcone, Numerical models and experiments on immiscible displacements in porous media. *Journal of fluid mechanics*, 1988. **189**: p. 165-187.
11. Li, H., C. Pan, and C.T. Miller, Pore-scale investigation of viscous coupling effects for two-phase flow in porous media. *Physical Review E*, 2005. **72**(2): p. 026705.
12. Wei, N., et al., CO<sub>2</sub> flooding properties of Liujiagou sandstone: influence of sub-core scale structure heterogeneity. *Greenhouse Gases: Science Technology*, 2014. **4**(3): p. 400-418.

13. Goodman, A., et al., US DOE methodology for the development of geologic storage potential for carbon dioxide at the national and regional scale. *International Journal of Greenhouse Gas Control*, 2011. **5**(4): p. 952-965.
14. Krevor, S.C., et al., Relative permeability and trapping of CO<sub>2</sub> and water in sandstone rocks at reservoir conditions. *Water resources research*, 2012. **48**(2).
15. Ramstad, T., et al., Relative permeability calculations from two-phase flow simulations directly on digital images of porous rocks. *Transport in Porous Media*, 2012. **94**(2): p. 487-504.
16. Blunt, M.J., et al., Pore-scale imaging and modelling. *Advances in Water Resources*, 2013. **51**: p. 197-216.
17. Valvatne, P.H. and M.J. Blunt, Predictive pore-scale modeling of two-phase flow in mixed wet media. *Water resources research*, 2004. **40**(7).
18. Øren, P.-E. and S. Bakke, Reconstruction of Berea sandstone and pore-scale modelling of wettability effects. *Journal of Petroleum Science Engineering*, 2003. **39**(3-4): p. 177-199.
19. Ramstad, T., P.-E. Øren, and S. Bakke, Simulation of two-phase flow in reservoir rocks using a lattice Boltzmann method. *SPE Journal*, 2010. **15**(04): p. 917-927.
20. Yang, F., et al., Extraction of pore-morphology and capillary pressure curves of porous media from synchrotron-based tomography data. *Scientific reports*, 2015. **5**: p. 10635.

21. Blunt, M.J., et al., Detailed physics, predictive capabilities and macroscopic consequences for pore-network models of multiphase flow. *Advances in Water Resources*, 2002. **25**(8-12): p. 1069-1089.
22. Chen, C., et al., Optimization of lattice Boltzmann simulation with graphics-processing-unit parallel computing and the application in reservoir characterization. *SPE Journal*, 2016. **21**(04): p. 1,425-1,435.
23. Bernaschi, M., et al., A flexible high-performance Lattice Boltzmann GPU code for the simulations of fluid flows in complex geometries. *Concurrency Computation: Practice Experience*, 2010. **22**(1): p. 1-14.
24. McClure, J.E., J.F. Prins, and C.T. Miller, A novel heterogeneous algorithm to simulate multiphase flow in porous media on multicore CPU–GPU systems. *Computer Physics Communications*, 2014. **185**(7): p. 1865-1874.
25. Rinaldi, P.R., et al., A Lattice-Boltzmann solver for 3D fluid simulation on GPU. *Simulation Modelling Practice Theory*, 2012. **25**: p. 163-171.
26. Röhm, D. and A. Arnold, Lattice boltzmann simulations on gpus with espresso. *The European Physical Journal Special Topics*, 2012. **210**(1): p. 89-100.
27. Liu, H., et al., Multiphase lattice Boltzmann simulations for porous media applications. *Computational Geosciences*, 2016. **20**(4): p. 777-805.
28. Dou, Z. and Z.-F. Zhou, Numerical study of non-uniqueness of the factors influencing relative permeability in heterogeneous porous media by lattice Boltzmann method. *International Journal of Heat Fluid Flow*, 2013. **42**: p. 23-32.

29. Ghassemi, A. and A. Pak, Numerical study of factors influencing relative permeabilities of two immiscible fluids flowing through porous media using lattice Boltzmann method. *Journal of Petroleum Science Engineering*, 2011. **77**(1): p. 135-145.
30. Hao, L. and P. Cheng, Pore-scale simulations on relative permeabilities of porous media by lattice Boltzmann method. *International Journal of Heat Mass Transfer*, 2010. **53**(9-10): p. 1908-1913.
31. Huang, H., et al., Shan-and-Chen-type multiphase lattice Boltzmann study of viscous coupling effects for two-phase flow in porous media. *International journal for numerical methods in fluids*, 2009. **61**(3): p. 341-354.
32. Landry, C., Z. Karpyn, and O. Ayala, Relative permeability of homogenous-wet and mixed-wet porous media as determined by pore-scale lattice Boltzmann modeling. *Water Resources Research*, 2014. **50**(5): p. 3672-3689.
33. Yiotis, A.G., et al., A lattice Boltzmann study of viscous coupling effects in immiscible two-phase flow in porous media. *Colloids Surfaces A: Physicochemical Engineering Aspects*, 2007. **300**(1-2): p. 35-49.
34. Dalton, L.E., et al., Laboratory Foamed-Cement-Curing Evolution Using CT Scanning: Insights From Elevated-Pressure Generation. *SPE Drilling Completion*, 2018.
35. Dalton, L.E., et al., Foamed Cement Generation Methods: Insights from Macro-Porosity and Void Distribution. *ACI Materials Journal*, 2018. **115**(1).
36. Tudek, J., et al., In situ contact angle measurements of liquid CO<sub>2</sub>, brine, and Mount Simon sandstone core using micro X-ray CT imaging, sessile drop, and Lattice Boltzmann modeling. *Journal of Petroleum Science Engineering*, 2017. **155**: p. 3-10.

37. Dalton, L.E., et al., Methods to measure contact angles in scCO<sub>2</sub>-brine-sandstone systems. *Advances in water resources*, 2018. **122**: p. 278-290.
38. Chen, C., A.I. Packman, and J.F. Gaillard, Pore-scale analysis of permeability reduction resulting from colloid deposition. *Geophysical Research Letters*, 2008. **35**(7).
39. Chen, C., et al., Temporal evolution of pore geometry, fluid flow, and solute transport resulting from colloid deposition. *Water resources research*, 2009. **45**(6).
40. Chen, S. and G.D. Doolen, Lattice Boltzmann method for fluid flows. *Annual review of fluid mechanics*, 1998. **30**(1): p. 329-364.
41. Succi, S., *The lattice Boltzmann equation: for fluid dynamics and beyond*. Oxford university press. 2001: Oxford university press.
42. Li, Q., et al., Lattice Boltzmann methods for multiphase flow and phase-change heat transfer. *Progress in Energy Combustion Science*, 2016. **52**: p. 62-105.
43. Chen, L., et al., A critical review of the pseudopotential multiphase lattice Boltzmann model: Methods and applications. *International journal of heat mass transfer*, 2014. **76**: p. 210-236.
44. Chen, H., S. Chen, and W.H. Matthaeus, Recovery of the Navier-Stokes equations using a lattice-gas Boltzmann method. *Physical Review A*, 1992. **45**(8): p. R5339.
45. Succi, S., R. Benzi, and F. Higuera, The lattice Boltzmann equation: a new tool for computational fluid-dynamics. *Physica D: Nonlinear Phenomena*, 1991. **47**(1-2): p. 219-230.

46. Coon, E.T., M.L. Porter, and Q. Kang, Taxila LBM: a parallel, modular lattice Boltzmann framework for simulating pore-scale flow in porous media. *Computational Geosciences*, 2014. **18**(1): p. 17-27.
47. Grunau, D., S. Chen, and K. Eggert, A lattice Boltzmann model for multiphase fluid flows. *Physics of Fluids A: Fluid Dynamics*, 1993. **5**(10): p. 2557-2562.
48. Han, Y. and P.A. Cundall, Lattice Boltzmann modeling of pore-scale fluid flow through idealized porous media. *International Journal for Numerical Methods in Fluids*, 2011. **67**(11): p. 1720-1734.
49. Han, Y. and P.A. Cundall, LBM–DEM modeling of fluid–solid interaction in porous media. *International Journal for Numerical Analytical Methods in Geomechanics*, 2013. **37**(10): p. 1391-1407.
50. Gunstensen, A.K., et al., Lattice Boltzmann model of immiscible fluids. *Physical Review A*, 1991. **43**(8): p. 4320.
51. Pan, C., L.-S. Luo, and C.T. Miller, An evaluation of lattice Boltzmann schemes for porous medium flow simulation. *Computers fluids*, 2006. **35**(8-9): p. 898-909.
52. Fan, M., et al. Interaction between Proppant Packing, Reservoir Depletion, and Fluid Flow in Hydraulic Fractures. *Offshore Technology Conference*. 2017.
53. Fan, M., et al., Interaction between proppant compaction and single-/multiphase flows in a hydraulic fracture. *SPE Journal*, 2018. **23**(04): p. 1,290-1,303.
54. Anderson, W.G., Wettability literature survey-part 1: rock/oil/brine interactions and the effects of core handling on wettability. *Journal of petroleum technology*, 1986. **38**(10): p. 1,125-1,144.



55. Iglauer, S., C. Pentland, and A. Busch, CO<sub>2</sub> wettability of seal and reservoir rocks and the implications for carbon geo-sequestration. *Water Resources Research*, 2015. **51**(1): p. 729-774.
56. Anderson, W.G., Wettability literature survey part 5: the effects of wettability on relative permeability. *Journal of Petroleum Technology*, 1987. **39**(11): p. 1,453-1,468.
57. Donaldson, E.C. and R.D. Thomas. Microscopic observations of oil displacement in water-wet and oil-wet systems. Fall Meeting of the Society of Petroleum Engineers of AIME. 1971.
58. Blunt, M. and P. King, Relative permeabilities from two-and three-dimensional pore-scale network modelling. *Transport in porous media*, 1991. **6**(4): p. 407-433.
59. Zhao, H., et al., Relative permeability of two immiscible fluids flowing through porous media determined by lattice Boltzmann method. *International Communications in Heat Mass Transfer*, 2017. **85**: p. 53-61.
60. Gu, Q., H. Liu, and Y. Zhang, Lattice Boltzmann Simulation of Immiscible Two-Phase Displacement in Two-Dimensional Berea Sandstone. *Applied Sciences*, 2018. **8**(9): p. 1497.
61. Boek, E.S. and M. Venturoli, Lattice-Boltzmann studies of fluid flow in porous media with realistic rock geometries. *Computers Mathematics with Applications*, 2010. **59**(7): p. 2305-2314.
62. Li, R., et al., Lattice Boltzmann modeling of permeability in porous materials with partially percolating voxels. *Physical Review E*, 2014. **90**(3): p. 033301.

63. Alpak, F., S. Berg, and I. Zacharoudiou, Prediction of fluid topology and relative permeability in imbibition in sandstone rock by direct numerical simulation. *Advances in Water Resources*, 2018. **122**: p. 49-59.
64. Liu, H., et al., Pore-scale simulations of gas displacing liquid in a homogeneous pore network using the lattice Boltzmann method. *Transport in porous media*, 2013. **99**(3): p. 555-580.
65. Liu, H., et al., Pore-scale simulation of liquid CO<sub>2</sub> displacement of water using a two-phase lattice Boltzmann model. *Advances in water resources*, 2014. **73**: p. 144-158.
66. Armstrong, R.T., et al., Flow regimes during immiscible displacement. *Petrophysics*, 2017. **58**(01): p. 10-18.
67. Armstrong, R.T., et al., Beyond Darcy's law: The role of phase topology and ganglion dynamics for two-fluid flow. *Physical Review E*, 2016. **94**(4): p. 043113.
68. Chen, C. and D. Zhang, Lattice Boltzmann simulation of the rise and dissolution of two-dimensional immiscible droplets. *Physics of fluids*, 2009. **21**(10): p. 103301.
69. Blunt, M., M.J. King, and H. Scher, Simulation and theory of two-phase flow in porous media. *Physical Review A*, 1992. **46**(12): p. 7680.
70. Odeh, A., Effect of Viscosity Ratio on Relative Permeability Doctoral dissertation, University of California, Los Angeles--Engineering, 1959.
71. Avraam, D. and A. Payatakes, Generalized relative permeability coefficients during steady-state two-phase flow in porous media, and correlation with the flow mechanisms. *Transport in Porous Media*, 1995. **20**(1-2): p. 135-168.

72. Avraam, D. and A. Payatakes, Flow regimes and relative permeabilities during steady-state two-phase flow in porous media. *Journal of Fluid Mechanics*, 1995. **293**: p. 207-236.
73. Chen, C., A.I. Packman, and J.F. Gaillard, Using X-ray micro-tomography and pore-scale modeling to quantify sediment mixing and fluid flow in a developing streambed. *Geophysical Research Letters*, 2009. **36**(8).

## **Chapter 7 Combining Discrete Element Method with Lattice Boltzmann Modeling to Advance the Understanding of the Slow Migration of Detached Fine Particles through a Proppant Supported Fracture**

Ming Fan, Cheng Chen, Virginia Tech

### **Abstract**

Many of the hydrocarbon-bearing formations are composed of smaller sand grains and fine clay particles. During hydrocarbon production, pore pressure reduces, and thus the effective stress of the rock matrix increases, which leads to formation failure and fine particles production within the formation fluids. Invasion of fines into the proppant pack can affect proppant pack permeability, and subsequent conductivity loss. A discrete element method-lattice Boltzmann (DEM-LB) numerical framework was proposed to study the mechanism of fine particle migration in the proppant pack during reservoir depletion process. DEM was used to generate proppant packs and simulate effective stress increase and the resultant proppant compaction. Then, the DEM-simulated pore structure of the compacted proppant pack was extracted and imported into the LB simulator as internal boundary conditions for fluid flow modeling. Good match between the DEM-LB framework modeled and empirical correlations predicted deposition rates has been observed. Results of conducted simulations provided that a particle size with a minimum contact opportunity existed; smaller particles were transported by Brownian diffusion while larger particles were transported by interception and settling. This study indicates that proppant packs with a more heterogeneous particle-diameter distribution provide better fines control. The proposed computational framework can be used to effectively model fines of varying sizes migration at a pore scale. In practice, our DEM-

LB framework provides insights into fine particles migration through the compressed proppant pack, which helps control fines migration in reservoirs suffering from fines migration problems.

### **Keywords**

Fines Migration, Deposition Rate, Proppant Pack, Discrete Element Method, Lattice Boltzmann

### **7.1 Introduction**

Fines or fine particles are defined as loose or unconsolidated particles in porous media. These fines generally possess the colloidal characteristics with an equivalent spherical diameter between 1 nm and 10  $\mu\text{m}$  [1] and are usually small enough to pass through 400-US-mesh screens [2, 3]. In nature, these fines may be precipitated solids, like plutonium, soil materials, like clay, and biological materials, like viruses or bacteria [1]. Since they can stay in suspension in porous media for a long time due to small settling velocity, fine particle migration and associated internal structure of porous media erosion are challenging problems of both scientific and industrial importance. Many applications can be found in fields such as petroleum extraction, environmental, and water resources technologies. During oil and gas production, fines migration can cause damage throughout the fracture, consequently reducing fracture permeability and well productivity over time. Wastewater treatment and disposal are also highly dependent on maintenance of permeability to prevent suspended particle clogging in the soil column or aquifer [4]. Since the fines or pollutants can be transported by fluids, it is vital to develop a mechanistic analysis of fine particle migration through porous media.

As hydrocarbons are produced from a reservoir, an infinite supply of fines or loose particles provided by the reservoir formation would continuously invade into the proppant pack [5]. A common assumption in the oil and gas industry is that, it is better for the fines released from formations to migrate through the proppant pack in a propped fracture [6]. However, in an induced hydraulic fracture, because of increasing effective stress, proppant compaction, crushing, and embedment into rock formations occur, which result in changes to the pore structure and connectivity. As a result, the fine particles may get retained in the proppant pack easily, resulting in permeability loss and subsequent production decline.

Gravel pack completions were typically designed to minimize fines invasion into the proppant pack and maximize conductivity [6-8]. Many studies showed that a stable proppant pack and suitable proppant size in a propped fracture is the key in preventing formation fines damage [9, 10]. Weaver et al. [11] stated that choosing the optimal proppant size in frack-pack design is favorable for controlling fines migration. Since the reservoir depletion process during hydrocarbon production often leads to complex pore geometries in the proppant pack, fine particles with variable sizes may cause straining in the pore throat, which as a result, influences the fluids transport through the reservoir. Therefore, understanding the effect of proppant particle size and proppant pack pore structure changes under increasing effective stress on the fines migration is paramount to minimize formation fines damage.

According to Mohnot's study [12], the median size of fine particles is around 10  $\mu\text{m}$ , however, there is still a large portion (>30%) of clay particles suspended in petroleum reservoirs being about 1  $\mu\text{m}$  in size or smaller. Since the transport of fine particles with

different sizes are dominant by different migration mechanisms, a pore-scale understanding of the mechanisms controlling fines migration for different fine particle sizes is required. However, fines migration studies are usually performed in field scale and core scale laboratory experiments [13-15], which are unable to resolve the pore-scale phenomena of fine particle migration process and internal erosion of a proppant pack. This poses a need to establish a numerical model that can track the migration of fine particles at pore scale, which is critical to characterize the effects of fines migration on consequent permeability impairment in the proppant pack.

Fine particle migration is fundamentally controlled by pore fluid flow [16-19]. The migration of fines through porous space involves at least two steps: first, the transport of fine particles to the immediate vicinity of the solid-liquid interface; and second, the attachment of particles to this surface [16]. Cooksen [20] proposed a model to predict the fine particle migration trajectory in low liquid speeds, and stated that the fine particle may deviate from streamlines depending on the fine particle size. Other transport models presented by Spielman and Goren [21] and Yao et al. [16] predicted that larger fine particles ( $> 1\ \mu\text{m}$ ) are transported by interception and gravitational sedimentation; smaller particles are transported by Brownian diffusion. Therefore, a particle size with a largest filtration depth exists. According to Yao et al.'s study [16], the critical suspended particle size is around  $1\ \mu\text{m}$  in conventional water filtration practice. The emphasis in the paper will be the particle deposition in porous media, rather than the chemical reaction effects that affect the porous media geometrical structure.

Typically, the key components in evaluating fine particle migration through porous media are the internal pore structure and pore fluid flow. In this study, the discrete

element method (DEM) is used to generate proppant packs and model proppant pack compaction. DEM has proven to be very efficient to simulate the compaction of granular materials [22-25]. The discretized pore structures from proppant packs can be used as interior boundary conditions for lattice Boltzmann (LB) simulating fluid flow in the compressed pore space. The LB method simulates the fluid flow at a pore scale, which is suitable to obtain pore scale flow characteristics of a proppant pack in this study [19, 26]. Here, we combined DEM and LB methods to evaluate the role of proppant particle size heterogeneity (variation in proppant particle diameter) and effective stress on slow migration of detached fine particles in a proppant supported fracture. The findings of this study shed lights on the relationship between changing pore geometries, fluid flow, and fines migration through a propped hydraulic fracture during reservoir depletion process.

## 7.2 Methods

### 7.2.1 Models for Particle Migration through Porous Media

When particles migrate through a pore structure, deposited particles accumulate within porous media and alter the porous media surface. The particle removal from the solution equals particle accumulation in the porous media, as illustrated in Equation 7.1.

$$U \cdot dC \cdot A_{cs} \cdot dt = -\alpha \cdot (A_{cs} \cdot dx \cdot \phi \cdot C) \cdot dt \quad (7.1)$$

where  $C$  is particle mass concentration in the fluid ( $\text{kg}/\text{m}^3$ );  $U$  is fluid flow velocity ( $\text{m}/\text{s}$ );  $A_{cs}$  is the pore structure cross section area ( $\text{m}^2$ );  $x$  is the distance along the flow direction ( $\text{m}$ );  $t$  is time ( $\text{s}$ );  $\phi$  is porosity;  $\alpha$  is the rate of fine particle attached to porous media ( $\text{s}^{-1}$ )



<sup>1</sup>), which is the fraction of the suspended particles that deposit on grain surfaces per unit time. After rearranging equation 7.1, the filtration equation is given by

$$\frac{dC}{C} = -\alpha\phi \frac{dx}{U} \quad (7.2)$$

After integrating Equation 7.2 on both sides, the resulting particle mass concentration is

$$C = e^{(-\frac{\alpha\phi}{U}x+b')} = be^{-\frac{\alpha\phi}{U}x} \quad (7.3)$$

where  $b$  is a constant. When the influent particle concentration is  $C_0$  ( $x=0$ ), the constant  $b$  in Equation 7.2 can be determined, which is equal to  $C_0$ . The particle mass concentration along the flow direction is then obtained, as shown in Equation 7.4.

$$C = C_0 e^{-\frac{\alpha\phi}{U}x} \quad (7.4)$$

By defining the deposition rate ( $m^{-1}$ ),  $\lambda = \alpha\phi/U$ , one obtains the empirical particle concentration equation. The concentration of suspended particles declines exponentially along the flow direction in the porous media, as illustrated in Equation 7.5.

$$C = C_0 e^{-\lambda x} \quad (7.5)$$

As deposited particles accumulates within the pore space, the porous media surface is coated with attached particles. The analysis of particle deposit accumulation considers a mass balance between the fine particle concentration in the pore fluid ( $kg/m^3$ ),  $C$ , and the deposited particle concentration on solid surfaces ( $kg/m^3$ ),  $\sigma$ . This mass balance expression is given by:

$$U \cdot dC \cdot A_{cs} \cdot dt = -A_{cs} \cdot dx \cdot d\sigma \quad (7.6)$$

After rearrangement, one obtains

$$\frac{\partial \sigma}{\partial t} = -U \frac{\partial C}{\partial x} \quad (7.7)$$

Substituting Equation 7.5 into Equation 7.7 gives

$$\sigma = tUC_0\lambda e^{-\lambda x} + b_2 \quad (7.8)$$

where  $b_2$  is a constant,  $t$  is the time. At location  $x=0$ , time  $t=0$ , the particle deposition is 0,  $\sigma(x=0, t=0) = b_2 = 0$ . The distribution of deposited particles as a function of time and distance within a porous media can be represented by equation 7.9 [4]:

$$\sigma(x, t) = tUC_0\lambda e^{-\lambda x} \quad (7.9)$$

Particle migration following streamlines may collide with the solid surfaces by means of interception, which is described by the second term on the right hand side of Equation 7.10. When the particle is relatively large, the gravitational settling can cause particles to deviate from fluid streamlines and collide with the media surface, which is illustrated as the third term in Equation 7.10. When the particle size is relatively small, less than a micrometer, the particle bombards randomly in the porous medium and the dominant particle transport mechanism is Brownian motion, defined as the fourth term of Equation 7.10. Therefore, the suspended particles flowing through porous media is dominated by three transport mechanisms, namely interception, sedimentation, and Brownian motion. Particle migration through porous media is defined by Equation 7.10.

$$\mathbf{x}(t + \Delta t) = \mathbf{x}(t) + \mathbf{v}(\mathbf{x}(t)) \cdot \Delta t + \mathbf{v}_s(\mathbf{x}(t)) \Delta t + \sqrt{6D\Delta t} \boldsymbol{\xi} \quad (7.10)$$

$$v_s = \frac{2(\rho_p - \rho_f)}{9\mu} gr^2 \quad (7.11)$$

$$D = \frac{k_b T}{6\pi r \mu} \quad (7.12)$$

where  $v$  is convection velocity;  $v_s$  is the Stokes settling velocity of a spherical particle;  $D$  is the diffusivity of dilute solution;  $k_b$  is the Boltzmann constant,  $1.38 \times 10^{-23} \text{ m}^2 \text{ kg/s}^2 \text{ K}^{-1}$ ;  $T$  is the absolute temperature;  $r$  is the solute particle radius,  $\mu$  is the dynamic viscosity, (kg/ms);  $g$  is the gravitational acceleration ( $\text{m/s}^2$ );  $\rho_p$  is the mass density of particles ( $\text{kg/m}^3$ );  $\rho_f$  is the mass density of the fluid ( $\text{kg/m}^3$ ).

The clean bed deposition coefficient can be determined by an empirical correlation given by McDowell [4]. In this empirical correlation, particle transport is influenced by the mechanisms of Brownian motion, interception, and gravitational settling, and these displacements are additive. The first term within the brackets of Equation 7.13 accounts for Brownian motion mechanism, the second term represents the interception collection, and the gravitational sedimentation is represented by the third term, which strongly depends on the ratio of fine particle Stokes settling velocity to the fluid flow velocity. The empirical correlation model is described by

$$\lambda = \frac{3(1-\phi)}{2} \frac{1}{d_m} \left[ 4A_s^{1/3} \left( \frac{Ud_m}{D} \right)^{-2/3} + 0.56A_s \left( \frac{A}{\mu d_p^2 U} \right)^{1/8} \left( \frac{d_p}{d_m} \right)^{15/8} + 2.4 \times 10^{-3} A_s \left( \frac{v_s}{U} \right)^{1.2} \left( \frac{d_p}{d_m} \right)^{-0.4} \right] \quad (7.13)$$

where  $d_m$  is media diameter,  $d_p$  is particle diameter,  $A$  is the Hamaker's constant with a typical value in the range of  $10^{-13}$  to  $10^{-12}$  erg.  $A_s$  is a parameter correcting particle capture by a single isolated collector for capture within a packed porous media with

$$A_s = \frac{1 - \varphi^5}{1 - 1.5\varphi + 1.5\varphi^5 - \varphi^6} \quad (7.14)$$

where  $\varphi = (1 - \phi)^{1/3}$ .

### **7.3 Overview of Numerical Workflow**

In this study, Particle Flow Code 3D (PFC3D) was used for DEM modeling to simulate proppant particle movement and rearrangement under increasing mechanical loading due to reservoir depletion. An in-house numerical code was developed to discretize the pore structure of the proppant pack and imported it into the lattice Boltzmann (LB) simulator as boundary conditions to simulate single-phase flows in the compressed pore space. Using the DEM-LB numerical workflow, one can obtain the pore structure geometry and pore scale flow characteristics to study the fine migration through the compressed proppant pack. The following subsections provide details of the model's components.

#### **7.3.1 Basics of PFC3D**

PFC3D is a three-dimensional (3D) discontinuum mechanics simulator [27]. It describes the movement and interaction of rigid, spherical particles using the DEM scheme, which was first introduced by Cundall [28] for the analysis of rock mechanics problems and then applied to soils by Cundall and Strack [29]. In PFC3D, the spherical particles are generated independently and interact only at contacts or interfaces. The calculation cycle adopts a time-stepping algorithm, in which the position and velocity of each particle is determined by Newton's second law of motion, and the force-displacement relation is used to update the contact force at each contact. During simulation, contacts can be

created and separated simultaneously. However, Newton's second law of motion is not applied to boundary walls, since the motion of walls is specified by the user. The force-displacement relation is applied at each contact point, which is defined by a unit normal vector,  $n_i$ . When particles come into contact, the contact force is generated, the magnitude of which is determined by the relative displacement and specified stiffness between the two particles. The contact force can be decomposed into normal and shear components with respect to the contact plane, as illustrated in Equation 7.15. The normal contact force is computed by Equation 7.16. The magnitude of the shear contact force is initialized as zero and then incremented at each time step, as determined by Equation 7.17 [27].

$$F_i = F_i^n + F_i^s \quad (7.15)$$

$$F_i^n = K^n U^n n_i \quad (7.16)$$

$$\Delta F_i^s = -k^s \Delta U_i^s \quad (7.17)$$

In these equations,  $F_i^n$  and  $F_i^s$  denote the normal and shear components of contact force;  $K^n$  is the normal stiffness at the contact, which relates total normal displacement to force;  $k^s$  is the shear stiffness, which relates incremental shear displacement to force;  $U^n$  is the contact displacement in the normal direction, and  $U_i^s$  is the shear component of the contact displacement.

### 7.3.2 Discretization of 3D Proppant Pore Structure

3D proppant pore structures from DEM simulations were discretized, extracted, and imported into the LB model as boundary conditions to simulate pore-scale, single phase flows in the compressed pore space. Specifically, the 3D pore geometry was discretized

using a 3D mesh grid with a resolution of 0.05 mm/pixel in the x-, y-, and z-directions. When the average proppant particle diameter is close to 1 mm, which is 20 times larger than the pixel size, the proppant pack geometry is well resolved with this resolution.

### 7.3.3 Lattice Boltzmann Method for Single-Phase Flow Simulation

The LB method is a numerical method for solving the Navier-Stokes equations and based on microscopic physical models and mesoscale kinetic equations [30, 31]. In comparison with conventional fluid dynamic models, the LB method has many advantages. For example, it is explicit in evolution equation, simple to implement, natural to parallelize [32, 33], and easy to incorporate new physics such as interactions at fluid-solid interface [34-36].

The LB simulator used in this study has been validated by direct comparisons with analytical solutions and laboratory measurements [19, 37, 38]. It was then optimized with high-performance graphics processing unit (GPU) parallel computing, which enhances the computational speed by a factor of 1,000 and led to an in-house LB code, GPU-enhanced lattice Boltzmann simulator (GELBS) [39]. In this work, the D3Q19 lattice structure (19 velocity vectors in 3D space) was used because of its advantage in keeping a good balance between computational stability and efficiency [38].

Particle distribution in the Bhatnagar-Gross-Krook (BGK)-based, single-relaxation-time LB equation is given by

$$f_i(\mathbf{x} + \mathbf{e}_i \Delta t, t + \Delta t) = f_i(\mathbf{x}, t) - \frac{f_i(\mathbf{x}, t) - f_i^{eq}(\rho, \mathbf{u})}{\tau}, \quad (i = 0, 1, 2 \dots 18) \quad (7.18)$$

where  $f_i(\mathbf{x},t)$  is the particle-distribution function specifying the probability that fluid particles at lattice location  $\mathbf{x}$  and time  $t$  travel along the  $i^{\text{th}}$  direction;  $\mathbf{e}_i$  is the lattice velocity vector corresponding to direction  $i$ , defined as:

$$\mathbf{e}_i = c \begin{bmatrix} 0 & 1 & -1 & 0 & 0 & 0 & 0 & 1 & -1 & 1 & -1 & 0 & 0 & 0 & 0 & 1 & -1 & 1 & -1 \\ 0 & 0 & 0 & 1 & -1 & 0 & 0 & 1 & 1 & -1 & -1 & 1 & -1 & 1 & -1 & 0 & 0 & 0 & 0 \\ 0 & 0 & 0 & 0 & 0 & 1 & -1 & 0 & 0 & 0 & 0 & 1 & 1 & -1 & -1 & 1 & 1 & -1 & -1 \end{bmatrix}$$

where  $c = \Delta x / \Delta t$ , in which  $\Delta x$  is the lattice spacing and  $\Delta t$  is the time step;  $\tau$  is the dimensionless relaxation time related to kinematic viscosity by  $\nu = (2\tau - 1)\Delta x^2 / 6\Delta t$ ;  $f_i^{eq}(\rho, \mathbf{u})$  is the equilibrium distribution function selected to recover the macroscopic Navier-Stokes equations and given by

$$f_i^{eq}(\rho, \mathbf{u}) = \omega_i \rho \left[ 1 + \frac{3\mathbf{e}_i \cdot \mathbf{u}}{c^2} + \frac{9(\mathbf{e}_i \cdot \mathbf{u})^2}{2c^4} - \frac{3\mathbf{u}^2}{2c^2} \right] \quad (7.19)$$

where  $\omega_i$  is the weight coefficient calculated as:

$$\omega_i = \begin{cases} 1/3 & i = 0 \\ 1/18 & i = 1 \dots 6 \\ 1/36 & i = 7 \dots 18 \end{cases}$$

The macroscopic fluid density and velocity are calculated with the following two equations:

$$\rho = \sum_{i=0}^{18} f_i \quad (7.20)$$

and

$$\mathbf{u} = \frac{\sum_{i=0}^{18} f_i \mathbf{e}_i}{\rho} \quad (7.21)$$

Fluid pressure is calculated using  $p = c_s^2 \rho$ , where  $c_s$  is the speed of sound. In the LB *D3Q19* model,  $c_s^2 = c^2/3$ .

In practice, two-relaxation-time and multi-relaxation-time LB schemes have been developed to mitigate numerical instability in simulating high-Reynolds-number flows and avoid nonlinear dependency of numerical error on fluid viscosity [40, 41]. In this study, we replaced the BGK-based collision operator with a two-relaxation-time collision operator and selected the optimal combination of the symmetric and asymmetric eigenfunctions [42] in order to reduce numerical errors resulting from the bounce-back boundary condition.

For fluid flow simulation, we imposed a periodic boundary condition with a constant pressure difference,  $\Delta P$ , in the longitudinal direction and no-slip boundary conditions on the four lateral sides and interior solid surfaces [19, 43]. The Reynolds number was always much smaller than one to ensure that the macroscopic flow was well within the Darcy regime. A small pressure difference,  $\Delta P$ , generated an adequately small Mach number and density variation, which are necessary for accurate simulation of incompressible flows using the LB method. More details about the LB simulator and associated GPU optimization can be found in our previous papers [23, 24, 39].

At the continuum scale, the Darcy velocity,  $\mathbf{v}$ , is calculated by averaging the pore-scale flow velocity,  $\mathbf{u}$ , of each lattice node in the pore space throughout the entire computational domain. One can calculate the permeability tensor using the Darcy's law:

$$\mathbf{v} = -\frac{1}{\mu} \mathbf{k} \cdot \nabla p \quad (7.22)$$



where,  $\mathbf{v} = [v_x, v_y, v_z]^T$  is the Darcy velocity,  $\mathbf{k} = k_{ij} (i, j = x, y, z)$  is the permeability tensor, with  $i$  being the flow direction and  $j$  being the pressure gradient direction,  $\nabla p$  is the pressure gradient, and  $\mu$  is the dynamic viscosity of the fluid. The principal components of the permeability tensor are noted as  $k_{xx}$ ,  $k_{yy}$ , and  $k_{zz}$ . Since the principal directions of the permeability tensor in this study are the same as the principal coordinate direction, the off-diagonal elements in the permeability tensor are zero, written as  $k_{ij} = 0 (i \neq j)$ .

#### 7.4 Pore Structure Generation

Two proppant packs having the same average particle diameter but different size distributions were generated, as shown in Figure 7.1. The effective stress on the proppant packs is slowly increased up to 6000 psi. The proppant packs were compressed in the z-direction (the direction normal to fracture face) at a constant velocity, which was adequately slow to avoid rapid surge of effective stress between proppant particles and allow fluid within the pore space to flow away in the lateral (x-y) directions. In this way, the system was in the pseudo-steady state, where the transient pore-pressure changed and resultant stress acting on the proppant particles were negligible [23, 24]. In this study, a high strength ceramic proppant properties (e.g., stiffness and density) were used in all the simulations with the purpose of avoiding proppant crushing under high effective stresses. In addition, the higher sphericity of ceramic proppant minimize fines entrapment and subsequent permeability reduction within the proppant pack.

The initial dimension of the proppant pack was 20 mm  $\times$  20 mm  $\times$  20 mm. Proppant packs were generated following the 20/40 mesh size with an assumption of uniform

distribution of particle diameter between mesh 20 and mesh 40. The coefficient of variation (COV) of particle diameter is defined as the ratio of standard deviation of particle diameter to mean particle diameter, and two diameter COVs 5% and 25% were selected. Therefore, the two proppant packs had the same mean particle diameter but different diameter COVs, with one being 5% and the other being 25%, which suggests that one was more homogeneous whereas the other was more heterogeneous in terms of proppant size distribution. The proppant packs were discretized at a spatial resolution of 0.05 mm per LB length unit. In the LB simulation of Darcy flow, a pressure gradient was imposed along the x and y directions to drive single phase fluid flow through the pore space of the proppant assembly. We then generated multiple pairs of proppant packs with diameter COV being 5% and 25% to study the fine particle migration through the compressed proppant packs. In this paper, we assumed that the fines were generated mainly from reservoir formation rather than from ceramic proppants.

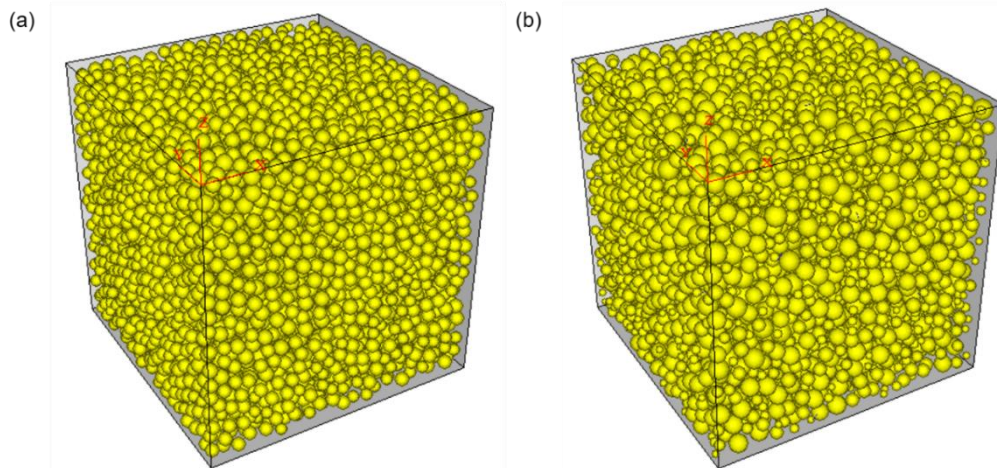


Figure 7.1. Proppant packs generated using PFC3D with diameter COV (a) 5% (b) 25%

## 7.5 Results and Discussion

Figure 7.2 illustrates LB-simulated pressure distributions within a 2D cross section cut along the x-y plane at the fracture center for proppant assemblies having diameter COVs of 5% and 25%. The pressure is presented in the LB unit. It can be seen that the proppant pack with diameter COV of 5% had a more homogeneous pore geometry whereas the proppant pack with diameter COV of 25% had a more heterogeneous pore geometry, because a higher diameter COV leads to a wider particle diameter distribution. Since all the simulations were conducted under  $Re$  numbers much lower than one, the flow was in the Darcy regime.

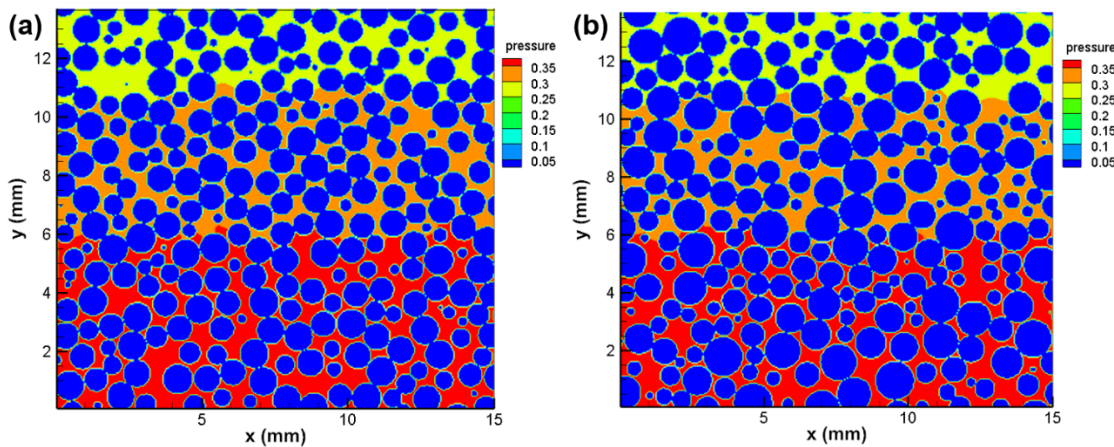


Figure 7.2. LB-simulated pressure distributions within the pore space of proppant assemblies having a) 5% diameter COV, and b) 25% diameter COV.

Figure 7.3 illustrates LB-simulated flow-velocity-magnitude distributions and associated velocity fields within the 2D central cross section, when the effective stress was 1000 psi and 6000 psi. Flow-velocity magnitude was presented in the LB unit. Figure 7.3a shows that, when the effective stress was 1000 psi, pore size was relatively large, and there existed multiple high-flow-velocity regions within the pore space, which suggested relatively good connectivity of the pore space. Conversely, under an effective stress of

6000 psi, proppant-assembly compaction was noticeable, pore-space connectivity was consequently reduced, leading to significant flow velocity reduction in preferential flow paths. The distribution of flow paths also illustrates that the streamlines converge at constrictions and diverge in zones of larger cross sections. This indicates that a particle may easily pass close to the grain surface when following converging streamlines and flow far away from grain surface when following diverging streamlines. The extent of deviations of fine particles from streamlines depends on particle size. When the size of particle is small, the Brownian motion dominates the particle migration; when the particle size is sufficiently large, the gravitational sedimentation mechanism dominates the migration of fines.

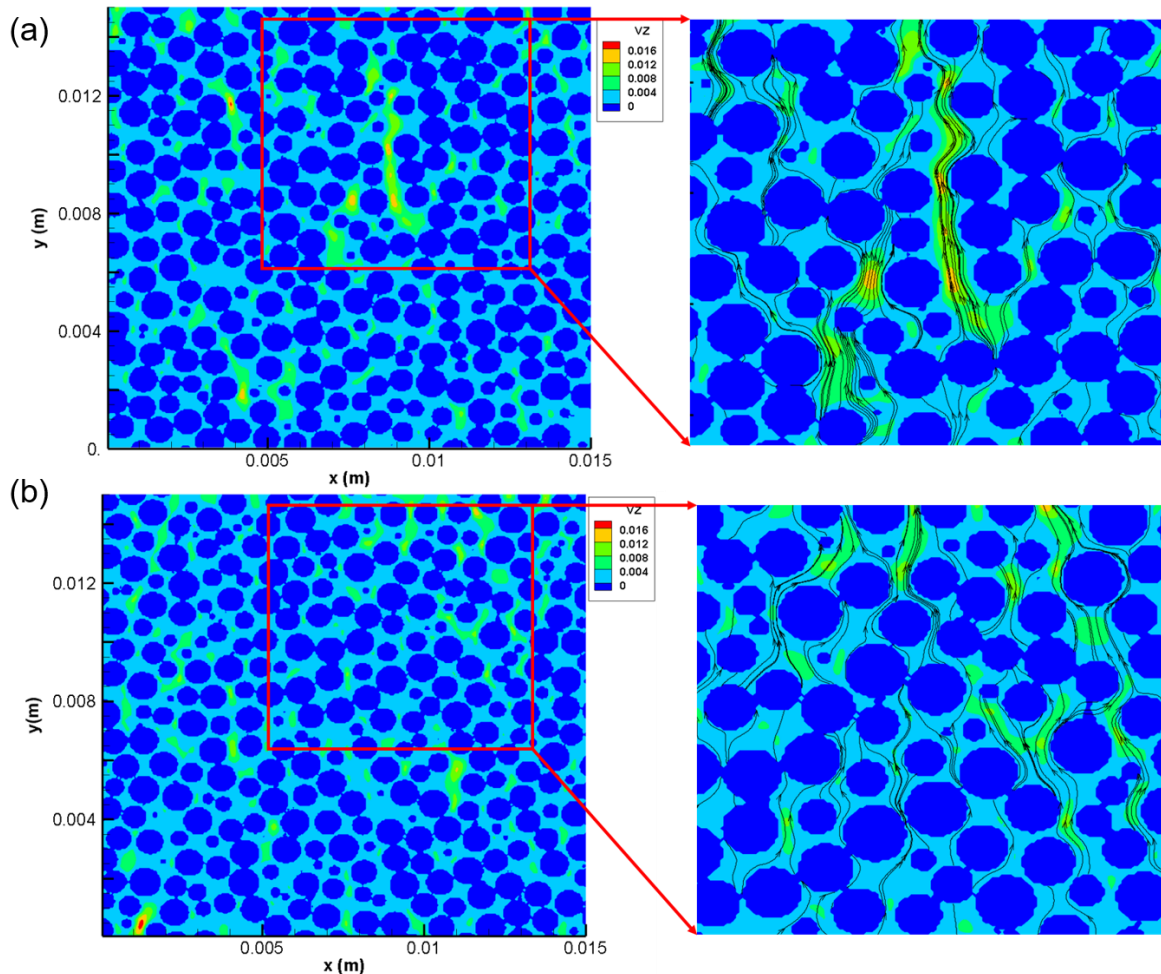


Figure 7.3. LB-simulated flow-velocity-magnitude distributions and associated velocity fields within the pore space of the proppant assembly under effective stress of (a) 1000 psi and (b) 6000 psi. In this realization, the proppant pack particle distribution has diameter COV5% and the average particle diameter is 0.63 mm.

Monte Carlo (MC) simulations on the random distribution of a particle migrating in a porous media were conducted based on the LB simulated flow field. In order to evaluate particle displacement distributions, a large number ( $10^4$ ) of tracer particles were introduced at the inlet of the proppant pack, and the motion of each particle was simulated using Equation 7.10. The number of tracer particles flow into each point at the inlet is determined by the velocity magnitude at that point. The location of each particle deposited in the porous media was recorded, and the cumulative particle distribution (CDF) was obtained as the fraction of tracer particles that deposited in the porous media at each location, as shown in Figure 7.4a. Since the CDF of fine particle migration distance is not a continuous function, we first fitted CDF with an expression and then took a direct derivative of the CDF expression. In this manner, the probability density function (PDF) was derived, as illustrated in Figure 7.4b. In this study, the PDF is a function of fine particle migration distance, which also indicates the relative likelihood of fines deposition location. By fitting Equation 7.9 through the PDF, we can obtain the deposition rate.

Figure 7.5 presents the deposition rate as a function of particle diameter under varying effective stresses. Specifically, the proppant packs were compressed under increasing effective stress, and proppant pack geometries under three effective stress, namely 1000 psi, 3000 psi, and 6000 psi, were selected to study fine particle migration through the porous media. The left panels are three effective stress results from realization 1 and the right panels are three effective stress results from realization 2. We generated ten pairs of

proppant packs with particle diameter COV5% and COV25%, and all the realizations showed similar results as listed in Figure 7.5.

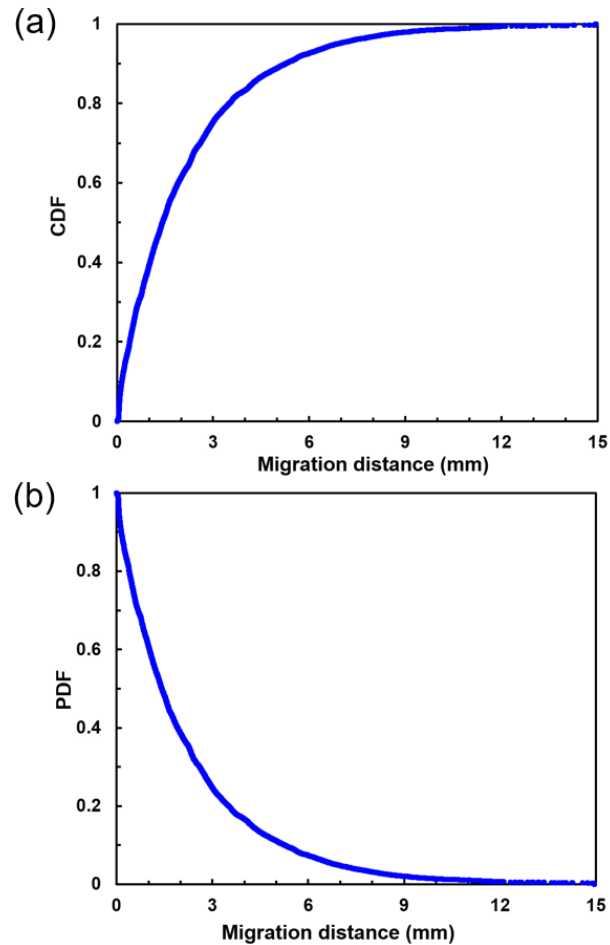


Figure 7.4. (a) Cumulative distribution function (CDF) and (b) probability density function (PDF) as a function of particle migration distance. In this realization, the proppant pack particle distribution has diameter COV5%, the average particle diameter is 0.63 mm, and the effective stress is 6000 psi.

The DEM-LB simulations agreed well with the empirical correlation results from Equation 7.10. The fine particle size with the minimum opportunity to be retained in the proppant pack is 0.1  $\mu\text{m}$  in the simulation. The empirical correlation prediction for the minimum contact opportunity particle size is 1  $\mu\text{m}$ , but the deposition rate of 0.1  $\mu\text{m}$  is

very close to that of 1  $\mu\text{m}$ . The general trend in the relationship between deposition rate and the size of fine particles predicted from simulations is in reasonable agreement with empirical correlation results. It can be seen that each of these curves can be divided into three regions, which is interpreted in different dominant migration mechanisms. When particle size is smaller than 0.01  $\mu\text{m}$ , the deposition rate increases with decreasing fine particle size. This is because when the particle size is small, more fine particles deviate from streamlines and collide with the proppant pack more easily due to the dominant Brownian motion migration mechanisms. As particle size increases, the deposition rates decrease due to the combination of Brownian motion, interception, and gravitational sedimentation mechanisms. When particle size is larger than 1  $\mu\text{m}$ , the gravitational sedimentation mechanism dominates the fine particle migration, and it is easy for fine particles to be intercepted by proppant packs, leading to large deposition rates again. In the empirical correlation, the uniform flow field assumption leads to the underestimation of deposition rates.

Figure 7.5 also illustrates that the deposition rates of the proppant pack with diameter COV5% are larger than that of the proppant pack with diameter COV25% for all three effective stresses. In this study, the proppant pack with diameter COV25% has more larger size particles due to the uniform distribution of particle diameter. As a consequence, larger flow channels were formed more easily, leading to more preferential flow paths, which are all favorable for fine particles transport through the proppant pack. Furthermore, more fine particles flow far away from grain surface in larger flow channels with diverging streamlines, resulting in smaller deposition rates. However, when the effective stress increases to 6000 psi, the deposition rate of COV25% is larger than that

of COV5% for larger fine particles ( $>10 \text{ } \mu\text{m}$ ). With identical stress increase, particles within the proppant pack with a larger diameter COV moved relatively easier, which led to unstable pore structures compared to the proppant pack with a more homogeneous particle diameter distribution. Consequently, the proppant assembly with diameter COV25% experienced more significant changes with respect to pore structure and pore space connectivity, and thus the larger flow channels were more susceptible to collapse. Since larger particles ( $10 \text{ } \mu\text{m}$ ) are dominated by the gravitational sedimentation mechanism, they are more sensitive to the changes in larger flow channels, leading to increased deposition rates at 6000 psi. For smaller fine particles, since their movement are dominated by Brownian motion, they are not sensitive to changes in larger flow channels. This study indicates that the mobility and retention of fine particles are affected by the fracture closure stress and proppant packs with a more heterogeneous particle-diameter distribution favors fine particle migration through the proppant pack.



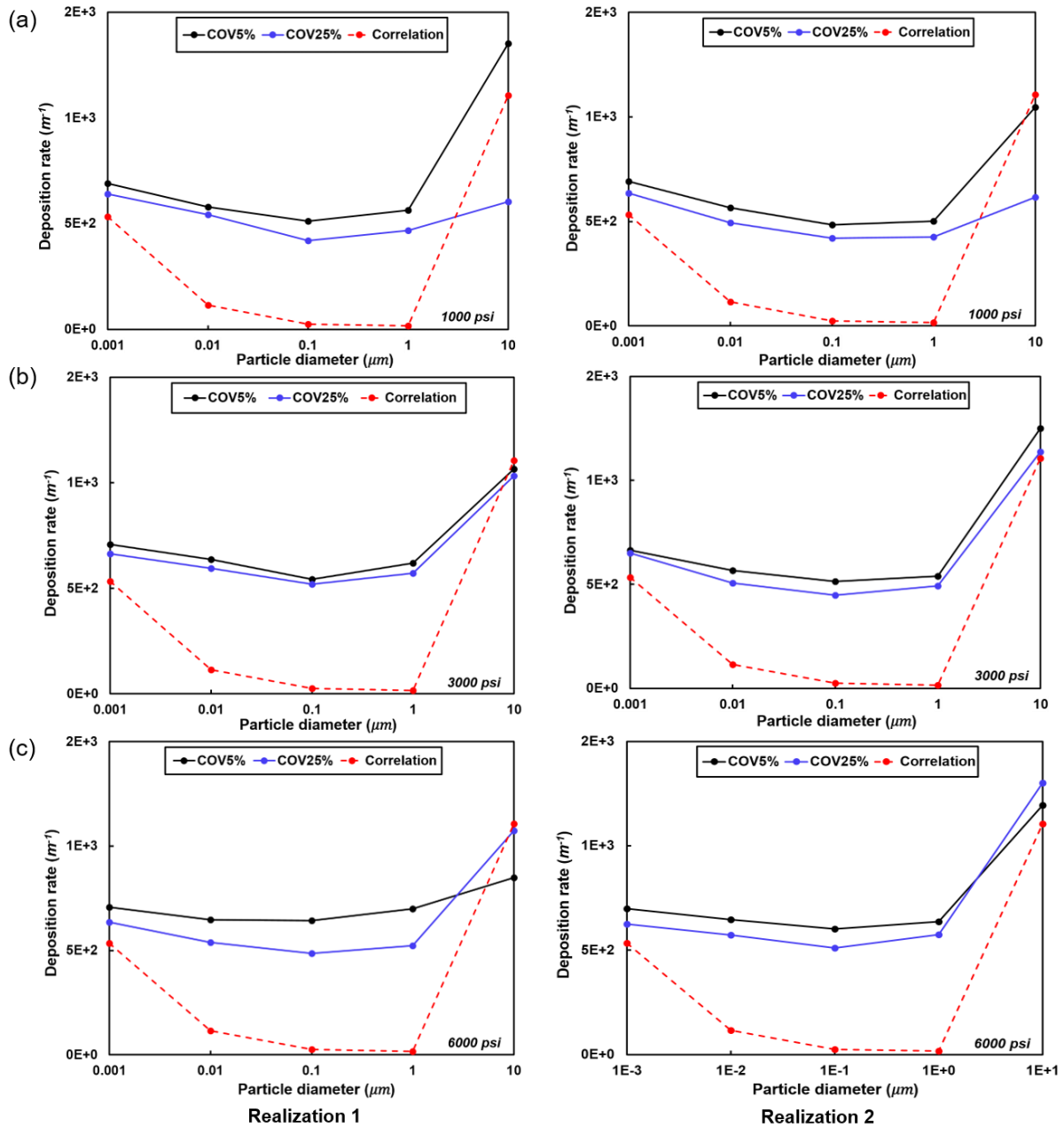


Figure 7.5. Deposition rate as a function of particle diameter under varying effective stresses. The proppant packs with diameter COV5% and COV25% are subjected to three effective stresses, namely a) 1000psi, (b) 3000 psi, (c) 6000 psi. The left panels are three effective stress results from realization 1 and the right panels are three effective stress results from realization 2.

During hydrocarbon production, pore pressure is reduced, and the effective stress of the rock matrix increases; longer pore flow paths and extensive low-velocity regions within

porous medium developed [19, 44]. Fine particle migration through the porous medium is not only influenced by the distribution of flow paths in the porous media, but also the distribution of velocity along those paths [19]. In order to quantify the flow velocity magnitudes between proppant pack with different diameter COVs and effective stresses, we calculated flow velocity distribution PDFs. The PDFs of pore velocity distributions were plot in Figure 7.6a and 7.6b for realization 1 and 2, respectively. In order to clearly present the results, we only listed two effective stress results for each proppant pack. The results associated with 3000 psi were in between 1000 psi and 6000 psi. The velocity distribution is highly skewed with a remarkable peak close to zero. For the same proppant pack, when effective stress increased, the probability distribution in low-velocity regions increased, while the probability distribution in high-velocity regions decreased. This is because under a higher effective stress, the proppant assembly compaction was significant, and pore size reduction was noticeable, and pore space connectivity was consequently reduced. For the same effective stress, the proppant pack with a larger diameter COV has smaller probability distribution in low-velocity-regions and larger probability distribution in high-velocity regions. These changes implies that fine particles migrate through the proppant pack with a larger diameter COV easily.

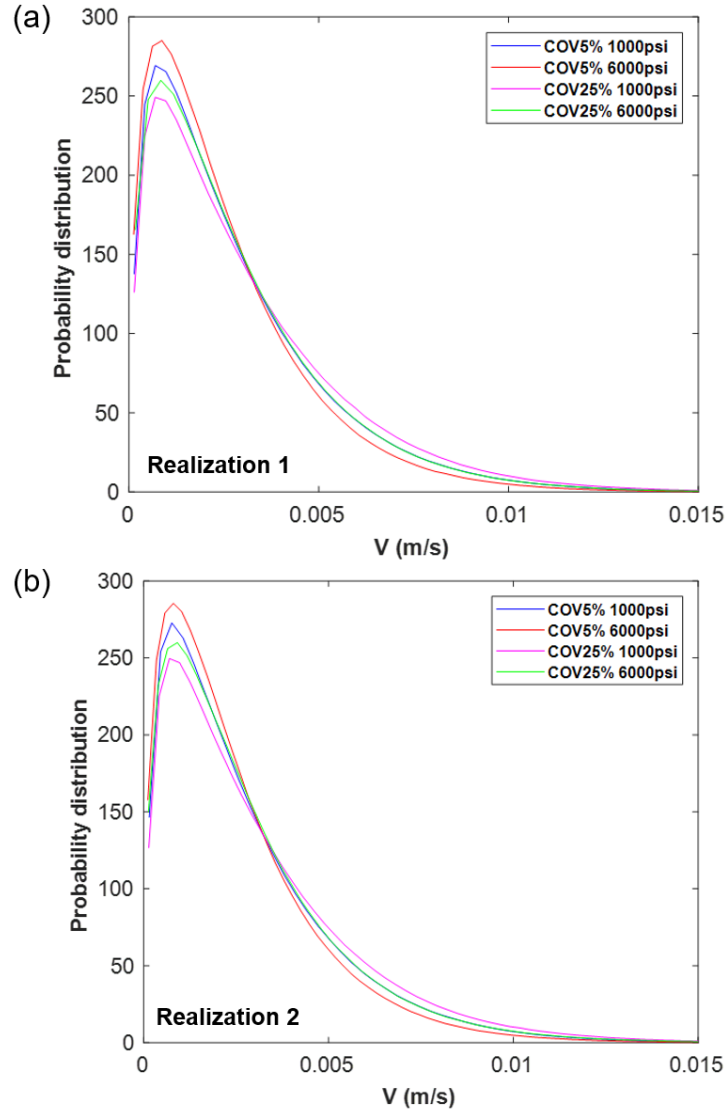


Figure 7.6. Probability density functions (PDFs) of overall Darcy velocity for (a) realization 1 and (b) realization 2 under different effective stresses and diameter COVs

Another important parameter relate to fine particle migration in the porous media is the transition time distribution  $\varphi(t)$ , which is the distribution of time required for particles to move across one pixel length ( $\delta x$ ). In this study, the transition time distribution was evaluated as the distribution of  $\delta x/u$ , where  $u = (u_x^2 + u_y^2 + u_z^2)^{1/2}$  [19, 26, 44]. Here the dimensionless time is defined as  $t^* = t/\delta t$ . The transition time distributions were determined for the two realizations, as shown in Figure 7.7a and Figure 7.7b. As shown

in Table 7.1,  $\varphi(t)$  decayed with time following a power law as  $\varphi(t) \propto t^{*-\alpha}$ . For the same proppant pack, the power law component  $\alpha$  decreased with increasing effective stress. When effective stress increased, the proppant pack experienced more dramatic changes with respect to pore structure and connectivity, which negatively impacted the transport of fine particles in the porous media. With identical effective stress increase, the slope of the transition time distribution for proppant pack with diameter COV5% is higher than that for proppant pack with COV25%. This is because the proppant pack with larger diameter COV provides larger flow channels, which is favorable for fine particles transport through the porous media. The longer transition time indicates that fine particles retained more easily in proppant pack with a smaller diameter COV.

Table 7.1. Power law component  $\alpha$  for two geometries

	Geometry 1		Geometry 2	
	COV5%	COV25%	COV5%	COV25%
1000psi	2.5387	2.5524	2.5381	2.5556
3000psi	2.4075	2.4116	2.3969	2.3989
6000psi	2.3840	2.3947	2.3877	2.3762

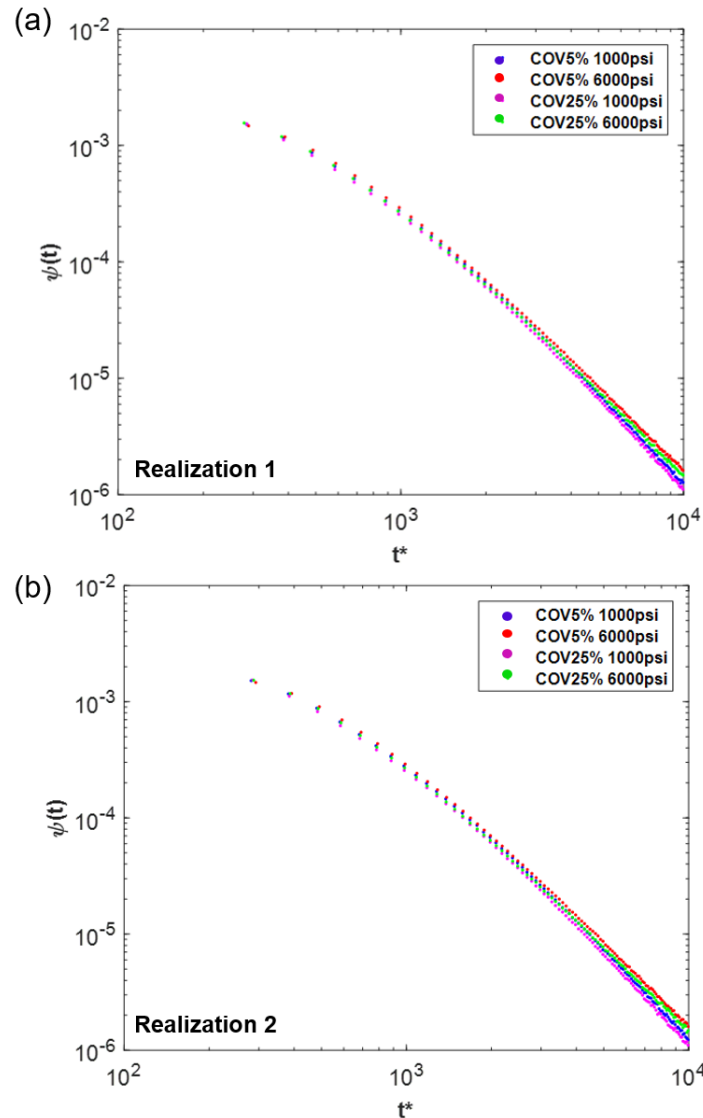


Figure 7.7. Probability density functions (PDFs) the transition time distributions for (a) realization 1 and (b) realization 2 under different effective stresses and diameter COVs

## 7.6 Conclusion

The migration of formation fines is one of the main causes for fracture permeability reduction and well productivity decline in geoenery reservoirs. As the fine particle migrates through the proppant pack, some of the particles become immobilized by means of a variety of deposition mechanisms. Invasion of fines into a proppant pack can affect proppant pack permeability, resulting in a decline in well productivity. This poses a

pressing need to study the effect of proppant particle size variations and pore structure changes on fines migration through the compressed proppant pack during hydrocarbon production. The proppant packs were generated using PFC3D and the fluid flow at a pore scale was simulated using lattice Boltzmann (LB) method. Here, we combined PFC3D and LB methods to evaluate the role of proppant particle size, particle size heterogeneity (variation in proppant particle diameter), and effective stress on slow migration of detached fine particles in a proppant supported fracture. Good match between the DEM-LB framework simulated and empirical correlations predicted deposition rates has been observed. Simulation results showed that a particle size with a minimum contact opportunity existed; smaller particles were transported by Brownian diffusion while larger particles were transported by interception and gravitational settling. With the same proppant diameter COV, the probability distribution in low-velocity regions increased while the probability distribution in high-velocity regions decreased when subjected to increasing effective stress. With identical effective stress, the transition time distribution increased with decreasing proppant particle diameter COV. This study indicates that proppant packs with a more heterogeneous particle-diameter distribution provide better fines control.

The increasing effective stress on the proppant pack during hydrocarbon production increases the degree of complexity for fine particle transport, which highlights the emphasis on how pore structure evolution influences fine migration through porous media. The DEM-LB framework provides a predictive tool to assess the influence of proppant particle size variation and pore structure changes on fines migration through the compressed proppant pack. The findings of this study shed lights on the relationship

between changing pore geometries, fluid flow, and fines migration through a propped hydraulic fracture during hydrocarbon production. This integrated approach provides insight into gravel packing design to minimize fines migration and maximize proppant pack conductivity.

### **Nomenclature**

$A_{cs}$  :Pore structure cross section area

$A$  :Hamaker's constant

$\alpha$  :Rate of fines attached to porous media

$c$  : Lattice speed

$c_s$  : Speed of sound

$C$  :Particle mass concentration in the fluid

$D$  :Diffusivity of dilute solution

$d_m$  :Media diameter

$d_p$  :Particle diameter

$e_i$  : Lattice velocity vector

$f_i$  : Particle-distribution function

$F_i^n$  :Normal components of the contact force

$F_i^S$  :Shear components of the contact force

$g$  :Gravitational acceleration

$K^n$  :Normal stiffness at the contact;

$k^S$  :Shear stiffness at the contact

$k_b$  :Boltzmann constant

$\mathbf{k}$  : Permeability tensor

$\phi$  :Porosity

$P$  : Fluid pressure

$\nabla p$  : Pressure gradient

$\rho_p$  :Mass density of particles

$\rho_f$  :Mass density of the fluid

$\lambda$  : Deposition rate

$r$  :Solute particle radius

$\tau$  :Dimensionless relaxation time

$T$  :Absolute temperature

$t$  : Time

$\Delta t$  : Time step

$\mathbf{u}$  : Flow velocity

$\mathbf{v}$  : Darcy velocity

$v_s$  :Stokes settling velocity of a spherical particle



$U^n$  :Contact displacement in the normal direction

$U_i^S$  :Shear component of the contact displacement

$\mu$  : Dynamic viscosity

$\nu$  : Kinematic viscosity

$\omega_i$  : Weights for D3Q19 model

$\Delta x$  : Lattice spacing

$x$  : Location

## References

1. Mays, D.C., Hydrodynamics of particle clogging in saturated granular media: Analysis and experiments. 2005.
2. Muecke, T.W., Formation fines and factors controlling their movement in porous media. Journal of petroleum technology, 1979. **31**(02): p. 144-150.
3. Habibi, A., M. Ahmadi, P. Pourafshary, and Y. Al-Wahaibi, Reduction of fines migration by nanofluids injection: an experimental study. SPE Journal, 2012. **18**(02): p. 309-318.
4. McDowell-Boyer, L.M., J.R. Hunt, and N. Sitar, Particle transport through porous media. Water Resources Research, 1986. **22**(13): p. 1901-1921.
5. Nguyen, P.D., J.D. Weaver, R.D. Rickman, R.G. Dusterhoft, and M.A. Parker, Controlling formation fines at their sources to maintain well productivity. SPE Production Operations, 2007. **22**(02): p. 202-215.

6. Nguyen, P., R. Dusterhoft, and B. Clarkson. Control of formation fines to provide long-term conductivity in weak, unconsolidated reservoirs. in Offshore Technology Conference. 2005.
7. Nguyen, P.D., J.D. Weaver, and R.D. Rickman. Prevention of geochemical scaling in hydraulically created fractures: laboratory and field studies. in SPE Eastern Regional/AAPG Eastern Section Joint Meeting. 2008.
8. Tiffin, D., G. King, R. Larese, and L. Britt. New criteria for gravel and screen selection for sand control. in SPE Formation Damage Control Conference. 1998.
9. Blauch, M., J. Weaver, M. Parker, B. Todd, and M. Glover. New insights into proppant-pack damage due to infiltration of formation fines. in SPE Annual Technical Conference and Exhibition. 1999.
10. Zou, Y., S. Zhang, and J. Zhang, Experimental method to simulate coal fines migration and coal fines aggregation prevention in the hydraulic fracture. *Transport in porous media*, 2014. **101**(1): p. 17-34.
11. Weaver, J., M. Blauch, M. Parker, and B. Todd, Investigation of Proppant-Pack Formation Interface and Relationship to Particulate Invasion, in SPE European Formation Damage Conference. 1999. p. 16.
12. Mohnot, S.M., Characterization and control of fine particles involved in drilling. *Journal of Petroleum Technology*, 1985. **37**(09): p. 1,622-1,632.
13. Gabriel, G. and G. Inamdar. An experimental investigation of fines migration in porous media. in SPE Annual Technical Conference and Exhibition. 1983.

14. Karazincir, O., W. Williams, and P. Rijken. Prediction of Fines Migration through Core Testing. in SPE Annual Technical Conference and Exhibition. 2017.
15. Gruesbeck, C. and R. Collins, Entrainment and deposition of fine particles in porous media. Society of Petroleum Engineers Journal, 1982. **22**(06): p. 847-856.
16. Yao, K.-M., M.T. Habibiyan, and C.R. O'Melia, Water and waste water filtration. Concepts and applications. Environmental science technology, 1971. **5**(11): p. 1105-1112.
17. Rajagopalan, R. and C. Tien, Trajectory analysis of deep-bed filtration with the sphere-in-cell porous media model. AIChE Journal, 1976. **22**(3): p. 523-533.
18. Elimelech, M., J. Gregory, and X. Jia, Particle deposition and aggregation: measurement, modelling and simulation. 2013: Butterworth-Heinemann.
19. Chen, C., B.L. Lau, J.F. Gaillard, and A.I. Packman, Temporal evolution of pore geometry, fluid flow, and solute transport resulting from colloid deposition. Water resources research, 2009. **45**(6).
20. Cookson Jr, J.T., Removal of submicron particles in packed beds. Environmental Science Technology, 1970. **4**(2): p. 128-134.
21. Spielman, L.A. and S.L. Goren, Capture of small particles by London forces from low-speed liquid flows. Environmental Science Technology, 1970. **4**(2): p. 135-140.
22. Zhu, H., J. Shen, and F. Zhang, A fracture conductivity model for channel fracturing and its implementation with Discrete Element Method. Journal of Petroleum Science Engineering, 2019. **172**: p. 149-161.

23. Fan, M., J. McClure, Y. Han, Z. Li, and C. Chen. Interaction between Proppant Packing, Reservoir Depletion, and Fluid Flow in Hydraulic Fractures. in Offshore Technology Conference. 2017.
24. Fan, M., J. McClure, Y. Han, Z. Li, and C. Chen, Interaction between proppant compaction and single-/multiphase flows in a hydraulic fracture. SPE Journal, 2018. **23**(04): p. 1,290-1,303.
25. Fan, M., Y. Han, and C. Chen. Hydraulic fracture conductivity as a function of proppant concentration under various effective stresses: from partial monolayer to multilayer proppants. in Unconventional Resources Technology Conference. 2017.
26. Chen, C., A.I. Packman, D. Zhang, and J.F. Gaillard, A multi-scale investigation of interfacial transport, pore fluid flow, and fine particle deposition in a sediment bed. Water Resources Research, 2010. **46**(11).
27. Itasca Consulting Group, I., PFC3D – Particle Flow Code in 3 Dimensions, Version 4.0 User’s Manual. Minneapolis: Itasca. 2008.
28. Cundall, P.A., A Computer Model for Simulating Progressive Large-Scale Movements in Blocky Rock Systems. Proc. Int. Symp. Int. Rock Mech, 1971(2(8)).
29. Cundall, P.A. and O.D. Strack, A discrete numerical model for granular assemblies. J geotechnique, 1979. **29**(1): p. 47-65.
30. Chen, S. and G.D. Doolen, Lattice Boltzmann method for fluid flows. Annual review of fluid mechanics, 1998. **30**(1): p. 329-364.
31. Succi, S., The lattice Boltzmann equation: for fluid dynamics and beyond. 2001: Oxford university press.

32. Succi, S., R. Benzi, and F. Higuera, The lattice Boltzmann equation: a new tool for computational fluid-dynamics. *Physica D: Nonlinear Phenomena*, 1991. **47**(1-2): p. 219-230.
33. Chen, H., S. Chen, and W.H. Matthaeus, Recovery of the Navier-Stokes equations using a lattice-gas Boltzmann method. *Physical Review A*, 1992. **45**(8): p. R5339.
34. Grunau, D., S. Chen, and K. Eggert, A lattice Boltzmann model for multiphase fluid flows. *Physics of Fluids A: Fluid Dynamics*, 1993. **5**(10): p. 2557-2562.
35. Han, Y. and P.A. Cundall, Lattice Boltzmann modeling of pore-scale fluid flow through idealized porous media. *International Journal for Numerical Methods in Fluids*, 2011. **67**(11): p. 1720-1734.
36. Han, Y. and P.A. Cundall, LBM–DEM modeling of fluid–solid interaction in porous media. *International Journal for Numerical Analytical Methods in Geomechanics*, 2013. **37**(10): p. 1391-1407.
37. Chen, C., A.I. Packman, and J.F. Gaillard, Pore-scale analysis of permeability reduction resulting from colloid deposition. *Geophysical Research Letters*, 2008. **35**(7).
38. Chen, C., D. Hu, D. Westacott, and D. Loveless, Nanometer-scale characterization of microscopic pores in shale kerogen by image analysis and pore-scale modeling. *Geochemistry, Geophysics, Geosystems*, 2013. **14**(10): p. 4066-4075.
39. Chen, C., Z. Wang, D. Majeti, N. Vrvilo, T. Warburton, V. Sarkar, and G. Li, Optimization of lattice Boltzmann simulation with graphics-processing-unit parallel computing and the application in reservoir characterization. *SPE Journal*, 2016. **21**(04): p. 1,425-1,435.

40. Li, Y. and P. Huang, A coupled lattice Boltzmann model for advection and anisotropic dispersion problem in shallow water. *Advances in Water Resources*, 2008. **31**(12): p. 1719-1730.
41. Ginzburg, I., Consistent lattice Boltzmann schemes for the Brinkman model of porous flow and infinite Chapman-Enskog expansion. *Physical Review E*, 2008. **77**(6): p. 066704.
42. Ginzburg, I., D. d'Humières, and A. Kuzmin, Optimal stability of advection-diffusion lattice Boltzmann models with two relaxation times for positive/negative equilibrium. *Journal of Statistical Physics*, 2010. **139**(6): p. 1090-1143.
43. Inamuro, T., M. Yoshino, and F. Ogino, Lattice Boltzmann simulation of flows in a three-dimensional porous structure. *International journal for numerical methods in fluids*, 1999. **29**(7): p. 737-748.
44. Zhang, X. and M. Lv, Persistence of anomalous dispersion in uniform porous media demonstrated by pore-scale simulations. *Water Resources Research*, 2007. **43**(7).

## Chapter 8 Conclusions and future work

### 8.1 Conclusions

In this dissertation, a geomechanics/fluid-mechanics coupled numerical workflow was developed to study the hydraulic and mechanical interactions between the reservoir rock, the proppant pack, and hydrocarbon fluids. DEM was used to simulate the process of proppant-particle compaction at different loading stresses. The pore-structure geometries were then extracted and imported into an LB simulator as internal boundary conditions of flow modeling to simulate single- and multiphase flows. Using this integrated workflow, the interactions between reservoir depletion, proppant-particle compaction, single-/multiphase flows and non-Darcy flows in a hydraulic fracture, fracture conductivity evolution from partial-monolayer concentrations to multilayer concentrations, the potential effects of mixed proppants of different sizes and types on the fracture conductivity, and the relationship between changing pore geometries, fluid flow, and fines migration through a propped hydraulic fracture during the reservoir depletion process, were comprehensively investigated. In order to understand multiphase flow phenomena in the formation rock, two-phase LB flow simulations were conducted directly based on the micro-CT scanned images and the influence of various combinations of the dimensionless numbers on relative permeability curves are analyzed. Based on the experimental and numerical studies and analyses, the following conclusions can be drawn:

1. Under the same effective stress, a proppant pack with a smaller diameter COV, had higher porosity and permeability as well as a smaller fracture-width

- reduction; these are all favorable for maintaining the fracture conductivity during the process of hydrocarbon extraction.
2. The relative permeability of oil was more sensitive to changes in geometry and stress, compared with that of water; when effective stress increased continuously, oil relative permeability in one proppant assembly increased first and then decreased; the combination of high diameter COV and high effective stress leads to a larger pressure drop and consequently stronger non-Darcy flow effects.
  3. The experiment/simulation-integrated framework accounts for all important multiphysics processes over the full range of the conductivity curve from partial-monolayer proppant concentrations to multilayer proppant concentrations; it can capture the local maximum of the conductivity curve and achieve considerable fracture conductivity using a partial-monolayer proppant structure, which has much lower material costs compared to conventional multilayer structures.
  4. Through the continuum mechanics-DEM-LBM workflow, the interaction between rock matrix and proppant as well as fluid flow in a hydraulic fracture was studied; it indicates that a fracture/proppant system with stronger rock matrix and uniform proppant particle diameter distribution provides better support to the fracture, in terms of sustaining fracture conductivity during the process of reservoir depletion.
  5. The study of proppant mixtures shows that mixing of similar proppant sizes (mesh-size-20/40) has less influence on the overall fracture conductivity than mixing a very fine mesh size (mesh-size-100); selection of proppant type is more important than proppant size selection when a proppant mixture is used. Increasing larger-size proppant composition in the proppant mixture helps



- maintain fracture conductivity when the mixture contains lower-strength proppants.
6. The main focus of Chapter 6 is the dependence of relative permeability curves on the contact angle,  $Ca$ , viscosity ratio, the various combinations between them, as well as the influence of flow direction and anisotropy of the rock sample on the relative permeability curves. Simulation results show that a decreasing contact angle causes a decrease in wetting-fluid relative permeability and an increase in non-wetting fluid relative permeability. An increasing  $Ca$  will facilitate both wetting and non-wetting fluid to move more easily. With the continuously decreasing contact angle, increasing viscosity ratio will help increase non-wetting fluid relative permeability and mitigate wetting fluid relative permeability reduction. Non-wetting fluid relative permeability experiences more variations when the flow direction is changed, which indicates that there exists strong anisotropy in large pore networks.
  7. Results of conducted simulations in Chapter 7 demonstrate that a critical fine particle size exists: when a particle diameter is larger or smaller than this size, the deposition rate increases. This study also indicates that proppant packs with a more heterogeneous particle-diameter distribution provide better fines control.

## **8.2 Future work**

The numerical workflow combines DEM simulation with LB simulation and provides an insightful tool to study the complicated, multiphysics processes within a proppant/fracture system, which will benefit the optimization processes for proppant

placement, completion design, and well production. Some aspects of this research can be further investigated in the future:

1. High-strength ceramic proppant can withstand stress of higher than 10,000 psi, while sand can be crushed at around 6,000 psi effective stress. Under higher effective stress, proppant crushing for both two types of proppants are expected. The crushed proppants can cause straining in the pore throat, and then affect the proppant pack permeability, leading to subsequent conductivity loss. This poses a pressing need for the numerical model to take into account the proppant crushing process in the high-stress regime. The future work aims to study the influence of proppant crushing on the fracture conductivity.
2. In the hydraulic fracturing treatment process, proppants are pumped along with fracturing fluids to prevent hydraulic fractures from closing during the reservoir depletion process and to maintain conductive channels between the reservoir and wellbore. The future work aims to study proppant transport in propagating fractures and fracture conductivity distribution through fractures.
3. Formation damage due to fines migration can affect the proppant pack permeability, resulting in subsequent conductivity loss. In this study, we assume that fines are mainly generated from the reservoir formation. However, in unconventional reservoirs, clay swelling can reduce the pore space, block the pore throat, and lead to the permeability deterioration. The future work aims to study fines migration in the rock-proppant system to account for the clay-swelling problem.

4. In the oil and gas industry, fracture conductivity is one of the most important factor to evaluate the effectiveness of hydraulic fracturing. It depends closely on the strength of fracture rock formation as well as the interaction between the proppant pack and the rock formation. In Chapter 4, the continuum mechanics, DEM, and LBM coupled approach is proposed, which can study the fracture conductivity evolution successfully. The future work aims to incorporate more factors into the model, such as rock surface roughness, strain-softening behavior, shear failure, etc.
5. For the experiment in Chapter 6, the contact angle has a distribution from  $8.6^\circ$  to  $104.2^\circ$ , but in the simulation only three contact angle  $0^\circ$ ,  $45^\circ$ , and  $90^\circ$  are used. The future work aims to apply the measured contact angle distribution into the simulation to study the influence of surface wettability heterogeneity on relative permeability curves.

### **8.3 Contributions**

Through this research work, a rock-fluid integrated numerical workflow to simulate the complicated processes within a proppant-supported hydraulic fracture was successfully developed. By using this workflow, the influence of the proppant size and distribution on porosity, permeability, conductivity, relative permeability, fine migration, as well as the conductivity evolutions from partial monolayer concentrations to multilayer concentrations were studied comprehensively. This study has the potential to benefit the prediction and optimization of hydrocarbon recovery from hydraulic fractures and improve water resources management. The multiphase flow study will benefit the fundamental understanding of petrophysical properties associated with multiphase flow

and relative permeability upscaling in natural geological formations. The developed numerical methods have the potential to make broader impacts and contribute to the study of other geomechanical, geoenergy, and geoenvironmental processes that involve single-/multiphase flows within a fracture filled with granular materials and subjected to closure pressure, such as rock-mass instability, geologic carbon sequestration, and nonaqueous phase-liquid transport.

## Appendix Copyright releasing documents from publishers

5/28/2019

RightsLink Printable Job Ticket

### SOCIETY OF PETROLEUM ENGINEERS ORDER DETAILS

May 28, 2019

Order Number	501488439
Order date	May 24, 2019
Licensed content publisher	Society of Petroleum Engineers
Licensed content title	SPE JOURNAL -RICHARDSON-
Licensed content date	Jan 1, 1996
Type of Use	Thesis/Dissertation
Requestor type	Academic institution
Format	Electronic
Portion	chapter/article
Number of pages in chapter/article	14
The requesting person/organization is:	Ming Fan
Title or numeric reference of the portion(s)	The whole article
Title of the article or chapter the portion is from	Interaction between Proppant Compaction and Single-/Multiphase Flows in a Hydraulic Fracture
Editor of portion(s)	N/A
Author of portion(s)	The first author
Volume of serial or monograph.	N/A
Issue, if republishing an article from a serial	23(4)
Page range of the portion	1-14
Publication date of portion	August 2018
Rights for	Main product
Duration of use	Life of current edition
Creation of copies for the disabled	no
With minor editing privileges	no
For distribution to	Worldwide
In the following language(s)	Original language of publication
With incidental promotional use	no
The lifetime unit quantity of new product	Up to 499
Title	Using an Experiment/Simulation-integrated Approach to Investigate Fracture Conductivity Evolution and Non-Darcy Flow in a Proppant-Supported Hydraulic Fracture
Institution name	Virginia Tech
Expected presentation date	Jun 2019
Total (may include CCC user fee)	0.00 USD

**SOCIETY OF PETROLEUM ENGINEERS ORDER DETAILS**

May 28, 2019

Order Number	501488438
Order date	May 24, 2019
Licensed content publisher	Society of Petroleum Engineers
Licensed content title	SPE JOURNAL -RICHARDSON-
Licensed content date	Jan 1, 1996
Type of Use	Thesis/Dissertation
Requestor type	Academic institution
Format	Electronic
Portion	chapter/article
Number of pages in chapter/article	17
The requesting person/organization is:	Ming Fan
Title or numeric reference of the portion(s)	The whole article
Title of the article or chapter the portion is from	Using an Experiment/Simulation-integrated Approach to Investigate Fracture Conductivity Evolution and Non-Darcy Flow in a Proppant-Supported Hydraulic Fracture
Editor of portion(s)	N/A
Author of portion(s)	The first author
Volume of serial or monograph.	N/A
Page range of the portion	1-17
Publication date of portion	May 1st
Rights for	Main product
Duration of use	Life of current edition
Creation of copies for the disabled	no
With minor editing privileges	no
For distribution to	Worldwide
In the following language(s)	Original language of publication
With incidental promotional use	no
The lifetime unit quantity of new product	Up to 499
Title	Using an Experiment/Simulation-integrated Approach to Investigate Fracture Conductivity Evolution and Non-Darcy Flow in a Proppant-Supported Hydraulic Fracture
Institution name	Virginia Tech
Expected presentation date	Jun 2019
Total (may include CCC user fee)	0.00 USD



**Title:** Comprehensive study of the interactions between the critical dimensionless numbers associated with multiphase flow in 3D porous media

**Author:** Ming Fan, Laura E. Dalton, James McClure, Nino Ripepi, Erik Westman, Dustin Crandall, Cheng Chen

**Publication:** Fuel

**Publisher:** Elsevier

**Date:** 15 September 2019

© 2019 Elsevier Ltd. All rights reserved.

Logged in as:

Ming Fan

Account #:

3001459201

LOGOUT

Please note that, as the author of this Elsevier article, you retain the right to include it in a thesis or dissertation, provided it is not published commercially. Permission is not required, but please ensure that you reference the journal as the original source. For more information on this and on your other retained rights, please visit: <https://www.elsevier.com/about/our-business/policies/copyright#Author-rights>

BACK

CLOSE WINDOW

Copyright © 2019 [Copyright Clearance Center, Inc.](#) All Rights Reserved. [Privacy statement](#). [Terms and Conditions](#). Comments? We would like to hear from you. E-mail us at [customercare@copyright.com](mailto:customercare@copyright.com)

---

## Paper reprint permission for thesis

3 messages

---

Patrick Fan <mingfan@vt.edu>  
To: info@armarocks.org  
Cc: Cheng Chen <chen08@vt.edu>

Fri, May 24, 2019 at 10:59 PM

Dear Peter,

I am graduating the following June and I am working on my PhD dissertation now. I am planning to include one paper that I submitted to ARMA last year.

The paper is : Investigating the Impact of Proppant Embedment and Compaction on Fracture Conductivity Using a Continuum Mechanics, DEM, and LBM Coupled Approach

Please, let me know how to get permission to include this papers in my dissertation and be reprinted.

Thank you very much for your time. I appreciate it.

Ming Fan, Ph.D. Candidate  
Virginia Tech  
Email: [mingfan@vt.edu](mailto:mingfan@vt.edu)  
TEL: [304-777-7974](tel:304-777-7974)

---

Peter Smeallie <peterhsmeallie@gmail.com>  
To: Patrick Fan <mingfan@vt.edu>, info@armarocks.org  
Cc: Cheng Chen <chen08@vt.edu>

Sat, May 25, 2019 at 8:45 AM

Dear Ming,

First and foremost, discuss with your advisor to assure compliance with academic requirements.

ARMA hereby gives you permission to use the paper as described below with proper attribution.

Best,

Peter

Peter Smeallie  
Executive Director  
American Rock Mechanics Association  
[600 Woodland Terrace](#)